Ultrasound Characterization of Structure and Density of Coral as a Model for Trabecular Bone

by

Yurong Sun

A Thesis

Submitted to the Faculty

Of the

Worcester Polytechnic Institute

in partial fulfillment of the requirements for the

Degree of Master of Science

in

Electrical and Computer Engineering

July 2000

APPROVED:

Prof. Peder C. Pedersen, Major Advisor

Prof. Allen H. Hoffman, Committee member

Prof. Denise W. Nicoletti, Committee member

Prof. Sean S. Kohles, Committee member

Extended Abstract

The goal of this thesis work has been to investigate improved diagnostic methods for both detecting osteoporosis and estimating fracture risk non-invasively, by assessing bone mass density (BMD) and bone microstructure. The thesis evaluates new approaches for analyzing through-transmission ultrasound signals using coral samples as models for trabecular bone. The measurement system was placed in a water tank and operated in pulse transmission mode using $0.5MHz$ transducers. The received signal was then digitized and further processed by signal processing software on a personal computer. The reference density and density distribution were determined by dual-energy x-ray absorptiometry (DEXA) and the coral sample dry weight. Physical observations and micrographs of the coral samples were used as references for microstructure and for dominant growth axes.

Nine coral samples with dimension of 1.45" in diameter and 2" in height were separated into 3 groups with 3 different dominant microstructure growth axes in each group. The density of 2 out of the 3 groups was changed by the decalcification process using formic acid. Thus, all 9 coral samples in 3 groups were analyzed at their original density level, the 6 coral samples in group 2 and group 3 were analyzed after an intermediate level of decalcification with their dry weights decreased by about 20%, corresponding to a DEXA value decrease by about 16%, and the 3 samples in group 3 were analyzed after heavy decalcification, with their dry weights decreased by about 40% and corresponding DEXA value decreased by about 33%.

From the acoustic wave transmitted through coral samples, 2 reproducible wave components, the fast and slow waves, were found present in the received signal and are

believed to be related to the anisotropic microstructure of coral samples. The amplitude of the fast wave varied periodically when the coral sample was rotated while the amplitude of the slow wave did not vary noticeably. To evaluate the effect of the direction of the growth axis relative to the measurement direction, two rotation approaches, rotation of the coral sample and rotation of the receiving transducer around the coral sample, were adopted in order to find the angular variation of received ultrasound signal and the correspondent ultrasound parameters. A reference orientation was determined for each coral samples at its original density level and defined as the orientation where the fast wave has the maximum amplitude. Three ultrasound signal parameters were extracted from received signal at different density levels in this thesis work:

Broadband Ultrasonic Attenuation (BUA). BUA represents the linearized frequency slope of the normalized attenuation of the coral sample, measured as a function of sample rotation angle and decalcification level. Due to the fact that the fast and slow waves exist in the received signal at original density level and the intermediate decalcified density level, we calculated BUA for the fast and slow waves as well as for the entire signal by using appropriate window functions. However, the fast wave and the slow wave overlap when the coral sample was decalcified below a certain density level, allowing only the BUA for the entire signal to be calculated.

Analytic signal magnitude of impulse response. The impulse response is obtained from inverse filtering by taking advantage of Wiener Filter theory, and its analytic signal magnitude is calculated via the Hilbert transform. The analytic signal magnitude of the impulse response is analyzed as functions of decalcification level and as a function of

either coral sample rotation angle or receiving transducer rotation angle. For coral sample rotation approach, the analytical impulse response analysis was processed not only for the entire signal, but also for the fast and slow waves when coral samples were at the original density level or the intermediate decalcification level. However, when the receiving transducer was rotated around the coral sample, the correspondent analytical impulse response was only calculated for the entire signal because the signal was much more complex due to the scattering and multi-paths effects on received signal.

Angular decorrelation. The angular decorrelation measures the analytic signal magnitude peak value of the normalized cross-correlation coefficient between the reference received signal and the received signals from a range of angular positions of the receiving transducers position around the reference angle, as a function of decalcification level. Thus, angular decorrelation determines the rate at which the received signal changes value when the angle between transmitting transducer and receiving transducer is varied. Because of scattering and multi-paths effects, the angular decorrelation was processed only on the entiresignal and was generated by rotating the receiving transducer for specific orientations of the coral sample.

Discussion. Based on the above ultrasound parameters, several results were obtained as described below: The BUA value exhibited angular periodicity for both the fast wave and the entire signal at the original density level. The degree of variation was influenced by the growth axis relative to measurement plane, that is, the periodicity is most apparent when the coral sample growth axis is parallel to the measurement plane. The periodicity disappeared at the intermediate decalcification level and then slightly appeared again in the entire signal BUA value after heavy decalcification. The results

indicate that decalcification of the coral samples produce complicated changes in the microstructure. The angular periodicity related to growth axis direction may have been masked by much stronger scattering effects from many new isolated trabecular element created after the elements connectivity was destroyed. The growth axis then became dominant again when the overall connectivity between the fine microstructural elements were removed and the number of microstructural elements reduced to below a certain density level. Furthermore, the average BUA values for the fast wave and for the entire signal increased when the coral sample density decreased to intermediate decalcification level and then decreased again at heavy decalcified density level. However, for the slow wave BUA, there was no apparent angular periodicity and apparent variation with respect to coral density. The average BUA value for the slow wave did neither change noticeably. This indicates that the BUA for the fast wave has most diagnostic information.

For the analytical signal magnitude of the impulse response, similar angular periodicity as a function of sample rotation was exhibited for both the fast wave and the entire signal at the original density level. The degree of variation was determined by the growth axis relative to the measurement plane. The periodicity disappeared at the intermediate decalcification level and then slightly reappeared in the entiresignal analytical impulse response after heavy decalcification. This also demonstrates the complex microstructure variation with respect to coral density. For the slow wave, no apparent angular periodicity and variation with density level was found. For the analytical signal magnitude of impulse response, observed as a function of transducer rotation, the received signal is very complex: when the receiving transducer angle is

smaller than 60^o, the received signal appears to be due to the signal transmitted through the coral sample; when the angle is larger than 60^o, the received signal appears to be due to the insonifying wave scattered by the coral sample. We observed that at original density level, the peak values of the analytical signal magnitude of impulse responses were smaller when the rotating angle of the transducer is less than 60^o comparing with the peak values when the rotating angle is larger than 60^o. However, as the density decreased, the analytical signal magnitude of impulse responses peak values became relatively angle independent. After samples were heavily decalcified, the peak values of the analytical signal magnitude of impulse responses became smaller again, but mainly for rotation angles of the transducer less than 60^o.

For most of the samples, the angular decorrelation exhibited slower change with angle after light decalcification compared with the change in the decorrelation at original density. The angular decorrelation became irregular after heavy decalcification. For the angular decorrelation analysis for specific orientations of the coral sample, in clockwise order with respect to the reference angle, we didn't observe consistent differences between their correspondent cross-correlation coefficient variations.

The above results indicate that these ultrasound parameters may be useful in detecting changes in both bone mineral density (BMD) and the presence of dominant trabecular bone structure axis.

Acknowledgements

I would like to thank Professor Peder C. Pedersen, my thesis advisor, for his guidance and encouragement throughout the thesis work. His incisive comments and research methodologies benefited me greatly. His continuous help, undying inspiration and persistent spirit encouraged me to overcome the obstacles and reach the goal. His friendliness and thoughtfulness made it really enjoyable to work with him.

I would also like to thank Dr. Jack Debes at Interpore Inc., CA, for providing the initial coral samples as well as the 10 larger coral samples that were used in this thesis work. The support from National Science Foundation is also acknowledged.

I appreciate Li Wan and Ruben Lara-Montalvo for their support and help. They made the working environment of the lab very warm and fun. I also appreciate Noah Cushing, who did a lot of work in software construction of this thesis work, which made it possible to finish the vast amount of work.

Lastly, but not least important, my sincere thanks go to my friends and my family, who gave me coverage and confidence when I was frustrated. Without their love, support and affection, this undertaking might not have been possible.

Table of Contents

List of Figures

List of Tables

Chapter 1

INTRODUCTION

1.1 Background

1.1.1 Health Care Significance of Osteoporosis

It has been estimated that osteoporosis is responsible for at least 1.2 million fractures a year in the US, and this incidence rate is expected to grow substantially due to the rapid increase in the aging population [1]. Therefore, it is pertinent to investigate potentially more efficient and safe bone measurement and analysis tools for early osteoporosis prediction.

There are actually two types of bone: the outer layer of dense bone which is called cortical bone, and the central bone structure, a two-component material comprised of a complex, interconnected structure of hard bone with cavities filled by soft tissue, which is termed cancellous or trabecular bone. These two kinds of bone can also be categorized based on the solid volume fraction which is the ratio of solid volume to overall bone volume. The bone with a low volume fraction of solid (less than 70%) is classified as trabecular (spongy) bone and above 70% cortical (compact) bone. To understand the nature of osteoporosis, the life period of bone should first be understood. Normally, bone is constantly formed and resorbed and there is balance between the two opposite processes. Generally, the formation and resorption processes are carried on primarily in trabecular bone.

When resorption of bone exceeds the formation over a long period of time, the bone structure is weakened and this pathology is referred to as osteoporosis, as illustrated in Figure1.1. Hence, osteoporosis is defined as a disease characterized by low bone mass and microarchitectural deterioration of bone tissue. It is usually a painless disease until a bone breaks or fractures. Fractures are the most common result of osteoporosis. These fractures are usually in the spine, hip and wrist, where exist a large amount of trabecular bone [1].

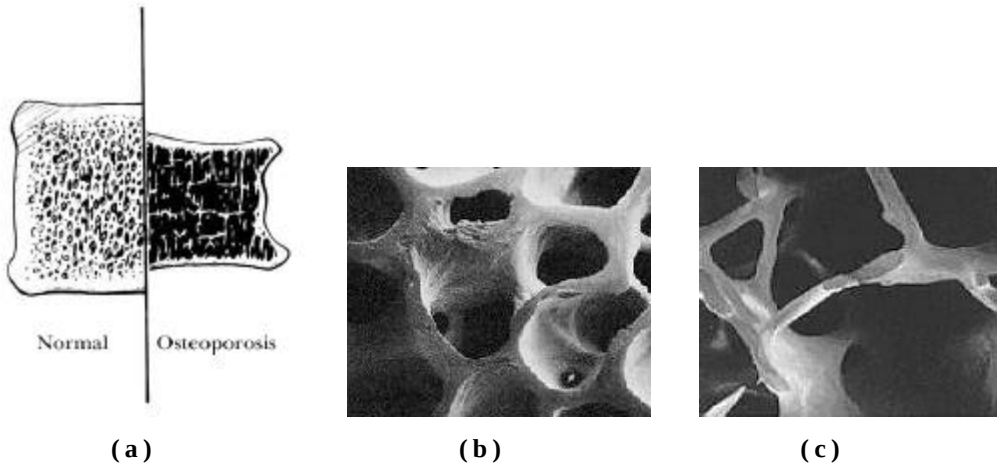

Figure 1.1 Comparison of normal bone sample and osteoporosis bone sample (a) overview (source: http://www.mayohealth.com); (b) microscope photo of normal bone (source: http://www.nof.org); (c) microscope photo of osteoporotic bone (source: http://www.nof.org)

From Figure 1.1 above, it can be noticed that osteoporotic bone has become much thinner and more porous than normal bone, deformed by the effect of osteoporosis. Clinically, osteoporosis may be differentiated into two types: Type I and Type II [1]. Type I osteoporosis is induced by estrogen deficiency (estrogen is an inhibitor of bone resorption) and therefore occurs in women after menopause. Type I primarily affects the trabecular bone and hence leads to fractures at sites with a large amount of trabecular bone, such as wrist, hip, etc. Aging is another factor in the cause of osteoporosis, as

shown in Figure 1.2 below. Senile osteoporosis, or Type II, affects both sexes after age 70 and results in a reduced bone density of both the cortical and trabecular bone.

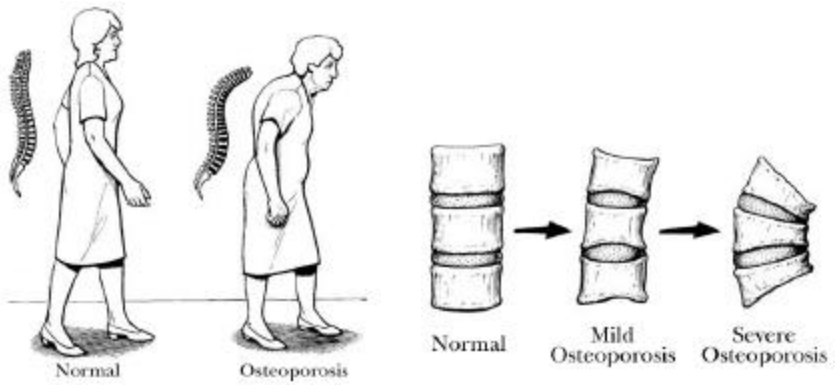

(a) **(b)**

Figure 1.2 a) Age is the other reason of osteoporosis; b) different osteoporosis owing to aging (source: http://www.mayohealth.com)

If people have osteoporosis, especially for postmenopausal women, there are several effective, well-tolerated and affordable medications in addition to maintaining an adequate calcium intake and exercising. These include (source: http://www.nof.org/osteoporosis):

- *Estrogen*. It prevents osteoporosis for women who are deficient in this hormone.
- *Alendronate (Fosamax)*. It is not a hormone but is almost as effective as estrogen and acts on bone in much the same way. The drawback is that Fosamax can be hard on stomach.
- *Calcitonin (Miacalcin)*. It is not quite as effective as either estrogen or Fosamax, however, its safe and has few side effects. Men can use it too.
- *Raloxifene (Evista)*. It is a synthetic estrogen and is not quite as effective as estrogen or Fosamax either.

In addition to the above successful medications for treating osteoporosis, people are exploring new treatments to prevent osteoporosis in order to save large costs of health care. Early detection of bone loss is the key for this purpose, and several diagnostic methods have been developed for detection and monitoring of osteoporosis.

For the early diagnosis of Type I osteoporosis, the major techniques can be separated into two categories: one category based on ionizing radiation, which here will be referred to as non-ultrasound diagnostic techniques, and the other category is based on ultrasound referred to as ultrasound diagnostic techniques, without utilizing ionizing radiation. This thesis work falls within the latter category.

1.1.2 Non-ultrasound Diagnostic Techniques

The common, non-ultrasound techniques are: single-photon absorptiometry, dual-photon absorptiometry, dual-energy x-ray absorptiometry (DEXA), and quantitative computed tomography (QCT) [2].

Single-photon absorptiometry uses a radioactive source (Iodine 125). The percentage of photons transmitted through the bone is measured to indicate the bone mineral content; however, the results are not very reproducible due to the effect of soft tissue around bone. Dual-photon absorptiometry has the advantage of being able to eliminate the effect of soft tissue and can therefore be applied to sites such as the proximal portion of the femur, which also contains mostly trabecular bone. It likewise measures bone mineral content, in the form of calcium along the path of the photon beam. Both of these techniques provide an integrated assessment of mineral content, but they do not give any information regarding the architecture and microstructure of the

trabecular bone. Dual-energy x-ray absorptiometry (DEXA) functions in a similar fashion to dual-photon absorptiometry and has similar advantages, but uses an x-ray beam for the measurement. In all of the above-mentioned techniques there is some amount of exposure to ionizing radiation [7].

Quantitative Computed Tomography (QCT) can extract information about a specific sample volume (localized measurements) and can therefore exclude the effect of the overlying cortical bone, but QCT is only sensitive to mineral content and not the architecture of the trabecular bone. The high cost and the ionizing radiation must also be considered disadvantages [6].

As stated, these techniques all measure bone mineral density (BMD), which measure bone mineral content. The greater the bone mineral content, the stronger or denser the bone is. However, inconsistencies between mechanical properties and the density measurements give evidence that other factors, such as the structural organization of trabecular bone should be considered in order to accurately detect osteoporosis [11].

1.1.3 Ultrasound Diagnostic Techniques

Ultrasound is in many aspects an ideal tool for diagnosis of osteoporosis, as it is non-invasive, painless, utilizes no ionizing radiation and is well suited for use in clinics. Furthermore, the instrumentation is relatively inexpensive.

The through-transmission ultrasound system is generally used for detecting osteoporosis, where 2 transducers are used, working in transmitting and receiving modes, respectively. The transmitting transducer will transmit the pulse, which then is received by the receiving transducer. Only in pulse-echo mode can the received signal be

processed so that information from a specific sample volume is obtained. The ultrasound parameters analyzed in this thesis work are obtained from through-transmission system.

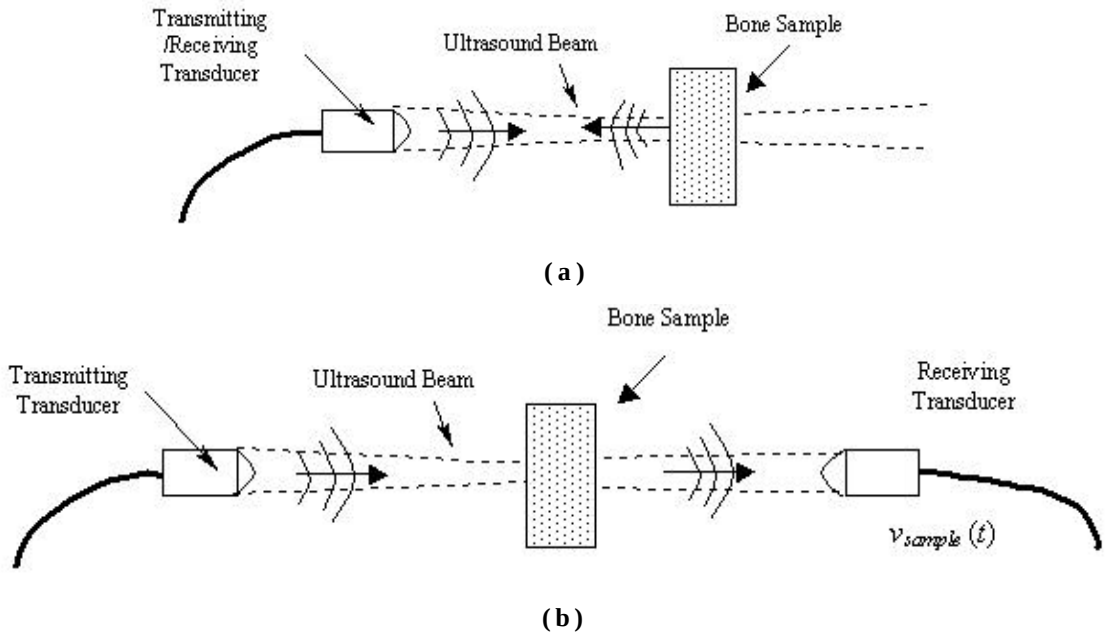

Figure 1.3 Illustration of ultrasound beam in 2 ultrasound measurement systems (a) pulse-echo system; (b) through-transmission system

1.2 Coral as a Model for Trabecular Bone

Coral is made by marine invertebrates that extract calcium and phosphorus from the sea to build a limestone exostructure in which to live [12]. Because of the macroscopic similarities of coral structures to bone, it is thought that these limestone structures might be appropriate as a material for modeling bone. Specifically, people have found that the coral genus *Goniopora* possesses a microstructure similar in appearance to that of trabecular bone and similar content as well.

Figure 1.4 (a) and (b) are the scanned electron micrographs with same magnification of the microstructure of human trabecular bone and calcium carbonate

structure of coral. Figure 1.4 (c) shows the cross section (left) and longitudinal section (right) of coral. Figure 1.4 (d) shows that the intrinsic porous structure of coral (left) is comparable to that of human trabecular bone (right).

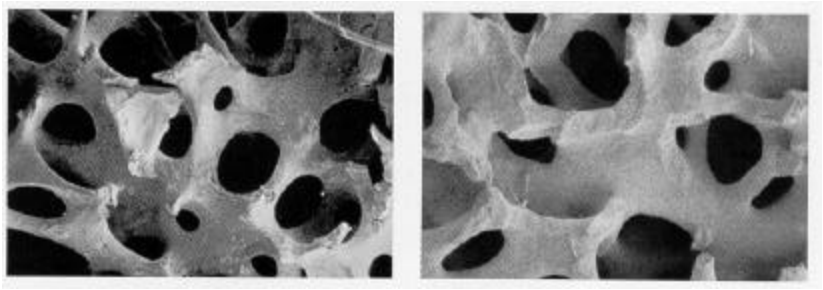

(a) **(b)**

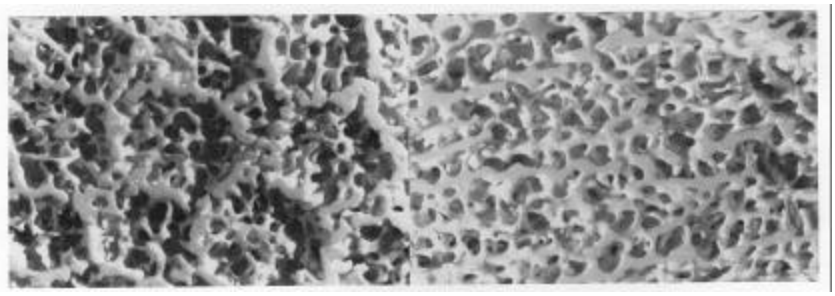

(c)

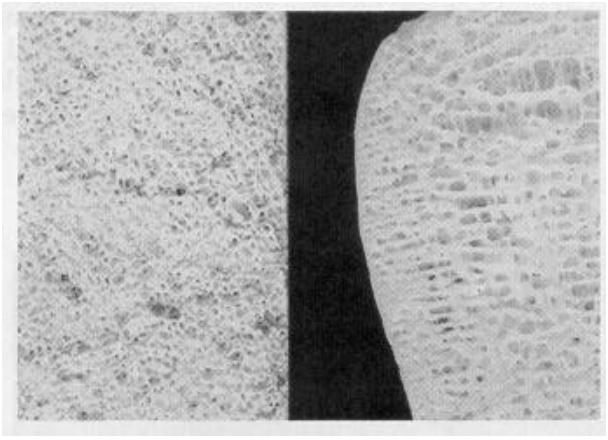

(d)

Figure 1.4. (a) Scanning electron micrograph of human trabecular bone; (b) Scanning electron micrograph of coral material; (c) Cross section (left) and longitudinal section (right) of coral material; (d) Intrinsic porous structure of coral (left) is comparable to that of human trabecular bone (right) (source: Information literature from Interpore Inc.)

From Figure 1.4 above, we can see that both trabecular bone and coral material are composed of a space-frame structure of trabeculae oriented along principal structure lines. Thus, they have an anisotropic behavior or different structural properties along different orientations. Therefore, the calcium carbonate skeletal structure of reef-building sea corals can be used to model the trabecular bone.

1.3 Illustration of Research Work

The goal of this thesis work is to investigate potentially better diagnostic methods for both detecting osteoporosis and estimating fracture risk non-invasively, by obtaining parameters that are influenced by bone mass density (BMD) and bone microstructure. The thesis evaluates new approaches for analyzing through-transmission ultrasound signals using coral samples as models for trabecular bone. The reference density and density distribution are determined by DEXA and the coral sample dry weight. Physical observations and micrographs of the coral samples are used as references for microstructure and for dominant growth axes.

By means of signal processing, 3 ultrasound parameters, Broadband Ultrasonic Attenuation (BUA), coral sample impulse response function, and angular ultrasound decorrelation are obtained in order to observe their variations as functions of the coral sample density and microstructure.

An overview of the measured parameters to be compared is given in Figure 1.5

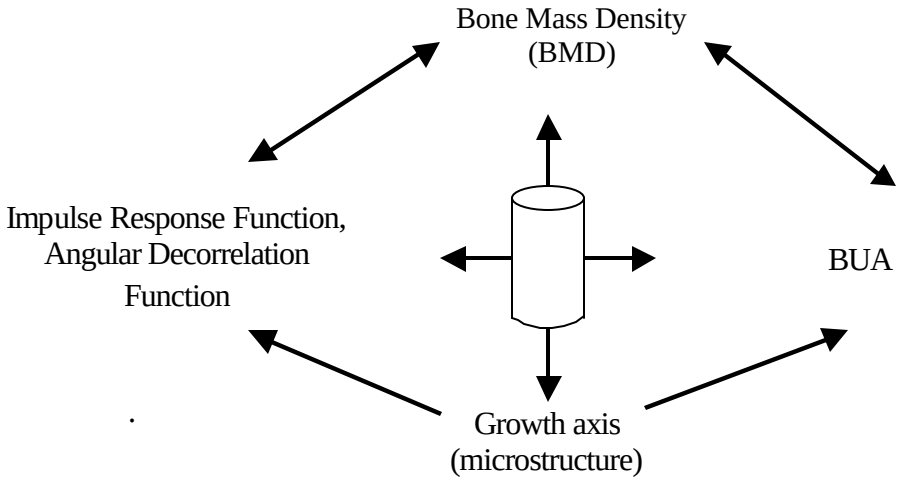

Figure 1.5 The key interrelationship of the research work

Chapter 2

ULTRASOUND PROPAGATION IN TRABECULAR BONE

2.1 Generation of Ultrasound Fields and Ultrasound Parameters

Ultrasound refers to the acoustic waves with frequencies higher than $20\,kHZ$, which is the upper limit for audible sound. For applying the ultrasound technology in osteoporosis diagnosis, one should first be familiar with the generation of ultrasound fields and the corresponding parameters.

2.1.1 Pressure Field of Piezoelectric Transducer

In order to carry out ultrasonic measurements, a means of generating and detecting ultrasound is necessary. The device to perform this electromechanical conversion is the piezoelectric transducer. The principle of piezoelectricity states that certain materials deform when a voltage is applied and produce a voltage when strained by an applied pressure. Such materials, most commonly lead zirconate titanite (PZT), barium titanate, and lead zirconate, can therefore be used to make ultrasound transducers that convert electric energy into ultrasound energy and vice versa.

Single-element transducers may take the form of disks, while linear-array transducers consist of a large number of single transducer elements. In this research work, single-element transducers are used. Specifically a focused transducer is used as the transmitting transducer and an unfocused planar transducer is used as the receiving transducer. Figure 2.1 illustrates the typical transducer structure. It consists of 2 important components in addition to the piezoelectric element: one is the backing layer

and the other is the matching layer. The backing material (usually a mixture of metal powder and a plastic or epoxy) is placed behind the piezoelectric elements to damp down the vibrations. The reason for the damping effect is to produce ultrasound pulses of short duration which can give high axial resolution, that is, ability to resolve two closely spaced reflectors. Transducers without backing material will generate pulses that are long so that echoes from closely spaced reflectors overlap. This is illustrated in Figure 2.2. Typically, pulses of one to three cycles are generated with damped diagnostic ultrasound transducers. For the transducer operating in pulse mode, the shorter the pulse is, the more frequencies will be present, and the wider the bandwidth of pulse will be.

The matching layer is placed on the transducer face. It has an acoustic impedance of intermediate value between the acoustic impedance of the transducer element and the acoustic impedance of the medium which the ultrasound wave will encounter. It reduces the reflection of ultrasound at the transducer element surface, thereby improving sound transmission across it.

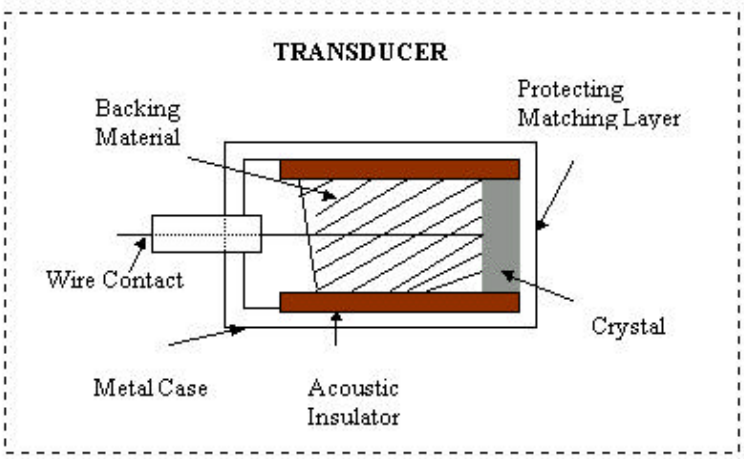

Figure 2.1 The structure of a basic transducer for generating pulsed ultrasound

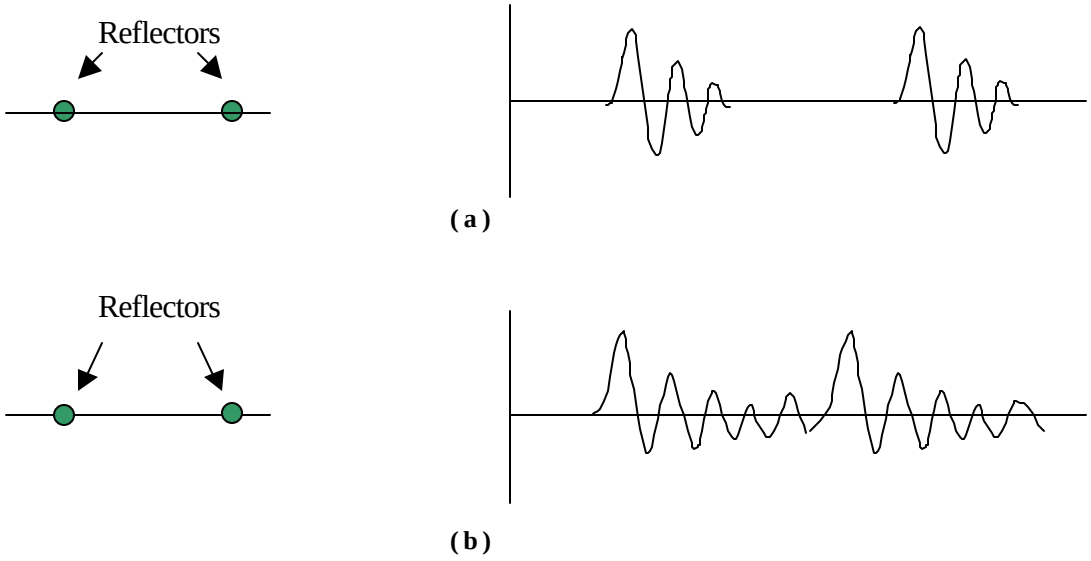

Figure 2.2 (a) Echo duration from transducers with backing material (broadband transducers) (b) Echo duration from transducers without the backing material (narrowband transducer)

From the structure of transducer, we can see that one of the important features of transducer is the ability to produce highly directional ultrasound beams. Based on the beam shape, there are two kinds of transducers: unfocused transducer and focused transducer. The unfocused transducer is constructed from a piezoelectric element with planar surfaces. The unfocused transducer beam is made up of two field regions, a near field and a far field, as illustrated in Figure 2.3. It can be seen that the beam does not diverge in the near field, whereas the beam begins to diverge in the far field. It should be noted that only with the continuous wave excitation are the near field and the fast field fully defined.

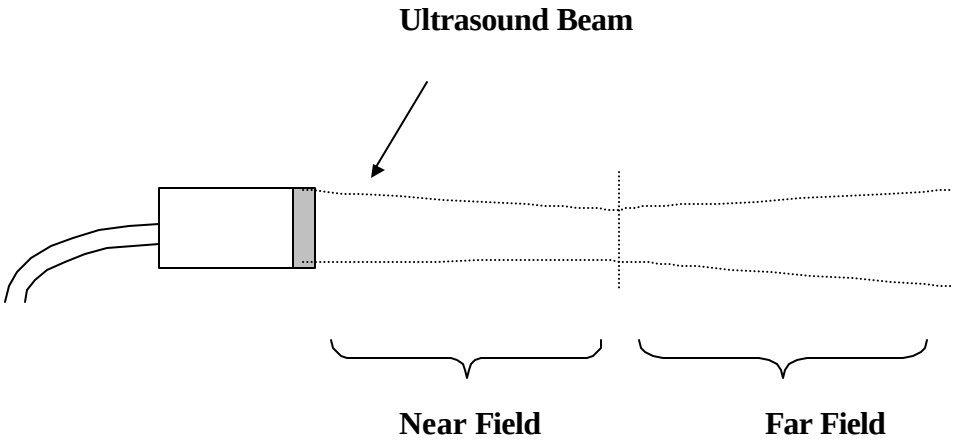

Figure 2.3 An unfocused transducer

Unfocused transducers generate ultrasound beams with poor lateral resolution due to a rather wide beam width. Therefore, if good lateral resolution is required over a limited axial range, a focused ultrasound transducer is necessary, as shown in Figure 2.4 below. The focused transducer can be produced by using concave crystals or by placing an acoustical equivalent of an optical lens in front of a flat crystal. Figure 2.4 illustrates that a focused transducer can have either a weak, medium or strong focus, and the traditional values of the focused beams are also shown in the figure, respectively. A transducer with weak focus produces a moderately narrow beam over a useful range, and such transducers are widely used in medical diagnosis. Figure 2.4(a) gives an illustration of a weakly focusing transducer. Medium focus gives narrow beams over a limited range, and is used in some diagnosis applications, as shown in Figure 2.4(b). Strong focus produces a very narrow beam over a small range, and is rarely used in diagnostic ultrasound, as shown in Figure 2.4(c)[16]. The disadvantage of strongly focused transducer is that although tight focusing of the beam can improves lateral resolution for detecting objects located in focal plane, it will compromise the lateral resolution at distances other than focal distance because the beam will be very wide on either side of

the focal point. However, the ultrasound beam diverges for all focused transducers beyond the focal point.

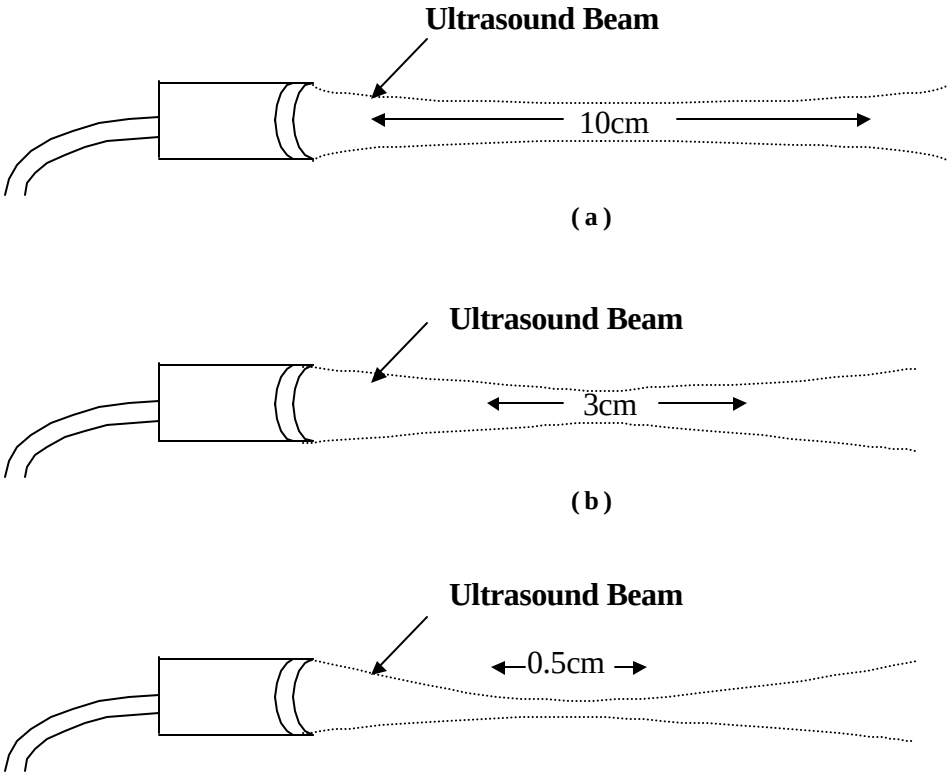

Figure 2.4 Focused transducer using concave crystal: (a) weak focusing; (b) medium focusing; (c) strong focusing

2.1.2 Basic Ultrasound Parameters

Since ultrasound technology is being used in a large number of applications today [16], more and more ultrasound parameters are being investigated. Following is an overview of some basic parameters.

Attenuation

Attenuation represents the combined effect of *absorption* and *scattering*. It is typically expressed in dB, i.e., on a logarithmic scale. It is not only an important parameter to measure in many types of materials characterization, but also the parameter that sets the upper limit for the ultrasound frequency that can be used for a given measurement situation.

Absorption refers to the conversion of acoustic energy into heat due to the viscosity of the medium or thermal conduction. For gases, the absorption associated with thermal conduction is somewhat less than that for viscous absorption but of the same magnitude. For most liquids, the absorption produced by thermal conductivity is negligible compared with that from viscosity. In general, the absorption coefficient is related to the medium viscosity and the thermal condition and is proportional to the square of the frequency, i.e., $a_c \propto f^2$, where a_c is the absorption coefficient and f is the ultrasound wave frequency [14].

Scattering refers to the change in the amplitude, spectral content, velocity or direction of a wave as a result of a spatial or temporal non-uniformity of the medium. In general, absorption dominates in homogeneous media (e.g., liquids, gases, fine-grained metals, polymers), whereas scattering dominates in heterogeneous media (e.g., composites, porous ceramics, large-grained materials, bone). The degree of scattering depends on many factors, such as the mean dimension of the scatterers relative to the wavelength of the insonifying wave, the acoustic impedance of the scatterer relative to the surrounding medium, the statistical distribution of the scatterers, scatterer geometry, volume percentage of scatterers, and etc. The actual attenuation and its frequency

dependence can be determined fairly unambiguously for gases and liquids, while for solids it is dependent on the manufacturing process, which determines the microstructure of the material, such as the grain structure. For porous media, such as the trabecular bone, the attenuation is correlated with microstructure and density of the media, which will be discussed in Chapter 5.

Ultrasound Velocity

To measure ultrasound velocity through the sample, arrival times of received through-transmission pulses are measured with and without the sample medium present. Ultrasound velocity in the sample medium, c_s, can then be computed from [4, 10]

$$c_s = \frac{c_w}{1 - \frac{c_s(t_1 - t_2)}{d}} \tag{2.1}$$

where d is the thickness of the sample medium, $t_1 - t_2$ is the time difference of arrival times with and without the sample present, and c_w is the speed of sound of the medium surrounding the sample. This may be a fluid, such as water, or gas, such as air.

Parameters Obtained Through Signal Processing

A number of parameters can be obtained from analysis of the received signals, based on amplitude, arrival time, and changes in spectral contents. The impulse response function of the material being tested, obtained from through-transmission measurements, and signal cross-correlation as functions of angular position of the receiving transducer are two important parameters among them. These two parameters will be discussed in detail at Chapter 6 and Chapter 7. Doppler spectra for velocity estimation is another example of information that is only attainable by means of signal processing.

2.2 Theory of Ultrasound Propagation

2.2.1 Elementary Equations of Acoustic Wave

As with acoustic waves in general, the ultrasound wave is fundamentally a mechanical vibration which means that a medium (e.g. fluid, gas or solid) is required for the waves to propagate. The generated dynamic acoustic pressure causes "particles" in the medium to oscillate back and forth in the direction of the wave propagation and transfer the pressure to adjacent particles, as shown in Figure 2.5. A particle of the medium is a small volume, which is small enough so that acoustic parameters can be assumed to be uniform across the volume while large enough to contain a very large number of molecules.

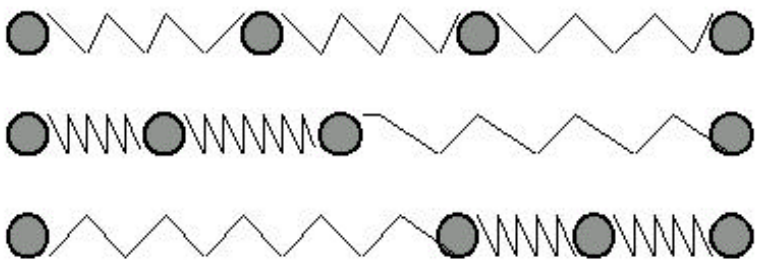

Figure 2.5 Wave propagation principle illustration

The wave equations for ultrasound propagation in homogeneous media and inhomogeneous media have been researched to a great extent. To arrive at the simplest equation for wave propagation, several assumptions are made, such as the medium (fluid or gas) is homogeneous, isotropic and is perfectly elastic (i.e., no losses). Furthermore, the analysis will be limited to waves of relatively small amplitude, so changes in the density of the medium will be small compared with equilibrium value [14].

Then the propagation of an arbitrary wave field can be defined by the wave equation for a source-free regionas

$$\nabla^2 p = \frac{1}{c^2}\frac{\partial^2 p}{\partial t^2} \qquad (2.2)$$

where ∇^2 is the Laplacian operator. Eq. 2.2 defines a linear, lossless wave equation for the propagation of acoustic wave in fluids with phase speed c. The wave equation above is in a general form. If the acoustic wave is a plane wave field, ideally formed by an infinitely large, planar source, operating at a single frequency, (also called a harmonic plane wave field), the solution to Eq. 2.2 will be

$$p(\vec{r},t) = A\exp[j(wt - \vec{k}\cdot\vec{r})] + B\exp[j(wt + \vec{k}\cdot\vec{r})] \qquad (2.3)$$

where $\bar{r}$ is an equilibrium position vector of a fluid element. This position vector can be expressed in Cartesian system as $\vec{r} = x\hat{x} + y\hat{y} + z\hat{z}$ where $\hat{x}$, $\hat{y}$ and $\hat{z}$ are the unit vectors in the x, y and z directions, respectively. $k = |\vec{k}| = \frac{w}{c} = \frac{2p}{l}$ is called as the wavenumber, which can also be expressed as $\vec{k} = k_x\hat{x} + k_y\hat{y} + k_z\hat{z}$ in Cartesian system.

In Eq. 2.3, the complete solution of $p(\vec{r},t)$ consists of two plane wave components, propagating in two directions defined by $\vec{k}$ and $-\vec{k}$. Normally, only one wave propagation direction exists, which gives

$$p(\vec{r},t) = A\exp[j(wt - (k_x x + k_y y + k_z z))] \qquad (2.4)$$

From the above equation, we can see that the amplitude of a plane wave is constant, but the phase varies with both time and space.

For spherical waves originating from a point source under the assumption of a single frequency, with the source placed at the origin of the coordinate system, the solution of Eq. 2.2 gives

$$p(r,t) = \frac{A}{r}\exp[j(wt - \vec{k}\cdot\vec{r})] + \frac{B}{r}\exp[j(wt + \vec{k}\cdot\vec{r})] \quad (2.5)$$

The first term is a diverging spherical wave, and the second term is a converging spherical wave. Since $\vec{k}$ and $\vec{r}$ always point in the same direction for spherical waves, the vector dot product in Eq. 2.5 can be replaced by normal product. Similarly, since in most cases only a diverging spherical wave exists, the spherical waves produced by a spherical source of radius *a* take the form as

$$p(r,t) = \frac{A}{r}\exp[j(wt - kr)], \quad r > a \quad (2.6)$$

The surfaces of constant phase for a diverging wave become nearly planar far from their sources, and therefore the properties of diverging sphere waves will become very similar to those of plane waves at large distances.

For wave propagation in heterogeneous medium, it is very difficult to accurately describe the mechanisms because of the complex structure of the medium. Some wave theories for wave propagation in the trabecular bone are discussed below.

2.2.2 Ultrasonic Wave Propagation in Trabecular Bone

Because of the complex anisotropy and inhomogeneity of trabecular and cortical bone, it is difficult to characterize bone tissues *in vivo* or *in vitro*. In particular, trabecular bone is very anisotropic and inhomogeneous and hence particularly difficult to analyze. Figure 2.6 shows the porous structure of trabecular bone in the bovine femur.

To understand the characteristics of ultrasound propagation in trabecular bone and to possibly improve the ultrasonic diagnosis of osteoporosis, the appropriate theoretical modeling of ultrasonic propagation in trabecular bone is pertinent. A number of theoretical models have been proposed for propagation in trabecular bone.

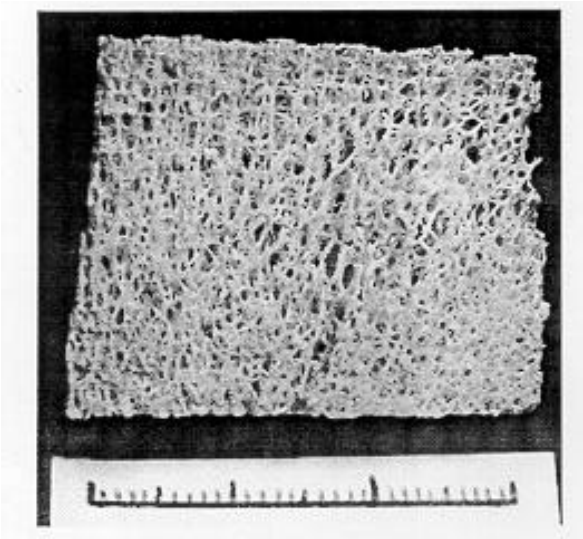

Figure 2.6. The porous structure in trabecular bone in the bovine femur. Scale is 3 cm wide, with mm gradings [17]

2.2.2.1 The Bar Equation

The bar equation has been used extensively to predict the elasticity of cortical (compact) bone, which is used typically for obtaining elastic properties [41] and also for quantifying bone strength [18,19]. It has also been applied to a trabecular bone assuming a wave travels along with the bar velocity [20]. The reason for using the bar equation is that the mathematical expressions for the transmission of acoustic plane waves through fluid media are very similar to those for the transmission of compressional waves along a bar. That is, whenever fluid is strained by acoustic wave pressure, elastic forces will be produced as in Eq. 2.7.

$$\text{stress} = f/S \tag{2.7}$$

where f represents the longitudinal wave force, S is the cross-sectional area.

If the strain is small, according to Hooke's law

$$f/S = -\mathrm{Y}\left(\mathrm{d}x/\mathrm{d}x\right) \tag{2.8}$$

where Y, the *Young's modulus* or *modulus of elasticity*, is a characteristic property of the material, x is the longitudinal particle displacement and x is the particle displacement at the reference orientation. The wave equation will be

$$\frac{\partial^2 x}{\partial x^2} = \frac{1}{c^2}\frac{\partial^2 x}{\partial t^2} \tag{2.9}$$

which is very similar to Equation 2.1. The phase speed c will then be given by

$$c = \sqrt{\left(\mathrm{Y}/r\right)} \tag{2.10}$$

where r is the density of material [14].

However, for wavelengths larger than the microstructural dimensions, the bar equation predicts one wave, but for such frequencies in trabecular bone, two waves have clearly been observed [21]. Hence, propagation in trabecular bone requires a more detailed model than that offered by the bar equation.

2.2.2.2 Biot's Theory

Biot initially proposed a general theory of acoustic wave propagation in a porous elastic solid saturated by a viscous fluid; this theory has been used extensively in geophysical applications [22, 23, 24]. In recent years, Biot's theory has been applied to analyze ultrasound propagation in trabecular bone by several investigations [25, 26, 27].

Biot's theory predicts that there would exist two longitudinal waves denoted as "waves of the first and second kind" and one shear wave. The two longitudinal waves are distinguished by their propagation mechanisms. The wave of the first kind has a higher speed, corresponding to the wave in the solid and fluid moving in phase, while the wave of the second kind has a slower speed, corresponding to the above motion out of phase. Therefore, in Biot's theory, the average motions of both the solid and fluid components of the medium are separately described. Generally, the waves of the first kind and the second kind are also known as *fast wave* and *slow wave*, respectively, which are believed to associated with solid and fluid components of the porous medium. The two longitudinal waves have nondispersive speeds $v_{fast,slow}$ given in Biot's theory of the form [27, 28]

$$v^2_{fast,slow} = \frac{2(HM - C^2)}{(M\rho + Hm - 2C\rho_f) \mp [(M\rho + Hm - 2C\rho_f)^2 - 4(HM - C^2)(m\rho - \rho_f^2)]^{1/2}} \quad (2.11)$$

where "$\mp$" in the denominator means that v^2_{fast} will be obtained when "-" is selected, and v^2_{slow} will be obtained when "+" is selected. ρ_f is the density of the fluid, ρ is the overall density, H, C and M are generalized elastic coefficients which can be related to the bulk moduli of the solid K_s, the pore fluid K_f, the bulk K_b, the shear moduli m of the skeletal frame, and the porosity β. β is defined as

$$\beta = \frac{\rho_s - \rho}{\rho_s - \rho_f} \quad (2.12)$$

where ρ_s is the density of the solid. According to Gibson [21], the bulk K_b and the shear moduli m of the skeletal frame of trabecular bone change as a function of bone volume fraction $V_f (= 1 - \beta)$:

$$K_b = \frac{E_s}{3(1-2\nu_b)} V_f^n \tag{2.13}$$

$$m = \frac{E_s}{2(1+\nu_b)} V_f^n \tag{2.14}$$

where n is a variable depending on the geometrical structure of the trabecular frame and ν_b is the Poisson's ratio of the frame. E_s is a constant, and m is the density parameter defined as

$$m = a\rho_f / b \tag{2.15}$$

This density parameter is used because not all of the pore fluid moves in the direction of the pressure gradient due to tortuosity. a is the structure factor and it is determined by the relation given by Berryman [7] as

$$a = 1 - r(1 - 1/b) \tag{2.16}$$

where r is a variable calculated from a microscopic model of a frame (the solid structure) moving in the fluid.

In order for the condition for Equation 2.11 to be valid, the wave frequency must be high enough so that the viscous skin depth d_s is much smaller than the pore size a_0. The viscous skin depth d_s equals to $\sqrt{2\eta/\rho_f \omega}$ for any angular frequency ω in general. It describes the extent of the viscous shear arising at an interface as fluid moves relative to the solid. Therefore, it determines the extent of the in-phase and out-of-phase solid and fluid motions and thus determines the validity of Eq. 2.11 for predicting the velocities of fast and slow waves. Since the viscous skin depth is related to wave frequency, acoustic propagation in porous media saturated with fluid (of shear viscosity, η, and density, ρ_f)

could be divided into low- and high-frequency ranges. These ranges intercept at the critical frequency,

$$w_{crit} = 2h / r_f a_0^2 \qquad (2.17)$$

when the viscous skin depth d_s equals pore size a_0.

In the low-frequency region of Biot's theory when $w \ll w_{crit}$, i.e., $d_s \gg a_0$, only the fast wave propagates. This is because viscous coupling locks solid and fluid together, preventing the relative motion associated with slow wave propagation.

If the frequency is high enough to satisfy the condition $w \gg w_{crit}$, i.e., $d_s \ll a_0$, viscous coupling effects will decrease. Both fast and slow waves will propagate because relative motion between fluid and solid allows the slow wave to propagate.

For the frequency region where $w \approx w_{crit}$, i.e., $d_s \approx a_0$, the mechanisms of wave propagation are complex and are not adequately described by Biot's theory.

Using data taken from the literature, shown in Table 2.1, the critical frequency, w_{crit}, for marrow-saturated trabecular bone is in the region of 1-10 kHz [29]. This implies that ultrasound wave propagation will fall in the high-frequency region of Biot's theory because the ultrasound frequency is above 20 kHz, and in most ultrasonic applications the frequency being used is much higher than that. Therefore, two compressional waves should propagate at ultrasonic frequencies in trabecular bone. The existence of two compressional waves in bovine trabecular bone was confirmed by Hosokawa and Otani [21] who were able to obtain agreement between predictions of phase velocity and measurements of both waves, shown in Figure 2.7 and Figure 2.8. Figure 2.7 shows a reference pulse waveform received with water only between the transmitting transducer and the receiving transducer. Figure 2.8 shows the pulse waveform received with

trabecular bone of low density and high density, respectively, present between the transducers.

Table 2.1 Biot's model parameters of trabecular bone [21]

Young's modulus of solid bone Y	22 GPa
Poisson's ratio of solid bone	0.32
Density of solid bone ρ_s	1960 kg/m^3
Bulk modulus of bone marrow K_f	2.0 GPa
Density of bone marrow ρ_f	930 kg/m^3
Poisson's ratio of skeletal frame	0.32
Variable r	0.25
Viscosity of bone marrow η	1.5 Ns/m^2

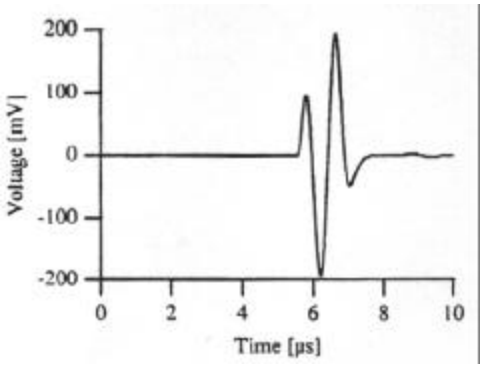

Figure 2.7 Pulsed waveform at 1 MHz traveling in water

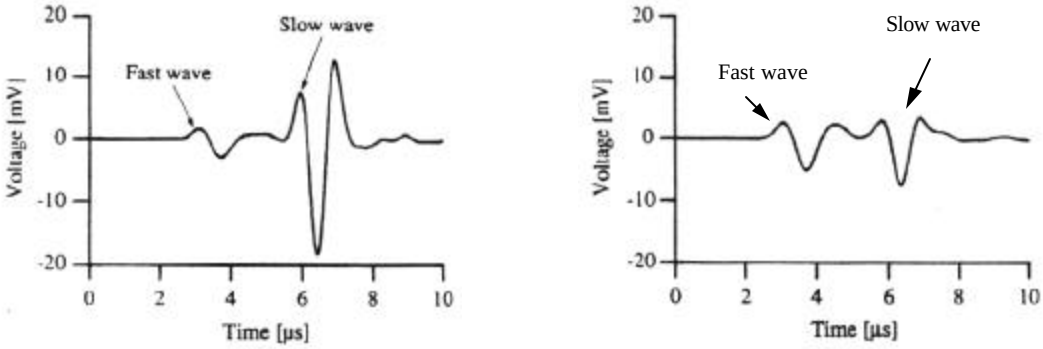

(a) **(b)**

Figure 2.8 Pulsed waveform at 1 MHz traveling through trabecular bone: (a) low density; (b) high density [21]

We have also obtained similar results from the coral samples, shown in Figure 2.9, where Figure 2.9 (a) illustrates the reference signal received with water only between the transducers, and Figure 2.9 (b) illustrates the received signal when the coral sample is placed on the path between the transducers.

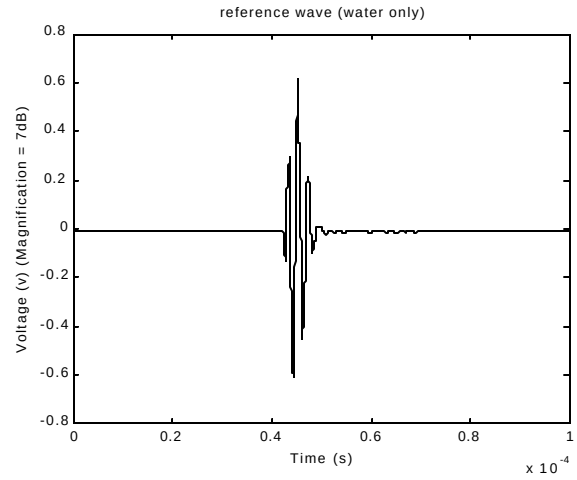

(a)

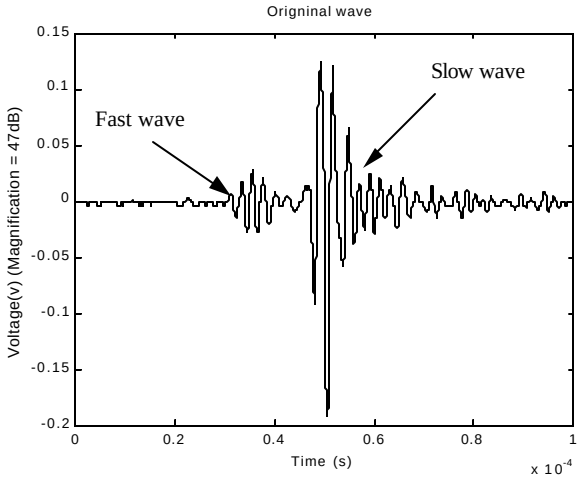

(b)

Figure 2.9 Ultrasound measurements results of the coral sample (a) Pulsed waveform at 500 kHz traveling in water; (b) Pulsed waveform at 500 kHz traveling through coral sample

Although Biot's theory has been applied successfully in analyzing ultrasonic propagation for geophysical testing, limitation has been found when it is applied in

analysis for trabecular bone. Biot's theory requires knowledge of up to 14 parameters, including the material parameters and structural parameters. The material parameters are fluid and solid densities; bulk moduli of fluid, solid and solid frame, Poisson ratio of the solid and the frame, and the shear viscosity of the fluid. The structural parameters required are porosity, tortuosity and permeability [17]. For trabecular bone, many of these parameters, particularly those of a geometric nature, cannot be easily evaluated *in vitro* or *in vivo.*

Furthermore, there has been a consistent discrepancy between measured and predicted attenuation by Biot's theory. This discrepancy may stem from the fact that Biot's theory also assumes that the porous material is macroscopically isotropic. Therefore, some new models to accurately describe the anisotropy of trabecular bone are necessary for future research.

However, despite the uncertainties that still exist in the differences between the theories and models for the ultrasound propagation in trabecular bone, two results can be derived from the research work up to now. One is the reproducible anisotropic response of fast and slow compressional waves in trabecular bone, and the other is the evidence that ultrasound signal is affected by the dominant trabecular structure contained in the trabecular bone.

Chapter 3

DESCRIPTION OF ULTRASOUND EXPERIMENT SYSTEM

In this chapter, the ultrasound experimental system for obtaining and processing the received signals transmitted through coral samples is described. The system utilizes through-transmission measurements to get the signal versus angle in two approaches. In one approach, the coral sample is rotated and in the other approach the receiving transducer is rotated around the coral sample. First the design of the ultrasound experimental system is discussed.

3.1 The Ultrasound Experimental System

Figure 3.1 (a) depicts the experiment system for measuring the signals when rotating the coral sample. Figure 3.1 (b) represents the approach when rotating the receiving transducer. In both systems, the coral sample and the two transducers are placed in the water tank. The transmitting transducer, driven by ultrasonic pulse/receiver, emits a short pressure pulse with PRF (pulse repetition frequency) of $1\,kHz$. The receiving transducer detects the pressure pulse and produces an electrical signal which is then sent to the connected oscilloscope. The oscilloscope will digitize the signal and send it to computer for further processing via GPIB (General Purpose Interface Bus) control interface.

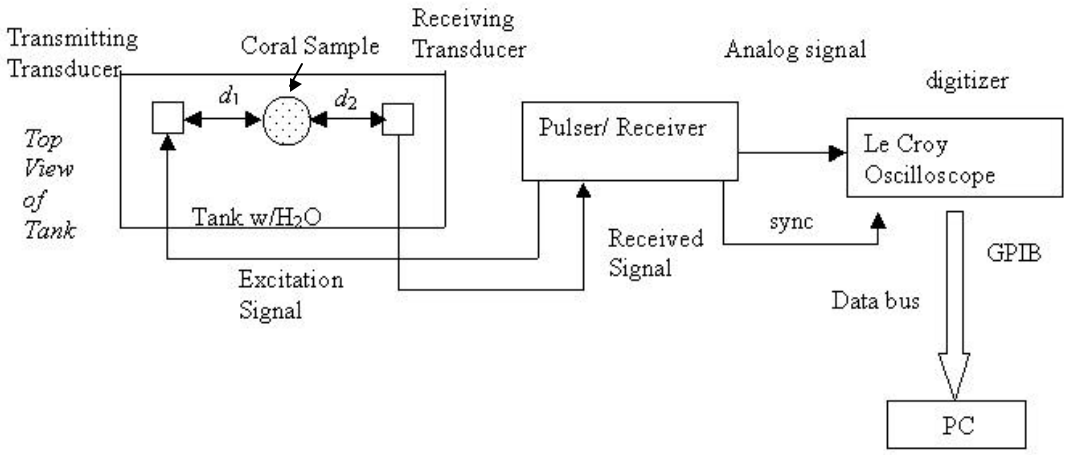

(a)

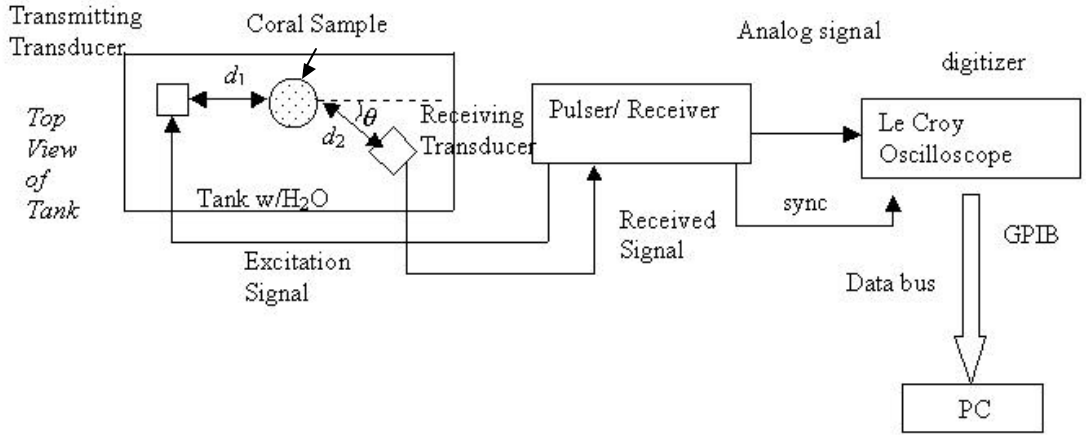

(b)

Figure 3.1 Block Diagram of Experimental System (a) rotating the sample approach; (b) rotating the receiving transducer approach

Below are the detailed descriptions of the roles of the experiment system components.

3.1.1 Ultrasonic Pulser/Receiver (Panametrics Model 5072)

The Ultrasonic Pulser/Receiver Model 5072PR (Panametrics, MA), shown in Figure 3.2, is a broadband ultrasonic pulser/receiver unit with a receiver gain which

can vary over a 118 dB range. When combined with an oscilloscope and appropriate transducers, it will provide a unique, low-cost ultrasonic measurement capability.

The pulser section of the instrument generates short, large-amplitude electric pulses of controlled energy which, when applied to an ultrasonic transducer, are converted into short ultrasonic pulses. The ultrasonic pulses are received either by the transmitting transducer (pulse-echo method), or by a separate receiving transducer (through-transmission method).

Figure 3.2 The Ultrasonic Pulser/Receiver (Panametrics Model 5072)

3.1.2 Digital Oscilloscope (LeCroy Model 9400)

The amplified output signal from the pulser/receiver is sent to the LeCroy 9400 digital oscilloscope (LeCroy Corp., NY) channel input via a coaxial cable. The input impedance of the device connected to the cable should be $50\,ohm$. A synchronizing pulse is also provided by pulser/receiver and is connected to the trigger input of LeCroy 9400. The synchronizing signal is important for obtaining a steady

picture of the received signal. Figure 3.3 shows the front panel of LeCroy 9400 digital oscilloscope.

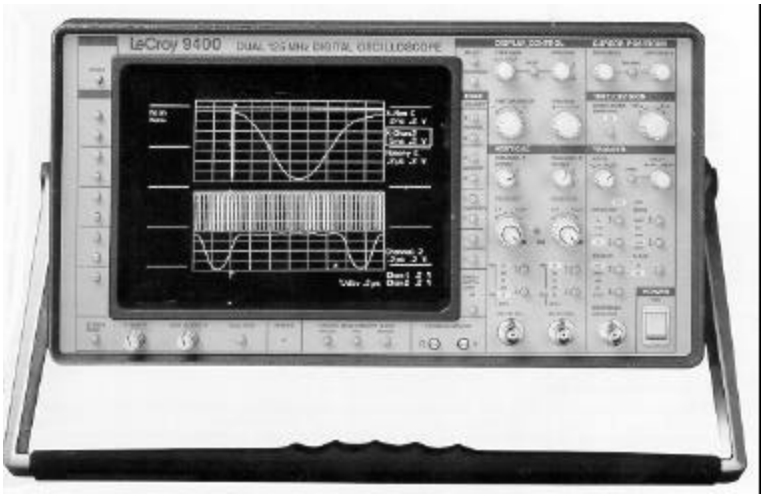

Figure 3.3 The Digital Oscilloscope (LeCroy Model 9400)

The LeCroy 9400 provides 125 MHz bandwidth, with an 8-bit analog to digital converter (ADC) which convert input signals with better than 1% accuracy. Each input can be sampled at a maximum affective rate of 5 Gigasample/sec for a repetitive waveforms and 100 Megasample/sec for single event.

3.1.3 Transducer

The categories of transducers and their pressure fields have been discussed in Section 2.1.1. In this research work, two 0.5 MHz center frequency, 1" diameter transducers (Model V301, Panametrics Corp., MA) are placed in a water-filled tank, at a separation of 6.5". The transmitting transducer is a focused transducer with focal distance of 1.65", while the receiving transducer is an unfocused transducer. The sample is placed between the transducers at a distance of 2.5" from the transmitter. Therefore, the coral sample is placed slightly beyond the focal point of transmitting

transducer, resulting in insonification of an approximately planar region of the surface of the coral sample.

Figure 3.4 below illustrates the water-sample-water path between the two transducers.

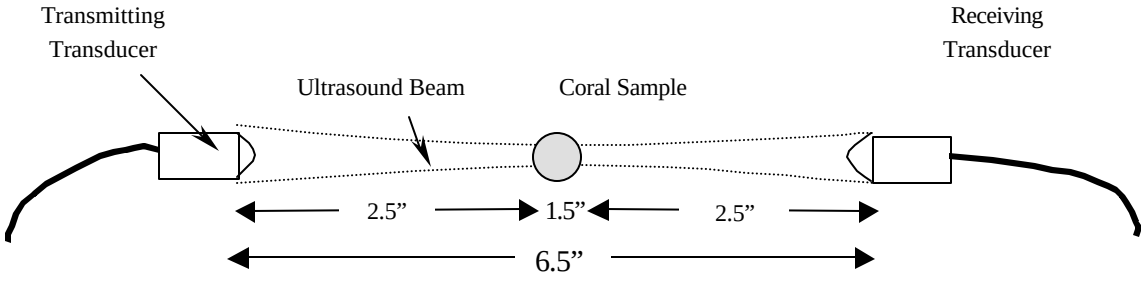

Figure 3.4 Illustration of the wave path between two transducers

The electro-acoustic response of a transducer operating in transmitting or receiving mode is described in a system point of view in Figure 3.5. The parameter $e(t)$ is the applied excitation signal in time domain, $v(t)$ is the received signal and $p_t(t)$ and $p_r(t)$ are the transmitted and received pressure fields on transducer surface in time domain, respectively. Finally, $g_t(t)$ and $g_r(t)$ are the impulse responses of the transducer in transmitting and receiving mode, respectively.

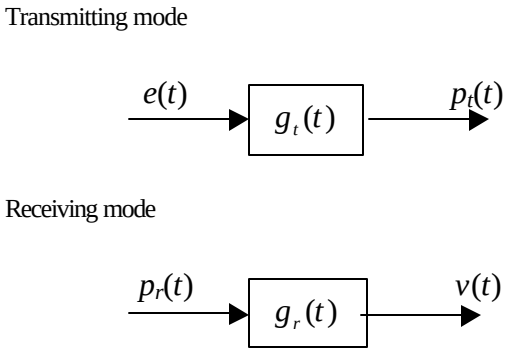

Figure 3.5 System diagram of the electro-acoustic response of the ultrasound transducer

The corresponding formulations for the above systems are (“$*$”denotes convolution):

Transmitting mode

$$p_t(t) = e(t) * g_t(t) \tag{3.1}$$

Receiving mode

$$v(t) = p_r(t) * g_r(t) \tag{3.2}$$

The magnitude of the frequency responses of the transducer, $G_t(w)$ and $G_r(w)$, have bandpass characteristics centered around the transducer's resonance frequency which is determined by the thickness of the piezo-electric plate, as shown in Figure 3.6.

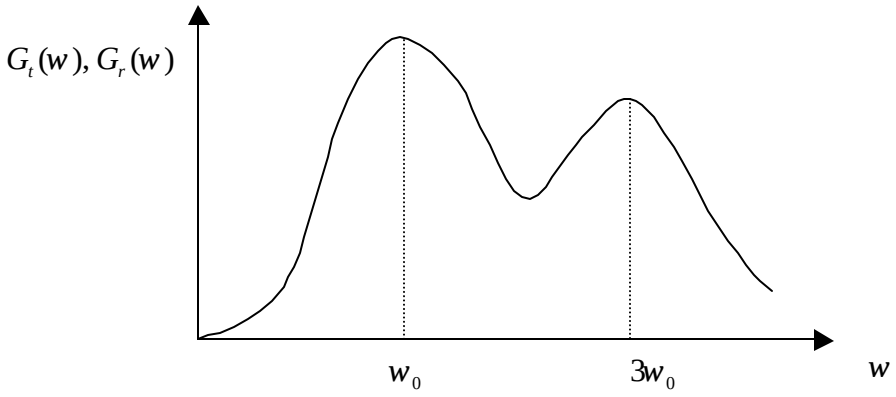

Figure 3.6 Electro-acoustic frequency response of a typical broadband piezoelectric transducer

3.1.4 Measurement Tank

In order to perform the experiments, an appropriate measurement tank and holders for transducers and the sample are needed. The tank is made of durable clear plastic with the dimension of 16" ×16" × 10", as illustrated in Figure 3.7 (a). The two transducers and the coral sample are mounted on a platform which is placed in the tank, as depicted in Figure 3.7 (b). A protractor is mounted at the bottom of the platform, with its center coinciding with the center of rotation for the receiving

transducer. This is seen in Figure 3.7 (c). Furthermore, all the measurements are carried out with the coral sample placed so that its center coincides with the center of rotation of the receiving transducer. The proper alignment is checked by using the laser pointer, shown in Figure 3.7 (b). The holder of the transmitting transducer is fixed at 0^o of the graduated protractor, while the holder of the receiving transducer is not fixed. Therefore, the receiving transducer can be rotated along the graduated circle. The holder for placing the coral sample is placed at the center of the protractor, thus, the coral sample could be rotated on its holder along the scale of the protractor as well.

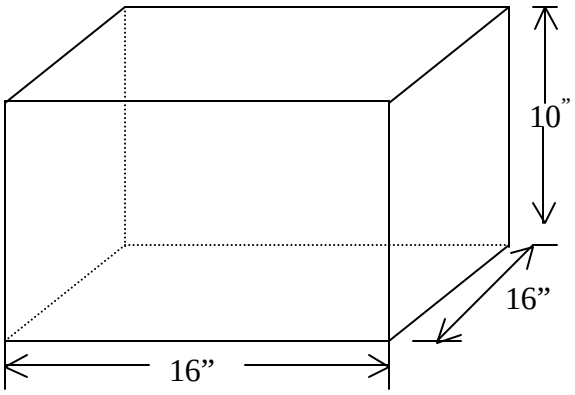

(a)

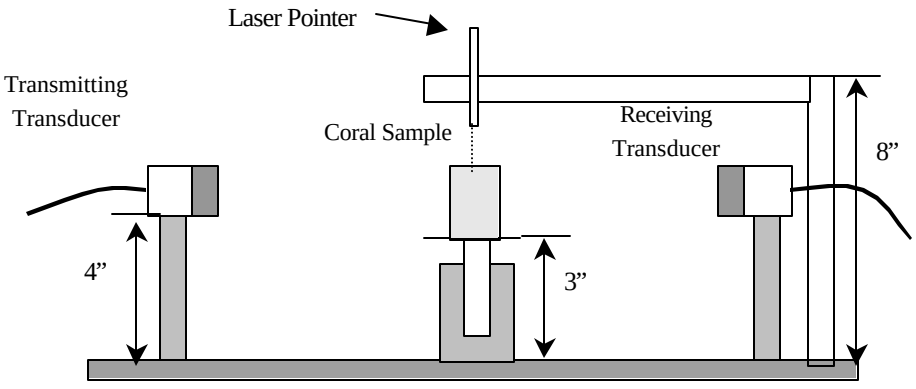

(b)

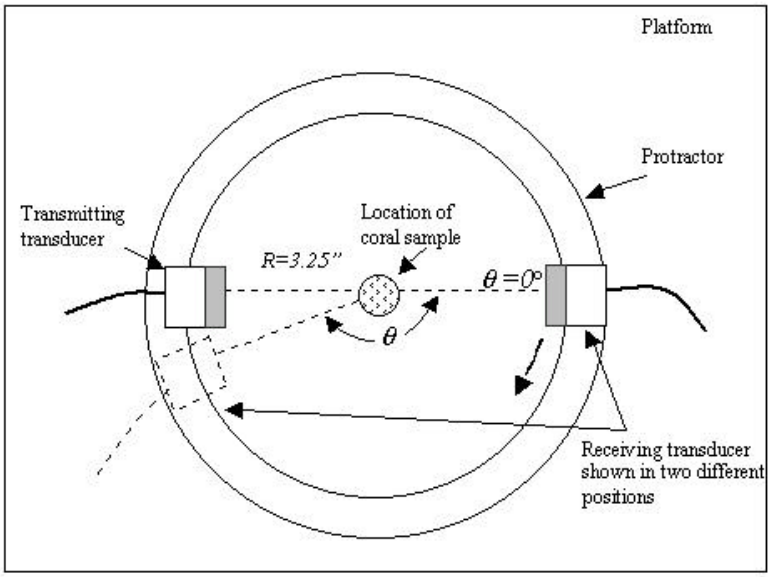

(c)

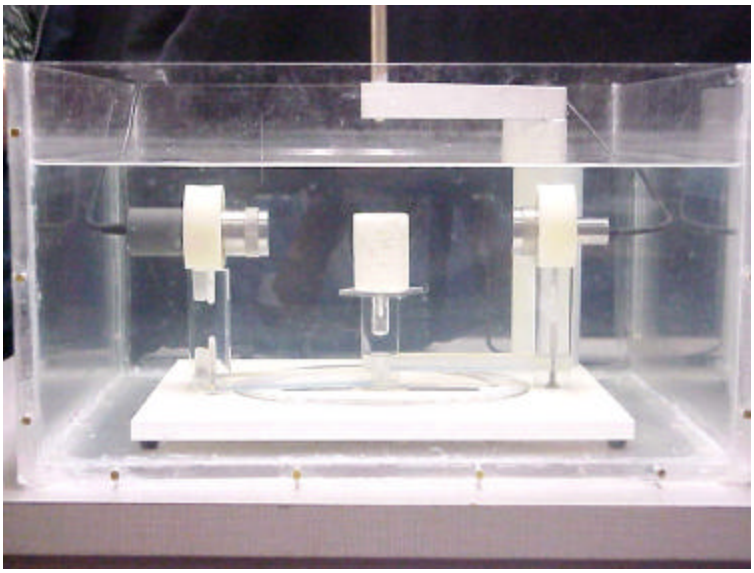

(d)

Figure 3.7 (a) The measurement tank; (b) the platform with the holders for the transducers and the sample; (c) the protractor, with locations of transducers and coral sample indicated; (d) photo of water tank with the transducers and a coral sample

3.2 Materials Preparation and Measurements Outline

In this section, the preparation of the coral samples and the protocol for the measurements will be discussed to complete the description of the measurement system in this research work.

3.2.1 Sample Description

Nine *Goniopora* coral samples of 1.45" in diameter and 2" in length (cylindrical shape) were obtained from Interpore, Inc, CA. As discussed earlier, the *Goniopora* coral samples have similar structure and characteristics to trabecular bone. The advantage of using the coral material modeling trabecular bone is that the coral material is stable and easy to be decalcified. Furthermore, the sample made from coral material is reproducible, which means that the measurement for obtaining the coral sample ultrasonic parameter is repeatable. Although the coral sample is not so strong as trabecular bone and is not deformable in any orientation, which is because the coral material lacks the collagen, it is ideal to model the trabecular bone in the ultrasound research since the ultrasound parameters will not be affected by its disadvantages. The use of observations and coral sample micrographs to determine the dominant grow axis of each coral sample will be discussed in Section 4.3.

Briefly, the growth axis for each of the nine coral samples lies in one of the 3 growth axis categories that are observed. Therefore, 3 groups of the coral samples are created, each of which contains 3 coral samples with different growth axis.

3.2.2 Measurement Protocol

3.2.2.1 Decalcification Procedure and Tool

Decalcification is an important component in the measurement protocol. Decalcification is the process by which the density of the coral samples is reduced so as to observe the ultrasound signal parameters variation as function of density level. The formic acid (Cal-EX^{TM} II, Fisher Diagnostics, NJ) is mixed with water with the ratio of 1:25 to decalcify the coral samples. The mixture ratio is determined to give a moderately slow and well-controlled decalcification rate. Specifically, the measurement observation shows that the procedure of allowing 3~4 minutes of repeated exposures of the coral samples to the diluted formic acid with ratio of 1:25 is a good way to meet the requirement for accurately decreasing the densities of the coral samples as expected.

However, in order to get the coral samples uniformly decalcified, a specific decalcification tool is needed which includes a tank with tubes connected at the bottom, shown in Figure 3.8 (a) and (b). The tank contains the decalcification solution, while the tubes hold the coral samples. When doing the decalcification, the diluted formic acid will flow through one of the two tubes and decalcify the coral sample.

The reason for using 8" long tubes with the coral samples placed at the bottom of the tube is to make the fluid pressure to be relatively constant during the decalcification process. The static pressure of fluid is proportional to the fluid height and since the height of tube is larger than the height of tank, the pressure of the fluid in tube will dominate the total pressure and give a nearly constant flow rate.

Therefore, during the most time of the decalcification process, the pressure will be relatively constant and the decalcification process can be better controlled and the coral samples can be uniformly decalcified.

The reason for not just immersing the coral sample into the decalcification solution is that the outer regions of the coral sample have been found to be decalcified much more than the inner regions of the coral sample in this method. By using the method designed in this research work, the pressure from the solution contained in the tank and the tube above the coral sample will make the solution go through the coral sample at a relatively uniform rate.

The inner dimensions of the tank are 10.45"×6"×4" which make the tank big enough to hold 2500ml fluid, the amount of the solution used in the decalcification measurement. This volume of solution goes through the coral sample in 3-5 minutes. The two tubes are 8" in length each; one is for holding the coral samples with diameter of 1.45" used in this research work and the other is for holding other coral samples with diameter of 1" which are not used in this research work. The whole decalcification device will be set on a holder with height of 16", so that a beaker can be placed below the tubes to collect the solution after it has been used.

Using the designed tool, the decalcification was carried out in two stages, one to an intermediate decalcification level, which decreased the dry weights of coral samples by around 21%, and the other one to a heavy decalcification, which decreased the dry weights of coral samples by around 41%. The result of decalcification was satisfactory, which will be described in Section 4.1.

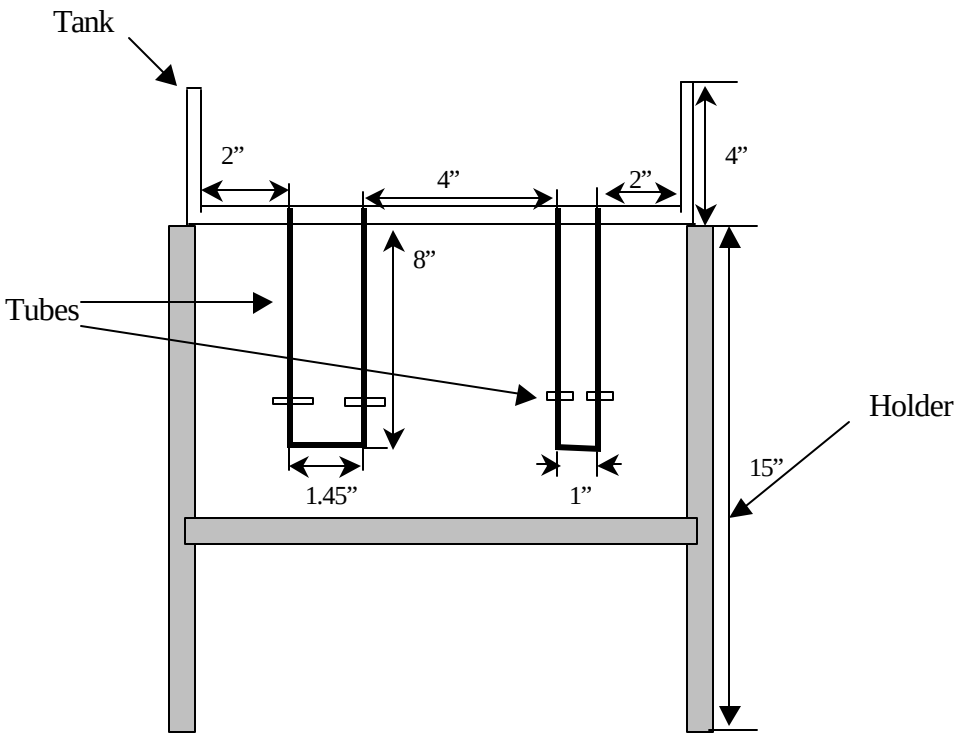

(a)

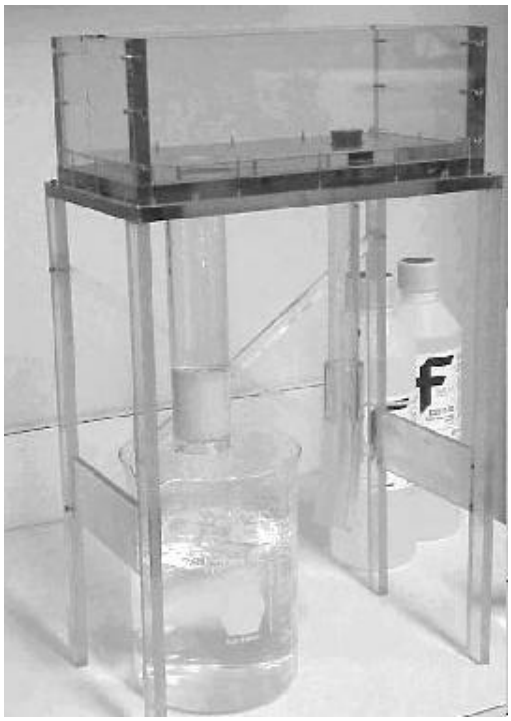

(b)

Figure 3.8 Decalcification tool. (a) Simplified illustration of dimension; (b) photograph.

3.2.2.2 Diagram of Measurement Protocol

The purpose of this research work is not only to compare the ultrasound parameters of different samples with similar densities but different microstructures, but also to compare the ultrasound parameters of the same sample at different density levels. Three different growth axis of the coral sample have been obtained from the physical observation, which will be discussed in detail in Section 4.3. Therefore, each coral sample is numbered and categorized into one of the three groups. Every group includes three coral samples with three different microstructure growth axes. Thus, the measurement protocol is designed so that all the coral samples are measured and analyzed first at original densities stage. Then the densities of 2 out of the three groups were changed by the decalcification process using formic acid. That is, the 6 coral samples in group 2 and group 3 were analyzed after decalcification to an intermediate density level, and the three samples in group 3 were analyzed after decalcification to a low density level.

The diagram of our measurement outline is shown below in Figure 3.9:

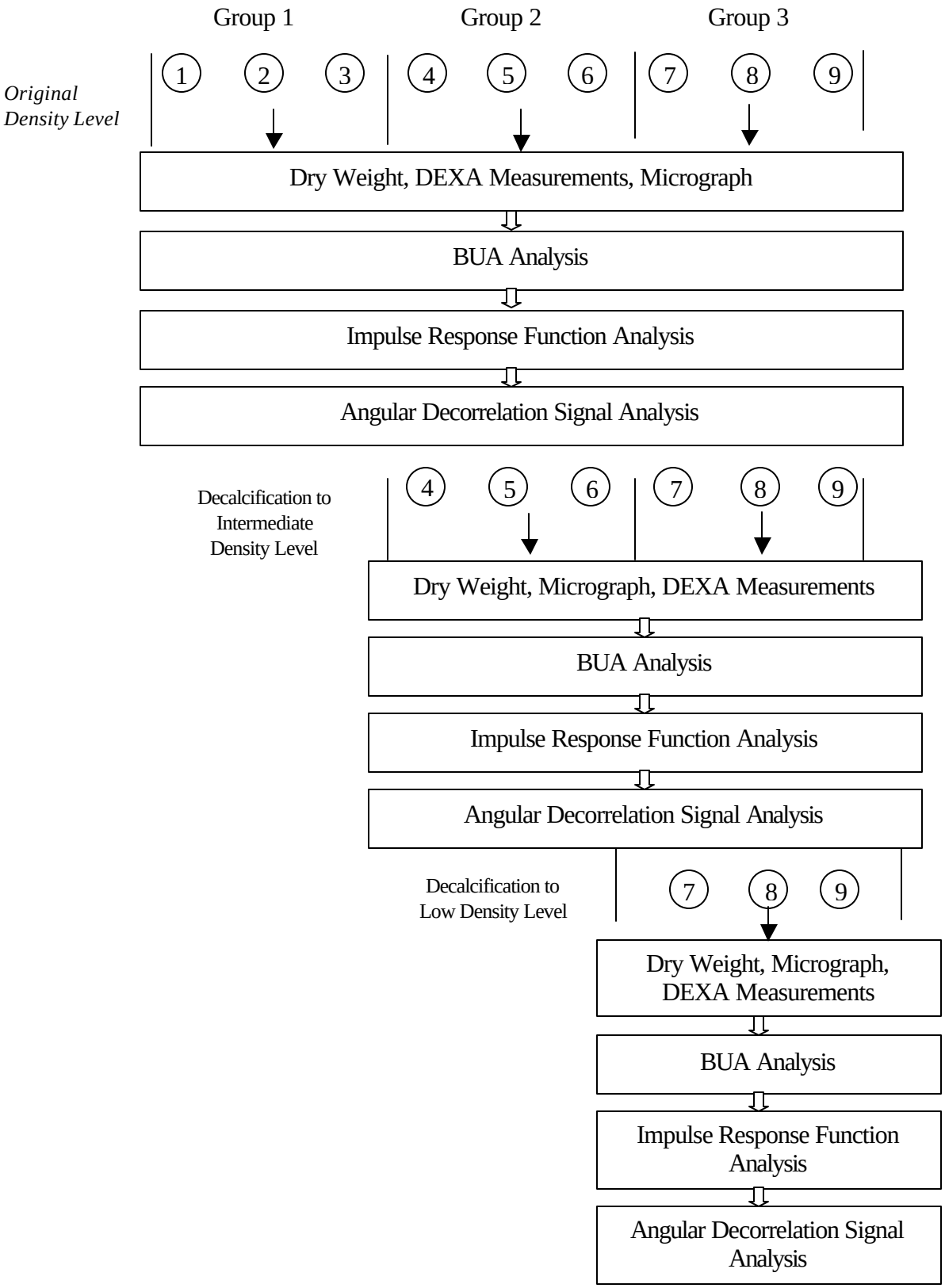

Figure 3.9 Diagram of Measurement Procedure

From the diagram in Figure 3.9, it is seen that 3 physical parameters as well as three ultrasound parameters are measured or calculated at each density level. The three physical parameters are the dry weight of the coral sample, the growth axis of each coral sample, and the dual-energy x-ray absorptiometry (DEXA) value. These parameters are used as references for the coral sample density and the microstructure. Three ultrasound parameters, BUA, impulse response and angular decorrelation are analyzed and correlated with the physical parameters. In the following chapters, these parameters will be discussed in detail.

3.3 Software Structure

After setting up the ultrasound experiment system, it is necessary to carry out various types of signal analysis on the received signal. For this purpose, the software protocol that enables the transfer of the acquired signals from the LeCroy digital oscilloscope to the PC is developed. Then, the signal processing procedures will be applied to the data, extracting the ultrasound parameters of interest. The software programs for GPIB controlling interface and for signal processing are implemented in Visual C++ (Microsoft Corp. WA) and Matlab (Mathworks, MA) respectively, which will be discussed in the following sections.

3.3.1 GPIB Control Interface

The GPIB interface of LeCroy 9400 oscilloscope is intended to provide high-speed data transfer in either the ASCII or binary format between the oscilloscope and

the computer to which it is interfaced. The GPIB interface complies with IEEE-488 (1978) standards. The maximum data transfer rate depends on the controller used, but may be as high as 400kB/s.

Most of the front panel and internal functions of the LeCroy 9400 oscilloscope can be remotely controlled using a set of high-level, English-like commands in GPIB control interface. Therefore, it is possible to read and adjust the oscilloscope settings, read data from and send acquisition to LeCroy 9400 oscilloscope. The remote control of the LeCroy 9400 oscilloscope allows complex measurement procedures and instrument setups, which is very useful in the measurement systems.

The NI-488.2M software for Windows 95 is the GPIB software for instrment control and is installed on the computer. The software includes a multi-layered device driver that consists of dynamic link library (DLL) components that run in user mode, and VxD components that run in kernel mode, as shown in Figure 3.10. User application can therefore implement various functions of control through gpib-32.dll, a 32-bit Windows 95 dynamic link library. The components which run in user mode can be accessed by the user, while the components in kernel mode can not be accessed by the user.

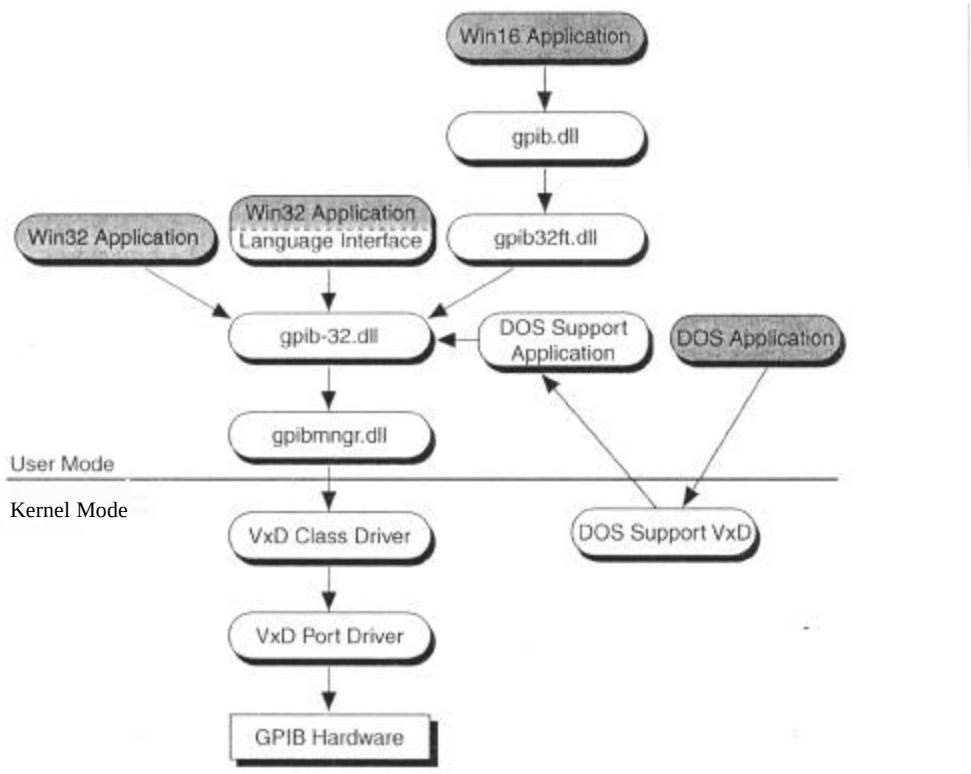

Figure 3.10 GPIB interface software hierarchy

The software program handling data flow and control settings between computer and the LeCroy 9400 oscilloscope via GPIB device was implemented by Noah W. Cushing in Fall, 1997 using Visual C++ 4.0 (Microsoft Corp.) and modified in Visual C++ 6.0 in 1999 by the thesis author. The major components of the program are contained in 3 files, which are briefly described below. More details for the software code are given in Appendix.

Interface.cpp It contains the routines for class CInterface, which is used to interface with a National Instrument GPIB card. No specific routines for the LeCroy 9400 oscilloscope are included which means that any instrument accessing GPIB device can call the functions in this file.

LC9400.cpp It contains the routines for class CLC9400, which are used to interface with LeCroy 9400 oscilloscope via GPIB. The routines contained in class CInterface are used to interface with the GPIB card in the PC. To interface with a different device, a class similar to CLC9400 should be created.

Control.cpp It contains the routines for controlling the operation of the data acquisition system which handles the procedure of getting data from the oscilloscope, translating it to voltages and outputting the data to files.

After getting all the components compiled and linked, the program can be executed with its graphical user interface shown below in Figure 3.11.

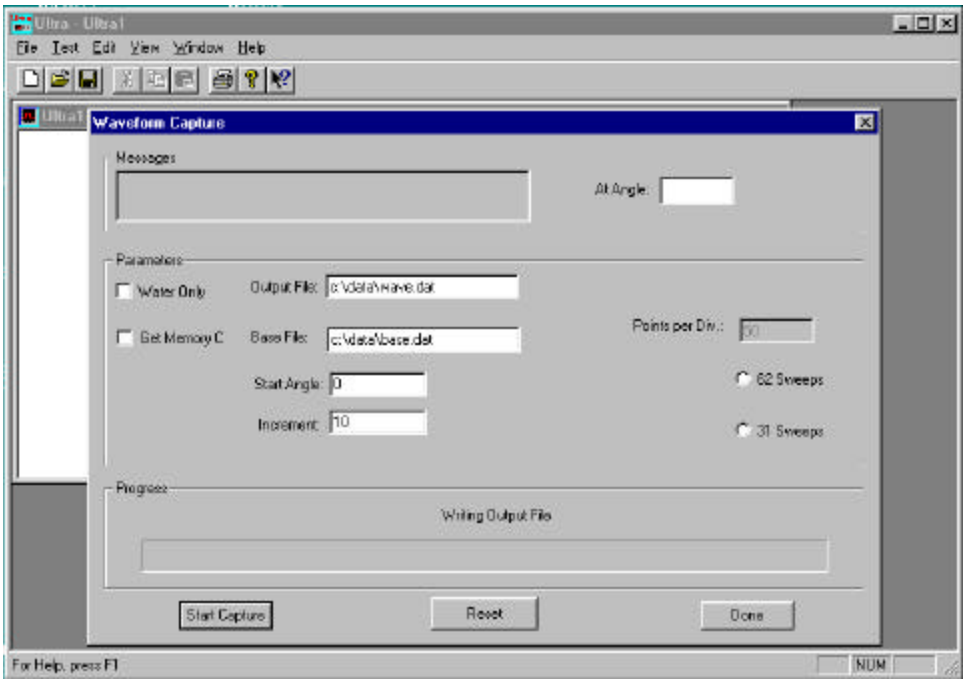

Figure 3.11 Graphical user interface for GPIB control interface program

As illustrated in Figure 3.11, the program will first initialize the GPIB device, opening a connection between computer and the LeCroy 9400 oscilloscope via GPIB interface. When the user acquires data from oscilloscope by clicking “Run” in the

"Test" submenu, the dialogue for waveform capture will appear, asking user to specify the output file name for the coming data, and the specific start angle and the angle increment in the measurement. The parameter "Water Only" will specify the output file name to be "base.dat", the parameter "Get Memory C" will make the program retrieve data from memory buffer C in oscilloscope, instead of the default setting which is Channel 1. Clicking "Start Capture" will begin the communication between the PC and the oscilloscope which is the procedure of sending commands and reading data. The "Reset" button will reset all the parameters specified and the "Done" button will finish the program and exit.

3.3.2 Signal Processing Flow Chart

Figure 3.12 below shows the signal analysis performed on the received signal, with and without the coral sample present. The signal processing flow chart is valid for both approaches: the rotation of the coral sample and the rotation of the receiving transducer. $v_s(t,q)$ is the received signal with coral sample present and $v_r(t)$ is the reference signal obtained with coral sample absent. $v_s(t,q)$ is a function of both time t and angle q because the received signal varies either with the coral sample rotation angle or with the receiving transducer rotation angle, in both rotation approaches.

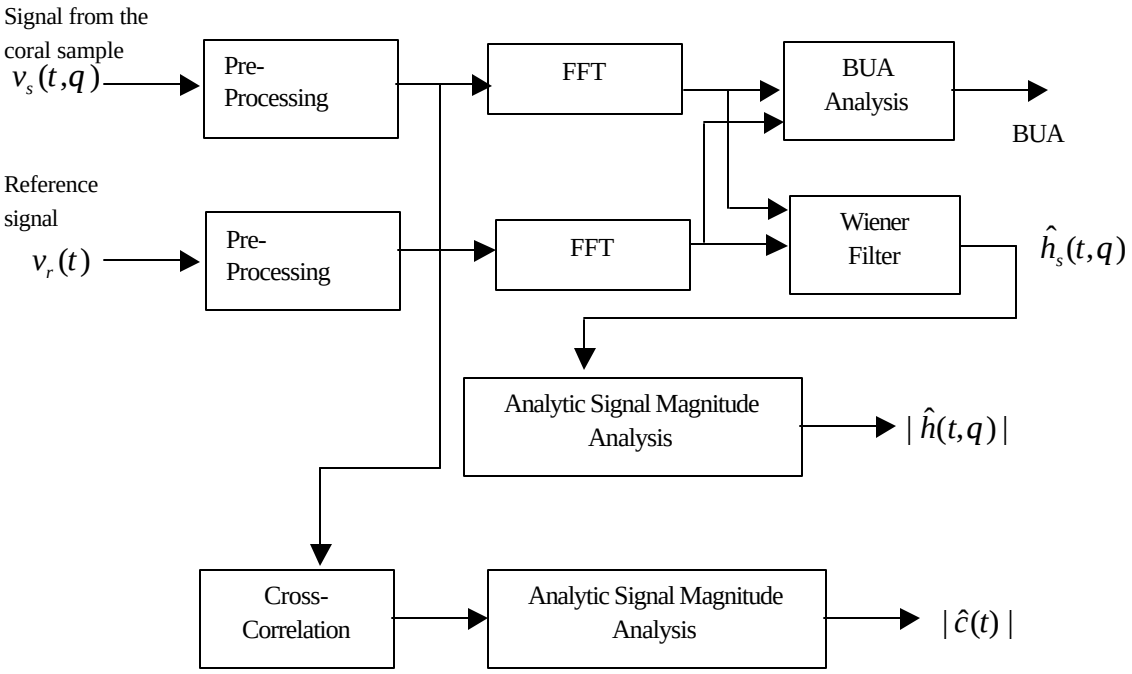

Figure 3.12 Signal processing flow chart

In Figure 3.12, $|\hat{h}_s(t,q)|$ represents the magnitude of analytical signal of the coral sample impulse response, $|\hat{c}(t)|$ represents the magnitude of analytical signal of angle cross-correlation. All together there are 3 ultrasound parameters, Broadband Ultrasonic Attenuation (BUA), impulse response function, and angle cross-correlation, which are computed in this research work.

Both the $v_s(t,q)$ and $v_r(t)$ signals undergo pre-processing before FFT (Fast Fourier Transform) or cross-correlation operations. The role of each component in pre-processing stage is described below.

Signal Sampling by LeCroy 9400 Digital Oscilloscope

For acquisition of all received signals, the Time/Division of the LeCroy 9400oscilloscope is set to be $10\,ms$ /div, and the vertical gain is adjusted to the highest

value at which the maximum signal amplitude will not be clipped. At $10\,ms/div$, the sampling interval is 10ns, and thus the corresponding sampling rate is 100 MHz. A given Time/Division used will give a defined number of samples to be displayed for a typical signal. Specifically, $10\,ms$/div will give us 10000 data points which is enough to acquire a signal window of appropriate data length.

Window Function

The time span of the received signal is $100\,ms$, while the time span for the signal samples of interest is always less than $60\,ms$. To improve the accuracy of analysis, a window function is used to remove the part of the signal which does not contain relevant information. The rectangle window function is used in the research work.

Removing DC components

To eliminate the DC shifting of received signal value, the mean of all the samples is subtracted from all the sample values. Therefore, the signal will not be effected by the DC shifting.

Downsampling

After the signal have been windowed to a $60\,ms$ time duration, the original 100 MHz sampling rate for signal can be reduced to 10 MHz. It is sufficiently high and will not create aliasing because the center frequency of the transmitting transducer is specified to be 0.5 MHz.

Zero-padding

The sampling rate is now at 1/10 of its original value. It is larger than the required corresponding Nyquist frequency. However, with the duration of signal being only $60\,ms$, the resolution of the signal spectrum might be not good enough, i.e., some significant details of the signal spectrum might be left out, and a misleading spectrum will be obtained. Since the duration of the time signal determines its frequency domain resolution, more samples are needed to make the time duration longer. Zero-padding which consists of adding dummy samples with a value of 0, increases the number of samples and will help in getting a better idea of the signal spectrum from its samples. In our program, the zero-padding makes the time span of the signal to be $100\,ms$ again. The number of zero padded samples is calculated as $\frac{100ms - window\ signal\ timespan}{100ns}$.

After all the pre-processing operations, the received signal will be further processed to obtain the ultrasound parameters.

3.3.3 Graphical User Interface of Signal Processing

The signal processing program is implemented in Matlab. Figure 3.13 below shows the Graphical User Interface (GUI) of the program. It makes the signal processing operations much easier to use. The related GUI program and signal processing code are given in the Appendix.

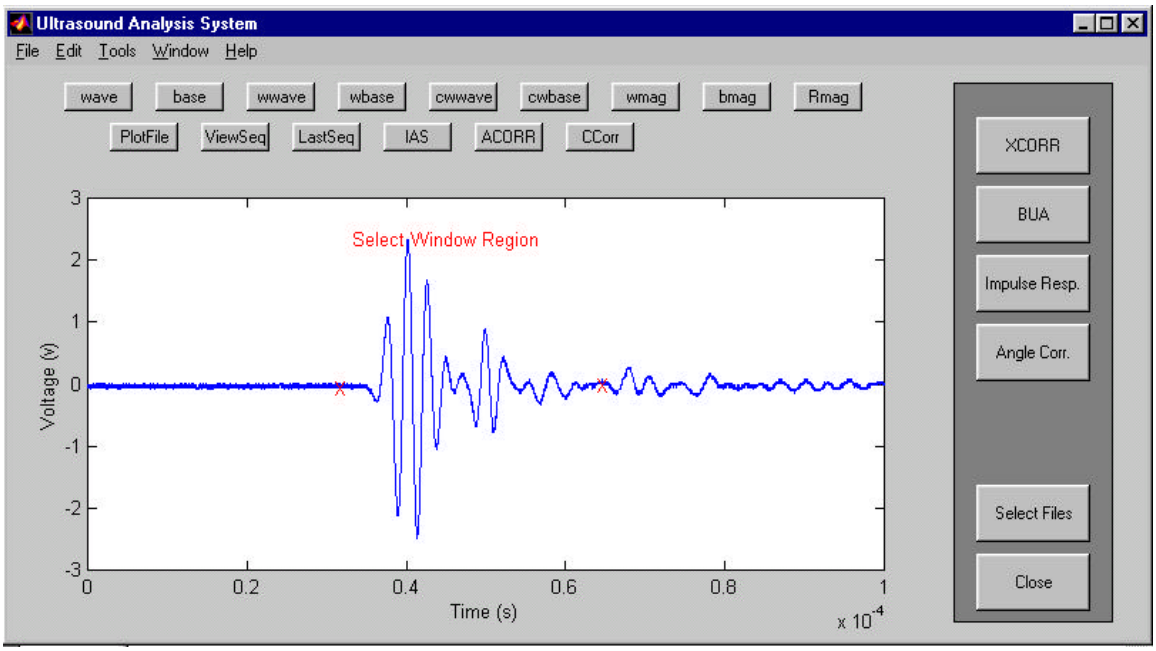

Figure 3.13 Graphical user interface of signal processing program

The command buttons shown in the window and their corresponding operations are listed below in Table 3.1:

Table 3.1 Commands Buttons and the Corresponding Function Descriptions

Command Buttons (at the right side of window)	Function Description
Close	Exits the analysis of software
Select Files	Selects the files to analyze
XCORR	Computes the normalized cross-correlation function of the waveforms contained in the selected files.
BUA	Calculates the Broadband Ultrasound Attenuation
Impulse Resp.	Calculates the magnitude of the analytic signal for the coral sample impulse response
Angle Corr.	Computes the magnitude of the analytic signal for the cross-correlation function of the reference wave and the measured wave, for each measurement angle.
Command Buttons (at top of the window)	Function Description

wave	Displays the measured (with sample in tank) waveform
base	Displays the base (water-only) waveform
wwave	Displays the time-windowed, measured waveform
wbase	Displays the time-windowed, base waveform
cwwave	Displays the compressed, time-windowed, measured waveform
cwbase	Displays the compressed, time-windowed, base waveform
wmag	Displays the magnitude spectrum of the measured waveform in dB
bmag	Displays the magnitude spectrum of the base waveform in dB
rmag	Displays the difference in dB of the magnitude spectra (bmag - wmag)
PlotFile	Plots the signal file, wave or base file
ViewSeq	Views a sequence of measured signals
LastSeq	Plots the last sequence viewed
IAS	Plots the integrated angle scattering (IAS) parameter for a set of measurements. This is not covered in this research work
ACORR	Plots the maximum value of the cross-correlation function of the base wave vs. the measured wave for each measurement angle
CCorr	Calculates the attenuation-corrected correlation function for the two waveforms. This is not covered in this research work

CHAPTER 4

NON-ULTRASONIC CHARACTERIZATION TECHNIQUES

Although this thesis work is aimed at developing ultrasonic techniques for analyzing the coral samples, the non-ultrasonic techniques are necessary as the references for density and structure information of the coral samples. The relationship between the ultrasonic and the non-ultrasonic techniques are examined for better comparison and understanding of the variation of the ultrasound signal as the density and structure of the coral samples change. Three non-ultrasonic parameters are used here: DEXA value, dry weight and the growth axis, which will be discussed below.

4.1 DEXA Measurement

4.1.1 Measurement Description

The densities of coral samples are measured by a QDR1000 pencil beam DEXA scanner (Hologic Inc., Bedford, MA) available in the School of Veterinary Medicine, Tufts University (North Grafton, MA). According to the measurement protocol in this research work, the DEXA value is used as the mineral density reference for each decalcification level. Therefore, all 9 coral samples were first characterized by the DEXA scanner before any decalcification, then 6 coral samples in Group 2 and Group 3 were measured again to obtain the values of DEXA after being lightly or intermediately decalcified. Finally the last 3 coral samples in Group 3 were scanned to obtain their DEXA density values after heavy decalcification.

During the DEXA measurements, the coral sample is placed in a tank with water which simulates the soft tissue around bone. The line drawn across the top of coral sample in Figure 4.1 (a) indicates the reference orientation, which is defined as the one where the fast wave is observed to have the maximum amplitude. The coral sample is oriented carefully so that the line on its top will be parallel with the long dimension of the tank, as shown in Figure 4.1 (a). It would make all the coral samples be scanned in a similar consistent orientation so that accurate comparison between coral samples will be achieved.

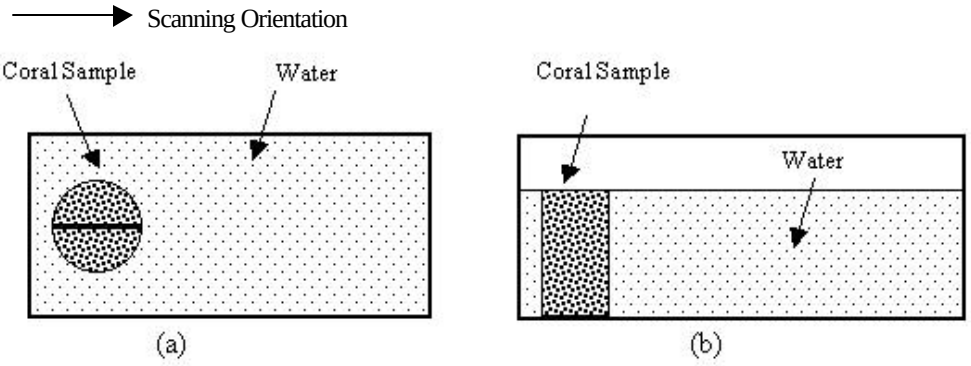

Figure 4.1 DEXA measurement setup. (a) top view showing the orientation of the coral sample; (b) side view of water tank with the coral sample

After scanned by the DEXA scanner, the cross-sectional area of each coral sample will be divided into sub-regions, and 7 of them are selected. The DEXA value of the selected region as well as of the whole surface is obtained which is the integrated mass weight of the region area with the unit of g/cm^2. The value is often referred to as the BMD (Bone Mass Density) since the DEXA technique is used clinically and is considered as the reference parameter of bone density. The BMD values are used to represent the coral sample density of each cross-section sub-region in this thesis, and the Global BMD represents the coral sample density of the whole cross-section region obtained form the DEXA measurements. Since the height of the coral samples used in

this research work is known, it is possible to divide the BMD value of each coral sample by its corresponding sample height to obtain a bone mass density in g/cm^3. BMD cannot give the information of the coral sample microstructures because it is an integrated weight value over a given area. The location, shape and geometry of each selected region of the coral sample are shown in Figure 4.2.

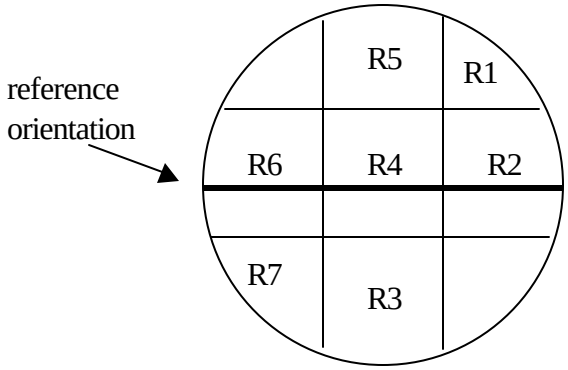

Figure 4.2 Regions of the cross-sectional area allocated in DEXA measurement

The BMD values of 9 coral samples when measured at their original densities are shown in Figure 4.3 below. The BMD values in Figure 4.3 are the measured BMD values, divided by the height of the coral samples.

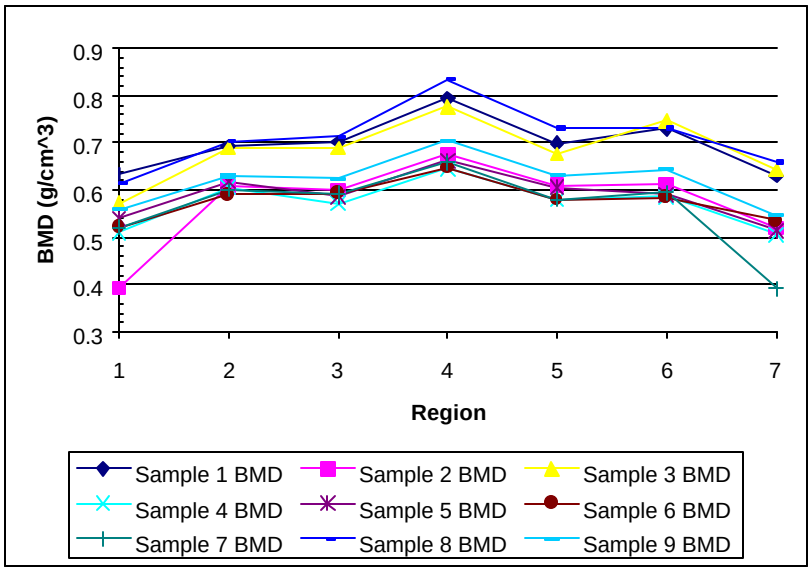

Figure 4.3 BMD value of each region of every sample

From the above figure, we can see that R4 region has a higher BMD value than the values of other regions. This may partly be due to imperfections in the edge detection and irregular geometry area approximation of DEXA scanner software, as shown in Figure 4.4 below. In Figure 4.4, all regions except R4 region are approximated by the areas with dotted lines confining the outside borders. The approximated areas are slightly larger than the actual areas for the regions. Therefore, the calculated BMD value of the approximate area is less than the actual BMD value.

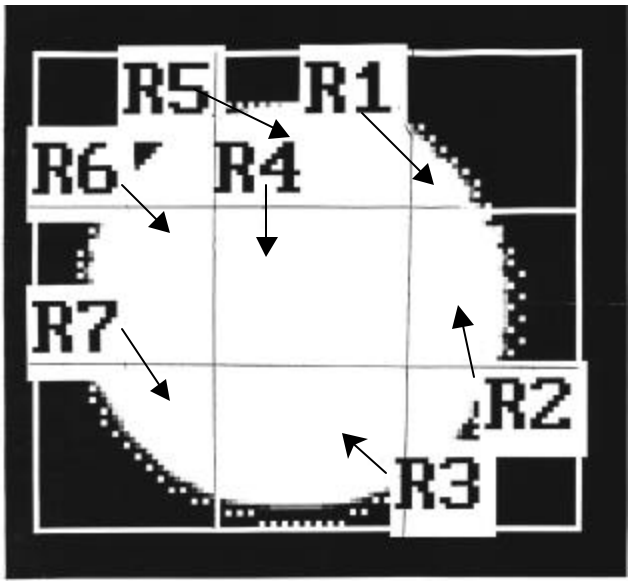

Figure 4.4 Image edge approximation by DEXA scanner software of individual regions of the coral sample cross-section

The average and the *coefficients of variance* of the BMD values for the selected regions are shown in Table 4.1. The average BMD for each coral sample is between 2.8 g/cm^2 to 3.7 g/cm^2. The *coefficients of variance* for most coral samples are between 0.08 ~ 0.09, with only two of them are around 0.15. The reason for using the *coefficients of*

variance here is that the standard deviation, defined as $s = \sqrt{\frac{n\sum x^2 - \left(\sum x\right)^2}{n(n-1)}}$, where x denotes each BMD value, n denotes the number of the BMD values, is affected by the average BMD value amplitude. Therefore, the coefficients of variance, which is the standard deviation divided by the average data value, will not affected by the average value amplitude.

Table 4.1 BMD Values of Regions for Coral Samples at Original Density (Unit: g/cm^3)

Region	Sample1	Sample2	Sample3	Sample4	Sample5	Sample6	Sample7	Sample8	Sample9
R1	0.635	0.393	0.51	0.573	0.541	0.522	0.614	0.522	0.56
R2	0.692	0.607	0.606	0.69	0.62	0.591	0.704	0.601	0.63
R3	0.702	0.601	0.572	0.69	0.587	0.594	0.713	0.593	0.625
R4	0.794	0.676	0.646	0.777	0.663	0.648	0.834	0.658	0.705
R5	0.699	0.611	0.58	0.677	0.606	0.58	0.732	0.581	0.631
R6	0.731	0.613	0.587	0.747	0.59	0.585	0.732	0.595	0.645
R7	0.631	0.521	0.506	0.642	0.515	0.536	0.66	0.392	0.547
Global BMD	0.699	0.6	0.577	0.685	0.593	0.581	0.714	0.587	0.625
Average	0.698	0.574	0.572	0.685	0.589	0.579	0.713	0.563	0.620
Standard Deviation	0.056	0.092	0.05	0.0668	0.0492	0.0414	0.0683	0.0853	0.0532
Coefficients of Variance	0.0803	0.16	0.0876	0.0975	0.0836	0.0715	0.0958	0.151	0.0858

Table 4.1 above shows that the densities of the coral samples are close and the density of each coral sample could be thought of as uniform. An important reason for calculating the coefficients of variance is to check that decalcification does not make the coral samples less uniform. This is checked by comparing the coefficients of variance before and after decalcification, which is discussed in the following section.

4.1.2 Density Loss after Decalcification

As stated in Chapter 3, decalcification is employed to change the densities of the coral samples so as to find the ultrasound signal parameters variation with density levels. As described earlier, the density of 2 out of the 3 groups was changed by the decalcification process using formic acid. Thus, all 9 coral samples in 3 groups were analyzed at their original density level, the 6 coral samples in group 2 and group 3 were analyzed after an intermediate level of decalcification and the 3 samples in group 3 were analyzed after heavy decalcification.

Light Decalcification

Table 4.2 and Figure 4.5 show the BMD values of 7 regions of coral samples 4 to 9 (Group 2 and Group 3) after light decalcification.

Table 4.2 BMD Values of Regions for Coral Samples After Light Decalcification (Unit: g/cm^3)

Region	Sample 4 BMD	Sample 5 BMD	Sample 6 BMD	Sample 7 BMD	Sample 8 BMD	Sample 9 BMD
R1	0.481	0.438	0.446	0.468	0.426	0.46
R2	0.536	0.49	0.527	0.576	0.516	0.526
R3	0.579	0.487	0.5	0.63	0.486	0.517
R4	0.649	0.555	0.555	0.714	0.544	0.589
R5	0.583	0.488	0.481	0.626	0.465	0.533
R6	0.641	0.493	0.489	0.64	0.472	0.541
R7	0.552	0.436	0.436	0.586	0.416	0.472
Mean	0.574	0.484	0.49	0.606	0.475	0.52
Std. Deviation	0.0588	0.0402	0.0414	0.0755	0.0458	0.0432
Coefficients of variance	0.1024	0.0831	0.0845	0.125	0.0964	0.0832

Table 4.2 shows that after light decalcification, the coefficients of variance of 7 regions BMD values of the coral samples are between 0.08 ~ 0.13. Compared with the

coefficients of variance of 7 regions BMD values of the coral samples at their original densities in Table 4.1, which are between 0.07~0.16, the coral samples can be thought of being uniformly decalcified because the differences between the regions are similar to what they were before decalcification. Figure 4.5 below shows the BMD values between the regions for each coral sample after light decalcification.

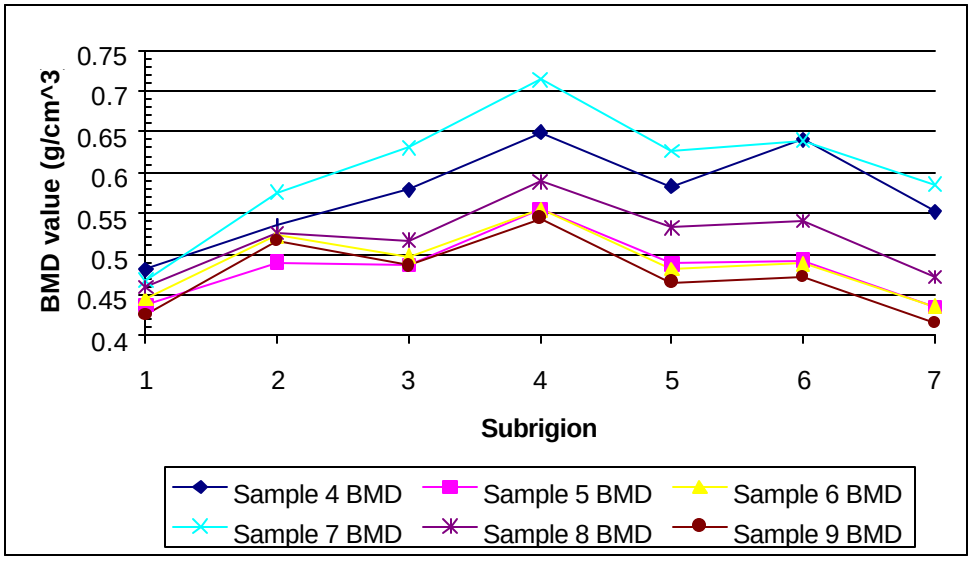

Figure 4.5 BMD values of the regions of each sample after light decalcification

Heavy Decalcification

The three samples in Group 3 are analyzed after heavy decalcification. Table 4.3 shows the BMD values of the 7 regions of sample 7 to sample 9 after heavy decalcification.

Table 4.3 BMD Values of Regions for Coral Samples After Heavy Decalcification

Region	Sample 7 BMD	Sample 8 BMD	Sample 9 BMD
R1	0.438	0.347	0.41
R2	0.442	0.432	0.412
R3	0.517	0.371	0.409
R4	0.583	0.441	0.469
R5	0.492	0.372	0.442
R6	0.499	0.35	0.42
R7	0.447	0.311	0.363
Mean	0.488	0.375	0.418
Std. Deviation	0.0521	0.0469	0.0327
Coefficients of variance	0.107	0.125	0.0782

The coefficients of variance of 7 regions BMD values of the coral samples are between 0.078 ~ 0.11. Figure 4.6 below shows the BMD values for the individual regions for each coral sample after heavy decalcification. Hence, the coral samples can be thought of having been uniformly decalcified.

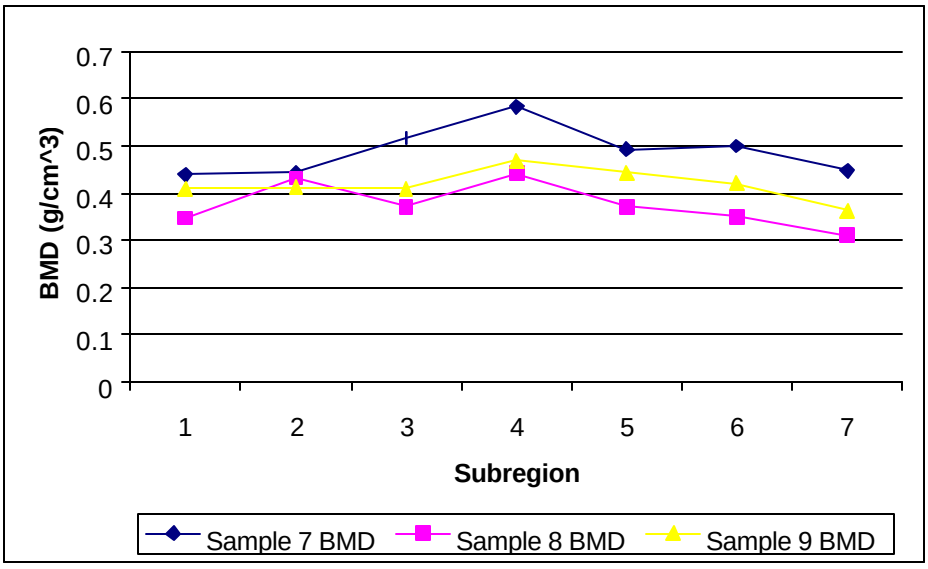

Figure 4.6 BMD values of the regions of each sample after heavy decalcification

4.2 Dry Weight of Coral Sample

4.2.1 Measurement Description

The dry weight is the other parameter used as the reference for the coral sample density. It is measured with a mechanical scale with digital readout (Acculab VI-1200, Cole-Parmer's Co., Canada) with precision of 0.1g. For further processing, the *apparent density* is defined here as the result of the dry mass of the coral sample divided by its external volume. It is observed that the value of the apparent density is larger than the value of the global BMD for each coral sample. The BMD values correlate very well (R^2=0.9868) with the apparent density for all the coral samples, as shown in Table 4.4 and Figure 4.7 below.

Table 4.4 Comparison of Dry Weight, Apparent Density and Global BMD of Each Coral Sample

Sample	Original Dry Weight (g)	Global BMD (g/cm^2)	Apparent Density (g/cm^3)	BMD (g/cm^3)
1	52.2	3.588	0.923	0.699
2	43.9	3.08	0.776	0.6
3	41.1	2.964	0.727	0.577
4	51.6	3.518	0.912	0.685
5	42.4	3.046	0.75	0.593
6	41.9	2.985	0.741	0.581
7	55.8	3.666	0.987	0.714
8	46	3.208	0.757	0.587
9	42.8	3.012	0.813	0.625
Average	46.411	3.23	0.821	0.629

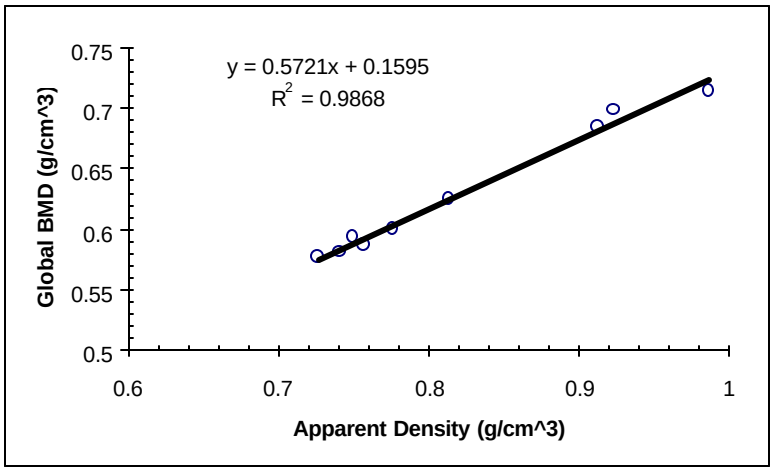

Figure 4.7 Relationship between the original weight and the density of each coral sample

4.2. 2 Density Loss after Decalcification

For comparison, the dry weight loss, or the apparent density loss after decalcification as well as the BMD loss are shown below.

Light Decalcification

Table 4.5 gives the comparison of the apparent density loss and the BMD loss of each sample from their original values after light decalcification.

Table 4.5 Comparison of Weight and BMD Losses After Light Decalcification

	Apparent Density (g/cm^3)	Apparent Density After Light Decalcification (g/cm^3)	Apparent Density Loss %	Original BMD (g/cm^3)	BMD After Light Decalcification (g/cm^3)	BMD Loss %	Ratio of Apparent Density Loss % to BMD Loss%
Sample4	0.911	0.732	19.6	0.685	0.582	15.1	1.302
Sample5	0.744	0.575	22.8	0.59	0.485	18.2	1.253
Sample6	0.737	0.585	20.6	0.582	0.49	15.9	1.298
Sample7	0.985	0.789	19.9	0.717	0.61	14.9	1.334
Sample8	0.753	0.571	24.2	0.588	0.479	18.5	1.307
Sample9	0.812	0.642	20.9	0.624	0.523	16.1	1.298

From Table 4.5, it is seen that the percentage of apparent density loss of the coral samples are between 19.6%~24.2%, or on average 21% lower than their original values.

The global BMD percentage loss is lower than apparent density percentage loss for each sample, where the latter is between 14.9%~18.5%. The ratio between the apparent density percentage loss and BMD percentage loss is constant and approximately 1.3, as shown in Table 4.5. The apparent density loss and the BMD loss correlate very well (R^2=0.9587), as shown in Figure 4.8.

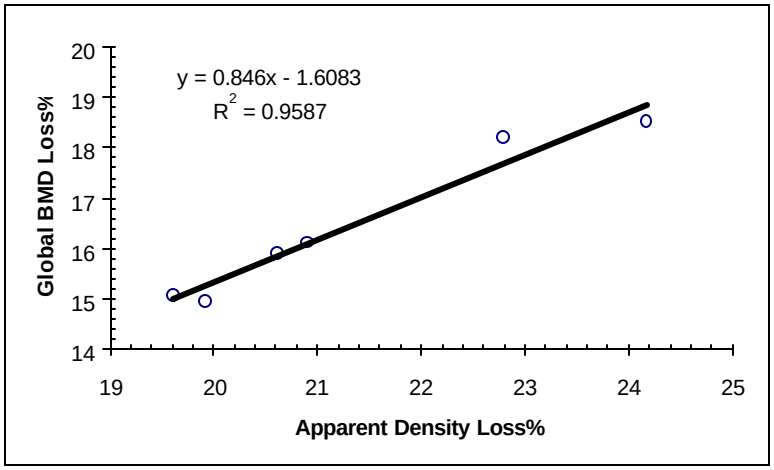

Figure 4.8 Correlation between global BMD percentage loss and apparent density percentage loss

Heavy Decalcification

Table 4.6 shows a comparison of apparent density and BMD losses after heavy decalcification.

Table 4. 6 Comparisons of Weight and BMD Losses After Heavy Decalcification

	Original Weight (g)	Weight After Heavy Decalcification (g)	Original BMD (g/cm^2)	BMD after heavy Decalcification (g/cm^2)	Weight Loss %	BMD Loss %	Ratio of Apparent density Loss % to BMD Loss%
Sample7	0.985	0.58	0.717	0.483	41.11	32.61	1.261
Sample8	0.753	0.43	0.588	0.383	42.96	34.77	1.235
Sample9	0.812	0.481	0.624	0.417	40.74	33.13	1.23

The apparent density loss of each sample is around 41% while the percentage of BMD loss is lower than weight loss which is around 33%. The ratio between them is constant, around 1.25. The correlation between the apparent density percentage loss and BMD percentage loss ($R^2 = 0.8568$) is shown in Figure 4.9.

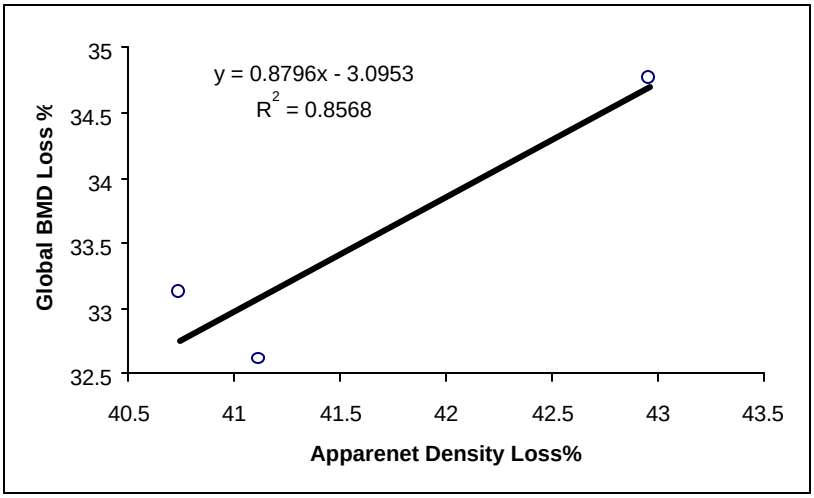

Figure 4.9 Correlation between global BMD percentage loss and apparent density percentage loss

The results above show that the coral samples have been uniformly decalcified, which is important for mimicking the gradual process of osteoporosis.

4.3 Coral Sample Growth Axis Determination

The growth axis is defined here as the dominant orientation observed from the coral sample microstructure distribution. It is found that the trabeculae of the coral samples are distributed along some specific dominant orientation, which looks like the trabeculae "growing" along a specific axis. It is another important characteristics of the coral samples and is believed to affect the ultrasound measurement and the ultrasound parameters extracted from the measurements. Two approaches, *physical observation* and

micrograph taken by microscope camera, are used to determine the growth axis for each coral sample.

4.3.1 Physical Observation

Approximately 3 different growth axes of the coral samples are observed from the coral samples, illustrated in Figure 4.10, Figure 4.11 and Table 4.7 and shown in the coral sample photos in Figure 412. The line on the top of the coral sample in Figure 4.10 has been described before, and it represents the reference orientation in which the amplitude of the fast wave in received signal will reach its maximum value. The arrows going through the coral samples in both Figure 4.10 and the photos in Figure 4.11 represent the growth axes.

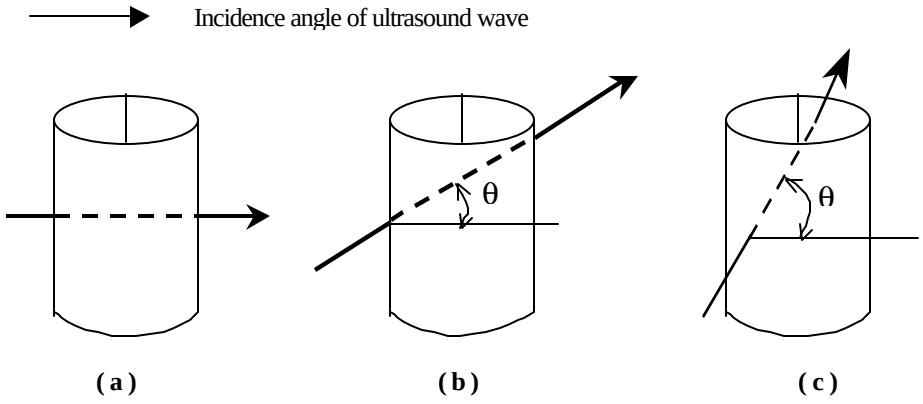

Figure 4.10 Different growth axes of coral sample (a) Horizontal growth axis; (b) 30^o ~ 40^o between growth axis and measurement plane; (c) 50^o ~60^o between growth axis and measurement plane

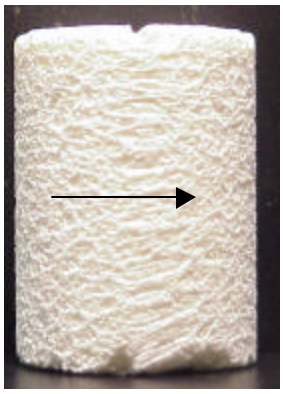

(a) Sample 1

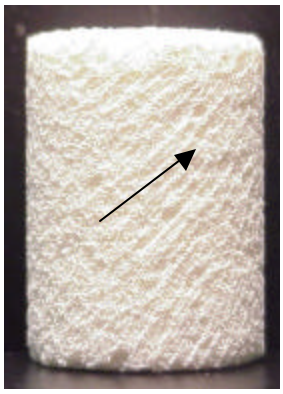

(b) Sample 2

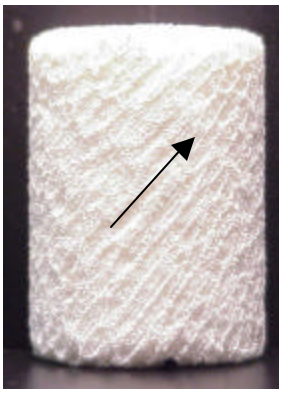

(c) Sample 3

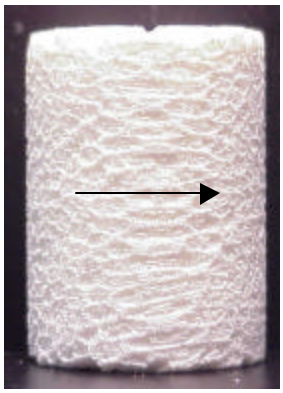

(d) Sample 4

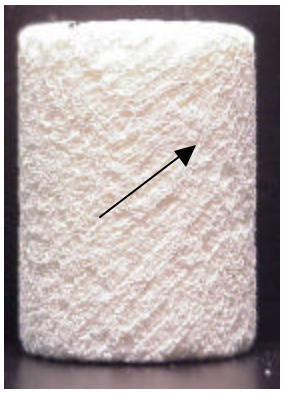

(e) Sample 5

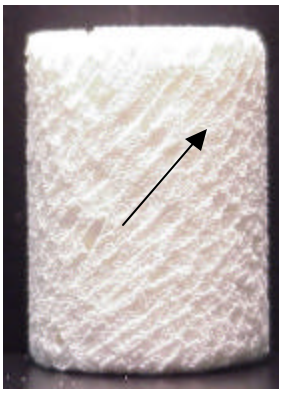

(f) Sample 6

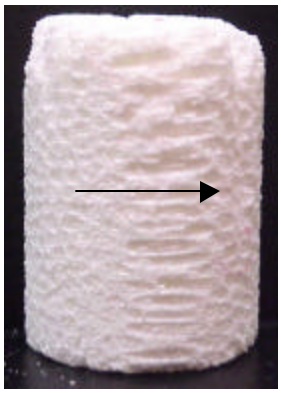

(g) Sample 7

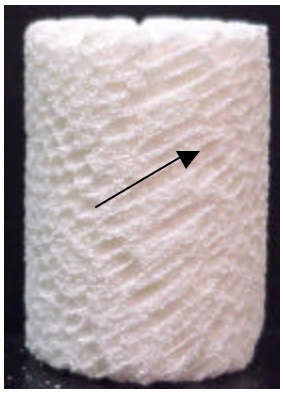

(h) Sample 8

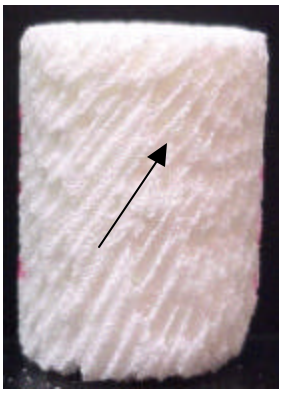

(i) Sample 9

Figure 4.11 Photos of the coral sample showing growth axes (a)~(c) Sample 1, 2, 3 at original density; (d)~(f) Sample 4, 5, 6 after light decalcification; (g)~(i) Sample 7, 8, 9 after heavy decalcification

Figure 4.10 and Figure 4.11 show that the first growth axis direction is nearly horizontally, i.e., parallels with the measurement plane, or the incident angle of ultrasound wave propagation. The second growth axis direction has an angle $\theta \approx 30^o \sim 40^o$ between the measurement plane, while the angle θ between the third growth axis direction and the measurement plane is around $50^o \sim 60^o$. The growth axis angle of each coral sample is listed in Table 4.7 below.

Table 4.7 Angle between the growth axis and the measurement plane for each coral sample

Sample		Angle
Group 1	Sample 1	0^o
	Sample 2	38^o
	Sample 3	50^o
Group 2	Sample 4	0^o
	Sample 5	38^o
	Sample 6	49^o
Group 3	Sample 7	0^o
	Sample 8	30^o
	Sample 9	60^o

Therefore, the growth axis of each coral sample falls in one of the above 3 growth axes categories, and the growth axis still exists after the coral sample is decalcified. In order to correlate the coral sample microstructure with its ultrasound parameters, each coral sample is numbered and categorized into one of the 3 groups. Each group includes coral samples with 3 different microstructure growth axes. Care is taken to maintain the 3 coral sample groups to be similar, and each coral sample to be measured with consistent orientation.

4.3.2 Coral Sample Micrograph

Microscope photos of the two ends of coral samples with 5x and 7.5x magnification factor are shown in the following pages. They are taken by using the

optical microscope combined with Nikon camera in the Material Science Program of WPI. Figure 4.12 to Figure 4.20 are the microscope photos of the 9 coral samples when they are at original density. Figure 4.21 to Figure 4.26 are the microscope photos of the 6 coral samples (sample 4 to sample 9) after they have been lightly decalcified. Figure 4.27 to Figure 4.29 are the microscope photos of the 3 coral samples (sample 7 to sample 9) after they have been heavily decalcified. All the photos are taken when the coral samples are placed along the reference orientation. The top end of the coral sample is defined as the end surface where the growth axis enters into, while the bottom end is defined as the end surface where the growth axis leaves.

Microscope Photos of the Coral Samples at Original Density

1) Group 1:

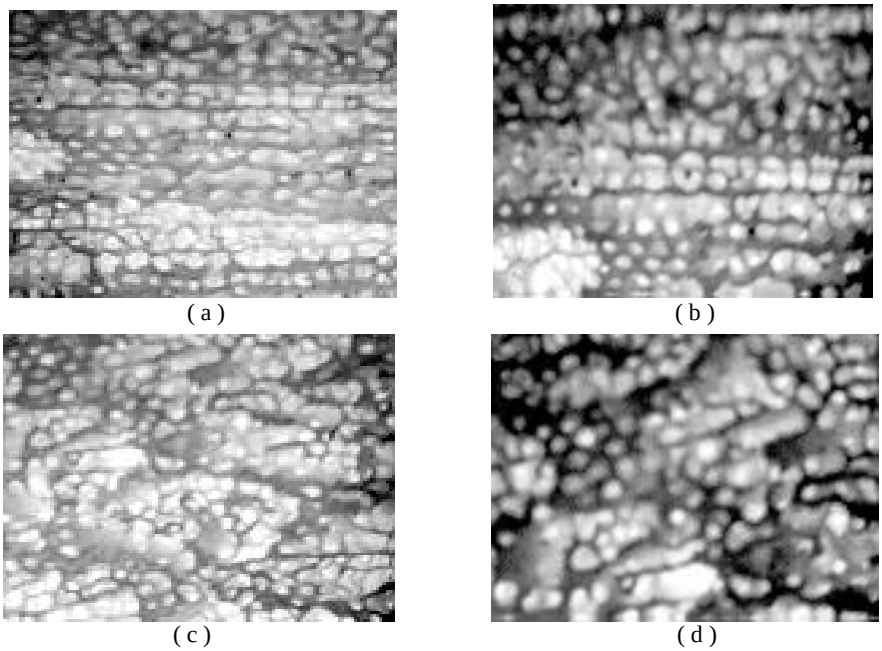

Figure 4.12 Photo of Sample 1: (a) Top-side with 5x magnification; (b) Top-side with 7.5x magnification; (c) Bottom-side with 5x magnification; (d) Bottom-side with 7.5x magnification

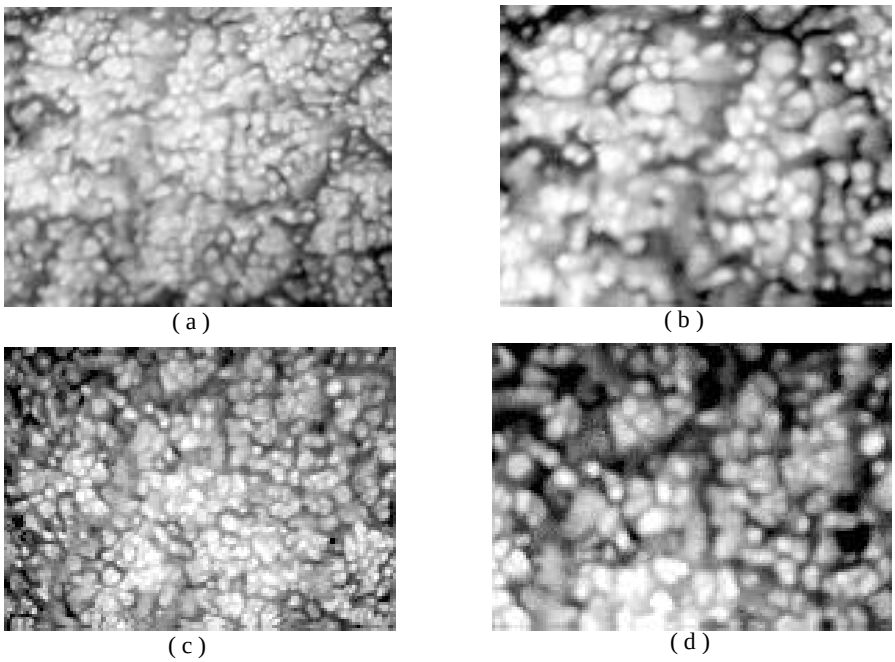

(a) (b)

(c) (d)

Figure 4.13 Photo of Sample 2: (a) Top-side with 5x magnification; (b) Top-side with 7.5x magnification; (c) Bottom-side with 5x magnification; (d) Bottom-side with 7.5x magnification

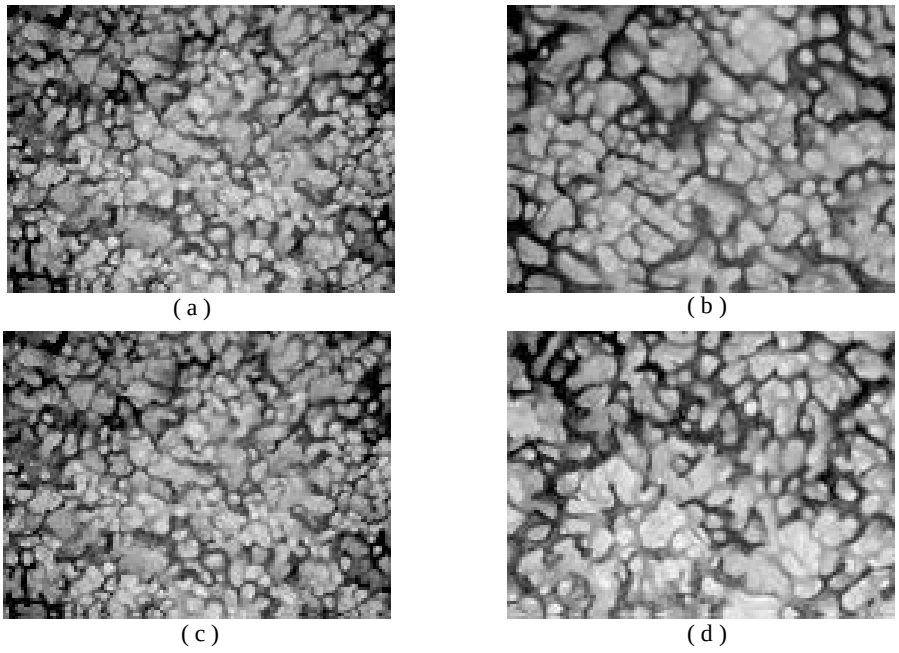

(a) (b)

(c) (d)

Figure 4.14 Photo of Sample 3: (a) Top-side with 5x magnification; (b) Top-side with 7.5x magnification; (c) Bottom-side with 5x magnification; (d) Bottom-side with 7.5x magnification

2) Group 2:

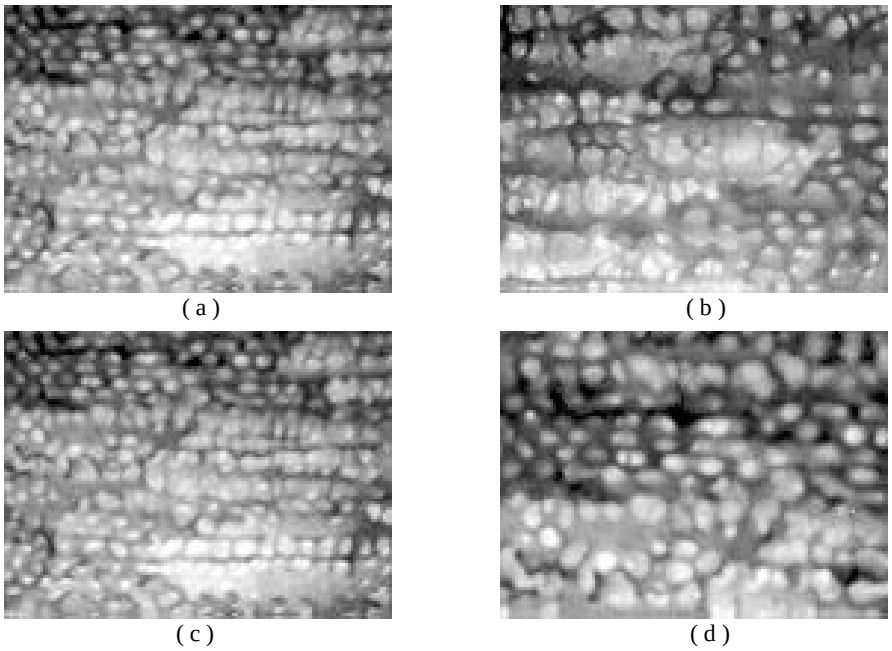

Figure 4.15 Photo of Sample 4: (a) Top-side with 5x magnification; (b) Top-side with 7.5x magnification; (c) Bottom-side with 5x magnification; (d) Bottom-side with 7.5x magnification

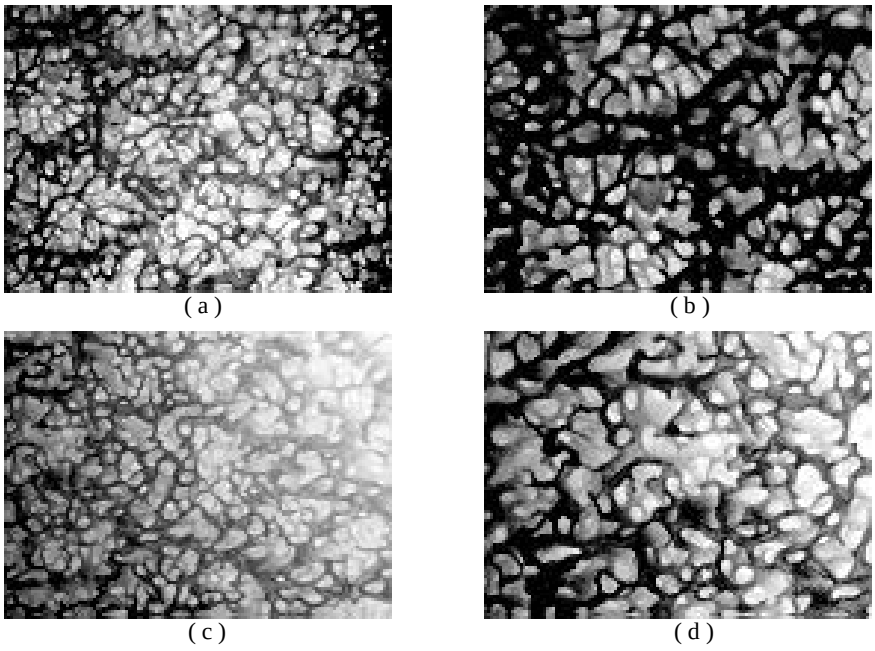

Figure 4.16 Photo of Sample 5: (a) Top-side with 5x magnification; (b) Top-side with 7.5x magnification; (c) Bottom-side with 5x magnification; (d) Bottom-side with 7.5x magnification

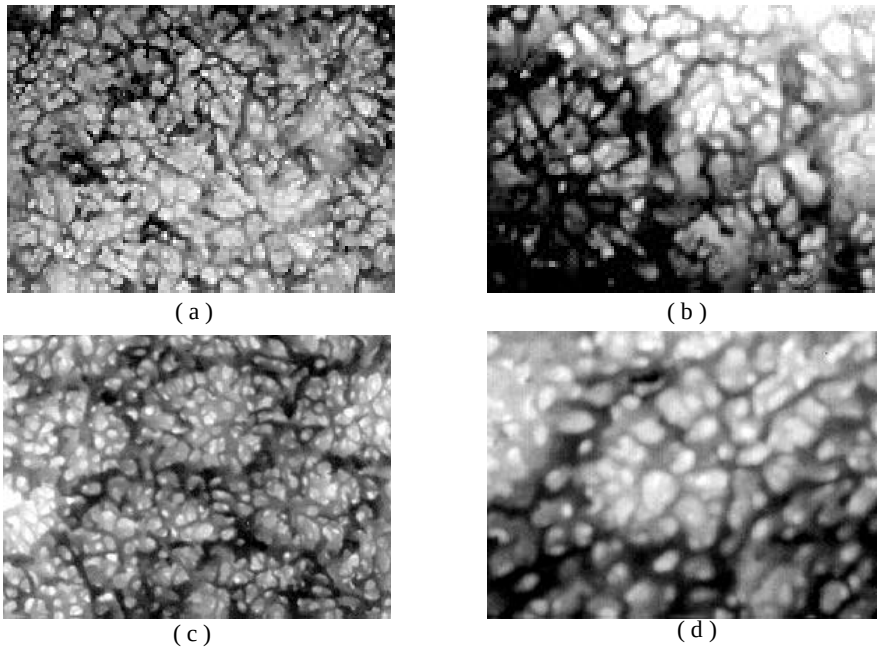

(a) (b) (c) (d)

Figure 4.17 Photo of Sample 6: (a) Top-side with 5x magnification; (b) Top-side with 7.5x magnification; (c) Bottom-side with 5x magnification; (d) Bottom-side with 7.5x magnification

3) Group 3:

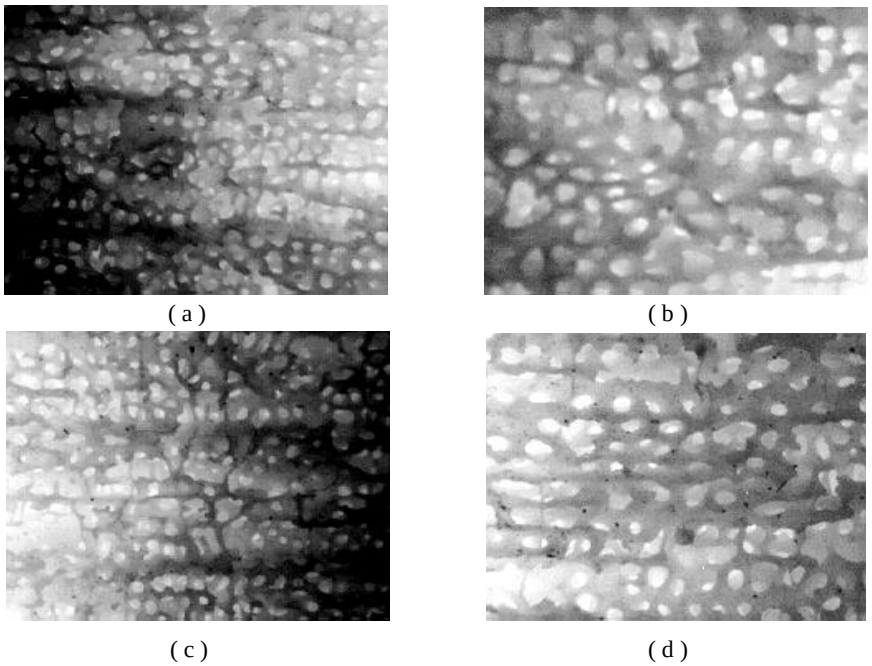

(a) (b) (c) (d)

Figure 4.18 Photo of Sample 7: (a) Top-side with 5x magnification; (b) Top-side with 7.5x magnification; (c) Bottom-side with 5x magnification; (d) Bottom-side with 7.5x magnification

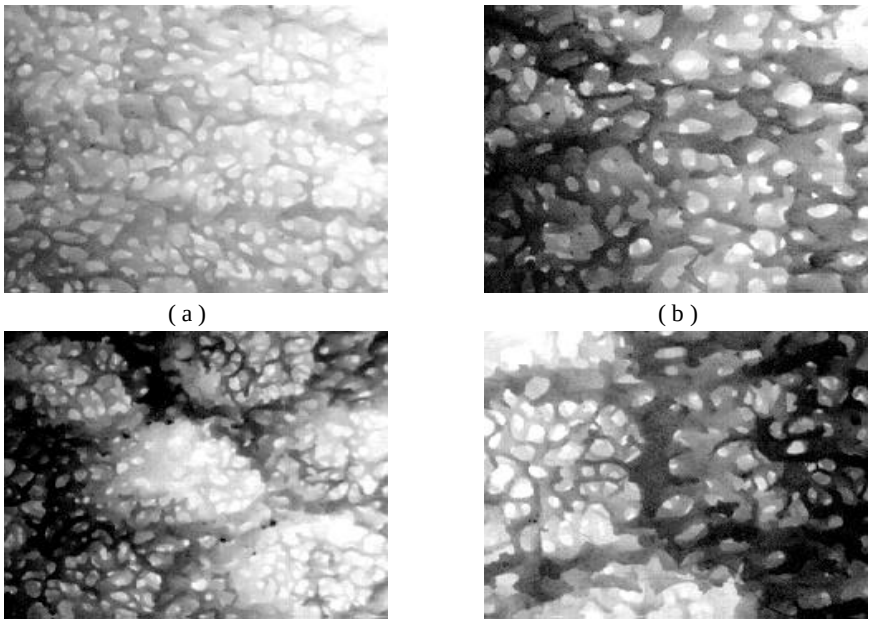

Figure 4.19 Photo of Sample 8: (a) Top-side with 5x magnification; (b) Top-side with 7.5x magnification; (c) Bottom-side with 5x magnification; (d) Bottom-side with 7.5x magnification

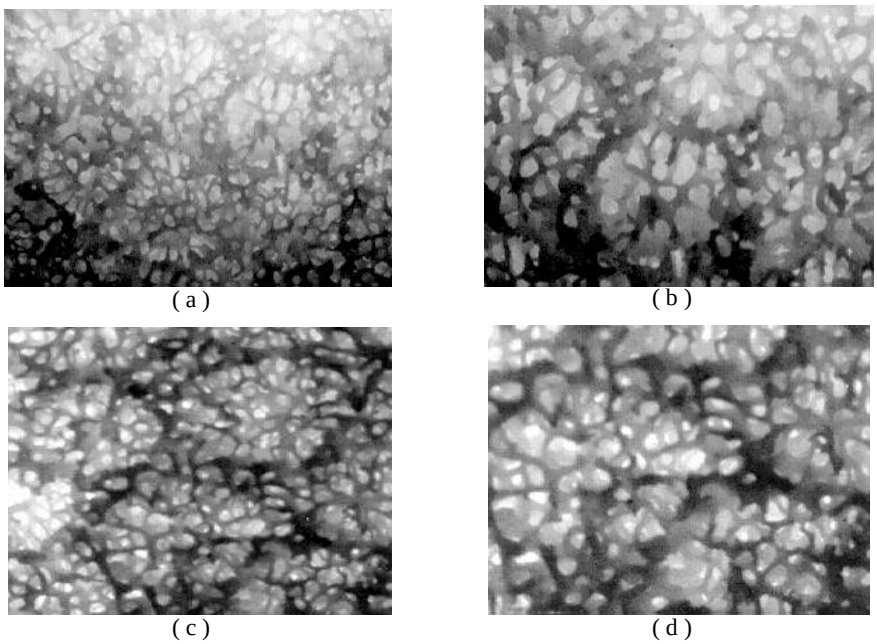

Figure 4.20 Photo of Sample 9: (a) Top-side with 5x magnification; (b) Top-side with 7.5x magnification; (c) Bottom-side with 5x magnification; (d) Bottom-side with 7.5x magnification

Microscope Photos of the Coral Samples After Light Decalcification

1) Group 2:

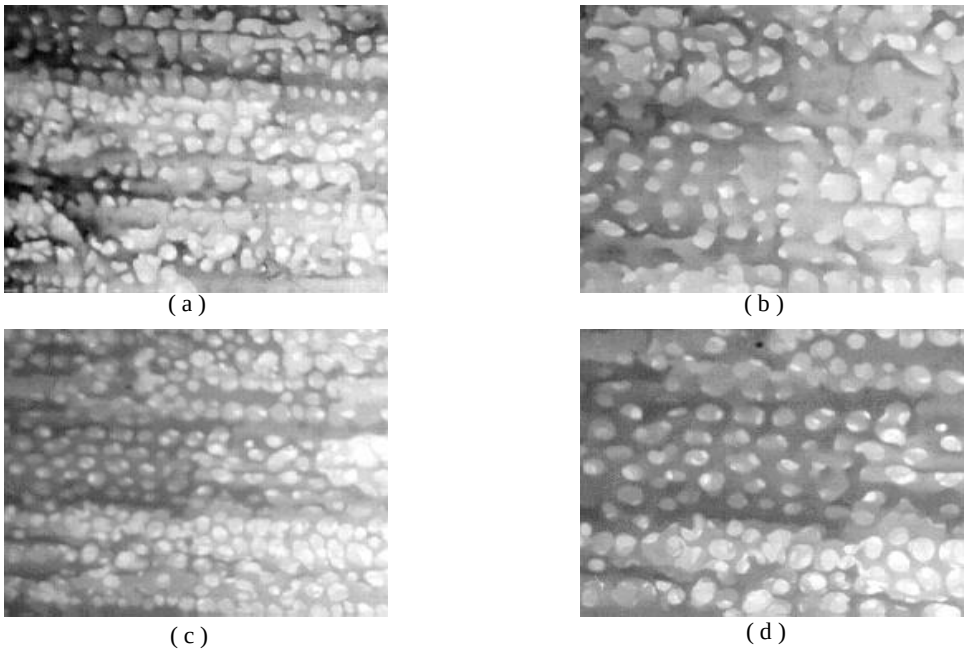

(a) (b)

(c) (d)

Figure 4.21 Microscope photos of sample 4 (a) 5x top surface; (b) 7.5x top surface; (c) 5x bottom surface; (d) 7.5x bottom surface

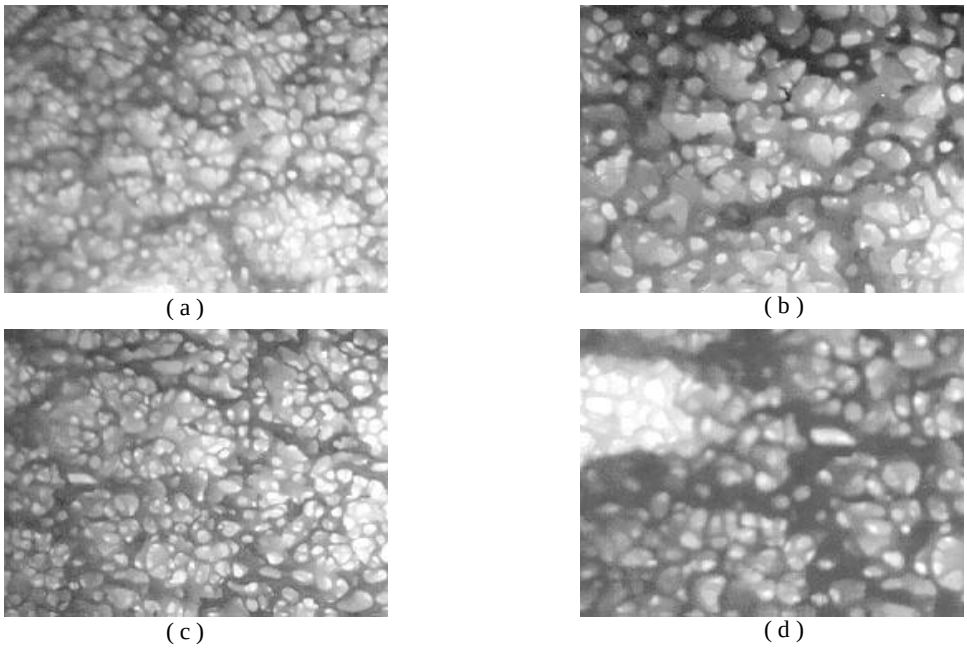

(a) (b)

(c) (d)

Figure 4.22 Microscope photos of sample 5 (a) 5x top surface; (b) 7.5x top surface; (c) 5x bottom surface; (d) 7.5x bottom surface

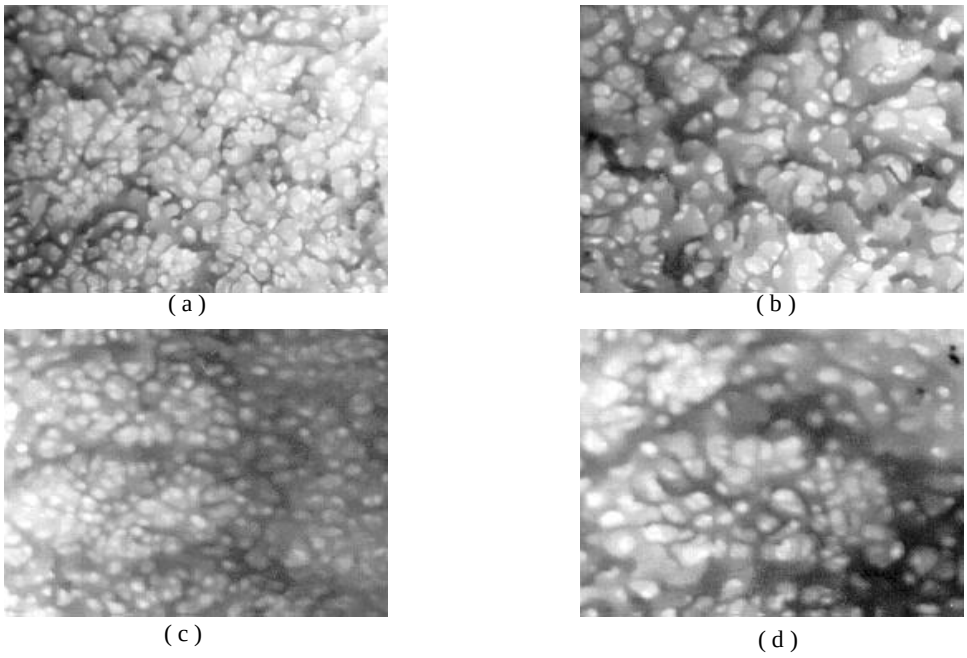

Figure 4.23 Microscope photos of sample 6 (a) 5x top surface; (b) 7.5x top surface; (c) 5x bottom surface; (d) 7.5x bottom surface

2) Group 3:

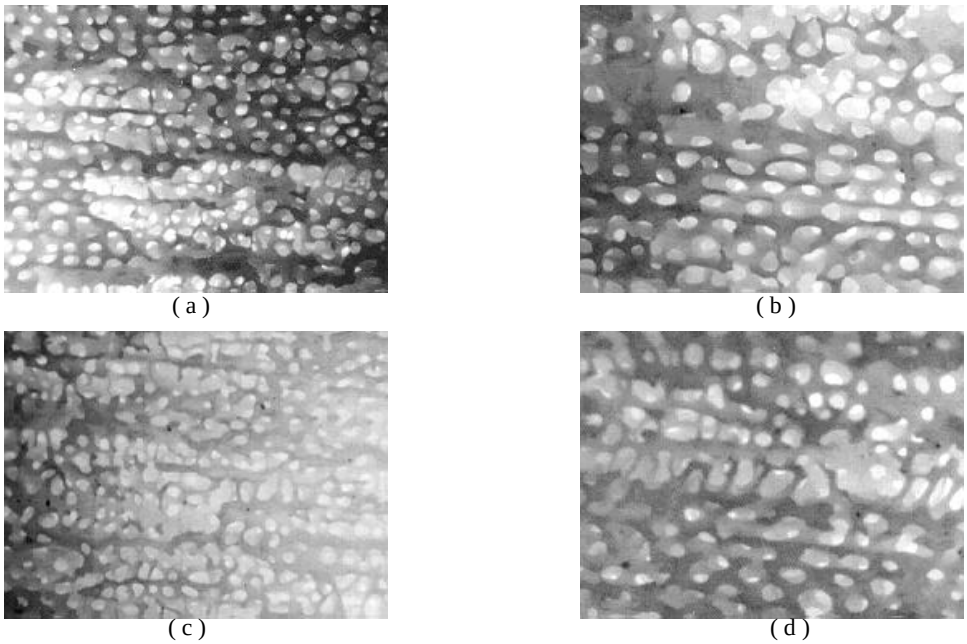

Figure 4.24 Microscope photos of sample 7 (a) 5x top surface; (b) 7.5x top surface; (c) 5x bottom surface; (d) 7.5x bottom surface

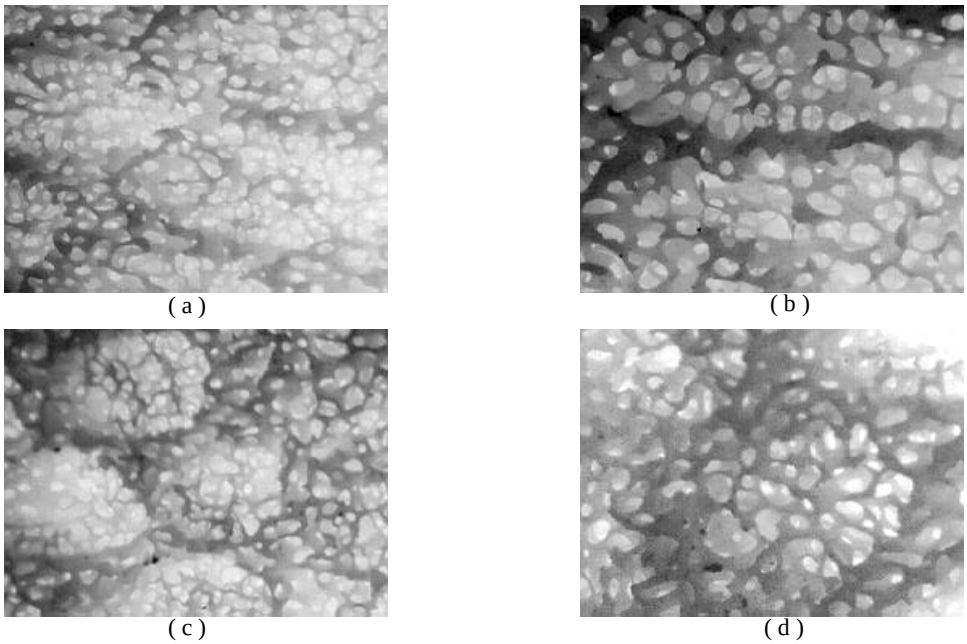

(a) (b)

(c) (d)

Figure 4.25 Microscope photos of sample 8 (a) 5x top surface; (b) 7.5x top surface; (c) 5x bottom surface; (d) 7.5x bottom surface

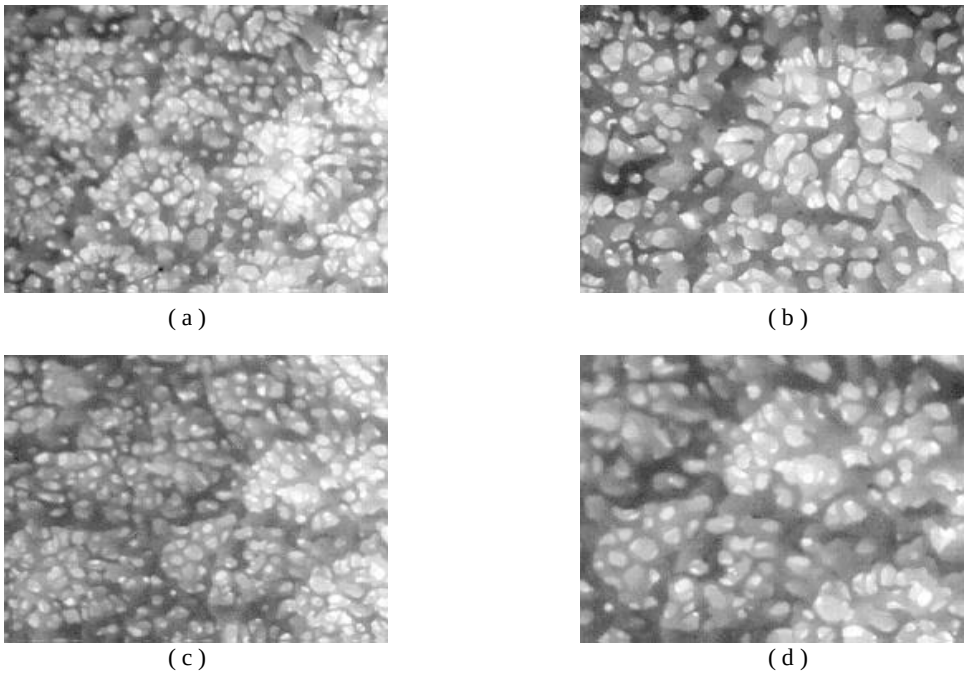

(a) (b)

(c) (d)

Figure 4.26 Microscope photos of sample 9 (a) 5x top surface; (b) 7.5x top surface; (c) 5x bottom surface; (d) 7.5x bottom surface

Microscope Photos of the Coral Samples After Heavy Decalcification

Group 3:

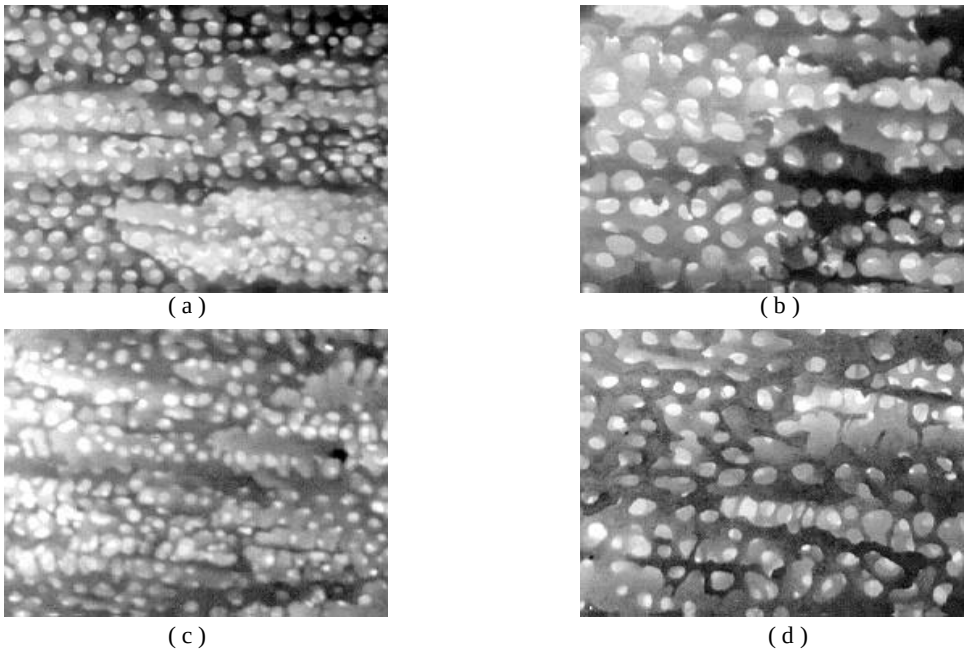

(a) (b)

(c) (d)

Figure 4.27 Microscope photos of sample 7 (a) 5x top surface; (b) 7.5x top surface; (c) 5x bottom surface; (d) 7.5x bottom surface

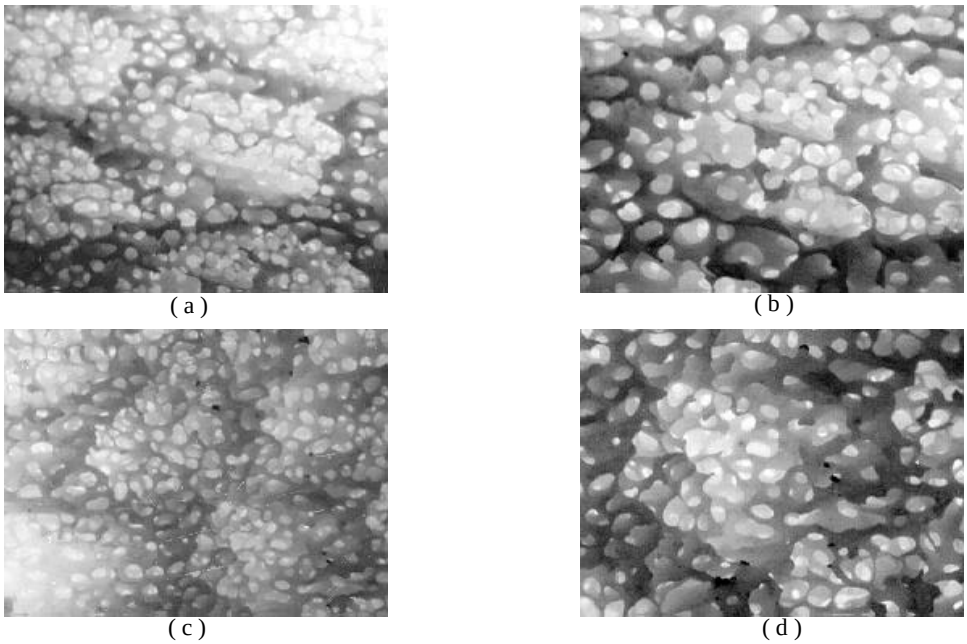

(a) (b)

(c) (d)

Figure 4.28 Microscope photos of sample 8 (a) 5x top surface; (b) 7.5x top surface; (c) 5x bottom surface; (d) 7.5x bottom surface

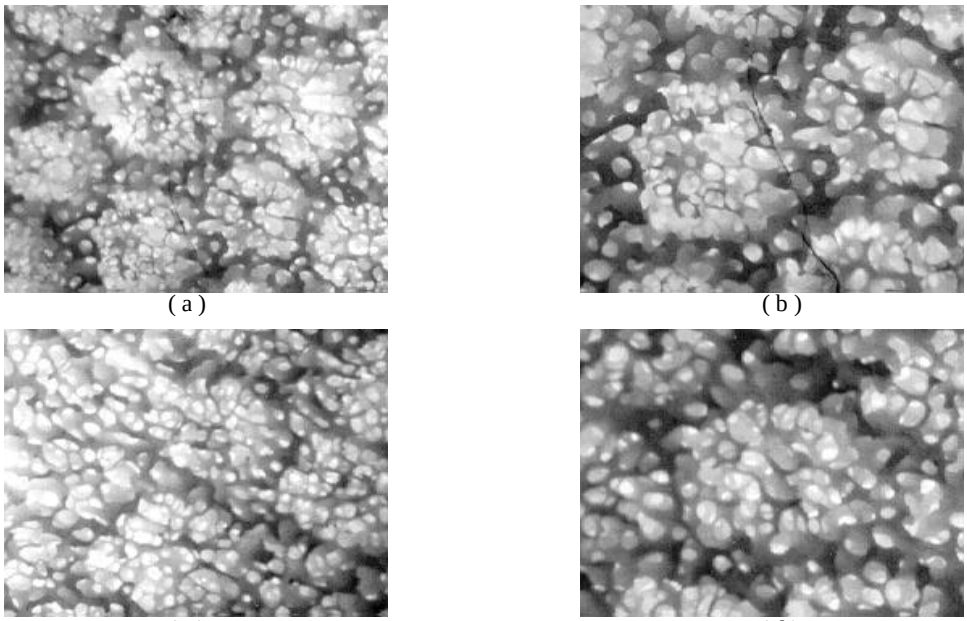

Figure 4.29 Microscope photos of sample 9 (a) 5x top surface; (b) 7.5x top surface; (c) 5x bottom surface; (d) 7.5x bottom surface

Due to the complex microstructure of the porous coral sample, it is hard to quantitatively analyze the difference between the coral samples with different growth axes and the difference between different density levels of each coral sample. However, qualitatively, different microstructures exist depending on the growth axes of the coral samples. The apparent horizontal microstructure orientation can be observed from the photos of sample 1, sample 4 and sample 7, which have a horizontal growth axis. The horizontal axes are parallel with the corresponding growth axes observed from the photos in Figure 4.11 for sample 1, 4, and 7. For other samples, sample 2, sample 5 and sample 8, which have growth axes around 30^{o}~40^{o} relative to horizontal, and sample 3, sample 6 and sample 9, which have growth axes around 50^{o}~60^{o} relative to horizontal, they have similar cell connections and much more fine structure elements on both ends of the coral samples are observed. After the coral samples are decalcified, the trabeculae in the coral samples become thinner and the pore size becomes larger.

CHAPTER 5

BROADBAND ULTRASONIC ATTENUATION (BUA) ANALYSIS

5.1 Broadband Ultrasound Attenuation (BUA)

The broadband ultrasound attenuation (BUA) is the first ultrasonic parameter determined in this research work. Its measurement method was introduced in a landmark study by Langton *et al* [31]. From the results of their research work, a linear relationship between the ultrasonic attenuation of the bone sample and the frequency *in vivo* was observed. Furthermore, they found that BUA was subject dependent. That is, young healthy women had significantly higher BUA values (70 dB/MHz) than older women with osteoporotic hip fractures (40 dB/MHz). These findings have resulted in several subsequent clinical studies, which have related BUA to bone mineral density (BMD). Nowadays, it is believed that BUA is not only related to the density but also to the microstructure of trabecular bone because a high degree of orientational anisotropy for BUA is observed, which is due to the trabecular bone structure [5, 6, 8].

Therefore, in this thesis work, the relationships between BUA and the coral sample density as well as the relationship between BUA and the coral sample microstructure is explored. The through-transmission ultrasound system with rotating the coral sample is used which has been described in Chapter 3. A simpler diagram of measurement setup is shown below.

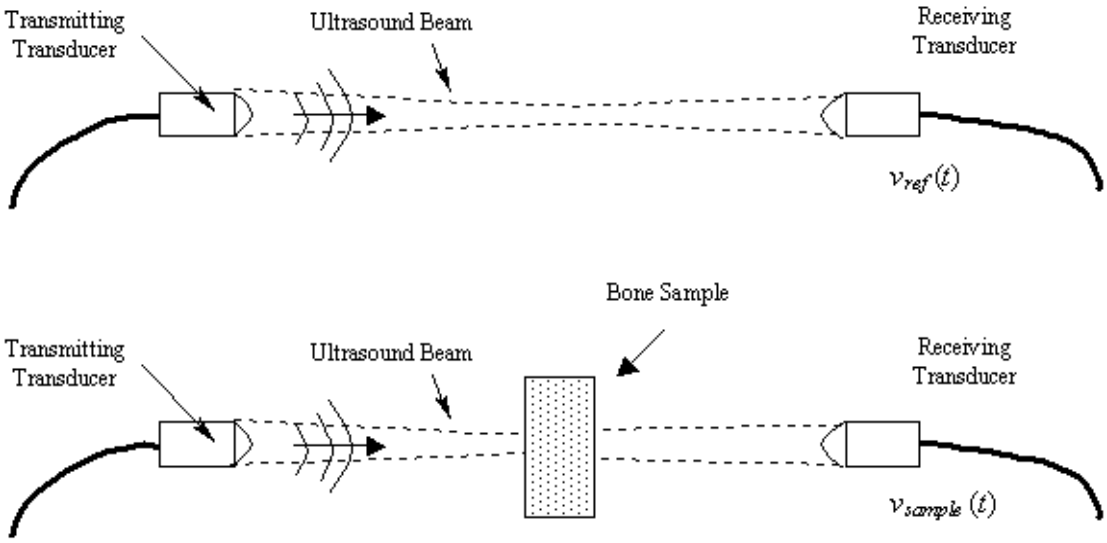

Figure 5.1 Transmission measurement of BUA

In Figure 5.1, $v_{ref}(t)$ and $v_{sample}(t)$ are defined as the received signal without and with the coral sample placed in the transmission path, respectively. Let $|V_{ref}(f)|$ and $|V_{sample}(f)|$ represent the magnitude of the Fourier transforms of $v_{ref}(t)$ and $v_{sample}(t)$, respectively. If $A(f)$ is the overall attenuation versus frequency, $\beta(f)$ is the attenuation coefficient as a function of frequency, d is the path length through the sample, and α_T is the combined transmission loss coefficient for the two coupling medium/sample interfaces, we have

$$A(f) = \frac{|V_{sample}(f)|}{|V_{ref}(f)|} = \frac{|V_{ref}(f)|(\alpha_T \exp(-\beta(f)d))}{|V_{ref}(f)|}, \qquad (5.1)$$

which leads to

$$\ln A(f) = \ln(\alpha_T) - \beta(f)d \qquad (5.2)$$

Assuming that the attenuation, in Neper, varies linearly with frequency, that is $\beta(f) = \beta f$, we have

$$\beta f d \cong \ln(\alpha_T) - \ln A(f) \tag{5.3}$$

If we define $\beta d =$ BUA, the BUA value can be obtained from the slope of the least squares fit of $\ln A(f)$ vs. f. It can be seen that BUA is dependent on the sample thickness, d, but is not affected by α_T. Since the coral sample diameter d is same for all coral samples in this thesis work, the effect of the thickness will not be considered in BUA analysis. The frequency between 0.3 MHz and 0.7 MHz is selected to calculate the BUA value because the center frequency of the transmitting transducer used is 0.5 MHz. Figure 5.2 below illustrates the reference waveform (with water only), the sample signal waveform (with coral sample) and the result BUA analysis result.

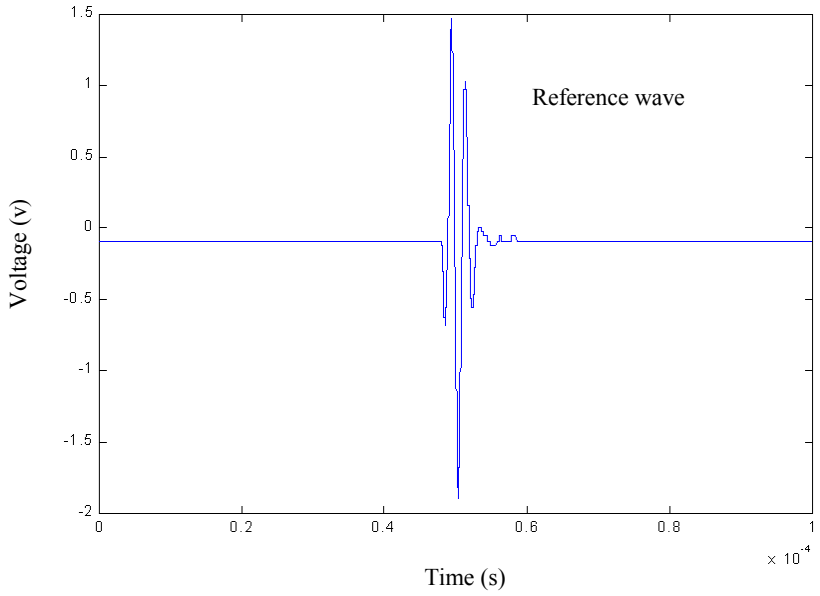

(a)

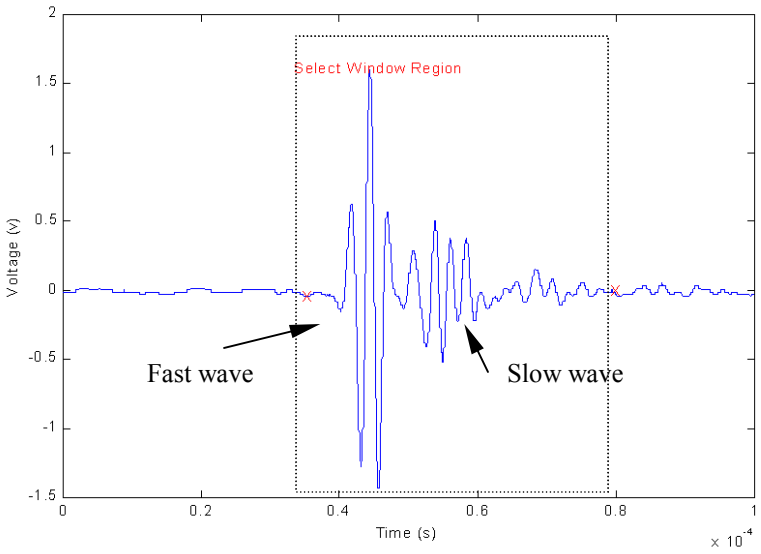

(b)

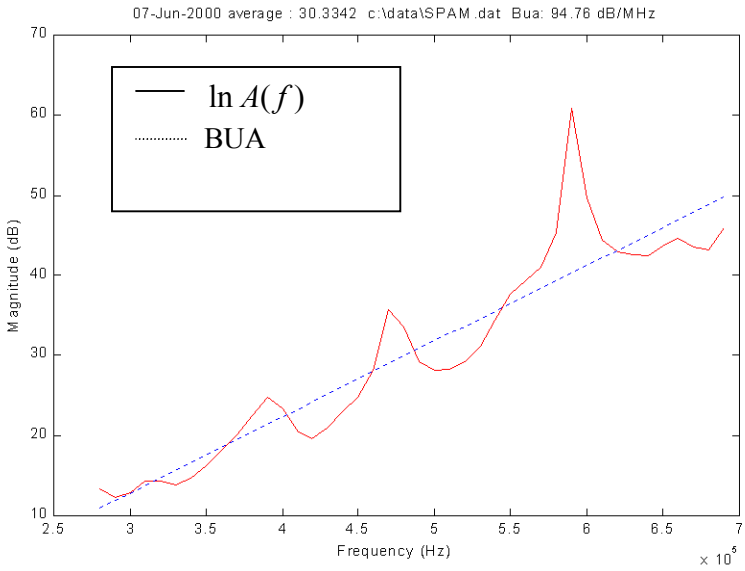

(c)

Figure 5.2 Illustration of BUA analysis. (a) $v_{ref}(t)$; (b) $v_{sample}(t)$; (c) BUA analysis based on entire waveform

From the entire signal $v_{sample}(t)$ shown in Figure 5.2 (b) above, two longitudinal waves, fast and slow waves, comprise the received signal when the coral sample is present. In Figure 5.2 (c), the dotted line is the best fit line of the function $\ln A(f)$ whose

slope is the BUA value. Since the Fourier spectrum of the entire signal includes the spectrums of both fast wave and slow wave, and these 2 waves are associated with the different solid and the fluid motions stated by Biot's theory in Section 2.2.2.2, an improved approach could be achieved if the two waves are analyzed separately by using appropriate window functions, shown in Figure 5.3 and Figure 5.4 below.

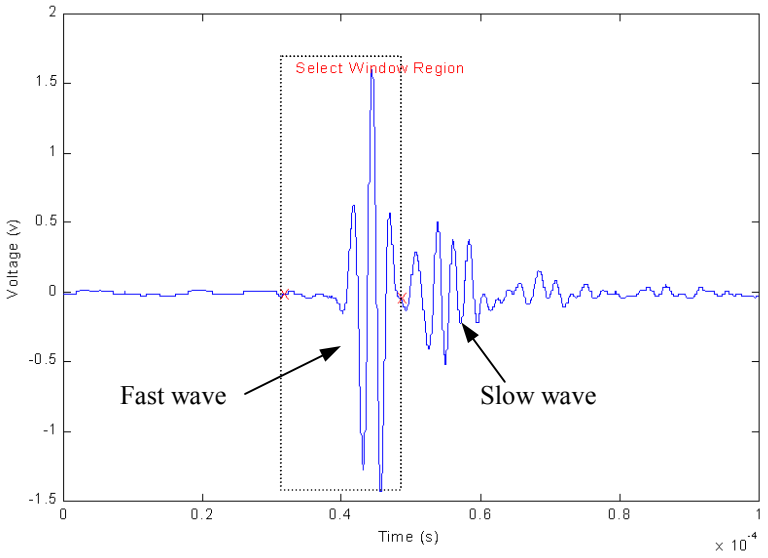

(a)

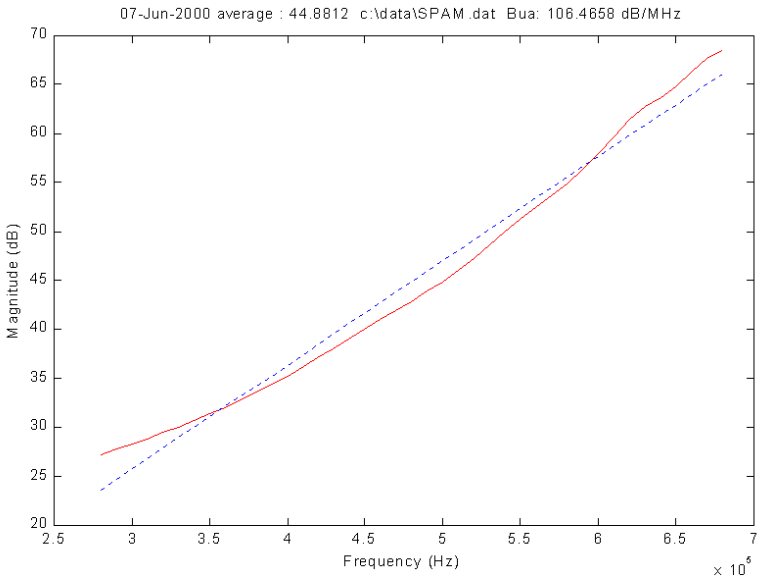

(b)

Figure 5.3 BUA analysis for fast wave. (a) fast wave selected by window function; (b) corresponding BUA value

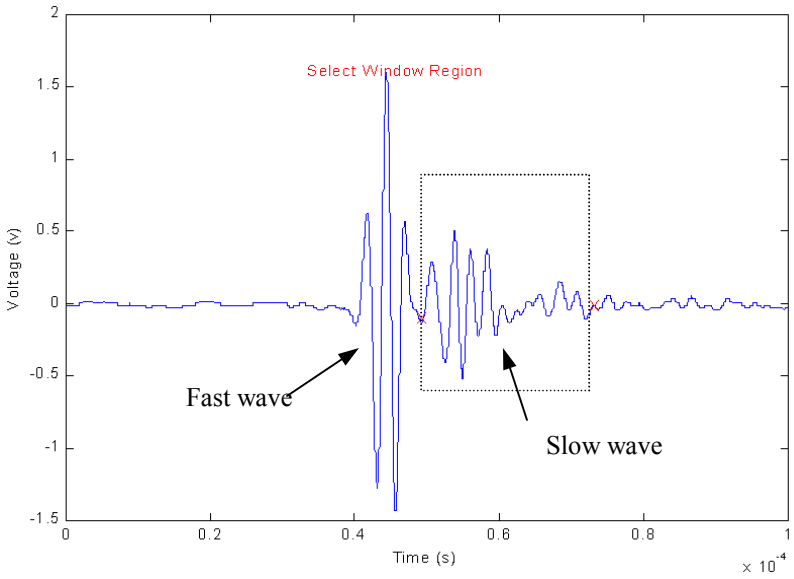

(a)

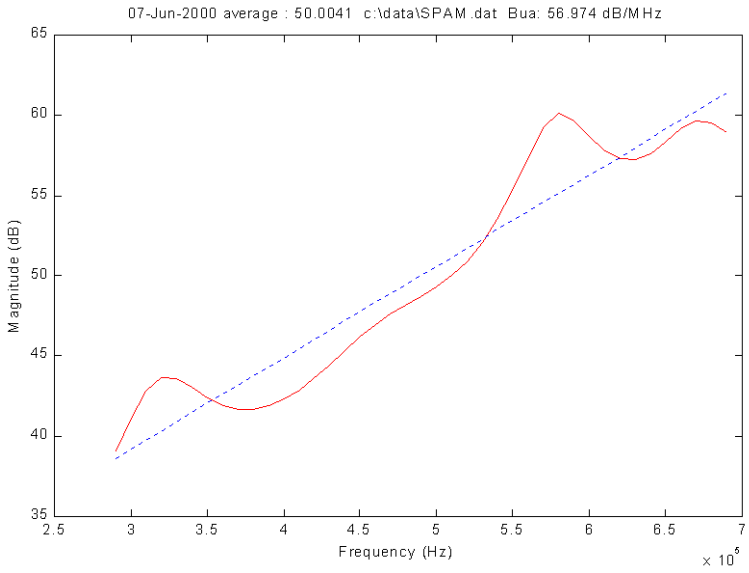

(b)

Figure 5.4 BUA analysis for slow wave. (a) slow wave selected by window function; (b) corresponding BUA value

From Figure 5.3 and Figure 5.4, it can be seen that after being selected by window function, the $\ln A(f)$ function corresponding to the fast wave and slow wave is much more linear than the $\ln A(f)$ function corresponding to the entire signal. Therefore, 3

different BUA are obtained in this research work: *entire signal BUA*, which is the BUA value of the entire signal; *fast wave BUA*, which is the BUA value of the fast wave; *slow wave BUA,* the BUA value of the slow wave. Their variations as functions of angle of rotation of coral samples and density level are discussed in the following sections.

The measurements will begin when the reference signal is obtained, and the coral sample is placed on the middle of the path between the 2 transducers. All the coral samples are oriented first at their reference angle where the fast wave amplitude reaches its maximum value. Furthermore, the measurements concerning the reproducibility of BUA variation are also made during the measuring process.

5.2 Results

Before the discussion of BUA results, the observations of the fast wave and slow wave will be described first.

5.2.1 Fast Wave and Slow Wave Observations

From the received ultrasound signals, the peak amplitude of the fast wave is observed to have periodic variation with angle for each coral sample at original density, as shown in Figure 5.5 to Figure 5.7, and in Figure 5.8 (a) to Figure 5.13 (a). That is, for all the coral samples, the fast wave amplitude will reach its maximum value at 0^o or 180^o, at which angle the coral sample is orientated parallel to its reference angle. The fast wave amplitude will get its minimum value at around 90^o or 270^o, when the coral sample is orientated perpendicular to its reference angle. Owing to the limit of displaying the received signals, Figure 5.5 to Figure 5.13 only show the received signals corresponding to the rotation angle from 0^o to 180^o. For better comparison, the growth axis of each

sample is drawn beside the waveforms shown in Figure 5.5 to Figure 5.13. And the line on the top of the cross-section area represents the reference angle of the coral sample.

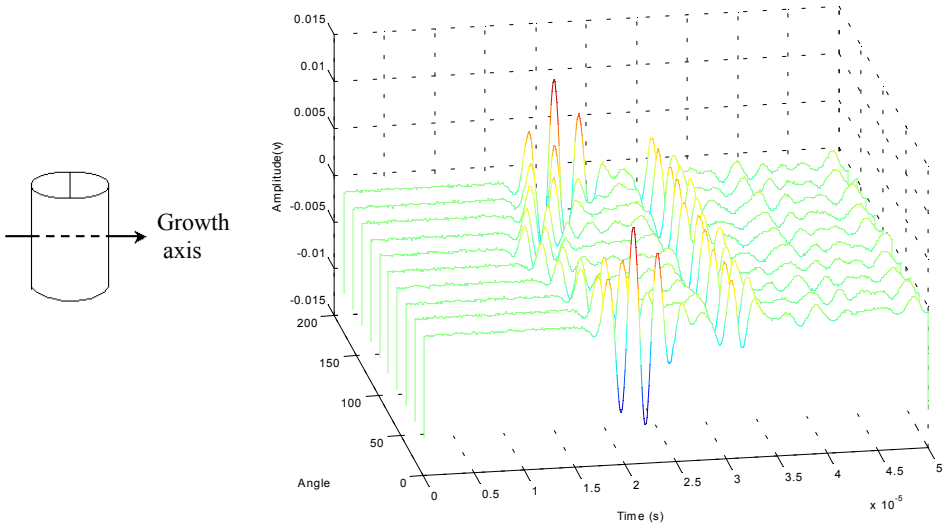

Figure 5.5 Received ultrasound waveforms variation as a function of rotation angle for Sample 1 at original density

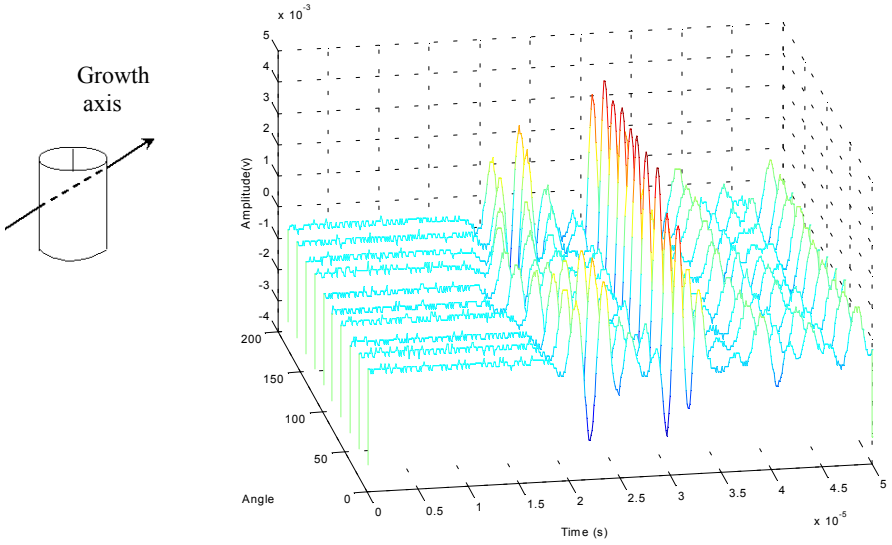

Figure 5.6 Received ultrasound waveforms variation as a function of rotation angle for Sample 2 at original density

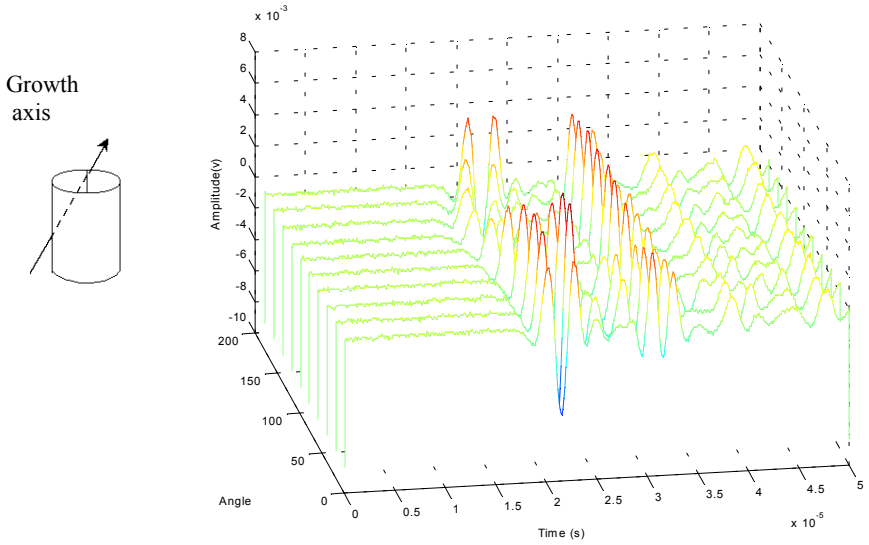

Figure 5.7 Received ultrasound waveforms variation as a function of rotation angle for Sample 3 at original density

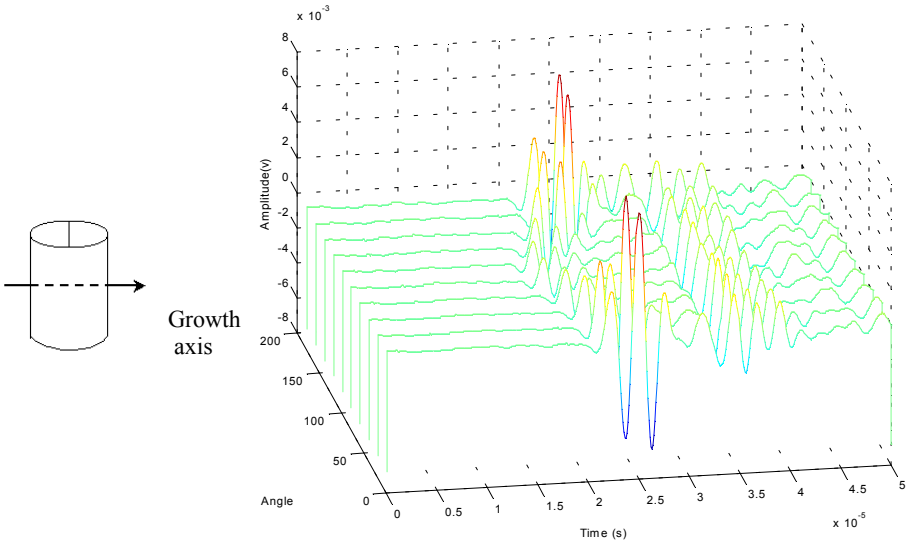

(a)

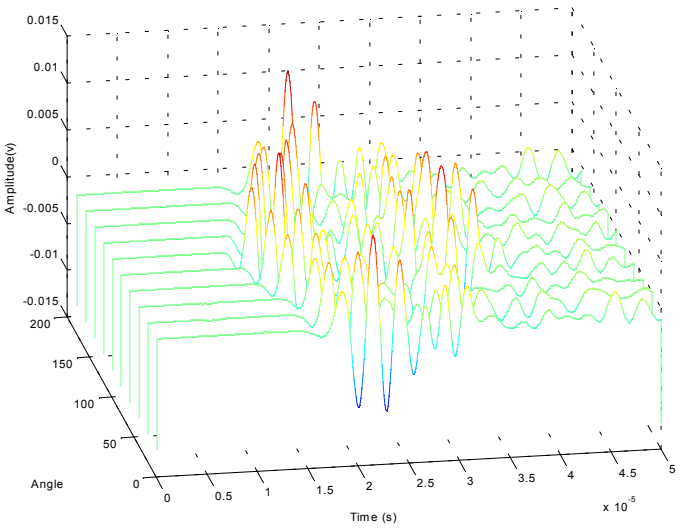

(b)

Figure 5.8 Received ultrasound waveforms as a function of rotation angle for Sample 4. (a) at original density; (b) at density with 15.07% DEXA BMD loss

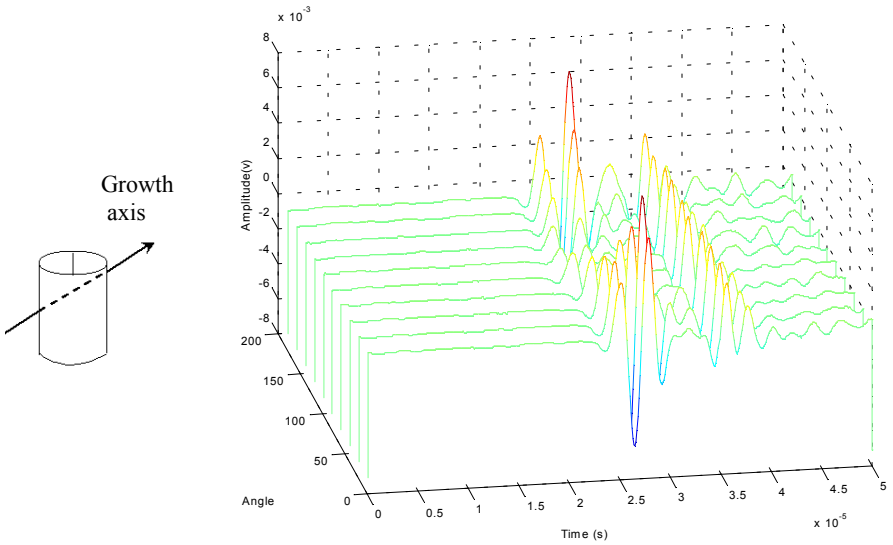

(a)

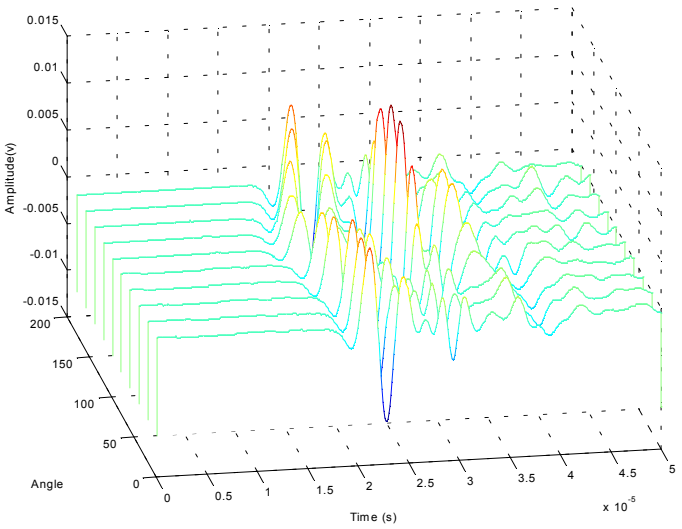

(b)

Figure 5.9 Received ultrasound waveforms as a function of rotation angle for Sample 5. (a) at original density; (b) at density with 18.19% DEXA BMD loss

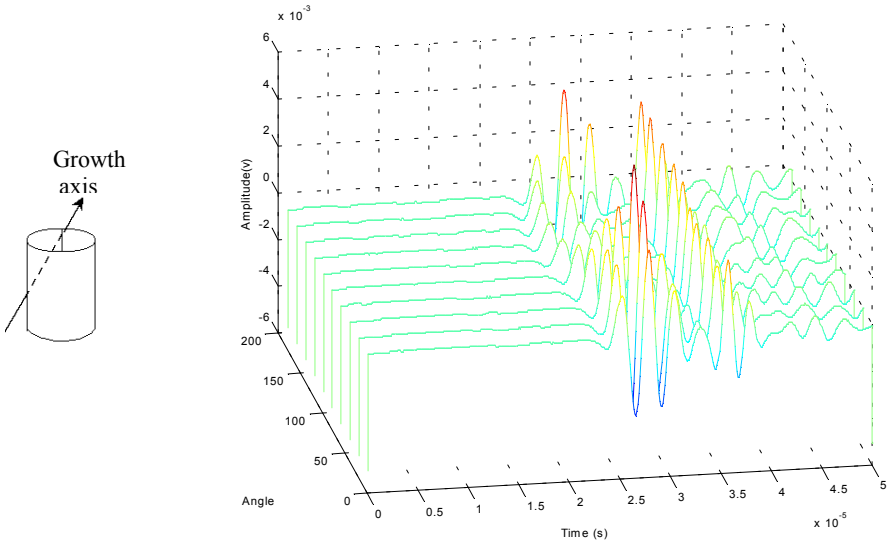

(a)

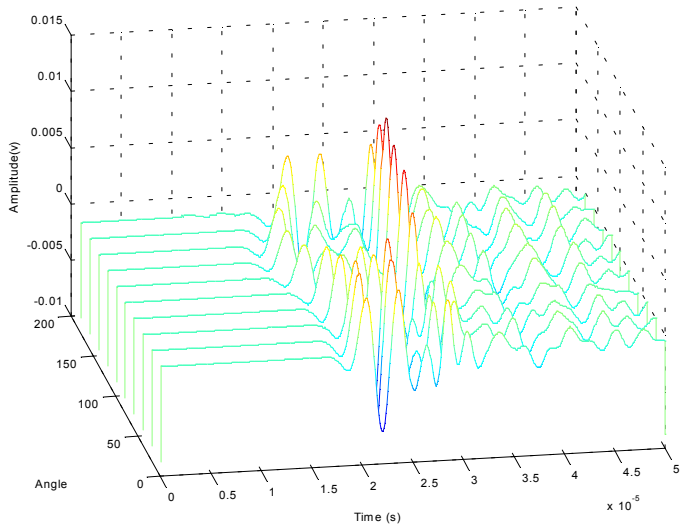

(b)

Figure 5.10 Received ultrasound waveforms as a function of rotation angle for Sample 6. (a) at original density; (b) at density with 15.89% DEXA BMD loss

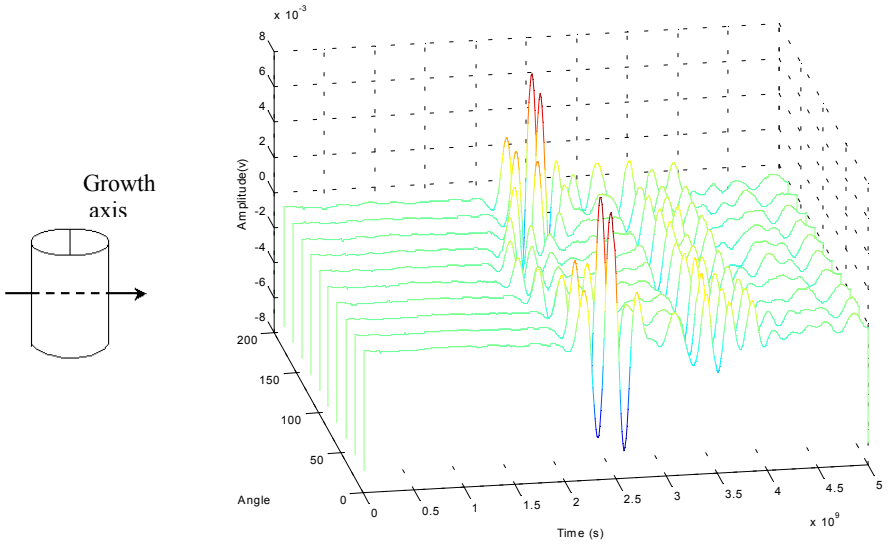
Growth
axis
x 10^-3
Amplitude(v)
Angle
Time (s)
x 10^9

(a)

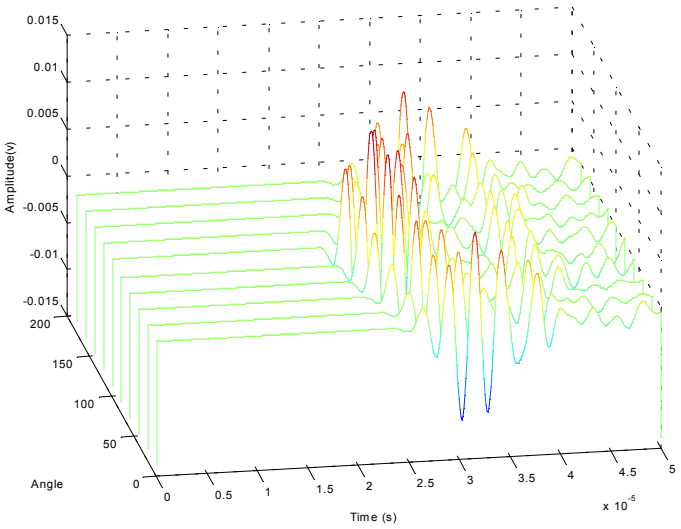
Amplitude(v)
Angle
Time (s)
x 10^-5

(b)

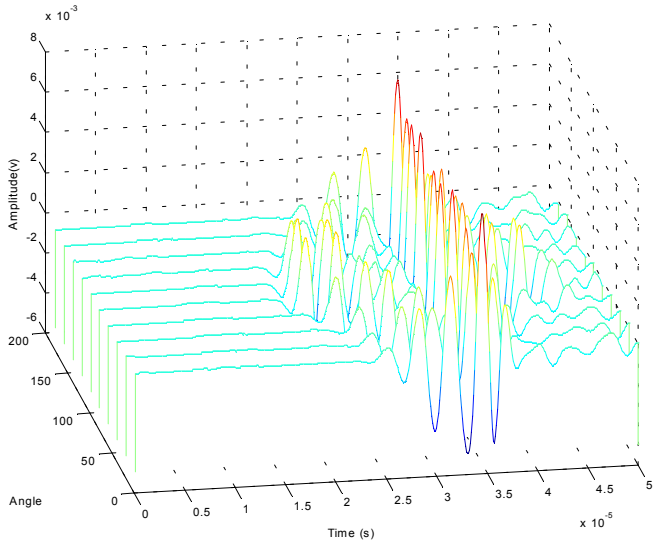

(c)

Figure 5.11 Received ultrasound waveforms as a function of rotation angle for Sample 7. (a) Original density; (b) 14.93 % lower BMD after light decalcification; (c) 32.61% lower BMD after heavy decalcification

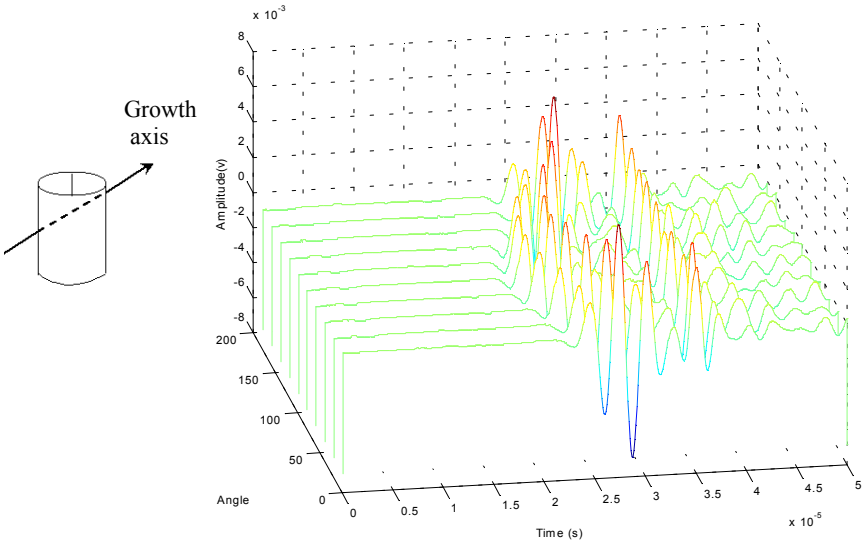

(a)

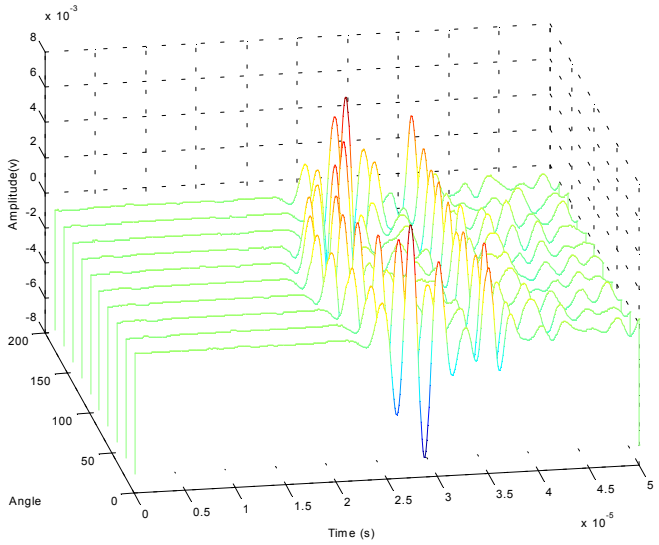

(b)

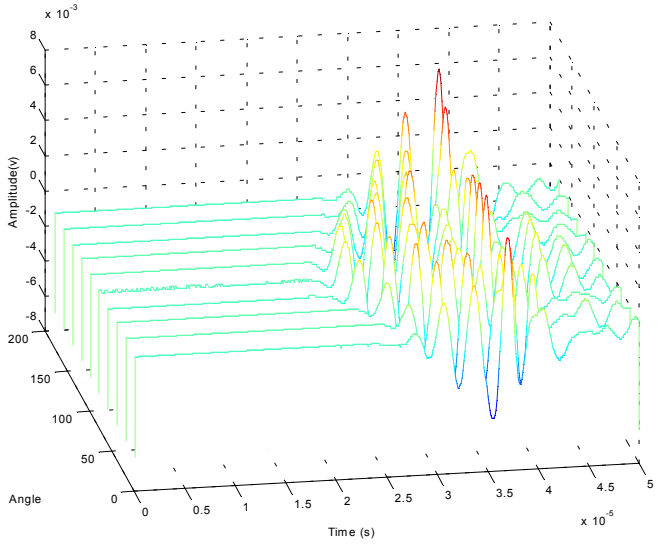

(c)

Figure 5.12 Received ultrasound waveforms as a function of rotation angle for Sample 8. (a) Original density; (b) 16.11 % lower BMD after light decalcification; (c) 33.13% lower BMD after heavy decalcification

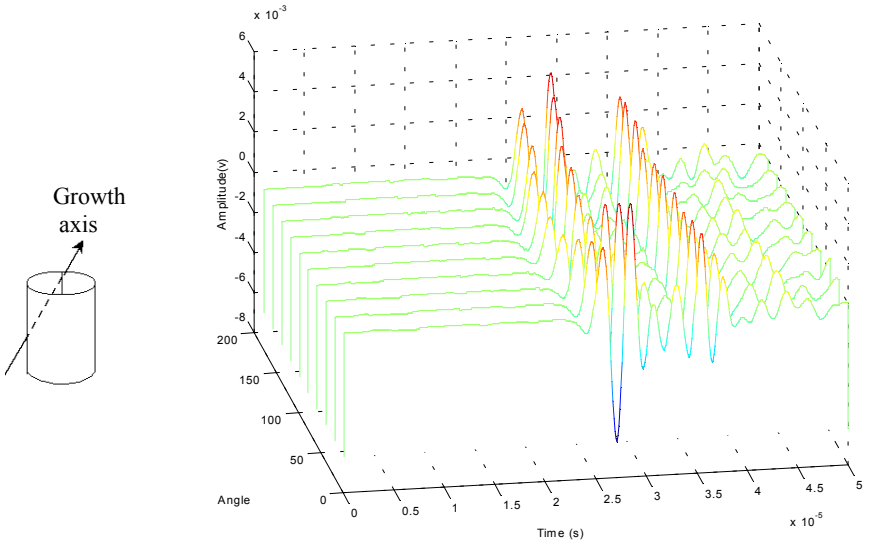
Growth
axis
x 10^-3
Amplitude(v)
Angle
Time (s)
x 10^-5

(a)

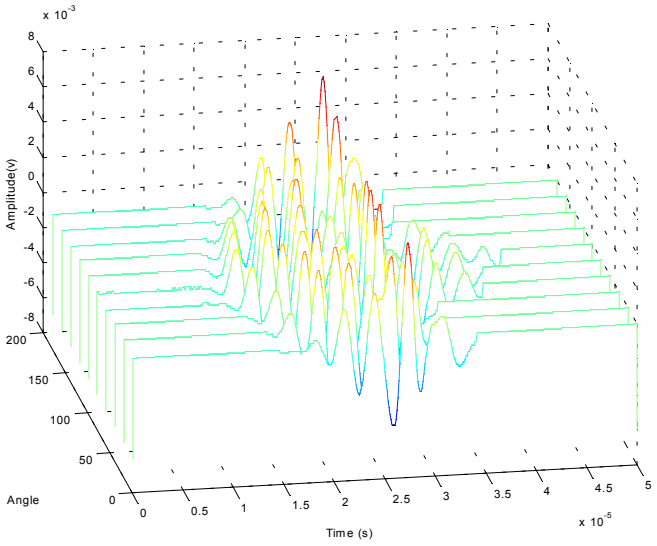
x 10^-3
Amplitude(v)
Angle
Time (s)
x 10^-5

(b)

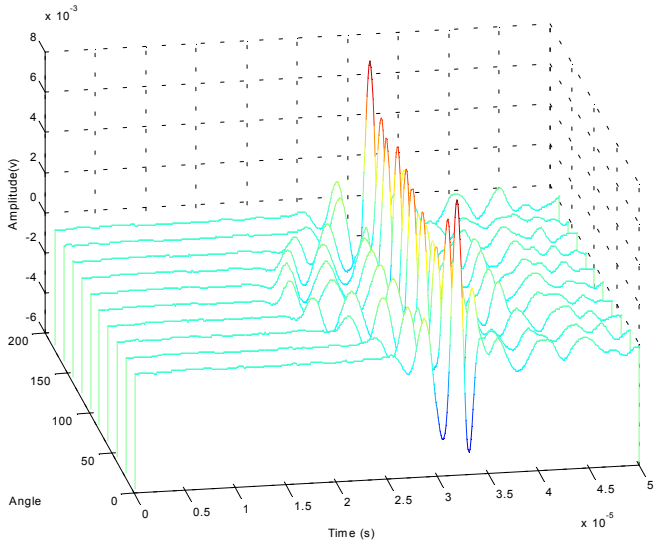

(c)

Figure 5.13 Received ultrasound waveforms as a function of rotation angle for Sample 9. (a) original density; (b) 18.5 % lower BMD after light decalcification; (c) 34.77% lower BMD after heavy decalcification

In general, the peak amplitude value of fast wave decreases while the peak amplitude value of the slow wave increases as the coral sample density decreases. Comparing the amplitude values of fast wave and slow wave at the intermediate decalcification level with the values at the original density, the changes are not apparent, but comparing the amplitude values at the heavy decalcification level with the original density, the changes are large. The peak amplitude values of fast waves and slow waves for the 9 coral samples at different density levels are shown in Table 5.1. The "Min. " and "Max." in Table 5.1 refer to the minimum value and maximum value of the peak amplitude of fast wave and slow wave over the angle range of 0 to 180^{o}, respectively.

Table 5.1 Comparisons of the fast and slow waves amplitude (x 10^{-3}) variations as density decreases (Min.: minimum value of the peak amplitude; Max.: maximum value of the peak amplitude)

	Original Density				Light Decalcification				Heavy Decalcification			
	Fast wave peak amplitude value		Slow wave peak amplitude value		Fast wave peak amplitude value		Slow wave peak amplitude value		Fast wave peak amplitude value		Slow wave peak amplitude value	
	Min. (v)	Max. (v)	Min. (v)	Max. (v)	Min. (v)	Max. (v)	Min. (v)	Max. (v)	Min. (v)	Max. (v)	Min. (v)	Max. (v)
Sample1	1.8	12	3.13	4.9								
Sample2	0.9	2.7	3.6	5.4								
Sample3	0.9	6.7	1.6	3.13								
Sample4	1.34	7.1	1.34	2.23	1.34	7.1	2	4.5				
Sample5	0.9	6.7	2.23	3.13	2.23	3.13	1.34	6.3				
Sample6	0.9	4.5	2.23	3.6	1.8	2.7	1.34	3.13				
Sample7	2.23	13.4	1.34	3.6	4.5	12	2.23	4.5	1.34	2.7	4	6.3
Sample8	2.7	4.5	1.34	3.6	1.34	2.23	2.7	3.6	0.45	0.9	4.5	6.7
Sample9	2.23	6.7	2.23	4.5	2.7	4	2.23	6.7	0.9	1.8	4.5	7.6

The observed changes indicate that the fast wave is associated with the trabeculae of coral samples, while the slow wave is associated with the propagation in the fluid of coral samples because there is less solid for fast wave to propagate in, but more space for the slow wave to propagate in the fluid as the density decreases.

Another observation from the received signals of coral samples is that the velocity of fast wave varies periodicly as the coral sample rotation angle is changed. That is, the fast wave velocity will reach its maximum value when the rotation angle of the coral samples approaches 90^o or 270^o, while reaching its minimum value when the rotation angle approaches 0^o or 180^o. This variation is 90^o out of phase with the variation of the fast wave amplitude. In all circumstances, slow wave velocity does not have apparent variation with rotation angle, and is around 1480 *m/s* for all coral samples. The value is

close to the sound speed in water, which is expected because the water is the fluid which fills the pores of the coral sample in this research work, mimicking the soft tissue of bone, is water.

Furthermore, the velocity of the fast wave decreases as the density decreases for the same coral sample. However, the velocity of the fast wave corresponding to the angle of 90^{o}, i.e., when the coral sample is oriented perpendicular to the reference angle, doesn't change apparently when the density of coral sample decreases. Therefore, it is hard to separate fast and slow waves corresponding to most rotation angles after the coral sample density has been decreased because the fast and slow waves overlap. Specifically, the velocities of fast waves for the coral samples are shown in the Figure 5.14 to Figure 5.20. Figure 5.14 shows the fast wave velocities of sample 1, 2 and 3 at original density. Figure 5.15 to Figure 5.20 illustrate the fast wave velocities of sample 4 to sample 9 at original density and after light decalcification.

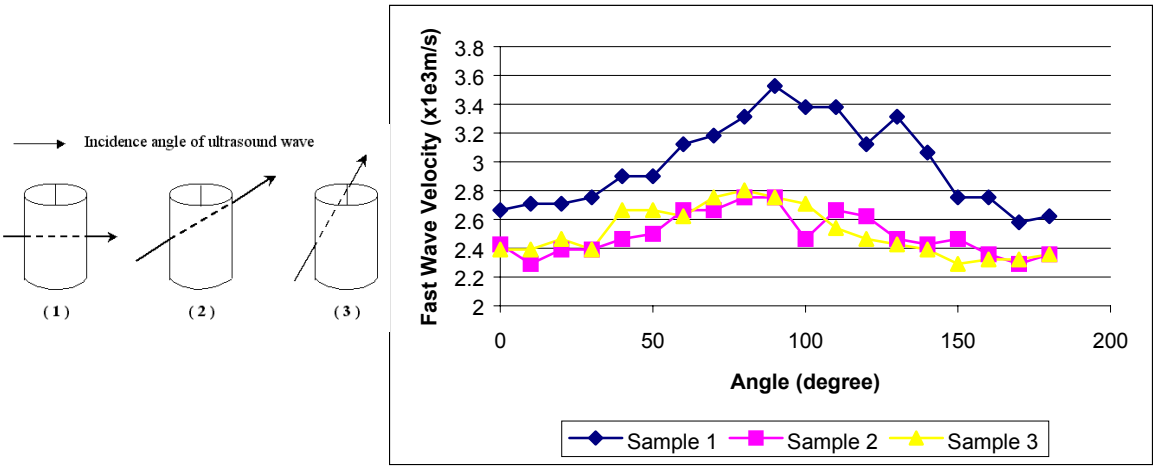

Figure 5.14 Fast wave velocity as function of the angle of rotation for the coral sample 1, 2 and 3 at original density

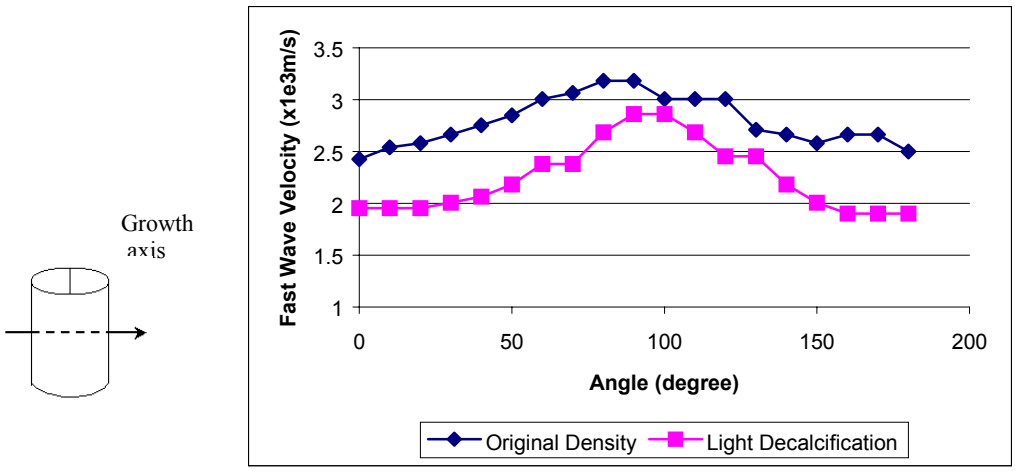

Figure 5.15 Fast wave velocity as function of the angle of rotation for the coral sample 4 at two different density levels

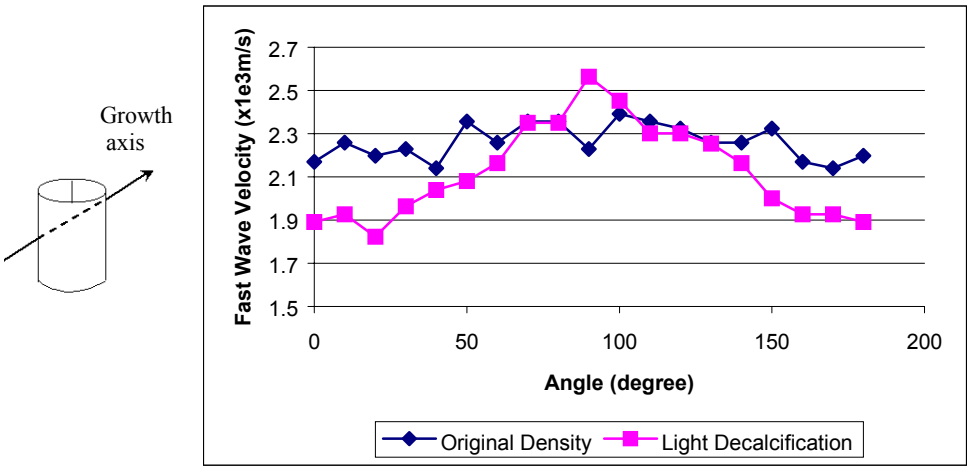

Figure 5.16 Fast wave velocity as function of the angle of rotation for the coral sample 5 at two different density levels

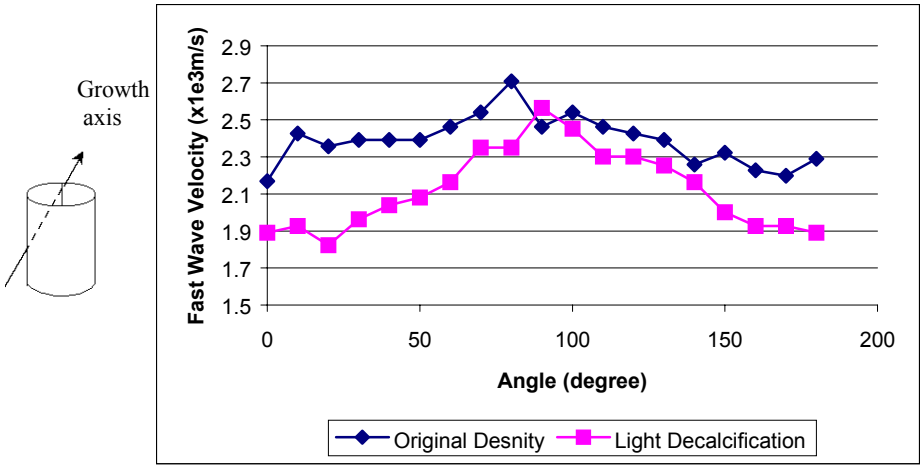

Figure 5.17 Fast wave velocity as function of the angle of rotation for the coral sample 6 at two different density levels

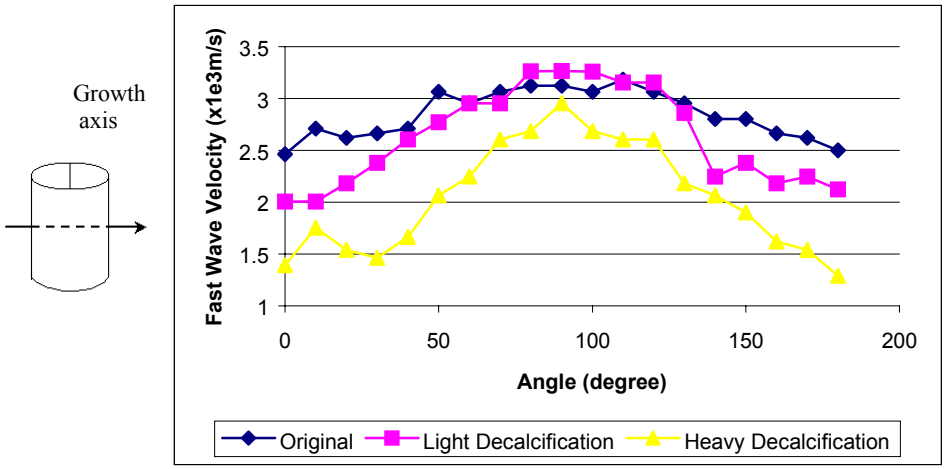

Figure 5.18 Fast wave velocity as function of the angle of rotation for the coral sample 7 at three different density levels

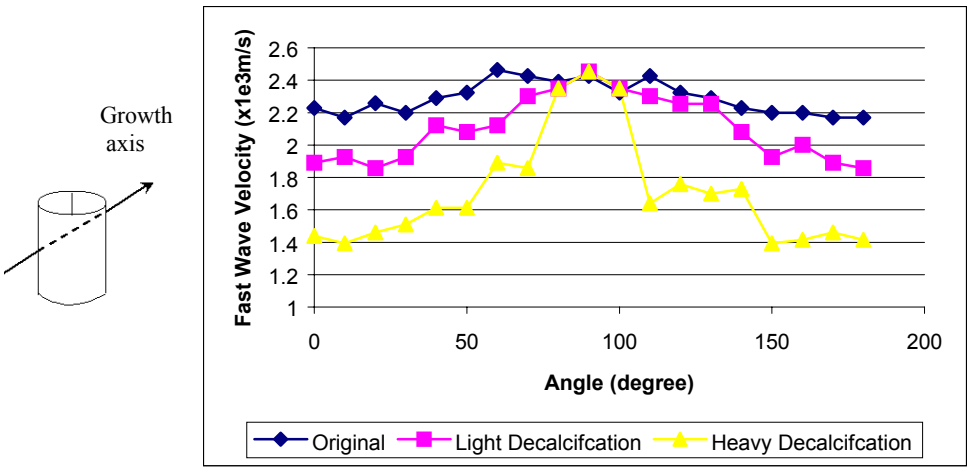

Figure 5.19 Fast wave velocity as function of the angle of rotation for the coral sample 8 at three different density levels

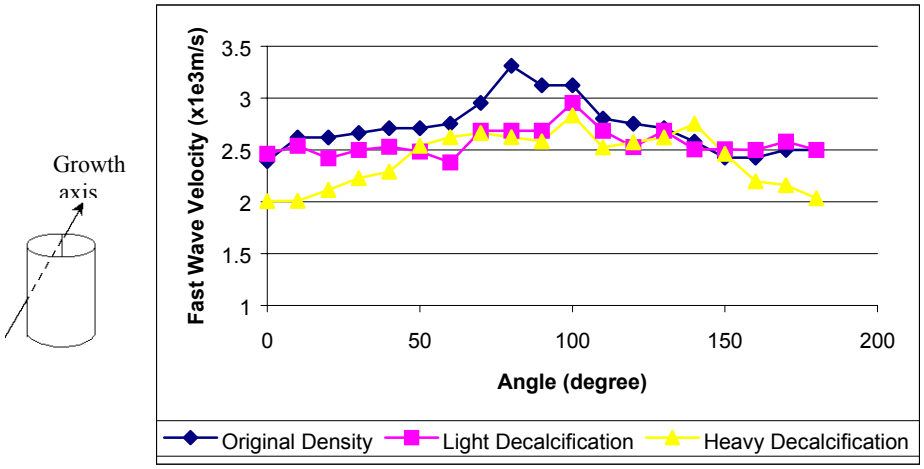

Figure 5.20 Fast wave velocity as function of the angle of rotation for the coral sample 9 at three different density levels

From Figure 5.5 to Figure 5.20 above, it can be seen that with respect to the 3 different categories of growth axes that the coral samples can be divided into, the waveform variation patterns of the coral samples with same growth axis are found to be similar. For example, the waveform variation pattern of the coral samples 1, 4 and 7 with

horizontal growth axis has a much more apparent periodic pattern than the patterns of other coral samples with different growth axes.

By analyzing the received signals for all nine coral samples, it appears that information about the microstructure of coral samples can be obtained from the signals. It is known that ultrasound wave propagates faster in the solid trabeculae than in the water, therefore, the thicker the trabeculae along the ultrasound wave path will be, the higher the fast wave velocity will be since the fast wave is related with the trabeculae component of the coral sample However, on the other hand, the thicker the trabeculae, the more attenuated it will be, therefore, the amplitude of fast wave become less. Since it is observed that both fast and slow wave propagate through the coral sample when it is orientated parallel to its reference angle, while lower amplitude fast wave will travel through when the coral sample is orientated perpendicular to its reference angle but with faster velocity, the potential reason could be that there is denser distribution of trabeculae along the orientation which is perpendicular to the reference angle.

The effect of decalcification on the microstructures can also be explained on the basis of the hypothesis given above, that is, the fast wave propagates slower since the trabeculae becomes thinner when the density of the coral sample decreases. The observation that the slow wave does not vary with the rotation angle of the coral sample nor with coral sample density indicates that the major propagation medium for the slow wave has no apparent anisotropical orientation or distribution variation. In this research work, this medium is water which fills the pores in the coral samples. Similar observation of fast wave and slow wave variation in the bovine trabecular bone experiment were reported and explained via Biot's theory by Hosokawa et al [32].

5.2.2 Results of BUA Analysis

The results of entire signal BUA, fast wave BUA and slow wave BUA analysis are presented and discussed in this section.

5.2.2.1 Entire Signal BUA

As stated before, the entire signal BUA is the BUA analysis for the entire signal without separating fast and slow waves. Periodic variation with rotation angles is also found from entire signal BUA when each coral sample is at original density, as shown in Figure 5.21. For all the coral samples at their original density, the entire signal BUA exhibits similar periodic variations, i.e., the maximum BUA values are found at around 0^o, 180^o and 360^o, while the minimum BUA values are found at around 90^o and 270^o. However, the periodicities of the entire signal BUA are found to be destroyed at the intermediate decalcification level while somewhat appearing again after heavy decalcification. This is shown in Figure 5.22 and Figure 5.23. The different growth axes of the coral samples are drawn beside Figure 5.21 to Figure 5.23 for better reference and comparison. The arrows going through the sample cylinder represents the growth axis direction. The average values of entire signal BUA for each coral sample is listed beside the BUA variation figure.

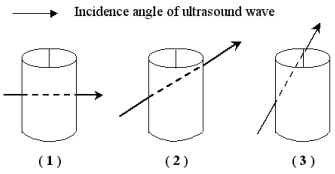

Average Value:

Sample 1: 52.54418
Sample 2: 49.39466
Sample 3: 76.14523

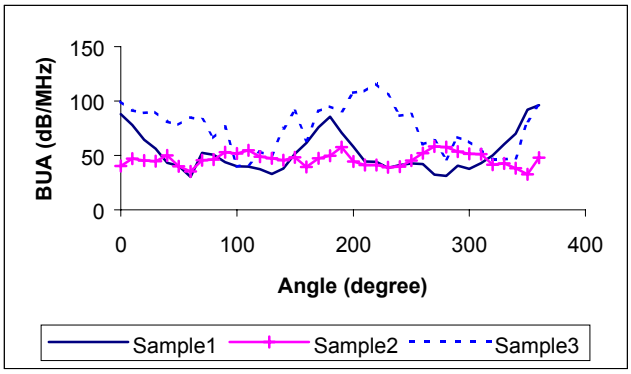

(a)

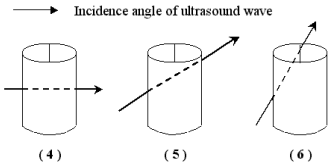

Average Value:

Sample 4: 58.00099
Sample 5: 64.02886
Sample 6: 59.53662

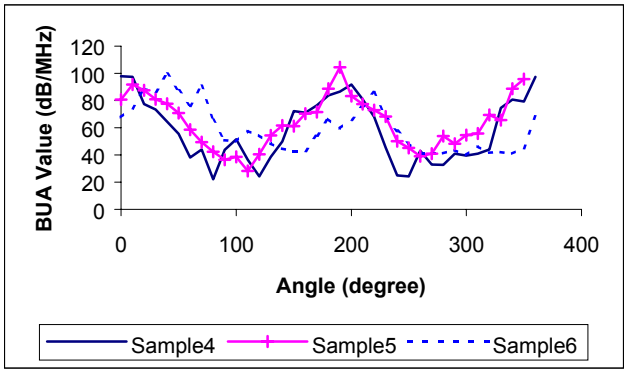

(b)

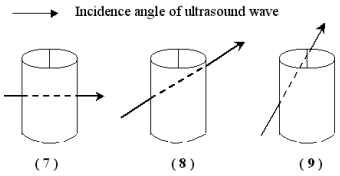

Average Value:

Sample 7: 57.29368
Sample 8: 65.92414
Sample 9: 69.06505

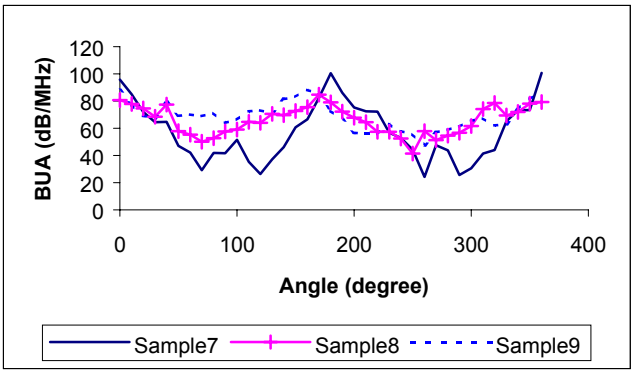

(c)

Figure 5.21 Entire signal BUA variation with angles at the original density of the coral samples

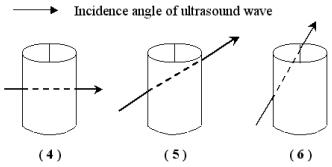

Average Value:

Sample 4: 72.45681
Sample 5: 75.34842
Sample 6: 75.18999

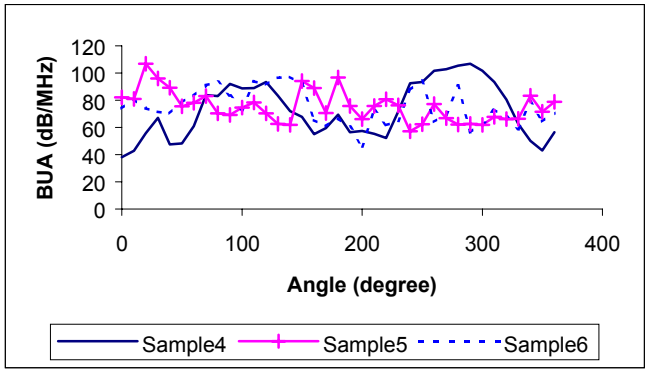

(a)

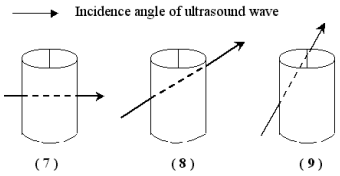

Average Value:

Sample 7: 92.33626
Sample 8: 84.39044
Sample 9: 78.98999

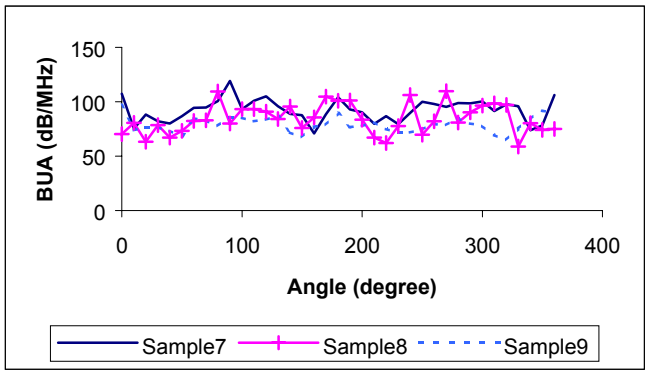

(b)

Figure 5.22 Entire signal BUA variation after intermediate decalcification of the coral samples

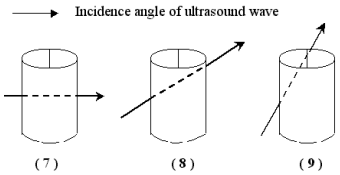

Average Value:

Sample 7: 53.09722
Sample 8: 52.12399
Sample 9: 44.05111

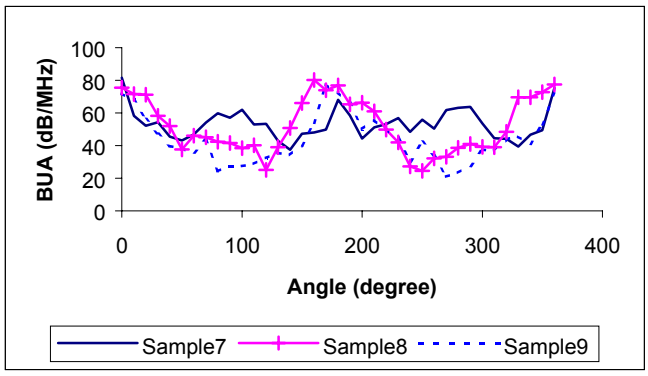

Figure 5.23 Entire signal BUA variation with angles after heavy decalcification of the coral samples

5.2.2.2 Fast Wave BUA

For fast wave BUA values of the coral samples with original density, periodicities are also observed. This is shown in Figure 5.24. However, two periodicity patterns are found among them. For sample 1, 4 and 7 with horizontal growth axis, fast wave BUA have obvious periodic patterns, and the periodic patterns are similar to the corresponding entire signal BUA periodic patterns, while for other samples, fast wave BUAs have opposite periodic patterns to their corresponding entire signal BUAs periodic patterns, and the periodic patterns are not so obvious.

As to the effect of decalcification, fast wave BUA periodicities still exist for sample 5, 6, 8 and 9 after intermediate decalcification, but for sample 4 and 7, which have the horizontal growth axes, no periodicity pattern is apparent after intermediate decalcification, as shown in Figure 5.25. Since after heavy decalcification, fast wave BUA and slow wave BUA overlap, the fast wave BUA cannot be obtained after heavy decalcification. Similar to the entire signal BUA illustrations, the growth axis figures and the average values of fast wave BUA are shown beside the fast wave BUA figures for better reference.

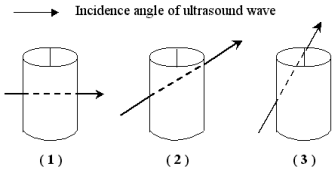

Average Value:

Sample 1: 40.55886
Sample 2: 82.25136
Sample 3: 81.1551

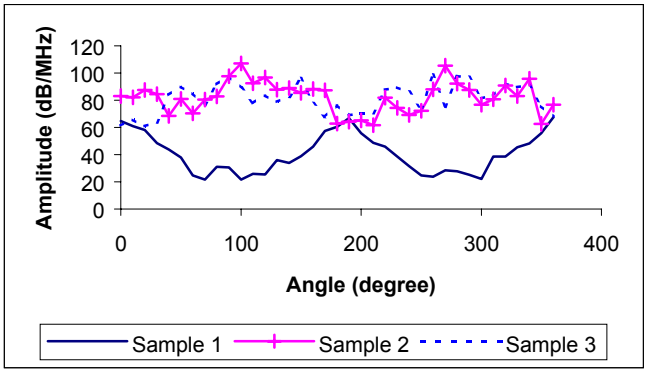

(a)

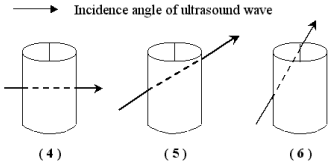

Average Value:

Sample 4: 48.67425
Sample 5: 77.83575
Sample 6: 80.44884

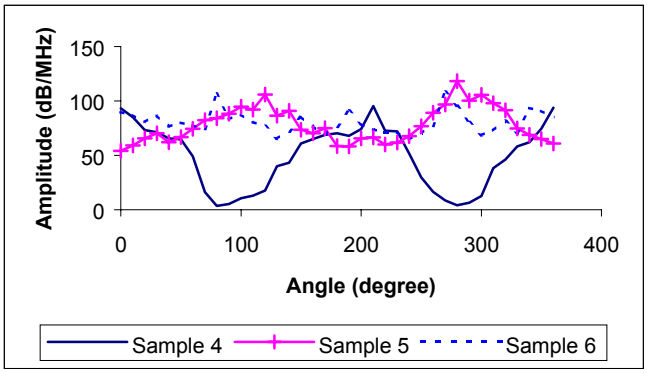

(b)

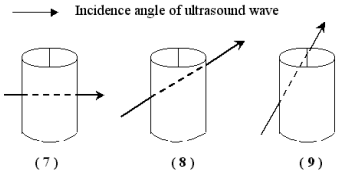

Average Value:

Sample 7: 43.02054
Sample 8: 80.28075
Sample 9: 67.15312

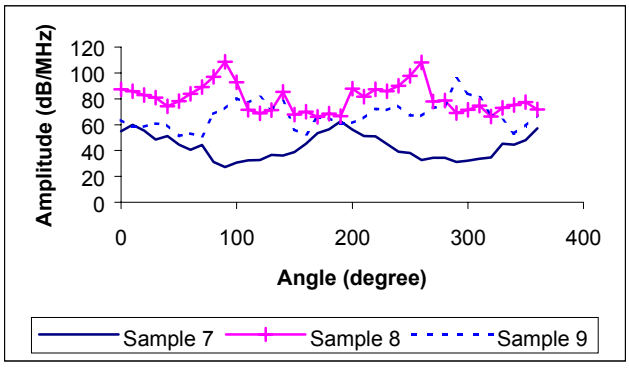

(c)

Figure 5.24 Fast wave BUA variation with angle for fast wave at the original density of the coral samples

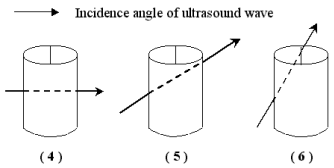

Average Value:

Sample 4: 78.44817
Sample 5: 77.83575
Sample 6: 81.09172

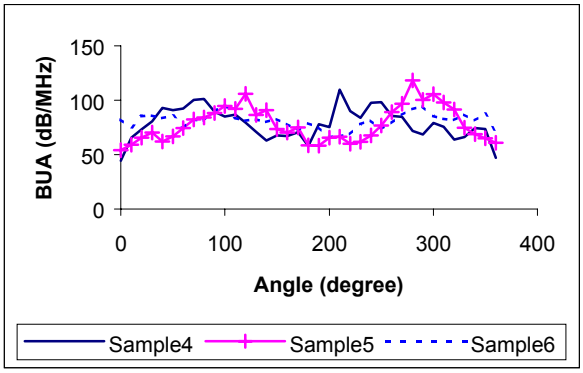

(a)

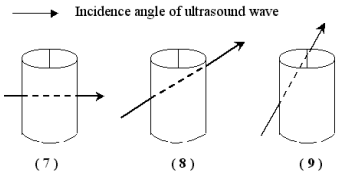

Average Value:

Sample 7: 56.38246
Sample 8: 72.31882
Sample 9: 71.80363

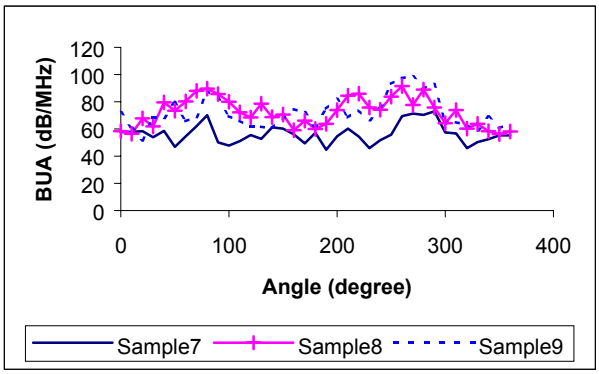

(b)

Figure 5.25 Fast wave BUA variation with angles after intermediate decalcification of the coral samples

5.2.2.3 Slow Wave BUA

For slow wave BUA, it is hard to find the periodicity with angle for any of the nine coral samples at original density level or for any of the six coral samples (Sample 4 to 9) at intermediate density level. This is illustrated in Figure 5.26 and Figure 5.27. For the same reason as that of fast wave, the slow wave BUA value after heavily decalcification cannot be calculated.

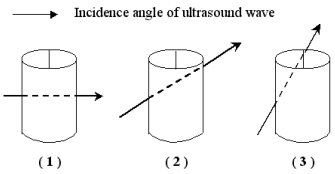

Average Value:

Sample 1: 33.16839
Sample 2: 33.87528
Sample 3: 27.77969

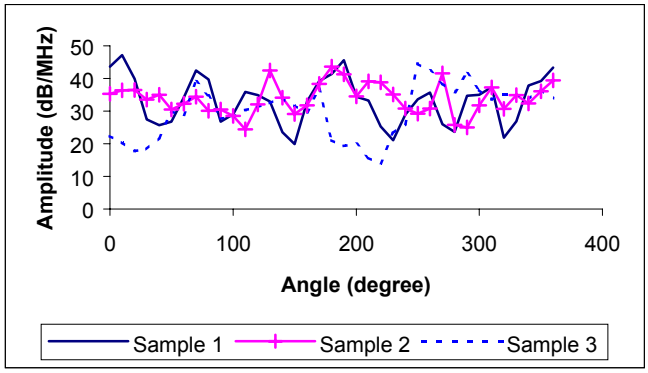

(a)

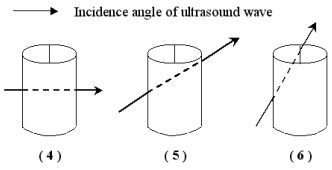

Average Value:

Sample 4: 25.07916
Sample 5: 33.62095
Sample 6: 37.13234

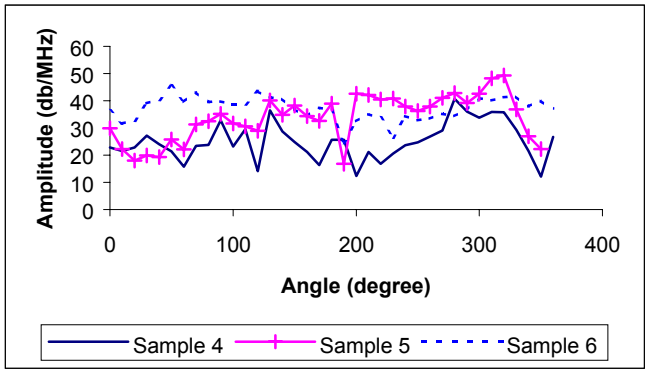

(b)

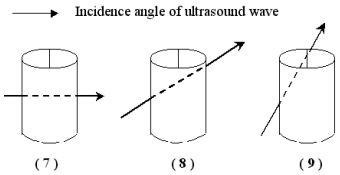

Average Value:

Sample 7: 29.5263
Sample 8: 37.83988
Sample 9: 34.66148

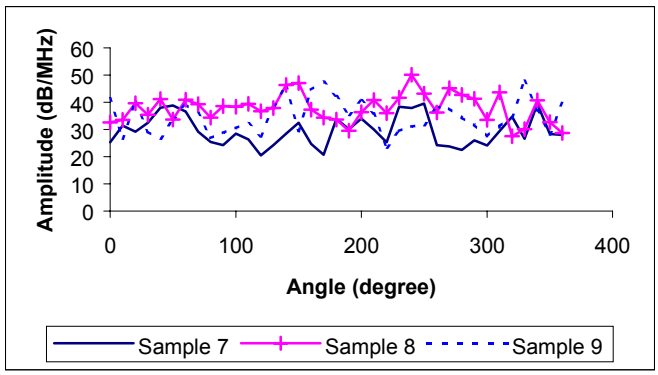

(c)

Figure 5.26 Slow wave BUA variation with angle at the original density of coral samples

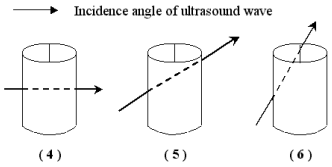

Average Value:

Sample 4: 26.87312
Sample 5: 27.60377
Sample 6: 35.2641

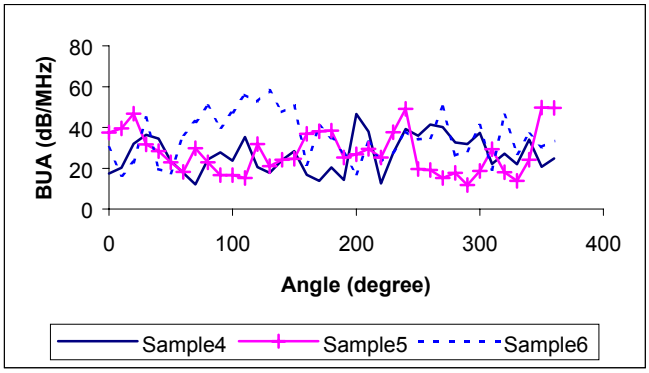

(a)

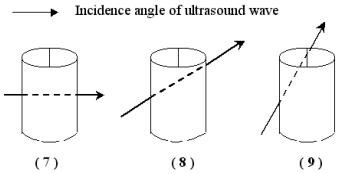

Average Value:

Sample 7: 33.66517
Sample 8: 30.11398
Sample 9: 33.19771

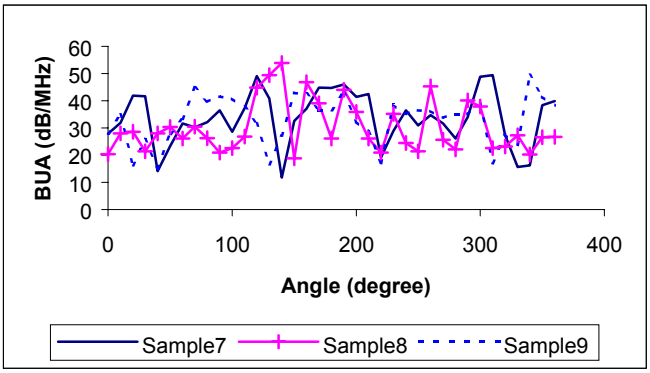

(b)

Figure 5.27 Slow wave BUA variation with angles at intermediate density level of Coral Samples

5.2.2.4 BUA Reproducibility Measurements

To check the reproducibility of the BUA results, measurements on sample 5 and sample 9 were carried out twice, both at original density and intermediate decalcification levels for sample 5, and at original density, intermediate and heavy decalcification levels for sample 9. The normalized mean square difference between the 2 repeated measurements for the values of the entire signal BUA, fast wave BUA and slow wave BUA when the 2 samples are at different density levels are shown in Table 5.2:

Table 5.2 BUA Normalized Mean Square Difference between the Repeated Measurements

	Sample 5		Sample9		
	Original Density	After Light Decalcification	Original Density	After Light Decalcification	After Heavy Decalcification
Entire signal BUA	0.0564	0.0233	0.045477	0.044	0.136
Fast wave BUA	0.1421	0.0995	0.108	0.082	N/A
Slow wave BUA	0.0321	0.06322	0.071284	0.0453	N/A

The normalized mean square difference between the BUA values for the two measurements for sample 5 and sample 9 are under 15%, which illustrates that BUA values of 2 measurements are close. The periodicities of entire signal BUA and fast wave BUA are also repeatable, shown in the Figure 5.28 below for sample 5 when it is at original density and after intermediate decalcification. Slow wave BUA does not exhibit periodic variation, and for that reason it is not shown here.

From the Table 5.2 above and Figure 5.28 shown below, it can be seen that although there are differences between two measurements results on entire signal BUA and fast wave BUA for sample 5 after light decalcification, the measurements results could be thought as reproducible because the mean values of BUA and the variation with angles are similar.

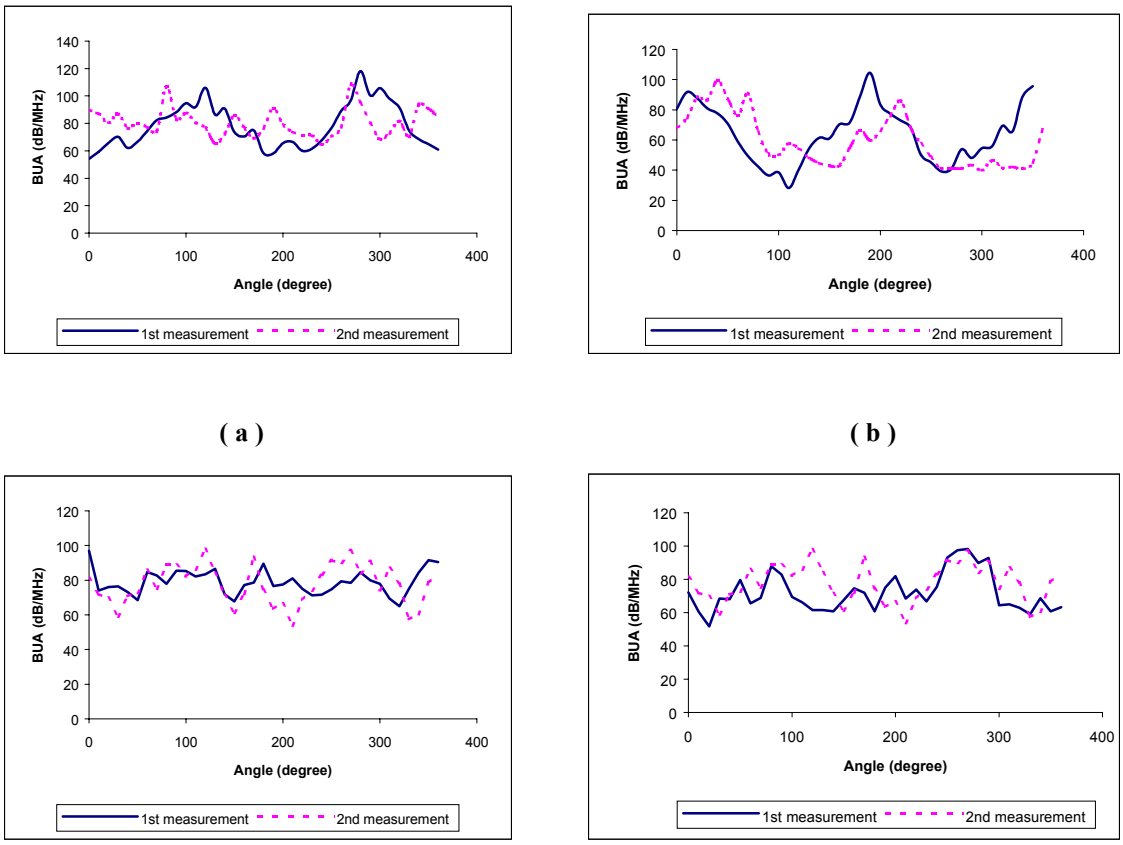

Figure 5.28 Reproducibility test of ultrasound measurements: (a) Entire signal BUA value comparison of 2 measurements on sample 5 at original density; (b) Fast wave BUA values comparison of 2 measurements on sample 5 at original density; (c) Entire signal BUA value comparison of 2 measurements on sample 5 after intermediate decalcification; (d) Fast wave BUA values comparison of 2 measurements on sample 5 after intermediate decalcification;

5.2.3 Discussion

From the observations above, three hypotheses are formulated, trying to explain the periodic characteristics of fast wave BUA and entire signal BUA variations:

1) There is an actual periodic variation in density distribution across the coral sample;

2) The apparent growth axis in the coral sample microstructure contributes to the variation;

3) Phase cancellation effect changes the BUA value of the coral samples at different angles.

Regarding the first hypothesis, the results of DEXA scanner, which are BMD values measured across the sample, have already shown that the densities are quite uniform over the cross-sectional areas for all the coral samples. With respect to the effect of phase cancellation on the BUA variation, there is no abrupt waveform change observed when the coral samples are rotated, which means that phase cancellation is a minor factor. Therefore, the microstructure growth axis is the major factor for the periodical variation with angle of the entire signal BUA and the fast wave BUA. With respect to the lack of periodic variation in the slow wave BUA, it is assumed that the slow wave is related to wave propagation through fluid or water, which has no anisotropic orientation. Therefore, it might be the reason that we do not see any periodic variation in the slow wave BUA.

Furthermore, a nonlinear relationship is found between the entire signal BUA value and the BMD value of each coral sample as measured with DEXA. That is, the values of entire signal BUA increase when the samples are intermediately decalcified and then decrease after the samples being heavily decalcified. Figure 5.29 (a) and (b) show such relationship when the coral samples are rotated oriented 0^o and 90^o. The entire signal BUA at other angles have been observed to have the similar nonlinear relationship with their BMD values. The average of the entire signal BUA varies in a non-linear fashion as well, as shown in Figure 5.30.

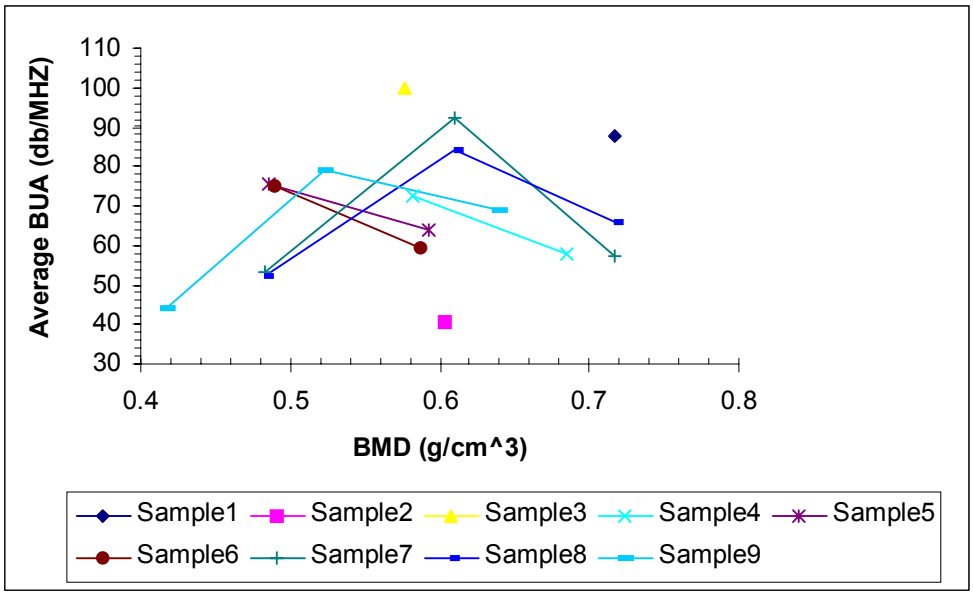

(a)

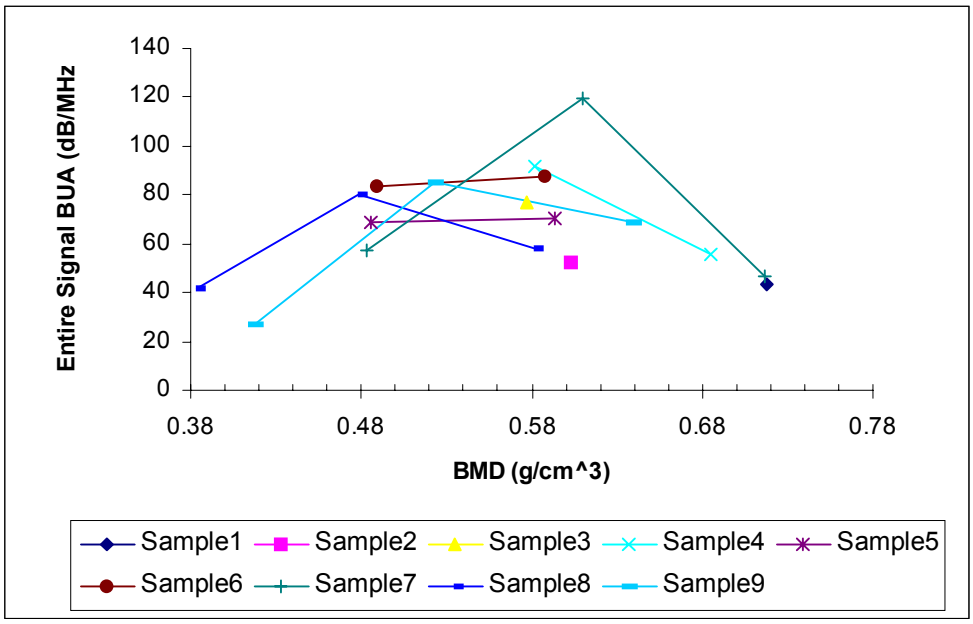

(b)

Figure 5.29 Non-linear relationship of entire signal BUA with BMD value for each coral sample for the orientation angle of (a) 0^{o}; (b) 90^{o}

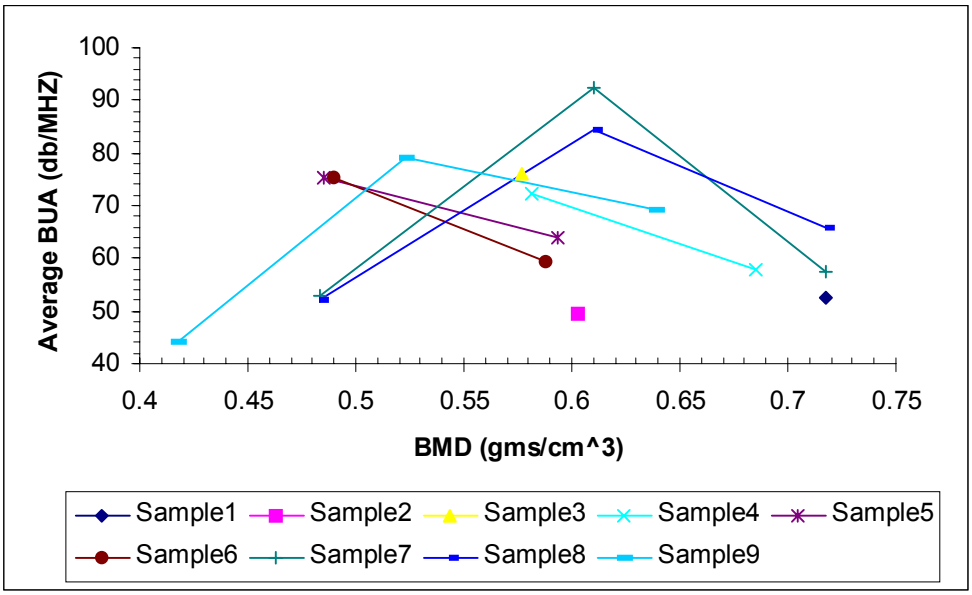

Figure 5.30 Non-linear relationship of the average of the entire signal BUA value with the BMD value of each coral sample

Instead of tracing the entire signal BUA values for different density levels of each coral sample separately, the relationship between average over all angles of the entire signal BUA and the corresponding DEXA BMD values is shown in Figure 5.31. The coral samples with BMD value at around 0.5g/cm^3 have relative higher BUA value than the BUA values of the coral samples with either higher or lower BMD values.

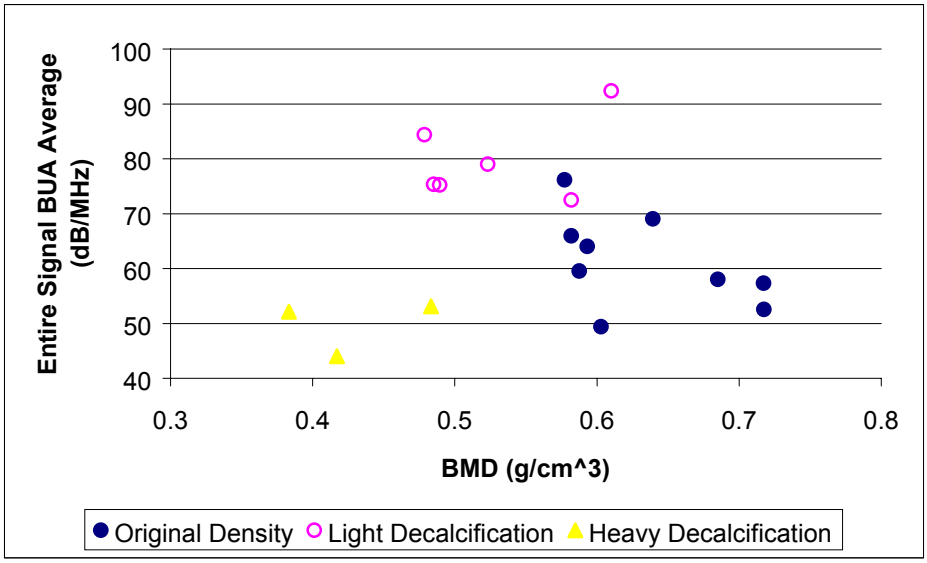

Figure 5.31 Non-Linear relationship of entire signal BUA with BMD

Figure 5.32 show the relationship between the average over all angles of the fast wave BUA and the BMD values for all the coral samples. It can be seen that the fast wave BUA average values of the 9 coral samples at original density exhibit a nearly linear relationship with the corresponding coral sample BMD values, while the fast wave BUA average values of the 6 samples after light decalcification exhibit a somewhat similar linear relationship with their corresponding BMD values, but with different slope ratio and y-axis intercept. Figure 5.33 show the corresponding relationship between the slow wave BUA and the BMD values. Due to the overlap of the fast wave and the slow wave of the coral samples after they have been heavily decalcified, the Figure 5.32 and Figure 5.33 only show the average fast wave BUA values and the average slow wave BUA values for each coral sample at original density and after intermediate decalcification. It can be seen that the values of the fast wave BUA are generally larger for the coral samples that are lightly decalcified than the values when the coral samples

are at original density, and no relationship is found between slow wave BUA and the coral sample density.

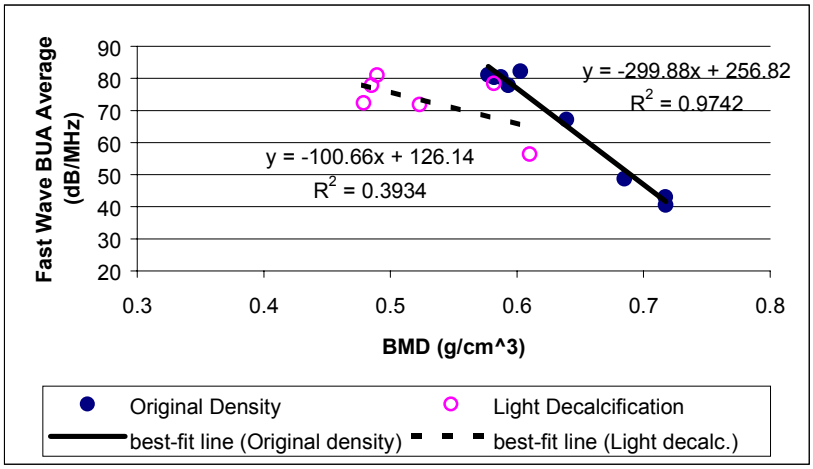

Figure 5.32 Relationship between the average fast wave BUA and BMD value

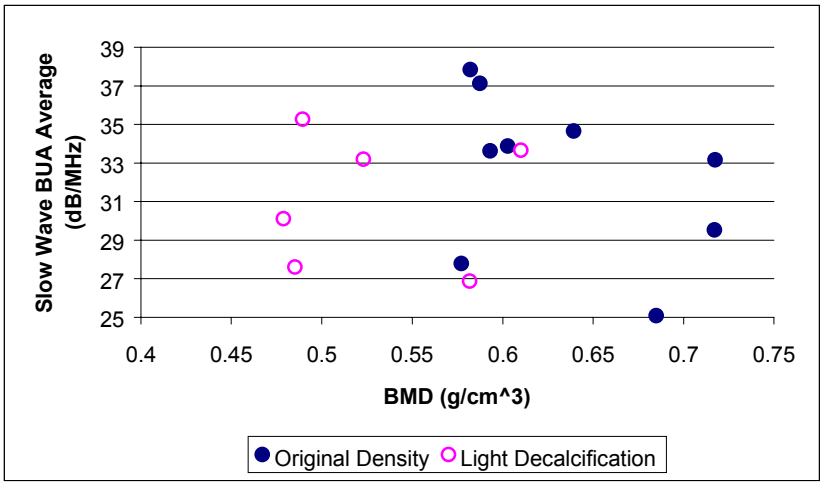

Figure 5.33 Relationship between the average slow wave BUA and BMD value

The nonlinear relationship between BUA and BMD value is similar to the nonlinear relationship between BUA and the porosity of a gelatine/epoxy resin trabecular bone phantom, observed by Clarke et al [33], who demonstrated that a peak BUA

appeared at 50% porosity, and R. Hodgskinson et al [34], who found a BUA peak at 75% porosity in human trabecular bone.

The potential explanation for the nonlinear relationship is that among the two factors which contribute to the ultrasonic attenuation in porous media: absorption and scattering, scattering is the dominant one [37]. The scattering process will take place at the boundaries between the solid core and the soft tissue filling the pores (which in this research work is water), and it is the boundary area available for scatterers which will determine the amount of scattering. The more scattering is created, the more attenuation there will be. And the attenuation variation across the frequency range which is the BUA value will probably increase as well.

Therefore, the increase of BUA when density decreases could be explained by an increase in the boundary area. This may be produced by the effects of decalcification, i.e., either increasing the diameter of existing pore sizes or by introducing "new, essentially isolated (at least in two dimensions) pore spaces" [34] into the coral sample framework. BUA values will keep increasing as long as the boundary area increases. However, as the decalcification continues to perforate the trabecular elements in the coral sample microstructure, the boundary area for scattering will decrease and thus cause a decrease in BUA.

Such non-linear relationship observed between BUA and BMD for the coral samples in this research work could possibly indicate that the osteoporosis prediction is quite complex. If such non-relationship is also observed in the bone samples, the diagnosis of osteoporosis may need to be based not on BUA alone, but on BUA in combination with other ultrasound parameters.

Chapter 6

Ultrasound Signal Analysis Using Analytic Impulse Response Magnitude

For calculating the impulse response function of the coral samples, two approaches (which have been discussed in Chapter 3) are explored. In one approach, the coral sample is rotated between each measurement with an angle increment of θ_1=10^o from 0^o to 180^o. In the other approach shown in Figure 6.1, the receiving transducer is rotated between each measurement with the same angle increment θ_2 = 10^o from 0^o to 90^o. The reason for choosing 90^o as the maximum angle in the second approach is that after the receiving transducer is rotated larger than 90^o, the received signal will be dominated by the signal scattered from the surface of the coral sample.

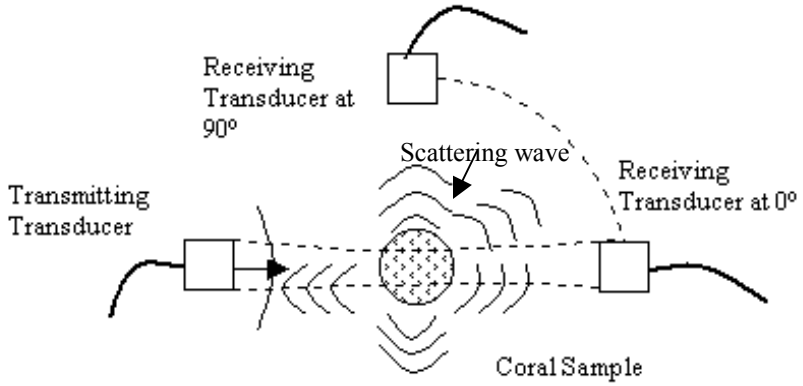

Figure 6.1 Scattering from the coral sample surface

The first approach is a much easier and more accurate way to analyze the effect of coral sample microstructure and density. The reason is that at any angular position of the coral sample, the major transmitting path of ultrasound is largely the same. Therefore, the

difference between the measured impulse response functions will relate to the difference of the microstructure and density along the propagation path for the ultrasound pulse for a given coral sample. However, the second approach, that is, rotating the receiving transducer each time to obtain the information contained in the receiving signal variation, is a much more practical and clinically useful approach. For example, it is unacceptable if a patient's heel has to be rotated during the ultrasound measurement. But the result of the second approach is much more complex to analyze than the result of the first approach because a lot of factors will affect the received signal, such as the scattered and reflected signal from the coral sample surface, the multi-path and refraction phenomena of ultrasound transmission due to the different receiving transducer position, etc. This is the reason why we did not explore the second approach in the BUA analysis because BUA is intended to be based only on the ultrasound attenuation of the coral sample. Despite the complexities, the two approaches are compared in the impulse response function analysis, in the hope of applying the information for the future osteoporosis analysis. The signal processing procedure for the impulse response analysis is described below.

6.1 Impulse Response Function

The ultrasound through-transmission measurement set-ups for both approaches discussed above can be described as a linear, time invariant causal system. This is shown in Figure 6.2. Causality naturally comes from the fact that the received signal does not arrive earlier than the input signal from the transmitting transducer.

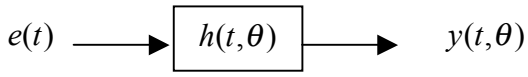

Figure 6.2 Time invariant system representation of experiment set-ups

As shown in Figure 6.2, the system input $e(t)$ represents the excitation signal to the transmitting transducer, the output $y(t,\theta)$ is the received signal, and $h(t,\theta)$ is the impulse response of the system, including the two transducers and the acoustic path with the coral sample present. The reason that both $y(t,\theta)$ and $h(t,\theta)$ have an angle component is that both of them are a function of the rotation angle, θ, of the coral sample.

Since it is known that the output of a linear time-invariant system is equal to the convolution of the input with the impulse response function, the time domain formula of this system may be given as

$$y(t,\theta) = \int_0^t e(\tau)h(t-\tau,\ \theta)d\tau\ +\ noise(t) = e(t) * h(t,\theta) + noise(t), \qquad (6.1)$$

where $*$ denotes convolution and $noise(t)$ represents noise component in the system. The corresponding frequency domain formula is given as

$$Y(f,\theta) = E(f)H(f,\theta) + Noise(f) \qquad (6.2)$$

However, in the practical measurement system, only the received signal is measurable. Thus, when Eq. 6.1 is applied, the excitation pulse $e(t)$ needs to be replaced by the reference signal $x_{ref}(t)$, which is the output signal from the receiving transducer received after the ultrasound pulse propagates through the water path between the transducers, as shown in Figure 6.3. The signal $x_{ref}(t)$ is actually the excitation signal $e(t)$ convolved with the impulse response of the transmitting transducer and the receiving transducer and with ultrasound propagation time delay of the water path (if we

think of water as perfect material without attenuation) between the 2 transducers, as shown in Figure 6.3.

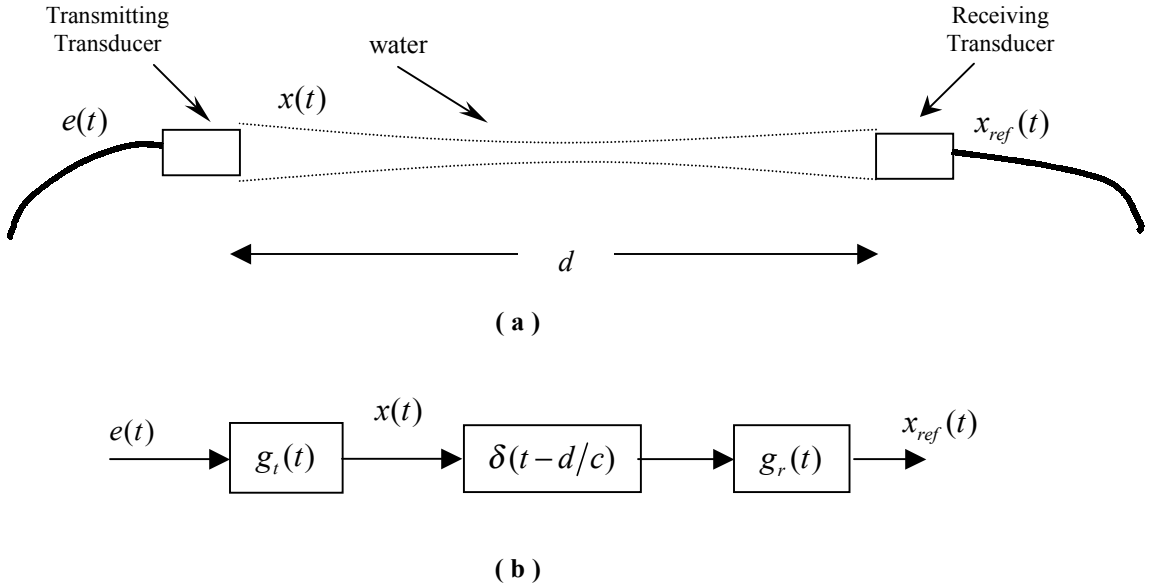

Figure 6.3 (a) The diagram of measuring reference signal; (b) the system diagram for obtaining the reference signal

In Figure 6.3, $g_t(t)$ and $g_r(t)$ are the impulse responses of the transmitting transducer and the receiving transducer, respectively, which have been defined in Section 3.1.3. So, $x_{ref}(t)$ is given as

$$x_{ref}(t) = e(t) * g_t(t) * \delta(t - d/c) * g_r(t) \tag{6.3}$$

According to the commutative property of convolution, Eq. 6.3 can also be written as

$$\begin{aligned} x_{ref}(t) &= g_t(t) * \delta(t - d/c) * g_r(t) * e(t) \\ &= g(t) * \delta(t - d/c) * e(t) = g(t - d/c) * e(t) \end{aligned} \tag{6.4}$$

where $g(t) = g_t(t) * g_r(t)$ and c is the velocity of ultrasound in water (1480m/s). That is, the responses of the receiving transducer and the transmitting transducer are combined. After further incorporating the time delay of the water path, the impulse response of the

transducers $g(t)$ can be approximated to be a delayed filter impulse response, $g(t-t_0)$, where $t_0 = d/c$.

Now we can go back to analyze the measurement systems with the coral sample present. Figure 6.4 below shows the physical arrangement of the measurement system with the coral sample placed between the transducers and the same measurement system shown as a system block diagram.

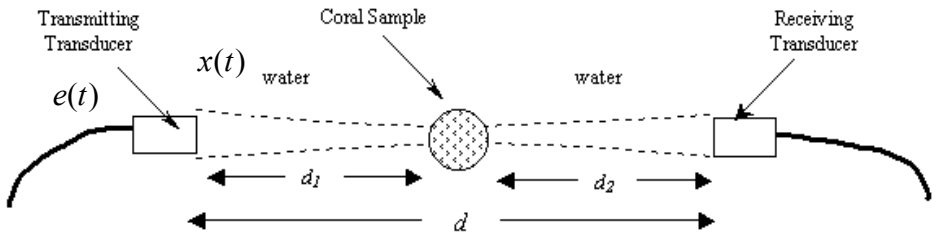

(a)

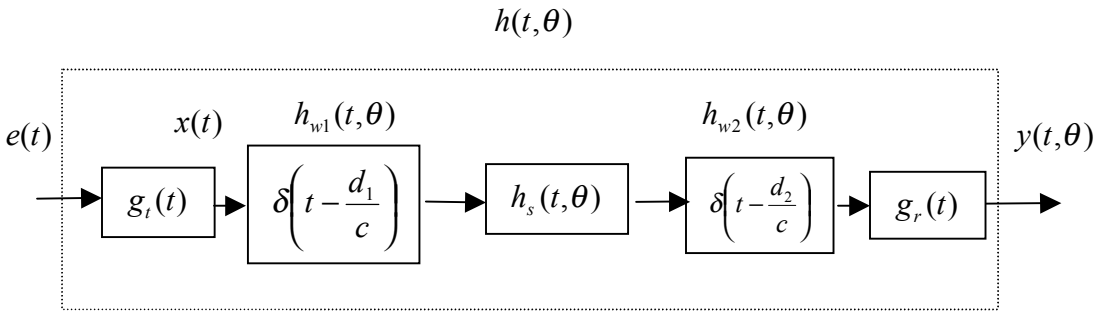

(b)

Figure 6.4 Detailed Diagram of System Impulse Response

In Figure 6.4, $e(t)$ is the excitation signal, $x(t)$ is the ultrasound pulse, $h_{w1}(t,\theta)$ and $h_{w2}(t,\theta)$ are the impulse responses due to the ultrasound transmission time delays of the two water paths between the coral sample and the transducers and $h_s(t,\theta)$ is the impulse response of the coral sample. The whole system impulse response $h(t,\theta)$ is

$$h(t,\theta) = g_t(t) * \delta(t - d_1/c) * \ h_s(t,\theta) * \ \delta(t - d_2/c) * g_r(t) \tag{6.5}$$

in time domain. Since $d \cong d_1 + d_2$, Eq. 6.5 can be rewritten as

$$\begin{aligned} h(t,\theta) &\cong g_t(t) * g_r(t) * \delta(t - d/c) * h_s(t,\theta) \\ &\cong g(t - d/c) * h_s(t,\theta) \end{aligned} \tag{6.6}$$

This can also be shown in Figure 6.5 below:

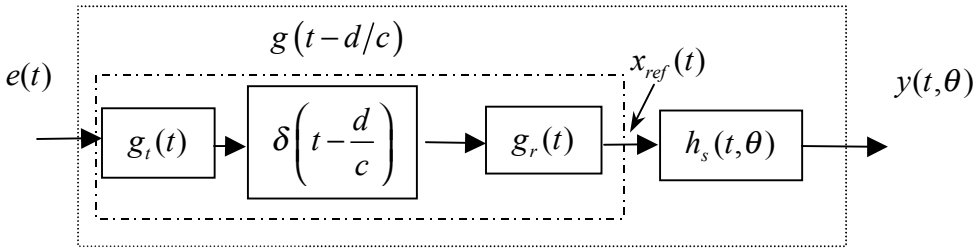

Figure 6.5 Simplified Diagram of System Impulse Response

We can see that after being convolved with $g_t(t)$, $\delta(t - d/c)$, and $g_r(t)$, the excitation signal $e(t)$ becomes to be $x_{ref}(t)$. Therefore, the system can be represented by

$$y(t,\theta) = x_{ref}(t) * h_s(t,\theta) + noise(t) \tag{6.7}$$

in time domain and

$$Y(f,\theta) = X_{ref}(f) H_s(f,\theta) + Noise(f). \tag{6.8}$$

in frequency domain. Therefore, the impulse response of the coral sample can be analyzed based on Eq. 6.8.

Furthermore, to improve the ability of determining $H_s(f,\theta)$, it is necessary to make the noise component in Eq. 6.8 as small as possible. Two approaches to achieve this goal are described below:

1) Use the "summed averaging" function of the digital oscilloscope LeCroy 9400. The summed averaging consists of repeated additions of the source waveform with equal weight. In statistic signal analysis view, such approach can minimize the uncorrelated

(non-coherent) noise effect. We choose the number of repeated additions of the received signal, $y(t,\theta)$, to be 1250 in the experiments, which theoretically should reduce the noise amplitude by a factor of $\sqrt{1250} = 35.4$.

2) Set $Y(f,\theta) = 0$, $X_{ref}(f) = 0$, for $f \geq 800\ kHz$ because it is reasonable to think that the signal with frequency higher than $800\ kHz$ is mainly noise since the center frequency of the transmitting transducer is $500\ kHz$.

Therefore, we might further neglect noise component and simplify Eq. 6.8 to be

$$Y(f,\theta) = X_{ref}(f) H_s(f,\theta) \tag{6.9}$$

Thus, in principle, $H_s(f,\theta)$ can then be calculated as

$$H_s(f,\theta) = \frac{Y(f,\theta)}{X_{ref}(f)} \tag{6.10}$$

However, at frequencies in the 0-800 *k*Hz range where the reference signal spectrum $X_{ref}(f)$ is small, meaning that the signal to noise ratio is relatively poor, its inverse would be large and the impulse response would be affected heavily, i.e., become large, noisy and blow up. Therefore, we need some technique to compensate for this possible situation. The Wiener filter is one approach to extract the impulse response function from the received signal [38, 39]. The formula for the Wiener filter applied to Eq. 6.10 is defined as follows:

$$\hat{H}_s(f,\theta) = \frac{\left|X_{ref}(f)\right|^2 \bullet Y(f,\theta)}{\left|X_{ref}(f)\right|^2 \bullet X_{ref}(f) + \alpha * \max(\left|X_{ref}(f)\right|)} \tag{6.11}$$

The symbol over the H_s in $\hat{H}_s(f,\theta)$ indicates that it is an estimate of the true $H_s(f,\theta)$. The reason that the constant, $\alpha * \max|X(f)|$, is added to the denominator of Eq. 6.11 is

to avoid the possible undefined situation of Eq. 6.10 when its numerator is divided by too small a value. α is determined by the signal to noise power ratio. When the Wiener filter is used, the output of Eq. 6.11 will tend towards zero for frequencies when $|X_{ref}(f)|$ is small. Measurements and calculations are made to find the "best" α by observing the signal to noise ratio.

After the estimate of $H_s(f,\theta)$ is obtained, we can get the time domain impulse response as

$$\hat{h}_s(t,\theta) = ifft(\hat{H}_s(f,\theta)) \qquad (6.12)$$

by inverse Fourier transform. Then we can investigate whether important information of the coral sample microstructure will be obtained from it.

6.2 Hilbert Transform and Analytic Signal

In this research work, analytic signal theory is applied to further process the impulse response function. The reason is that for the acoustic signals, the analytic signal accurately represents the two coupled energy forms in propagating waveforms. The two energy forms are *potential energy* (pressure field) and *kinetic energy* (velocity field), and there is 90^o phase shift between corresponding spectral components of the real and imaginary parts of the analytic signal.

However, the ultrasound transducer can only detect pressure fields which is the real part of the analytic signal and corresponds to the potential energy. The square of the real signal magnitude will be zero at the instant when potential energy is zero while the kinetic energy is not zero. The square of analytic signal magnitude, on the other hand, is

proportional to the instantaneous rate-of-arrival of the total energy, which is the sum of potential energy and kinetic energy. Therefore, the magnitude of the analytic signal is an important parameter in signal processing. The detail principle of analytic signal is discussed below.

6.2.1 Definition of Analytic Signal

If $a(t)$ is a given real signal, the corresponding analytic signal is [40]

$$\hat{a}(t) = a(t) + j\tilde{a}(t) = a(t) + j\,\mathcal{H}\{a(t)\} \tag{6.13}$$

In Eq. 6.13, the real part of $\hat{a}(t)$ is the original $a(t)$ and the imaginary part is the Hilbert transform of $a(t)$. According to the definition of Hilbert transform,

$$\tilde{a}(t) = \mathcal{H}\{a(t)\} = \frac{1}{\pi}\int_{-\infty}^{\infty} a(\tau)\frac{1}{t-\tau}d\tau = a(t) * \frac{1}{\pi t} \tag{6.14}$$

where $*$ denotes convolution. The above expression gives the time-domain Hilbert transform. Further insight is obtained through Fourier analysis.

$$\mathcal{F}\{\tilde{a}(t)\} = \mathcal{F}\{a(t)\}\,\mathcal{F}\{\frac{1}{\pi t}\} = A(f)\,[-jSgn(f)] \tag{6.15}$$

where $-jSgn(f) = \begin{cases} -j = -90^{o} & f \geq 0 \\ +j = +90^{0} & f < 0 \end{cases}$. Therefore, the difference between the Hilbert transform pair is a -90^{o} phase shift for positive frequencies and a +90^{o} phase shift for negative frequencies.

The analytic signal magnitude is

$$|\hat{a}(t)| = \sqrt{a^2(t) + [\tilde{a}(t)]^2} \tag{6.16}$$

The signal $|\hat{a}(t)|$ corresponds to the true envelope signal of $a(t)$. The Fourier transform of Eq. 6.13 gives:

$$\begin{aligned}\hat{A}(f) &= A(f) + j[A(f)\bullet(-jSgn(f))] \\ &= A(f) + A(f)Sgn(f) \\ &= \begin{cases} A(f) - A(f) = 0, & f < 0 \\ A(f) + A(f) = 2A(f), & f \geq 0 \end{cases}\end{aligned} \tag{6.17}$$

We can see that the Fourier transform of an analytic signal contains only positive frequency components.

6.2.2 Analytic Signal of Impulse Response Function

The imaginary part of the coral sample impulse response $\hat{h}_s(t,\theta)$, obtained from the inverse Fourier transform process, is much smaller that its real part; an example of this is shown later in Figure 6.12 (b). Thus we can think of $\hat{h}_s(t,\theta)$ as represented by a real function (as it should be in reality). The corresponding analytic signal of $\hat{h}_s(t,\theta)$ is obtained when Hilbert transform is applied on it as

$$\hat{h}_{an}(t,\theta) = \hat{h}_s(t,\theta) + j \cdot \mathcal{H}(\hat{h}_s(t,\theta)) \quad . \tag{6.18}$$

In Eq. 6.18, the real part of $\hat{h}_{an}(t,\theta)$ is the original real $\hat{h}_s(t,\theta)$ and the imaginary part is the Hilbert transform of the real $\hat{h}_s(t,\theta)$.

Since the analytic signal magnitude is directly related to the rate of energy arrival, it provides an optimal analysis tool.

6.3 Measurement Process

The first two steps in using the Wiener filter process to determine the impulse response are: i) to find the appropriate time shift to be applied to $x_{ref}(t)$ so that the inverse filtering given in Eq. 6.11 becomes causal, and ii) to find "best" α value in Eq. 6.11.

i) Find the appropriate shifting time

As illustration, the procedure is described below on the measurement result for rotating the coral sample 1. Such procedure is implemented similarly on each result for other coral samples in the two approaches.

(a) Measure $x_{ref}(t)$ obtained when only water exists between the transmitting and receiving transducers. Figure 6.6 shows the downsampled $x_{ref}(t)$ with sampling frequency of 10MHz (the initial sampling frequency is 100MHz).

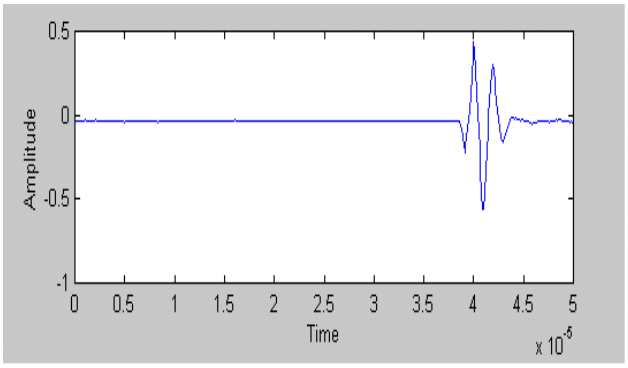

Figure 6.6 Downsampled $x_{ref}(t)$ with Sampling Frequency of 10MHz

(b) Measure $y(t,\theta)$ when θ = 0°. Figure 6.7 shows the downsampled $y(t,\theta)$ with the sampling frequency of 10MHz.

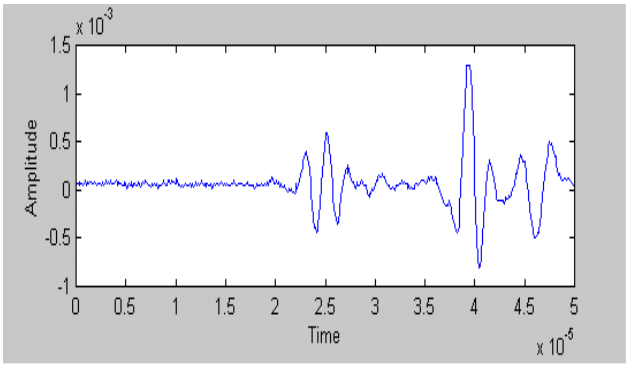

Figure 6.7 Downsampled $y(t,0)$ with Sampling Frequency of 10MHz

According to the causality characteristics of a time invariant system, the ultrasound pressure pulse of $x_{ref}(t)$ should begin no later than the onset of the received pulse signal of $y(t,\theta)$. Therefore, the time period between the ultrasound pulse in $x_{ref}(t)$ and the beginning of the received pulse signal $y(t,\theta)$ might conveniently be used as the shifting time reference for time delay, denoted as T_{shift} in Figure 6.8.

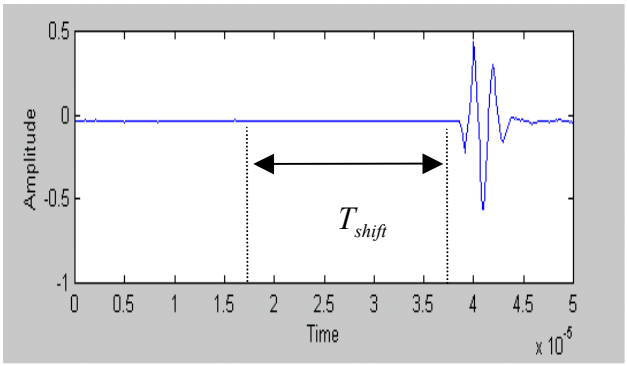

Figure 6.8 Downsampled $x_{ref}(t)$ with shifting time at sample frequency as 10MHz

However, the actual time shift for appropriate time delay is longer than T_{shift} because the ultrasound signal propagates faster in the coral sample than it propagates in

the water. Using $x_{ref}(t)$ with and without T_{shift}, and with different T_{shift} will result in different calculated $\hat{y}(t,\theta)$, shown in Figure 6.9 (a), (b) and (c).

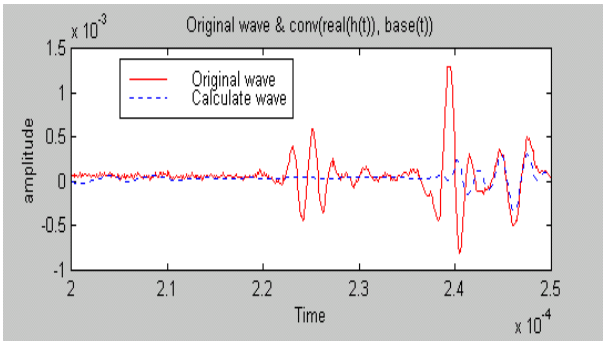

(a)

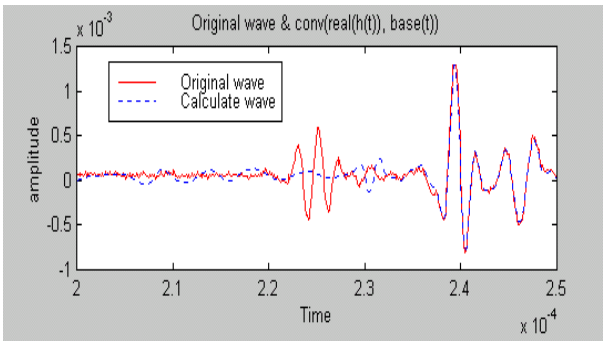

(b)

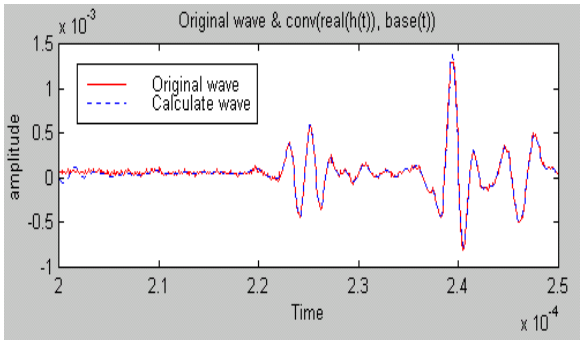

(c)

Figure 6.9 Original $y(t,0)$ compared with $\hat{y}(t,0) = x_{ref}(t) * \hat{h}_s(t,0)$ when

(a) $T_{shift} = 0\mu s$; (b) $T_{shift} = 20\mu s$; (c) $T_{shift} = 40\ \mu s$

From Figure 6.9, it can be seen that an insufficient amount of time shift will cause $\hat{y}(t,\theta)$ to be incorrectly shifted and wrapped. T_{shift} = 40 μs is calculated to be an appropriate shifting time for this measurement system for each measurement result in the

approach of rotating the coral sample. For the approach of the rotating the receiving transducer, the appropriate shifting time will be processed for each result.

ii) Find "best" α

(a) To find "best" α in Eq. 6.11, we need first to obtain the Fourier transform of $y(t,0)$, i.e., $Y(f,0) = fft(y(t,0))$, and set the real part of $Y(f,0) = 0$, for $f \geq 800KHz$. This process is implemented in order to minimize noise, as shown in Figure 6.10.

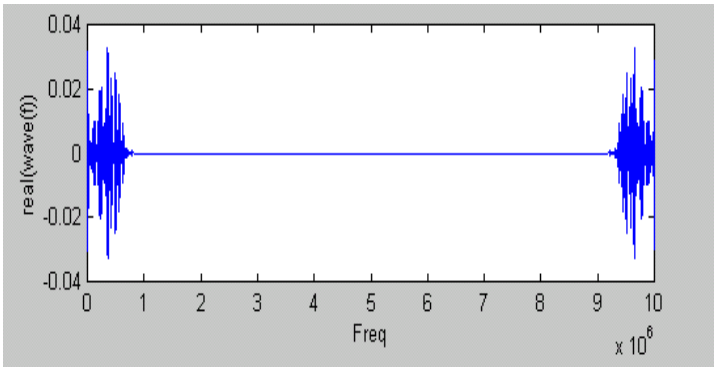

Figure 6.10 Real part of $Y(f,0) = fft(y(t,0))$, **with** $Y(f,0) = 0, \ f \geq 800KHz$

(b) The Fourier transform of $x_{ref}(t)$ should also be obtained, i.e., $X_{ref}(f) = fft(x_{ref}(t))$, and set the real part of $X_{ref}(f) = 0$, for $f \geq 800KHz$ in order to minimize noise, as shown in Figure 6.11.

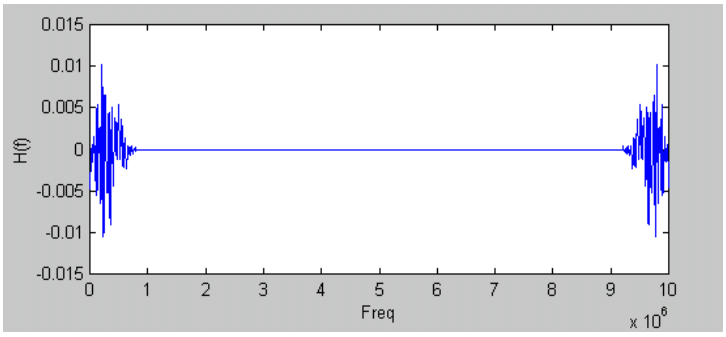

Figure 6.11 Real part of $X_{ref}(f) = fft(x_{ref}(t))$, **with** $X_{ref}(f) = 0, \ f \geq 800KHz$

(c) Now that we have already obtained $Y(f,0)$ and $X_{ref}(f)$, we can start with $\alpha = 0.3$ and substitute the value into Eq. 6.12 (a) to obtain $\mathrm{Re}\{\hat{H}_s(f,\theta)\}$, as shown in Figure 6.12. Then we can apply inverse Fourier transform to calculate the real part and imaginary part of $\hat{h}_s(t,0) = ifft(\hat{H}_s(f,0))$, as shown in Figure 6.12 (b).

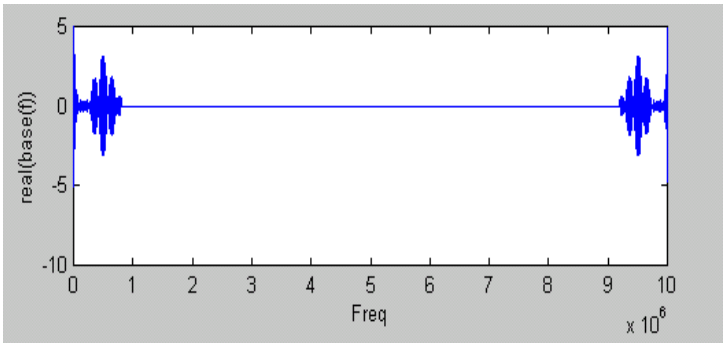

(a)

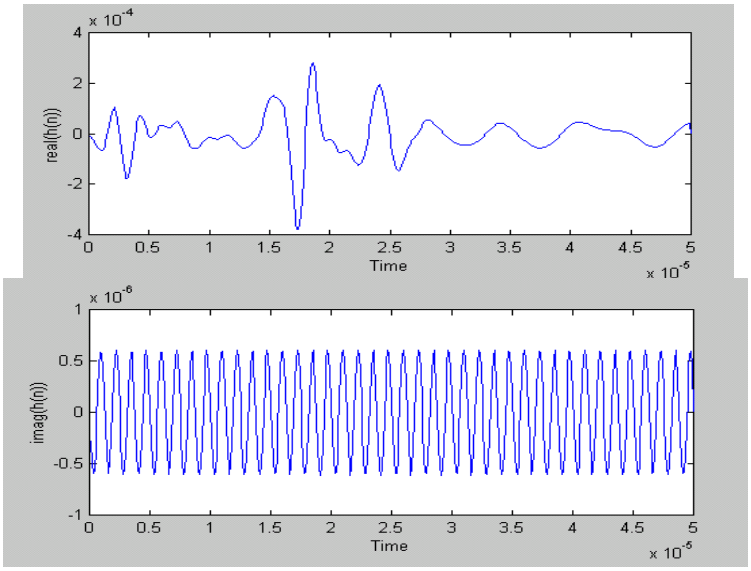

(b)

Figure 6.12 (a) Real part of $\hat{H}_s(f,0)$ calculated by Eq. 6.11; (b) real part and imaginary part of $\hat{h}_s(t,0) = ifft(\hat{H}_s(f,0))$

By comparing the calculated $\hat{y}(t,0) = x_{ref}(t) * \hat{h}_s(t,0)$ with original $y(t,0)$, we can determine whether the α value is good enough to be used in the Wiener filter, as shown in Figure 6.13.

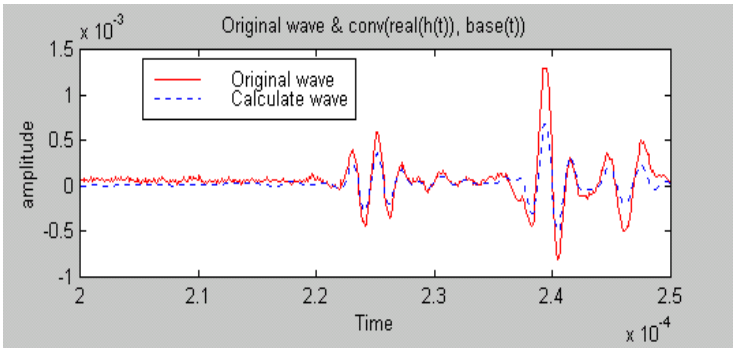

Figure 6.13 Original $y(t,0)$ compared with $\hat{y}(t,0) = x_{ref}(t) * \hat{h}_s(t,0)$ obtained for $\alpha = 0.3$

(d) Continue with $\alpha = 0.2, 0.15, 0.1, \cdots$, and substitute the value into Eq. 6.11 to obtain $\hat{H}_s(f,\theta)$. Then apply the inverse Fourier transform to calculate $\hat{h}_s(t,0) = ifft(\hat{H}_s(f,0))$ and compare calculated $\hat{y}(t,0) = x_{ref}(t) * \hat{h}_s(t,0)$ with original $y(t,0)$ to determine whether the α value is good enough to be used in the Wiener filter. The comparisons are shown in Figure 6.14 and Figure 6.15.

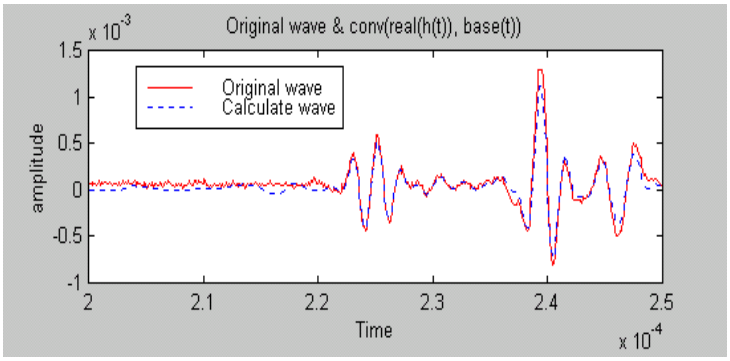

Figure 6.14 Original $y(t,0)$ compared with $\hat{y}(t,0) = x_{ref}(t) * \hat{h}_s(t,0)$ obtained for $\alpha = 0.05$

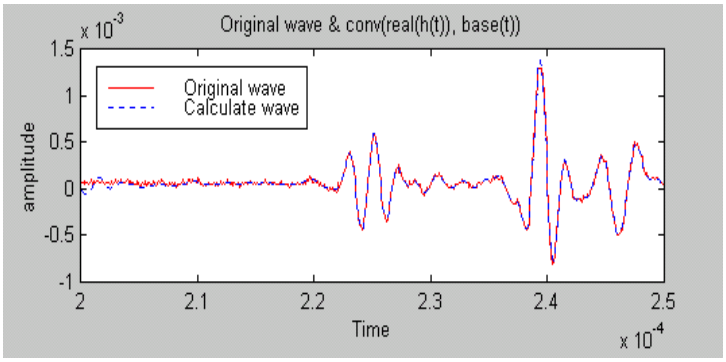

Figure 6.15 Original $y(t,0)$ **compared with** $\hat{y}(t,0) = x_{ref}(t) * \hat{h}_s(t,0)$ **obtained for** $\alpha = 0.007$

As it can be seen, 0.007 is found to be the "best" value. Since the signal to noise ratio is similar for each signal received under the same measurement condition, the best α is substituted in Eq. 6.11 for processing each signal. Therefore, with the appropriate shifting time, the Wiener filter is applied to obtain the impulse response function $\hat{h}_s(t,\theta)$ at different rotation angles. After that, Hilbert transform is performed on the $\hat{h}_s(t,\theta)$ and the magnitude of analytic signal is obtained. For easy comparison of $\hat{h}_s(t,\theta)$ vs. angle, the results will be displayed in a 3D figure.

In the same way as with the processing of BUA, we have analyzed the analytic impulse responses for: i) the entire signal, ii) the fast wave signal and iii) the slow wave signal, in the approach of rotating the coral sample. Only the impulse response for the entire signal will be obtained in the approach of rotating the receiving transducer because the fast wave and slow wave overlap after the rotation angle becomes large.

6.4 Results and Discussion

Here we display and discuss the results of the two measurement approaches separately.

6.4.1 The Approach of Rotating the Coral Sample

1. Fast Wave Analytic Impulse Response

For the approach of rotating the coral sample, due to the overlap of fast wave and slow wave when coral samples are heavily decalcified, the impulse responses of fast wave are only analyzed when the coral samples are at their original density and at their intermediate density after light decalcification.

The fast wave component of the received signal at original density and the corresponding magnitude of the impulse response in analytic signal form are shown in Figure 5.16 to Figure 5.24. The analytic impulse response depicts the same periodic variation with angle as does the fast wave waveform, i.e., the minimum peak value is found at around 90^o and maximum value at around 0^o and 180^o.

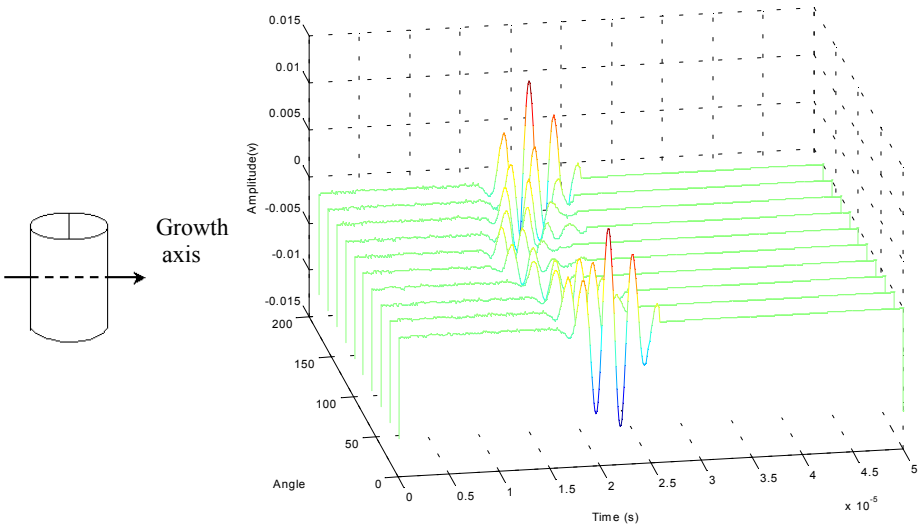

(a)

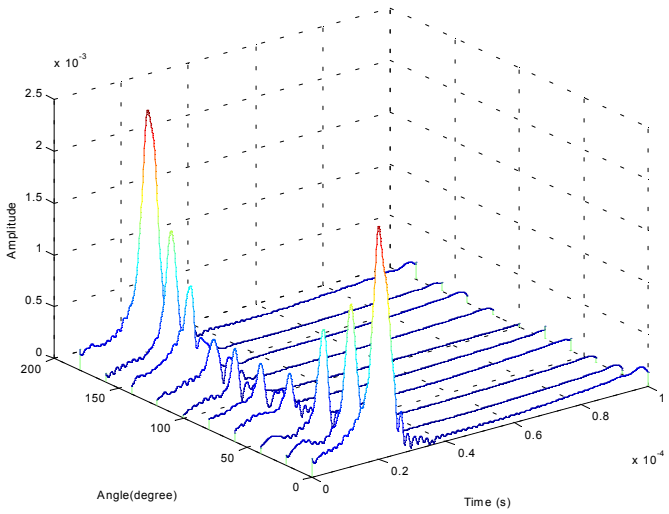

(b)

Figure 6.16 Fast wave variations with angle and the corresponding impulse responses with original density in rotating sample approach for Sample 1. (a) Waveforms; (b) Magnitude of the analytic signal

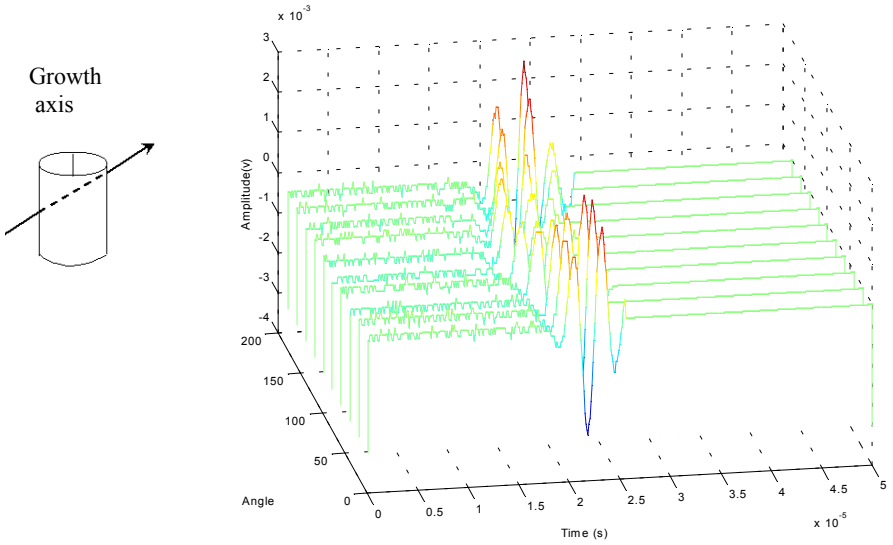

(a)

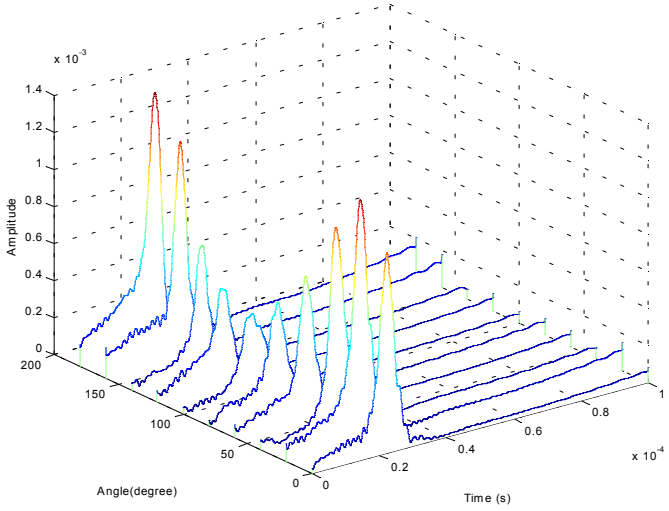

(b)

Figure 6.17 Fast wave variations with angle and the corresponding impulse responses with original density in rotating sample approach for Sample 2. (a) Waveforms; (b) Magnitude of the analytic signal

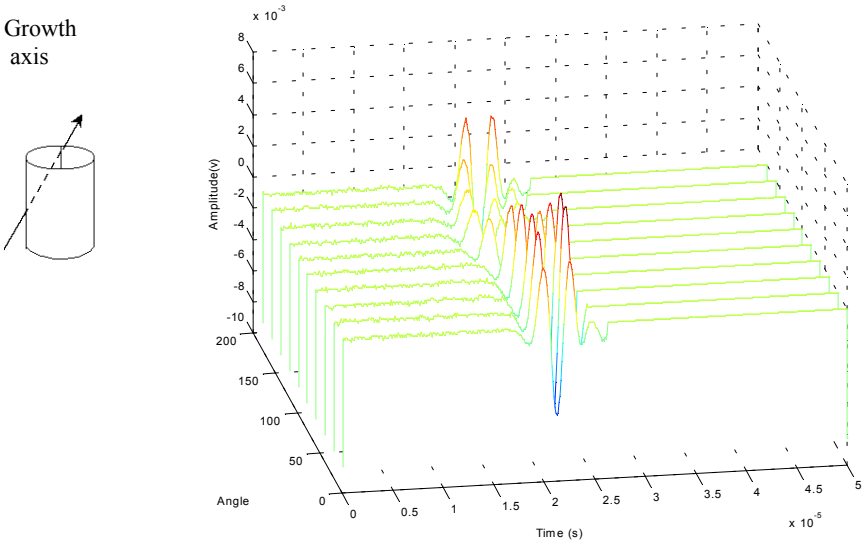

(a)

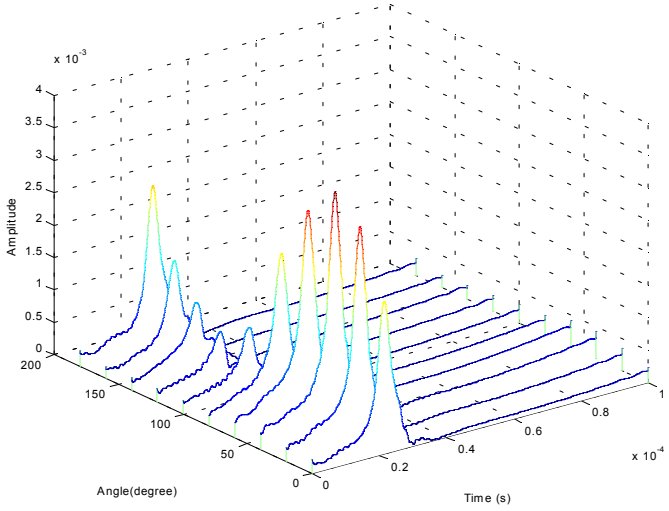

(b)

Figure 6.18 Fast wave variations with angle and the corresponding impulse responses with original density in rotating sample approach for sample 3. (a) Waveforms; (b) Magnitude of the analytic signal

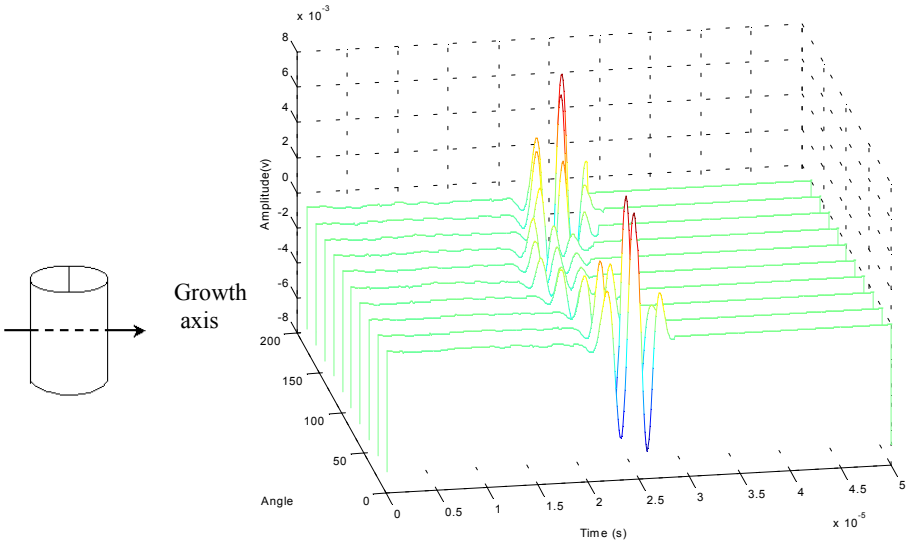

(a)

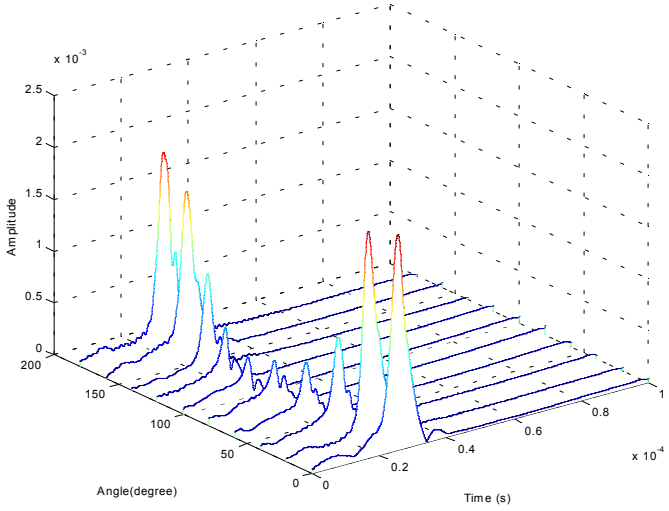

(b)

Figure 6.19 Fast wave variations with angle and the corresponding impulse responses with original density in rotating sample approach for Sample 4. (a) Waveforms; (b) Magnitude of the analytic signal

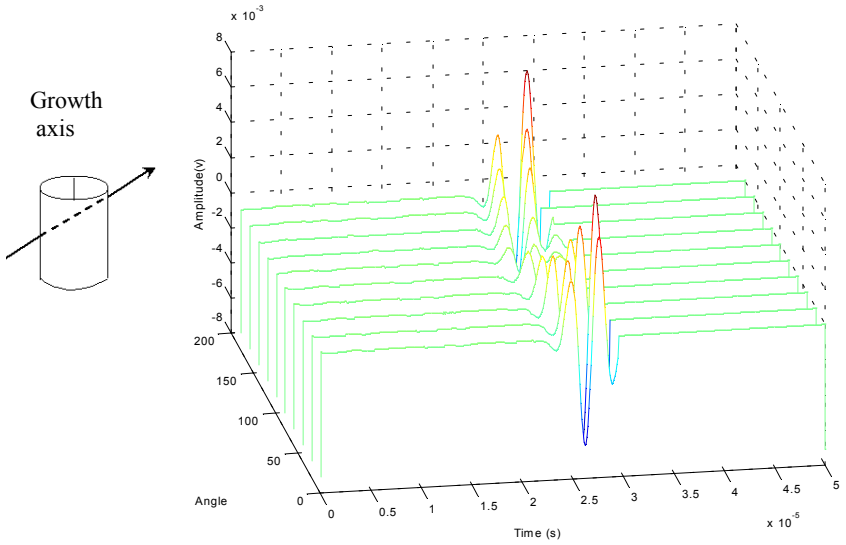

(a)

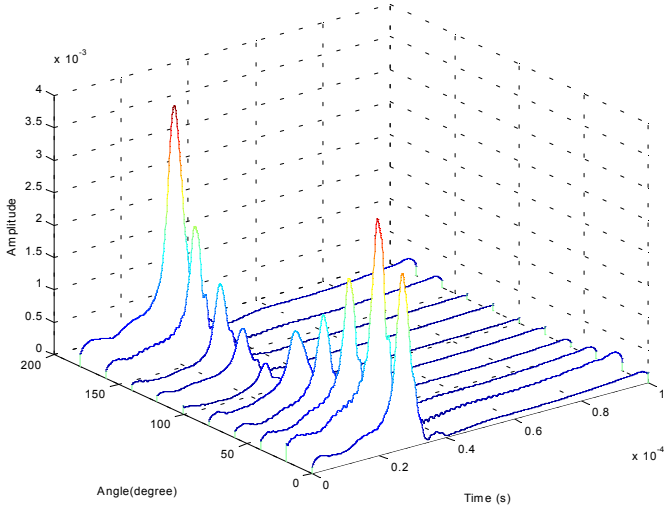

(b)

Figure 6.20 Fast wave variations with angle and the corresponding impulse responses with original density in rotating sample approach for Sample 5. (a) Waveforms; (b) Magnitude of the analytic signal

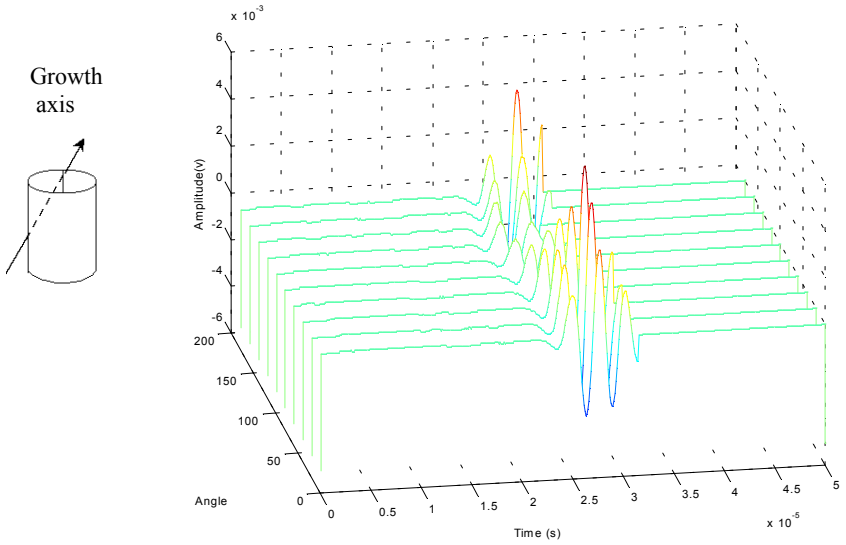

(a)

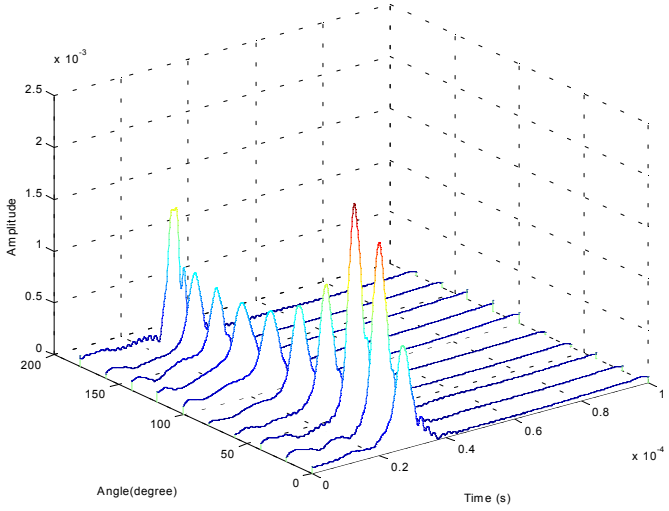

(b)

Figure 6.21 Fast wave variations with angle and the corresponding impulse responses with original density in rotating sample approach for Sample 6. (a) Waveforms; (b) Magnitude of the analytic signal

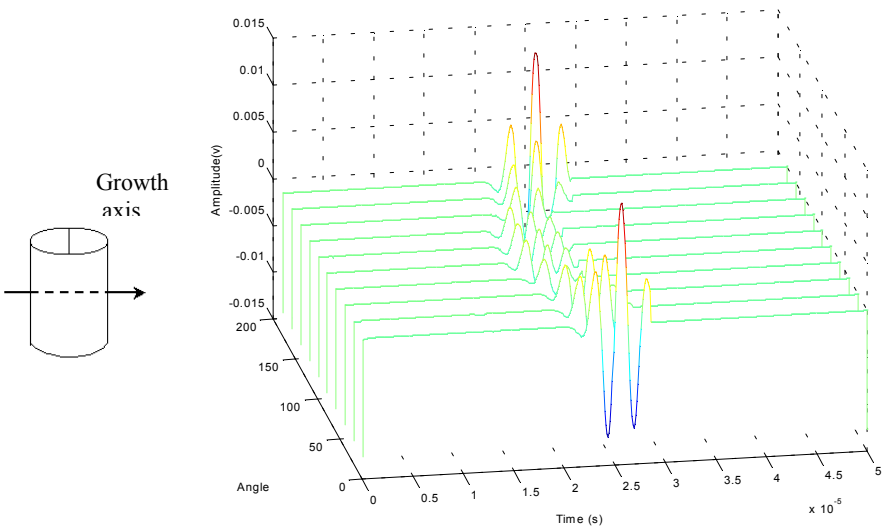

(a)

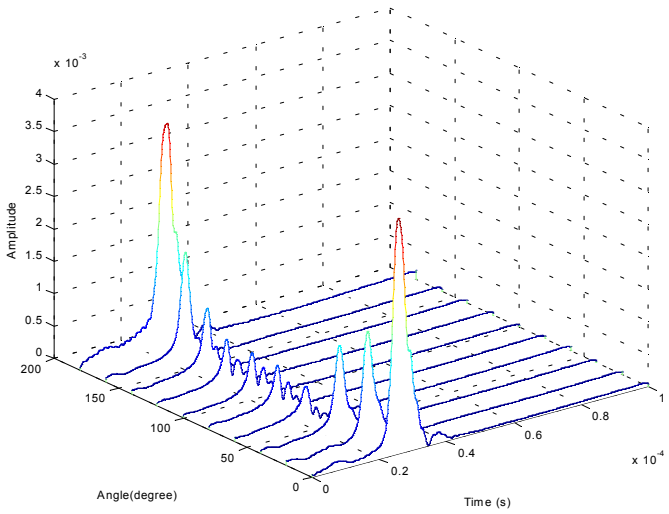

(b)

Figure 6.22 Fast wave variations with angle and the corresponding impulse responses with original density in rotating sample approach for Sample 7. (a) Waveforms; (b) Magnitude of the analytic signal

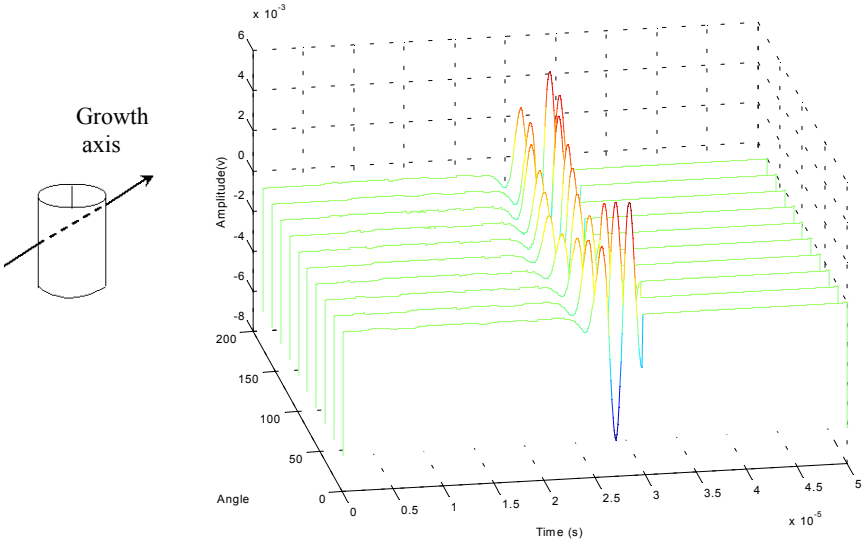

(a)

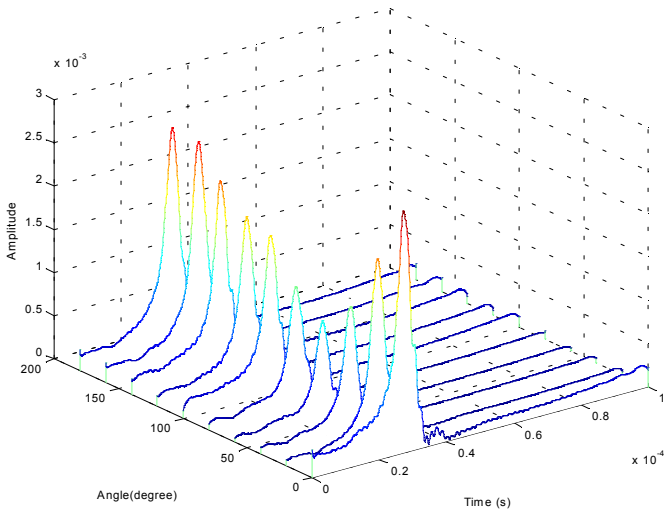

(b)

Figure 6.23 Fast wave variations with angle and the corresponding impulse responses with original density in rotating sample approach for Sample 8. (a) Waveforms; (b) Magnitude of the analytic signal

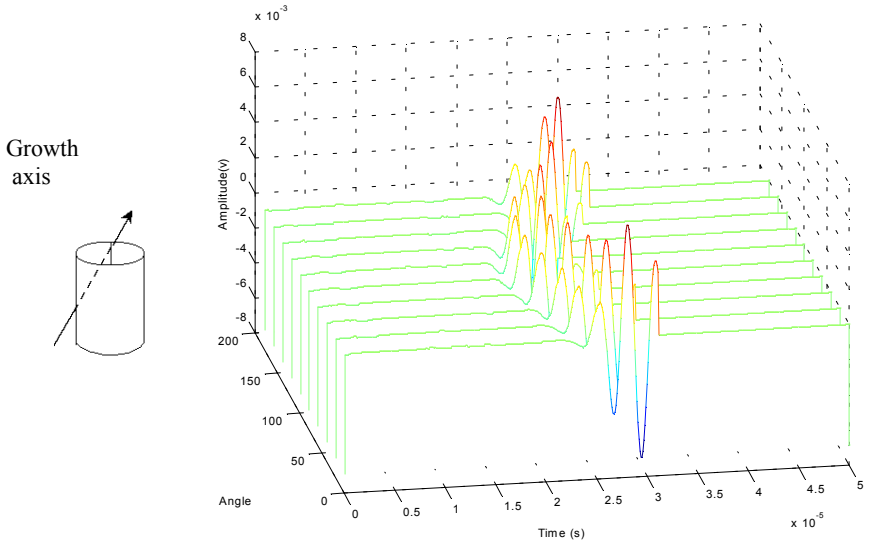

(a)

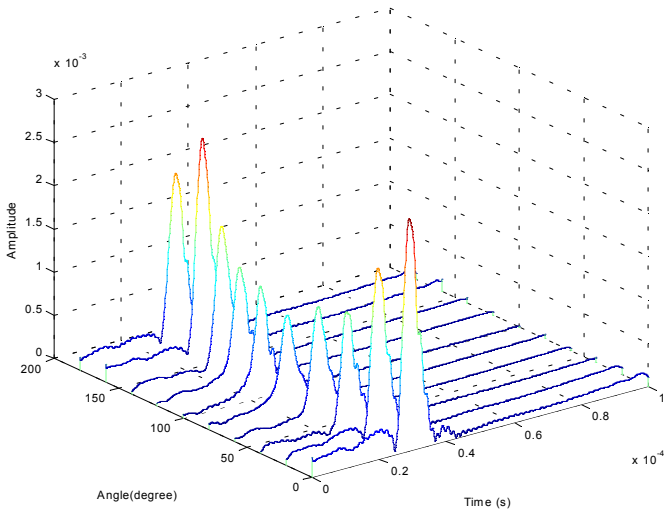

(b)

Figure 6.24 Fast wave variations with angle and the corresponding impulse responses with original density in rotating sample approach for Sample 9. (a) Waveforms; (b) Magnitude of the analytic signal

For better comparison, Figure 6.25 shows the peak amplitude of the analytic signal of the impulse responses as a function of angle for 9 coral samples at original density. The corresponding growth axis and the average value of the impulse response function are illustrated beside the figures.

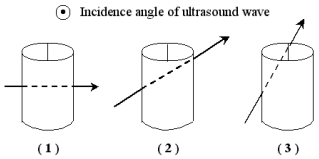

Average:

Sample 1: 0.00109532
Sample 2: 0.00088209
Sample 3: 0.00217082

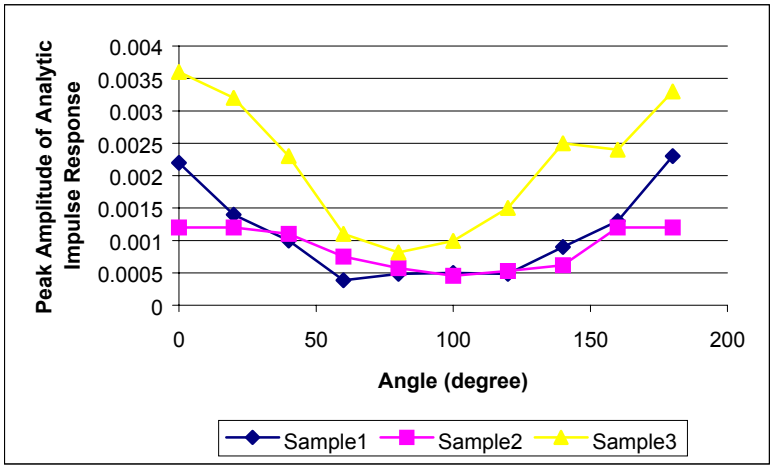

(a)

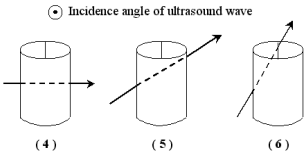

Average:

Sample 4: 0.00111649
Sample 5: 0.0018845
Sample 6: 0.0011111

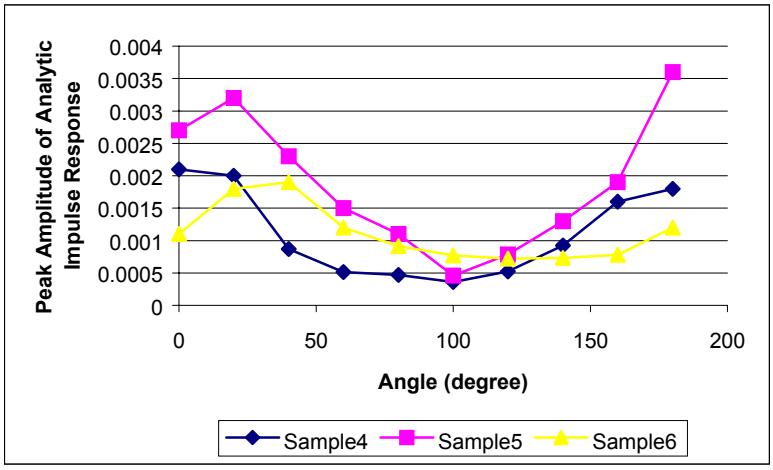

(b)

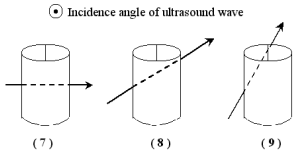

Average:

Sample 7: 0.0015202
Sample 8: 0.00199
Sample 9: 0.00162

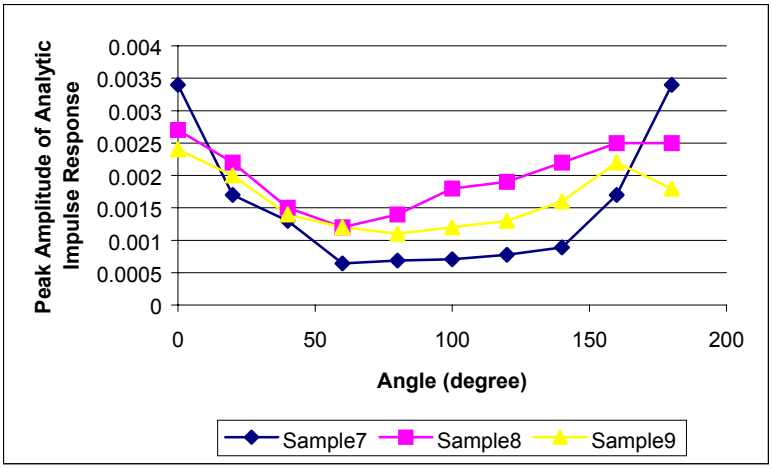

(c)

Figure 6.25 Results for the fast waves of all 9 coral samples at original density: peak amplitude of the analytic impulse responses as a function of angle

After the coral samples have been lightly decalcified, the periodic characteristics of fast signal waveforms and the corresponding analytic impulse responses changed. Figure 6.26 (a) shows the analytic signal of the impulse responses for sample 4, 5 and 6, and Figure 6.26 (b) shows the analytic signal of the impulse responses for sample 7, 8 and 9 after light decalcification.

For sample 4 and 7, the periodic patterns are opposite (180^o out of phase) to their patterns of original density, while for sample 5, 6, 8 and 9, the periodic pattern disappear.

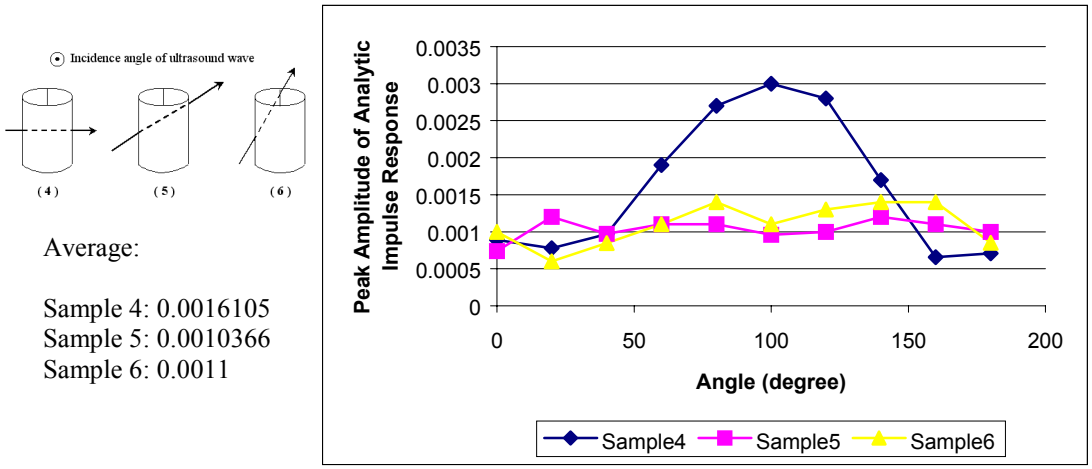

(a)

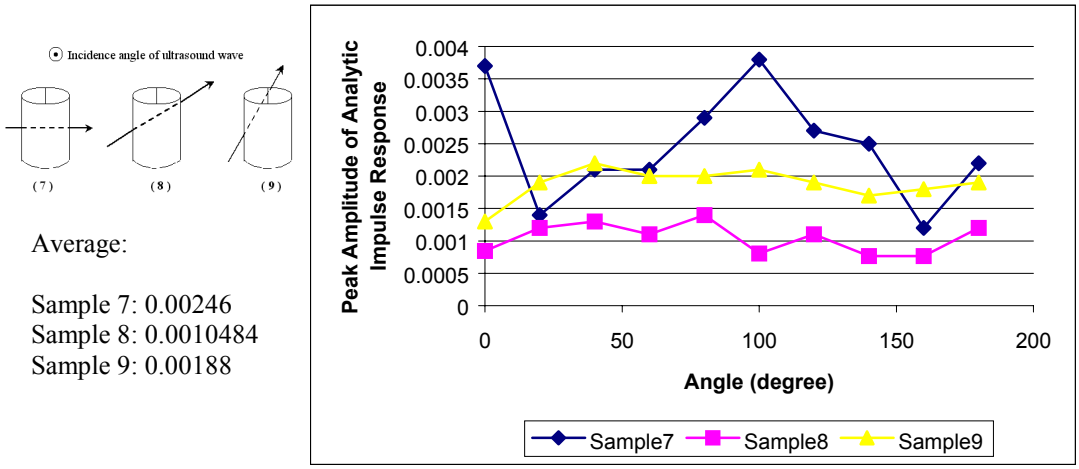

(b)

Figure 6.26 Results for the fast waves of 6 coral samples after light decalcification: peak amplitude of the analytic impulse responses as a function of angle

2. Slow Wave Analytic Impulse Response

From measurements of the coral sample impulse responses for slow wave and their corresponding analyticimpulse response, we did not observe periodic variation. Due

to the overlap of fast wave and slow wave after heavy decalcification, it is only possible to show the figures of slow wave analytic impulse response peak value variation with angle for all 9 coral samples at original density in Figure 6.27, and for the 6 samples (sample 4 to sample 9) after light decalcification in Figure 6.28.

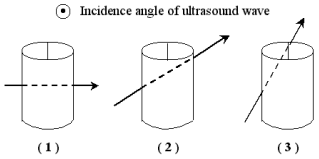

Average:

Sample 1: 0.0016039
Sample 2: 0.00168
Sample 3: 0.0012689

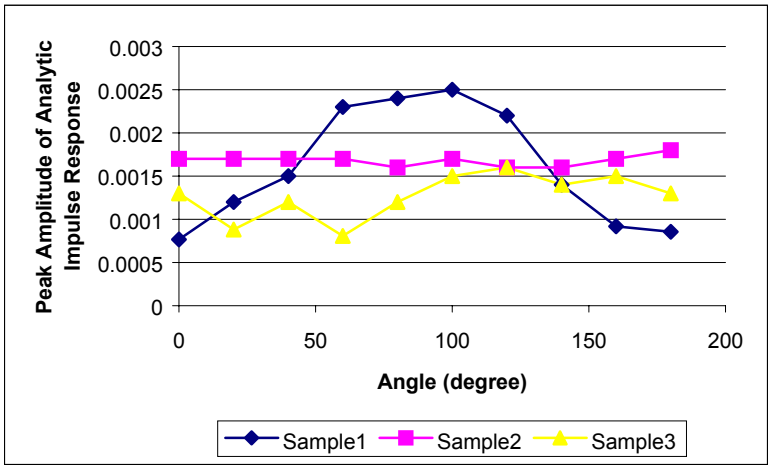

(a)

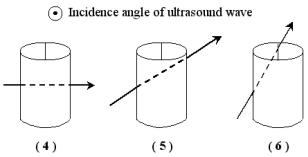

Average:

Sample 4: 0.0008854
Sample 5: 0.0011207
Sample 6: 0.0011

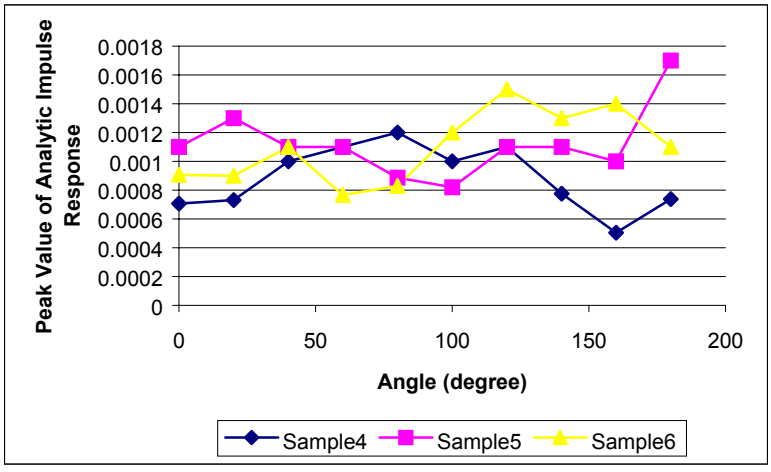

(b)

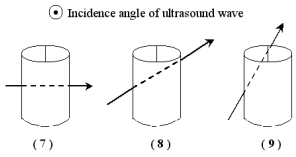

Average:

Sample 7: 0.0011157
Sample 8: 0.0010586
Sample 9: 0.0011817

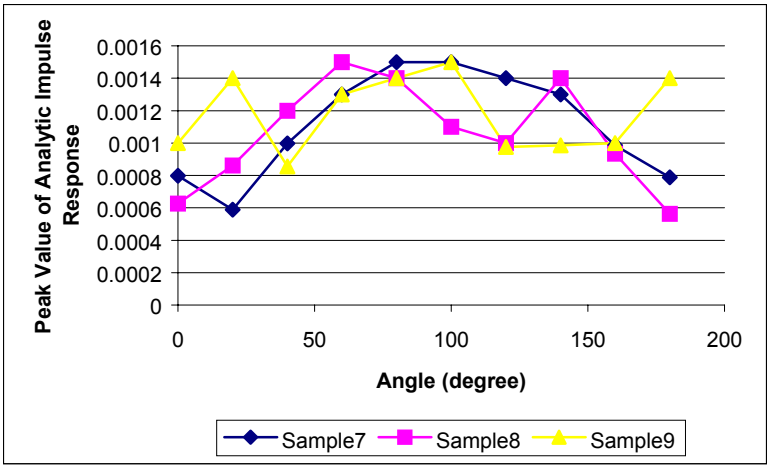

(c)

Figure 6.27 Results for the slow waves of all 9 coral samples at original density: peak amplitude of the analytic impulse responses with angle

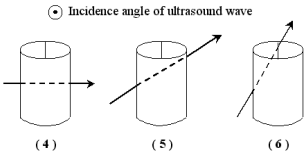

Average:

Sample 4: 0.0014913
Sample 5: 0.0008781
Sample 6: 0.0009987

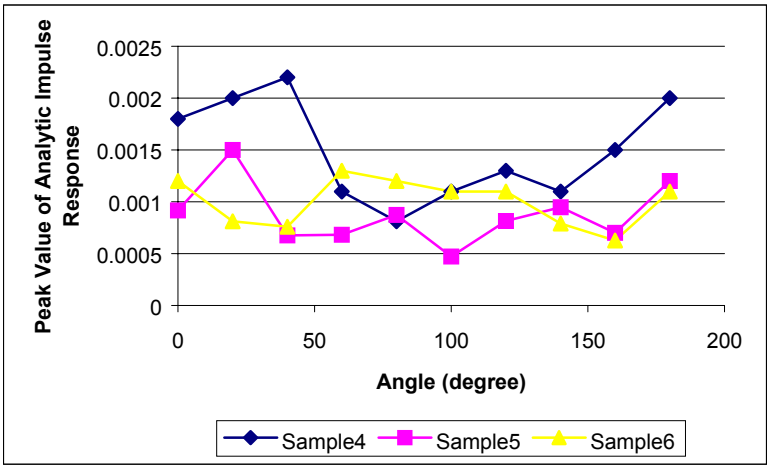

(a)

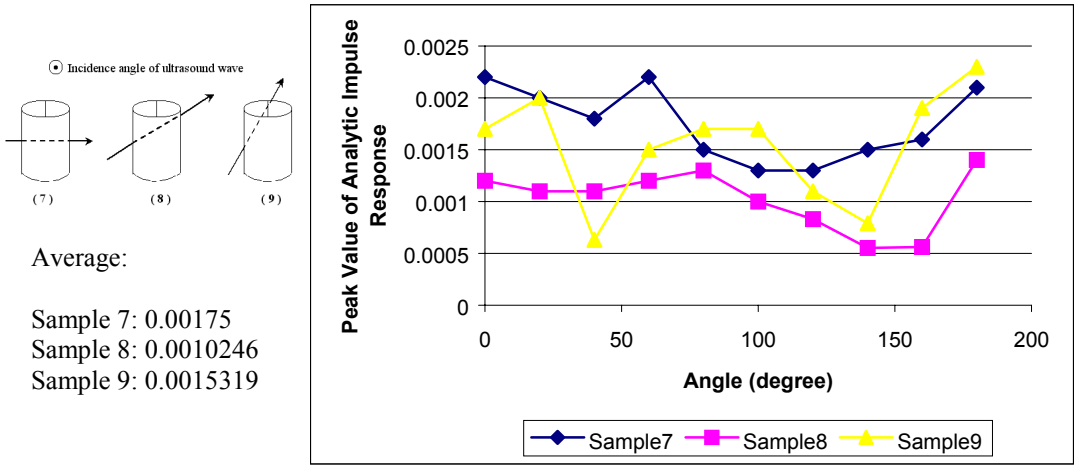

(b)

Figure 6.28 Results for the slow waves of 6 coral samples after decalcification: peak amplitude of the analytic impulse responses with angle

3. Entire signal Analytic Impulse Response

When fast and slow wave overlap after heavy decalcification, there is no alternative but to process the entire signal. Figure 6.29 to Figure 6.31 below show the variation of the peak value as a function of angle for the analytic signal of the impulse response, for the entire signal when the coral samples are at different densities.

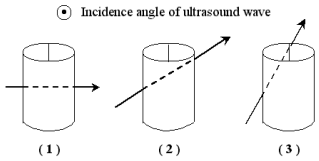

Average:

Sample 1: 0.00207
Sample 2: 0.00155
Sample 3: 0.00174

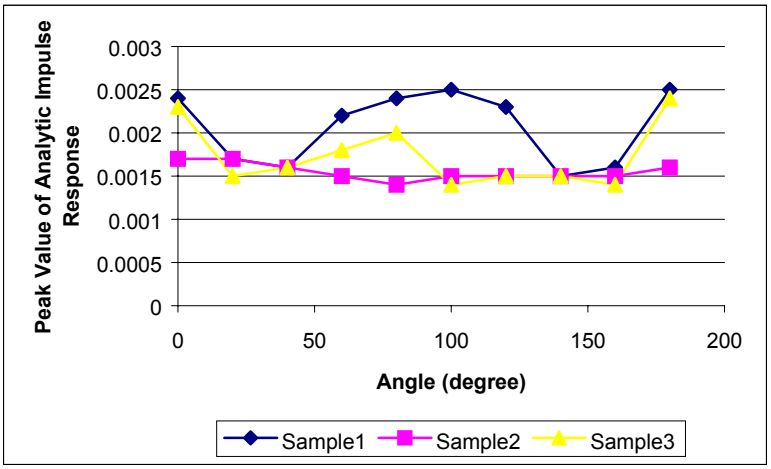

(a)

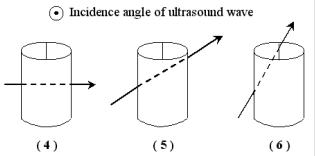

Average:

Sample 4: 0.00153
Sample 5: 0.0016272
Sample 6: 0.0012712

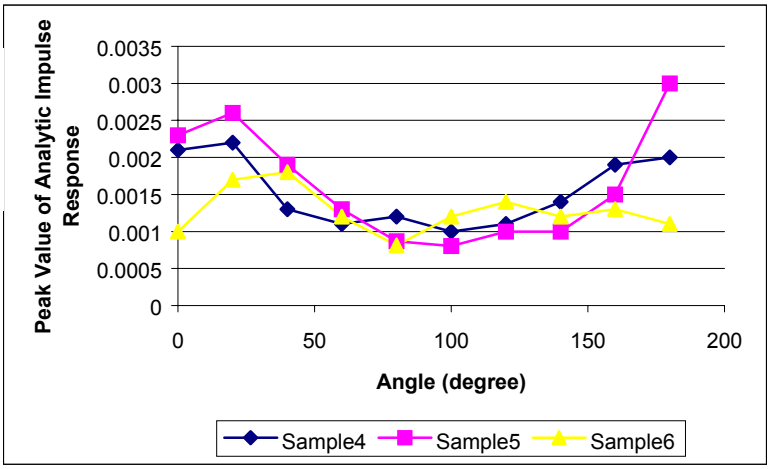

(b)

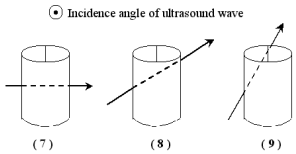

Average:

Sample 7: 0.002
Sample 8: 0.00195
Sample 9: 0.00154

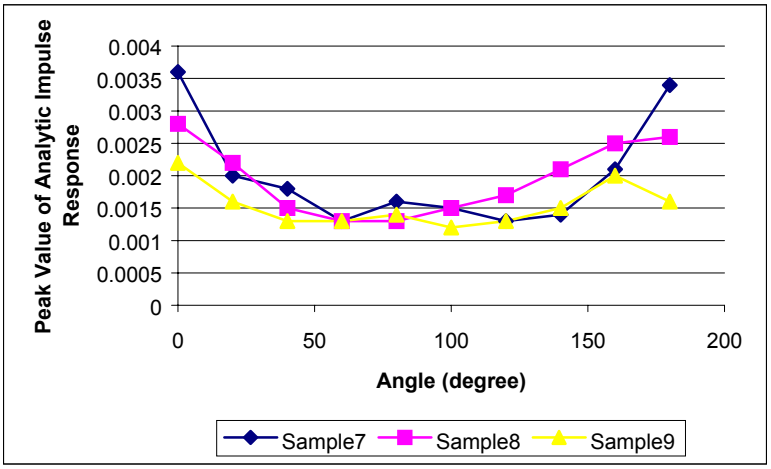

(c)

Figure 6.29 Results for the entire signal of all 9 coral samples at original density: peak amplitude of the analytic impulse responses with angle

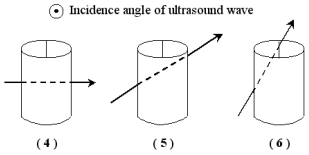

Average:

Sample 4: 0.00227
Sample 5: 0.0011987
Sample 6: 0.0014362

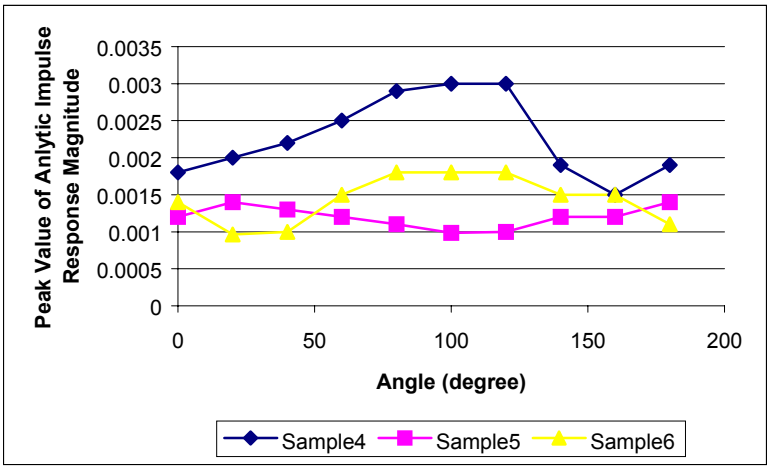

(a)

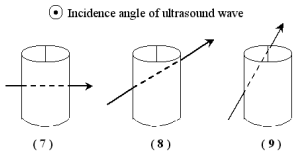

Average:

Sample 7: 0.00267
Sample 8: 0.0013226
Sample 9: 0.00221

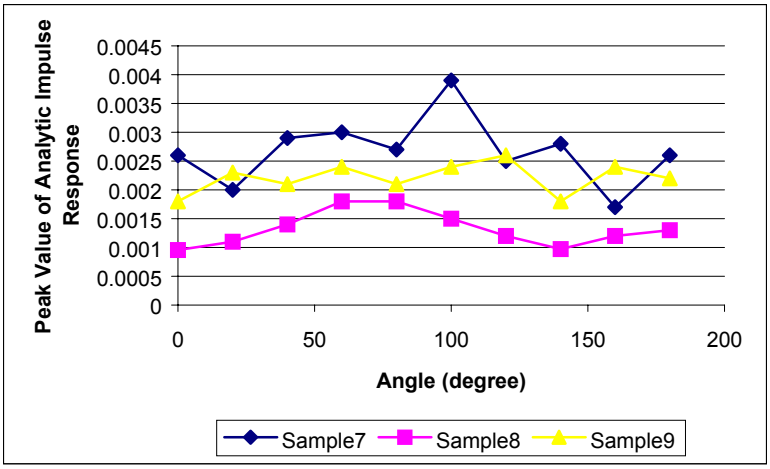

(b)

Figure 6.30 Results for the entire signal of 6 coral samples after light decalcification: peak amplitude of the analytic impulse responses with angle

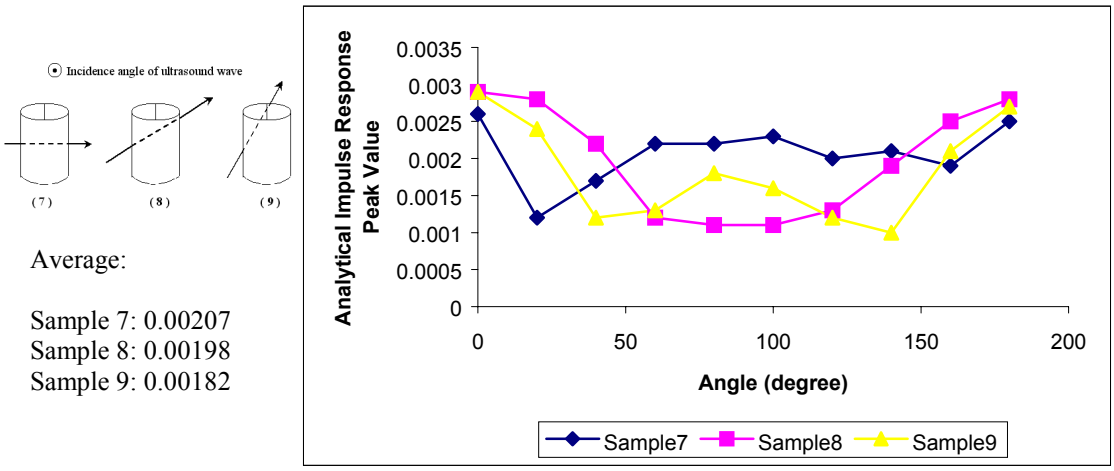

(a)

Figure 6.31 Results for the entire signal of 3 coral samples after heavy decalcification: peak amplitude of the analytic impulse responses with angle

From Figure 6.29 to Figure 6.31 shown above, it is found that when the coral samples are at original density, the peak magnitude of the analytic impulse response of the entire signals have similar periodic patterns as that of the corresponding fast waves, except for sample 1, which has relatively large analytic signal magnitude of the impulse response when the angle is between 50^{o}~140^{o}. However, for the entire signals, after light decalcification, the periodic patterns of the analytic impulse response for all 6 samples disappear, and the periodic patterns are not so apparent after heavy decalcification.

Since the coral sample impulse responses in analytic form are related to wave energy, it is observed that the variation with angle of the entire signal analytic impulse response is affected by both fast wave and slow wave and dominated by the one who has the most energy. Thus, if fast wave has peak amplitude value or energy value larger than that of slow wave, the entire signal and corresponding analytic impulse responses appear to vary similar to fast wave, and vice versa. In other words, the analysis for the entire

signal and its corresponding analytic impulse response is much harder than the analysis for fast and slow wave separately, but some trends can still be observed which are related to a decrease in density.

Next, we try to investigate the relationship between the average magnitude of the analytic impulse responses of the coral samples and their corresponding BMD values; the results are shown in Figure 6.32 (a) (b) and (c). Figure 6.32 (a) shows the relationship for fast wave where it is found that for sample 4 and 7, which have the horizontal growth axis, the average magnitudes of the analytic impulse responses increase after being lightly decalcified. For sample 5 and 8, which have the angle $\theta = 40^{o}$~50^{o} between their growth axes and the measurement plane, the average magnitudes of the analytic impulse responses decrease after being lightly decalcified, and for sample 6 and 9 which have the angles $\theta = 60^{o}$~70^{o} between their growth axes and the measurement plane, the average magnitudes of the analytic impulse responses do not vary significantly.

Figure 6.32 (b) shows the relationship between the average magnitude of the analytic impulse responses of the coral samples for slow waves and the BMD values. Similar correlation to that of fast waves between the average magnitudes of the analytic impulse responses of the coral samples and the corresponding growth axis is also found.

In Figure 6.32 (c), for the entire signal, the average magnitude of the analytic impulse responses of the coral samples 7 and 9 increase after the samples are lightly decalcified and then decrease after the samples are heavily decalcified. However, for sample 8, the average magnitude of the analytic impulse responses decrease after the samples are lightly decalcified and then increase after heavy decalcification.

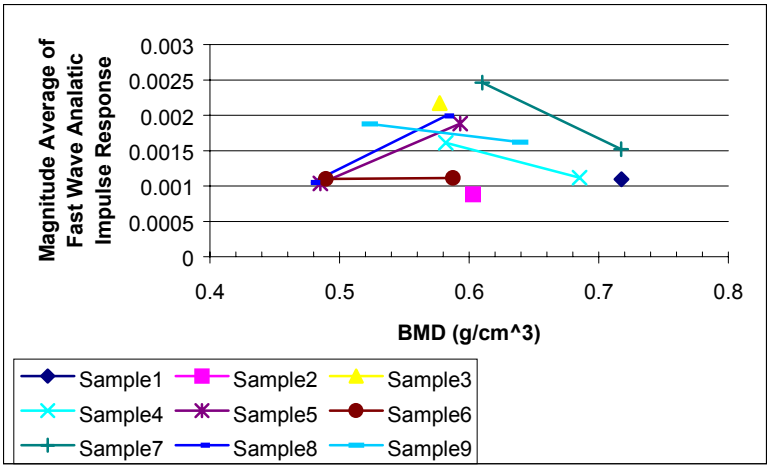

(a)

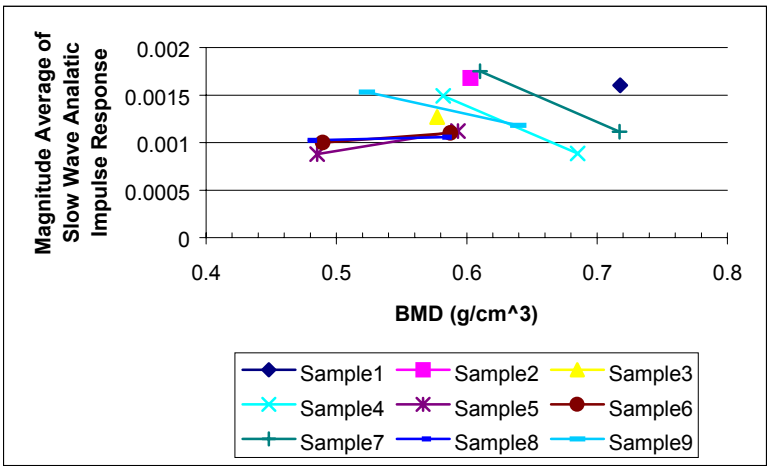

(b)

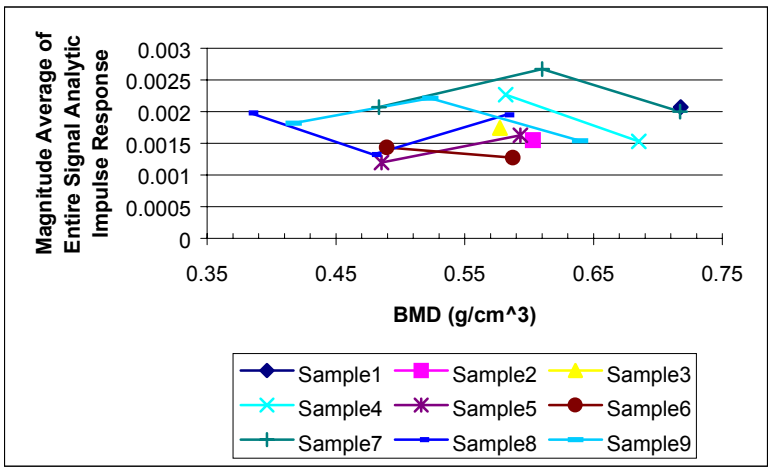

(c)

Figure 6.32 Average magnitude of the analytic impulse response vs. BMD values of the coral samples for (a) fast wave; (b) slow wave; (c) entire signal

6.4.2 Approach of Rotating the Receiving Transducer

The second approach consists of rotating the receiving transducer while its acoustic axis still points towards the coral sample. The received signal and the corresponding analytic impulse response are again analyzed. As it has been stated before, when the rotation angle of the receiving transducer relative to the reference position becomes large, the fast wave and slow wave overlap and the signal becomes much more complex due to the effect of scattering from the coral sample surface. Therefore, only the entire signal is analyzed in this approach.

Before investigating the signal received after propagating through the inhomogeneous coral samples when the receiving transducer is rotated, some calibrations are made to see what the signal would be when the ultrasound wave propagates through some homogeneous media.

Received signal vs. angle using homogeneous plastic sample

Figure 6.33 (a) ~ (c) show the result when the coral sample is replaced by a homogeneous sample with the same dimensions made from plastics. Figure 6.33 (a) shows the entire signal as the function of the rotating angle of the receiving transducer, presented in a 3D format. We can see that the amplitude of ultrasound signal becomes smaller and smaller and the signal arrives earlier and earlier as the receiving transducer rotates from 0^o to 90^o with respect to the wave transmission orientation. This is because less and less of the transmitting signal reaches the transducer as the receiving transducer is rotated and moved further and further away from the wave propagation path. And since the direct path between the receiving transducer and the transmitting transducer is reduced, the path between the two transducers becomes slightly shorter, which makes the

arrival time of the received signal earlier. Figure 6.33 (b) shows the corresponding analytic impulse response for the received signal where it is seen that the amplitude decreases as the angle increases. To make it much simpler to view, the peak analytic impulse response amplitude as a function of angle is plotted in Figure 6.33 (c).

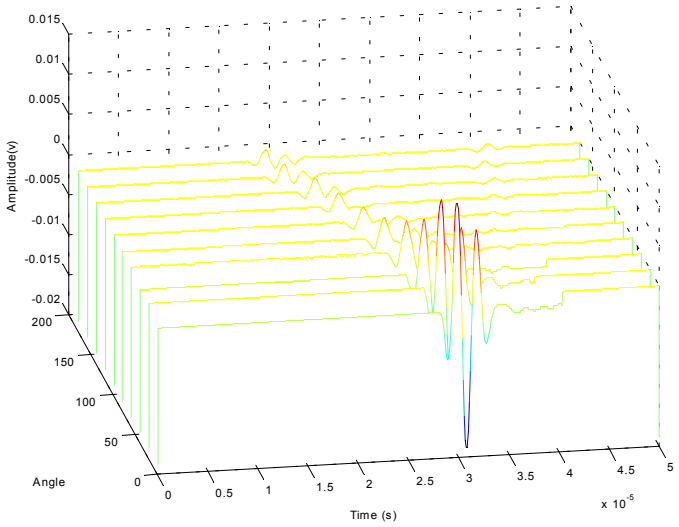

(a)

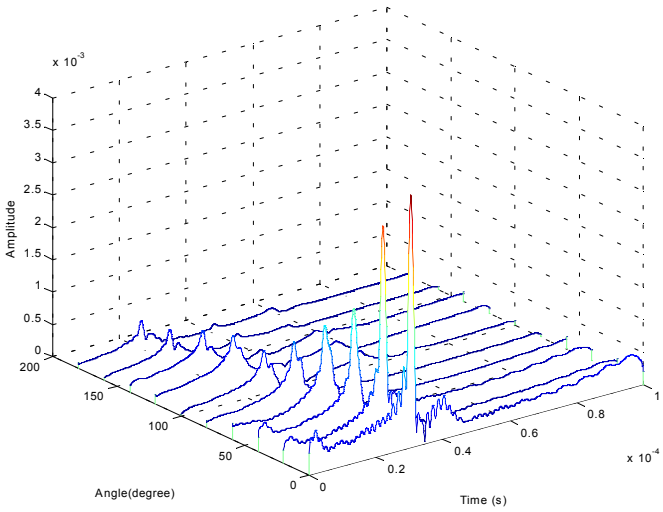

(b)

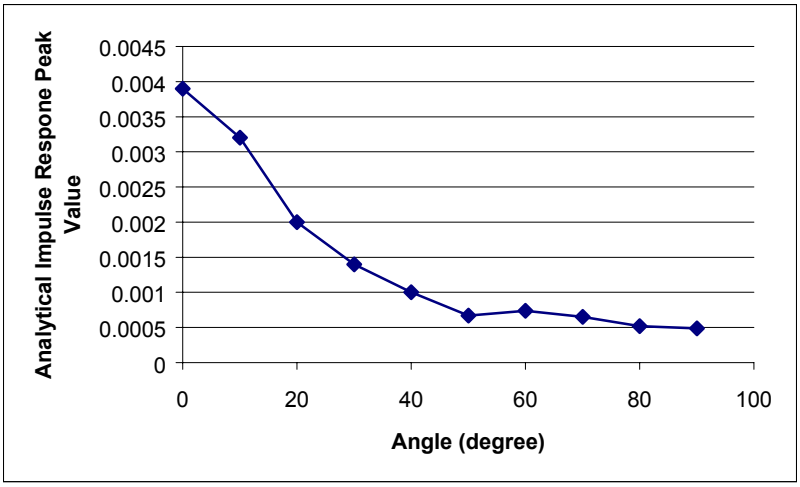

(c)

Figure 6. 33 (a) Received signal from homogeneous plastics sample in rotating transducer approach; (b) corresponding analytic impulse response; (c) variation in amplitude of analytic impulse response with angle.

Received signal vs angle using amplitude of the pure water

For an alternative comparison, the peak amplitude of the analytic impulse response as a function of angle for water is plotted in Figure 6.34. It can be seen that the peak amplitude of the analytic impulse response of water decreases faster than that of the homogenous plastic sample. Such result is what we expected since there is no scattering of the incident ultrasound pulse with only water between the two transducers.

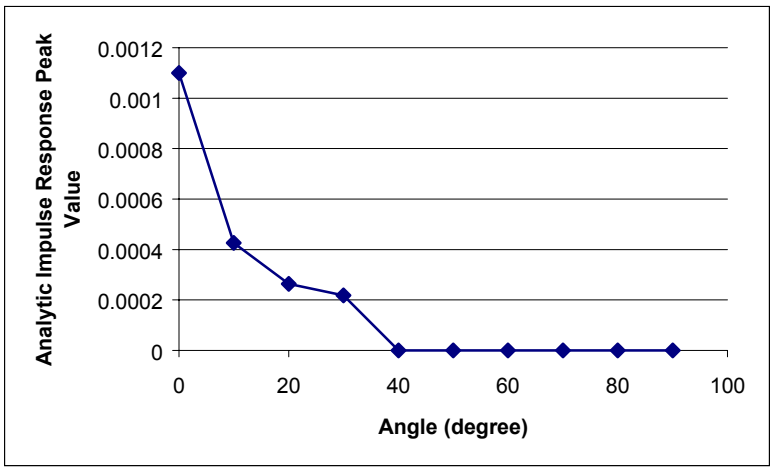

Figure 6.34 Peak analytic impulse response value variation with angle for water

Analysis of the Coral Sample

Now that we have observed what the signal would be for a homogeneous sample or for a homogeneous medium, we will next investigate the received signal for the coral samples. The coral samples are oriented at the 0^o with respect to their reference angle. Figure 6.35 (a), (b) and (c) shows the peak amplitude of the received signal when all 9 coral samples are at original density. Figure 6.36 (a), (b) and (c) show the peak amplitude of the corresponding analytic impulse responses for the coral samples.

It is observed that relatively large amplitude signals are received when the angle of rotating receiving transducer is at around 20^o~30^o and when the angle is larger than 60^o. Due to the cylinder shape of the coral samples, it is believed that the signal received when the angle is less than 60^o is primarily due to the signal transmitted through the sample, while the large amplitude signal when the angle is large than 60^o is primarily due to scattering from the coral sample surface.

With just one exception, the peak amplitude of the received signal reaches its maximum value when the rotation of angle is around 20^o~30^o and then decreases as the receiving transducer is rotated further and further away from the straight wave transmission path. However, when the angle is larger than 60^o, the peak amplitude again increases because the increased scattering signal of coral sample from surface compensates for the decreased signal amplitude.

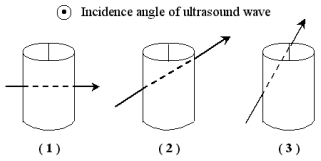

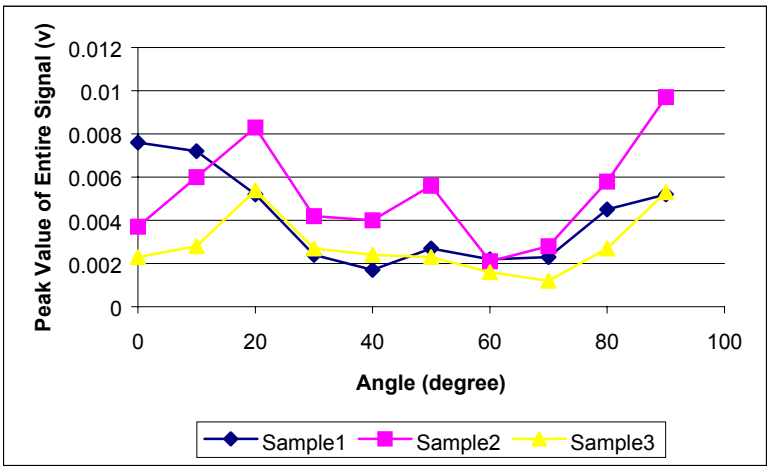

(a)

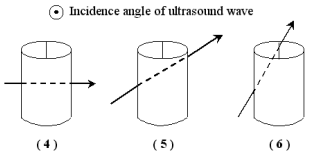

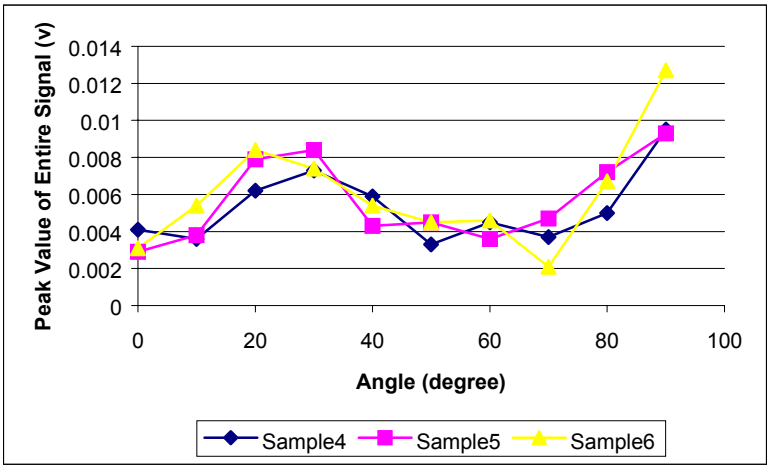

(b)

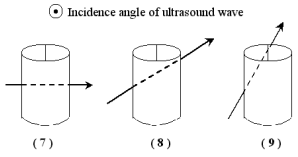

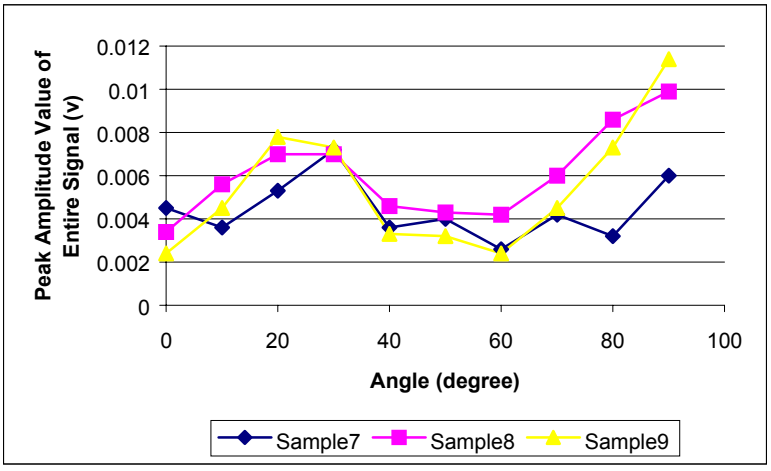

(c)

Figure 6.35 Results for all 9 coral samples at original density as a function of angle of rotation for the receiving transducer: peak amplitude variation with angles of received signal

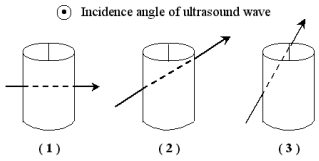

Average:

Sample 1: 0.0018408
Sample 2: 0.00321
Sample 3: 0.0016873

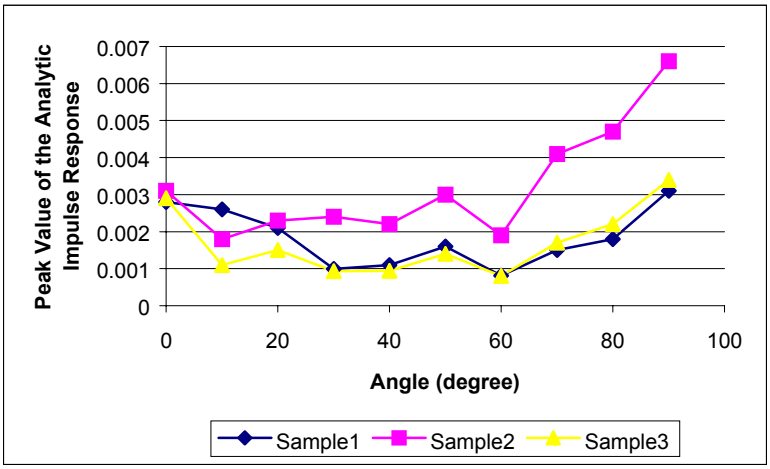

(a)

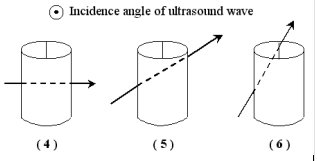

Average:

Sample 4: 0.00261
Sample 5: 0.00278
Sample 6: 0.00294

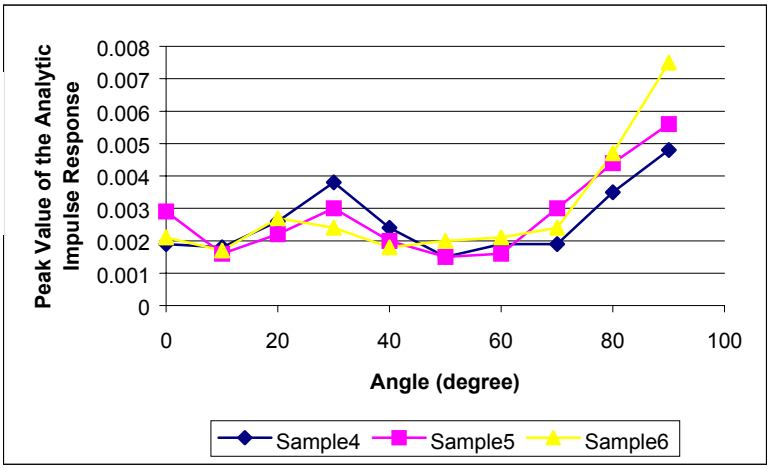

(b)

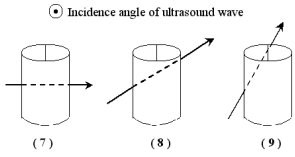

Average:

Sample 7: 0.00235
Sample 8: 0.00284
Sample 9: 0.00248

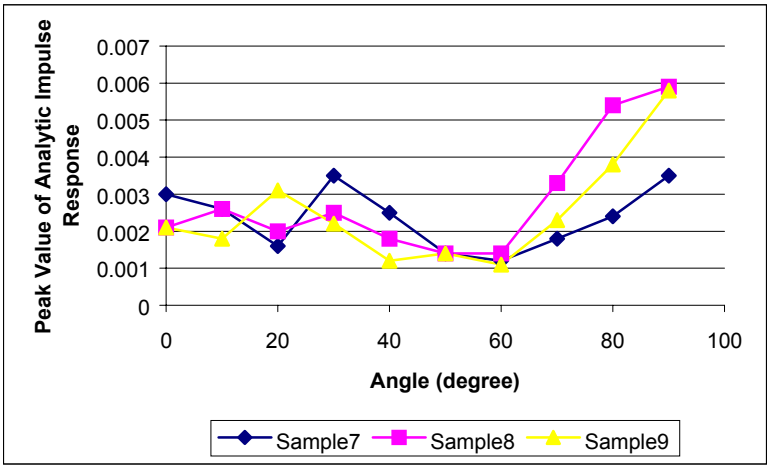

(c)

Figure 6.36 Results for all 9 coral samples at original density as a function of angle of rotation for the receiving transducer: peak amplitude of the analytic impulse response as a function of angle

From Figure 6.36, it can be seen that the peak values of the analytic impulse responses are smaller when the rotating angle of the transducer is less than 60° than when the rotating angle is larger than 60°. No apparent maximum or minimum value is found when the angle is less than 60°, which means the signal energy does not vary significantly in this angle range.

Figure 6.37 shows the peak values of the signal amplitude. The peak values of the signal amplitudes still have relatively large values at around 20°, but generally, the peak amplitude values are observed to be relatively independent of the angle.

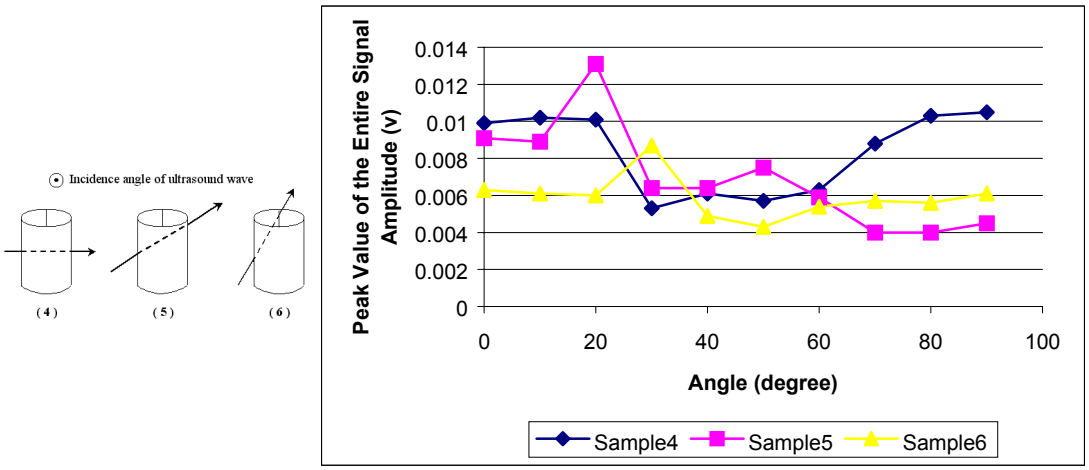

(a)

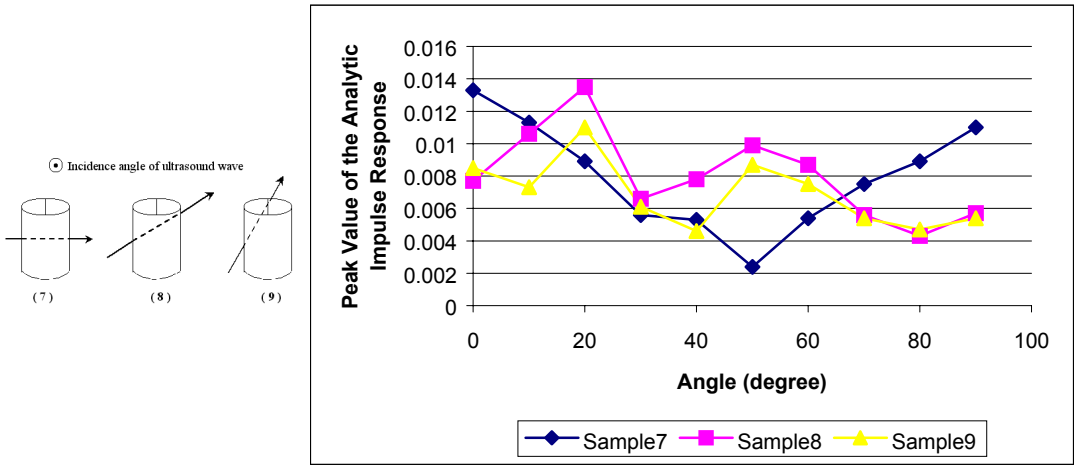

(b)

Figure 6.37 Results for 6 coral samples after light decalcification in the approach of rotating the receiving transducer: peak amplitude variation with angles of received signal

Figure 6.38 shows the corresponding peak value of the analytic impulse response amplitudes as a function of angle for coral samples after light decalcification. The peak amplitude value of the corresponding analytic impulse response has a variation similar to that of the received signal which was shown in Figure 6.37.

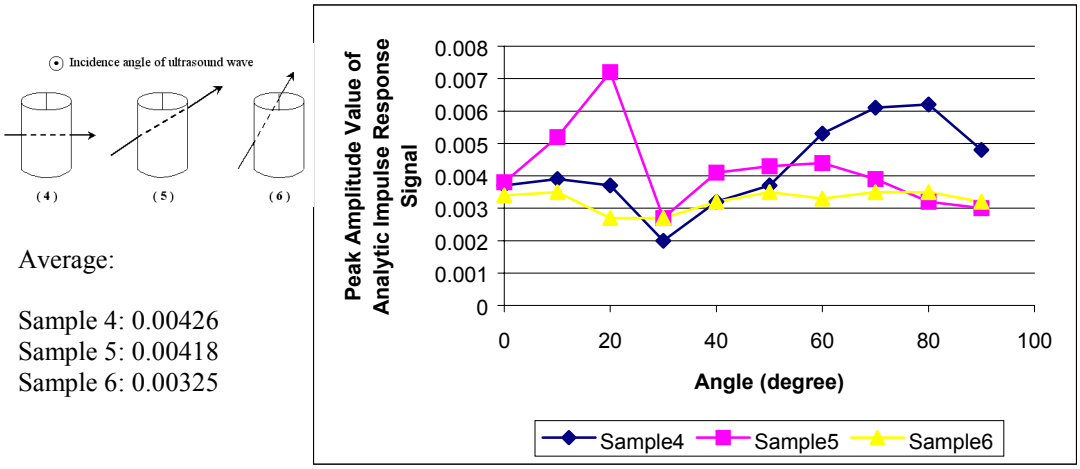

(a)

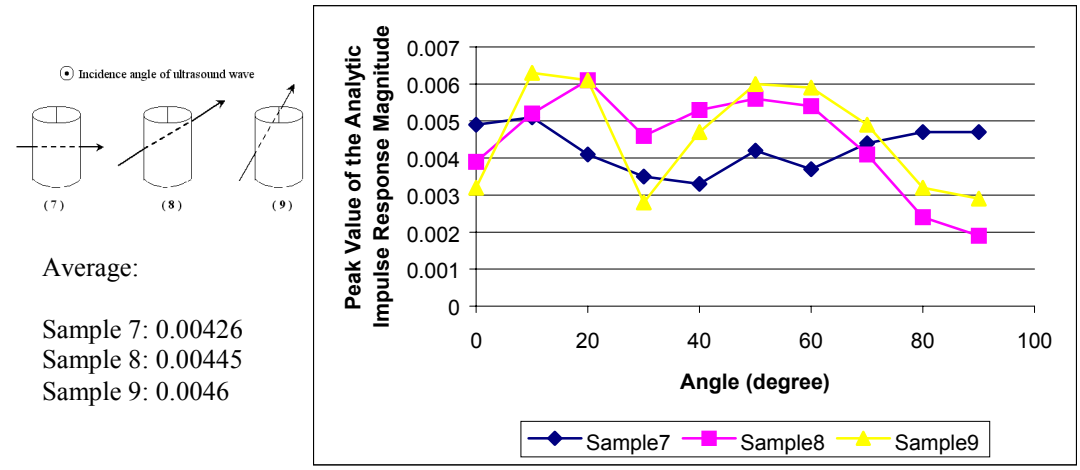

(b)

Figure 6.38 Results for 6 coral samples after light decalcification in the approach of rotating the receiving transducer: peak amplitude of the analytic impulse response as a function of angle

Figure 6.39 shows the peak amplitude values of the signals and of their corresponding analytic impulse response, as a function of angle for coral samples after heavy decalcification. The peak amplitude values of the signals still have the relatively

large values at around 20°~30°, but the peak values of the signals become smaller than before when the angle is larger than 60°.

However, the peak amplitude value of the corresponding analytic impulse response increases when the angle is larger than 60°, as shown in Figure 6.36 (b), which means that the energy of the scattering signal increases although the peak amplitude value decrease. We assume this to be the case because the duration of the received signal actually is observed to be longer after the coral samples are heavily decalcified.

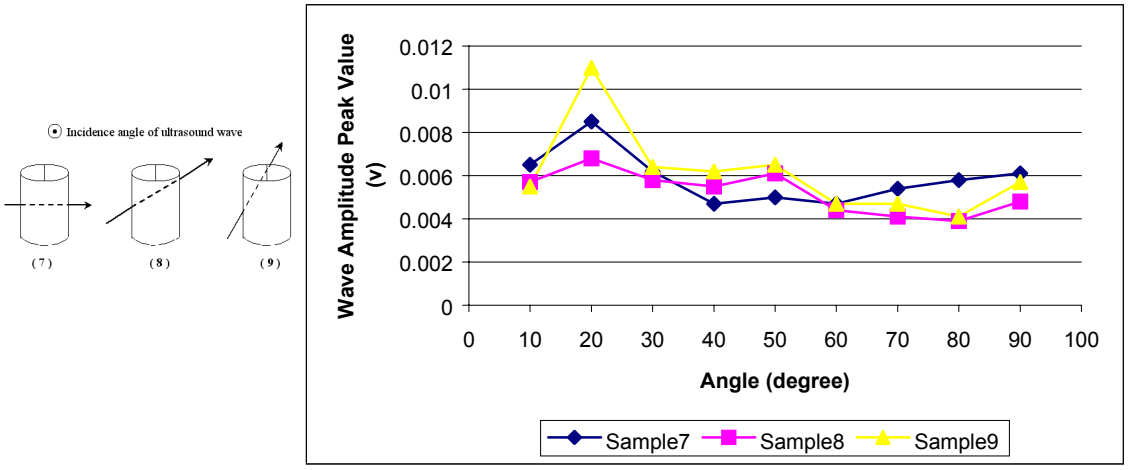

(a)

Average:

Sample 7: 0.00369
Sample 8: 0.00315
Sample 9: 0.00352

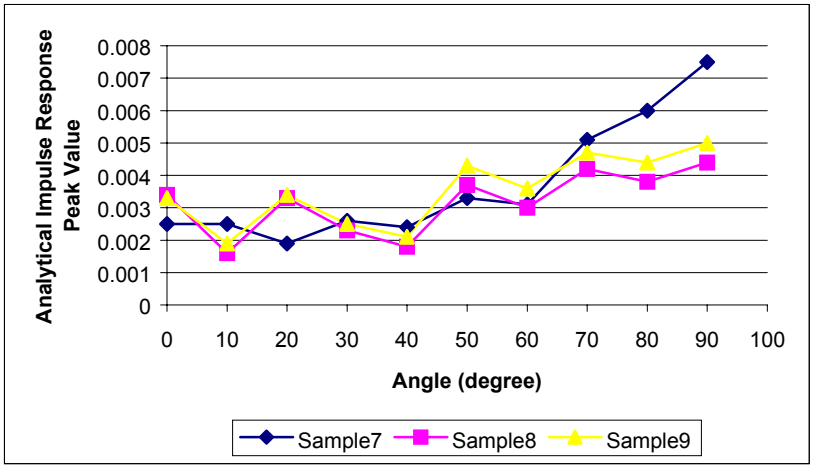

(b)

Figure 6.39 Results for 3 coral samples after heavy decalcification in the approach of rotating the receiving transducer. (a) peak amplitude variation with angles of received signal; (b) peak of the corresponding analytic impulse response magnitude as a function of angle

The variation of analyticimpulse response peak values for the coral samples 7, 8 and 9 as the density is changed is specifically illustrated in Figure 6.40. We can observe that the peak values of the analytic impulse response increase when the coral samples 7, 8 and 9 are lightly decalcified and then decrease after the coral samples are heavily decalcified.

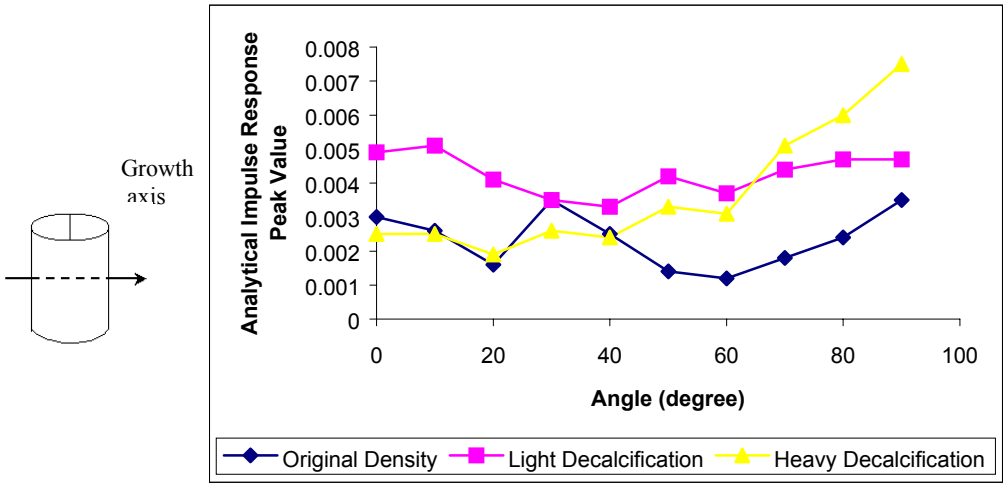

(a)

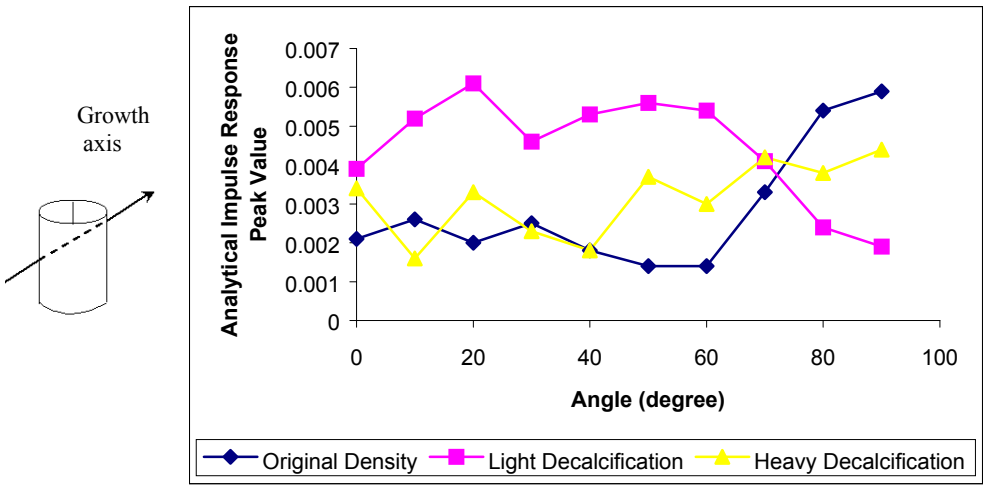

(b)

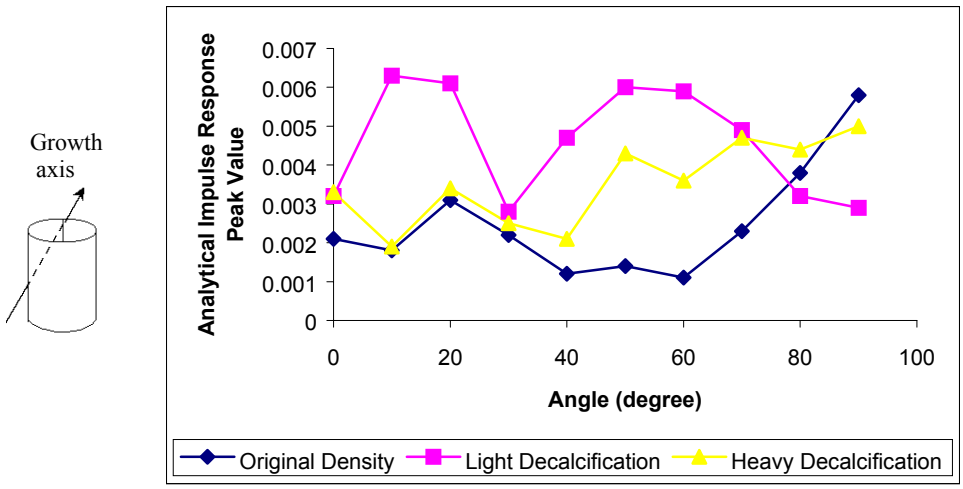

(c)

Figure 6.40 Analytic impulse response peak value variation with angle for different densities of coral samples: (a) sample 7; (b) sample 8; (c) sample 9

The variation with density of the "average" peak value of the analytic impulse response for all the coral samples is plotted in Figure 6.41. The "average" refers to the average over all angles.

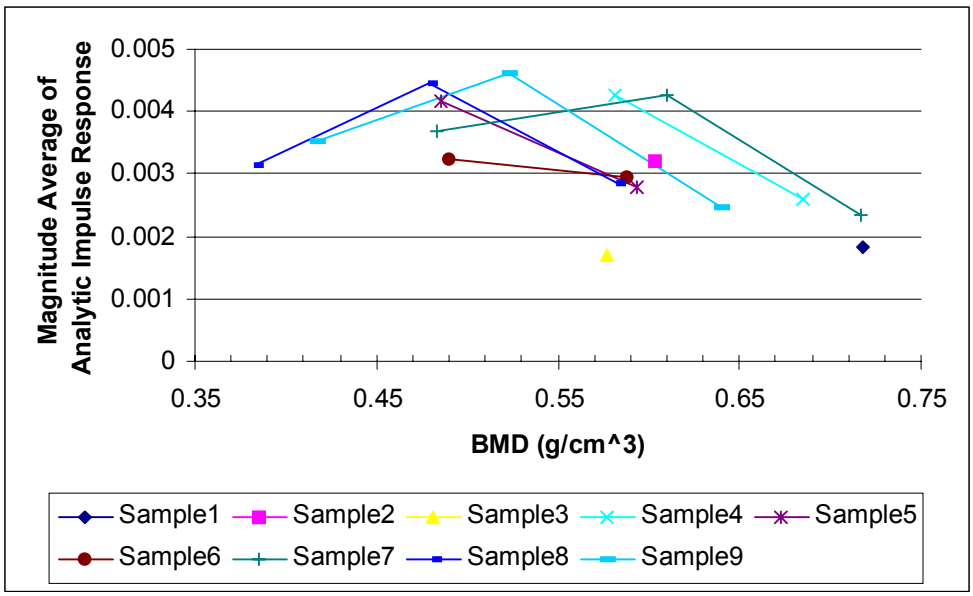

Figure 6.41 Analytic impulse response peak value variation with angle for different densities of all 9 coral samples

It is observed that the variation in the average value of the analytic impulse response as function of the coral sample density has a behavior similar to the BUA behavior, in the sense that initially the amplitude is increasing when going from original density to intermediate density level, but decreasing when going from intermediate density level to the heavy decalcified density level.

For the two measurement approaches, the results obtained when rotating the coral sample are found to be related to both the growth axes and to the densities of the coral samples, while the results obtained when rotating the receiving transducer is found to be related to densities, but barely related with the growth axis of the coral samples. The latter approach has more practical clinical usage, but due to the complex variation of analytic impulse response, it needs additional information to correctly identify the density and structure change or may be used to complement other analysis tools, such as BUA.

Chapter 7

Angular Decorrelation Analysis

7.1 Cross-correlation Theory

For signals that exhibit association, it may be of interest to investigate how strong that association is. The correlation $r_{xy}(\tau)$ between two continuous-time energy signals $x(t)$ and $y(t)$ is a measure of the association strength between them, which is given by

$$r_{xy}(\tau) = \int_{-\infty}^{\infty} x(t)y(t+\tau)dt = \int_{-\infty}^{\infty} x(t-\tau)y(t)dt \qquad (7.1)$$

Generally, the normalized correlation is used to eliminate the dependence of $r_{xy}(\tau)$ on the average values of the two signals. It is defined as

$$r_{xy}(\tau) = \frac{\int_{-\infty}^{\infty} x(t)y(t+\tau)dt}{\sqrt{\int_{-\infty}^{\infty} x(t)^2 dt \int_{-\infty}^{\infty} y(t)^2 dt}} \qquad (7.2)$$

Therefore, the value of the normalized $r_{xy}(\tau)$ cannot exceed 1. In frequency domain, Eq. 7.2 can be written as

$$R_{xy}(\omega) = \frac{X(\omega)Y^*(\omega)}{D} \qquad (7.3)$$

where $X(\omega)$, $Y(\omega)$ and $R_{xy}(\omega)$ are the corresponding Fourier transform of $x(t)$, $y(t)$ and $r_{xy}(\tau)$. $Y^*(\omega)$ represents the conjugation of $Y(\omega)$, and the constant $D = \sqrt{\int_{-\infty}^{\infty} x(t)^2 dt \int_{-\infty}^{\infty} y(t)^2 dt}$ represents the product of the energy of $x(t)$ and $y(t)$ in Eq.7.2.

For a series of changing signals, if a reference signal is preselected, the correlation coefficients between the signals and the reference signal will vary. Thus, the decorrelation technique is used to investigate how the correlation between a sequence of signals and the reference signal changes from signal to signal in the sequence.

In this research work, it is observed that the received signal varies with angle both when the coral sample is rotated and when the receiving transducer is rotated. And it appears that the growth axis and the density of the coral sample are important factors in determining the variation of the received signal and the corresponding ultrasound parameters. Therefore, to investigate how the angle-dependent signals correlate with the reference signal and how the correlation coefficients change as functions of the coral sample growth axis and the coral sample density, has lead to the analysis of the decorrelation between the received signals.

Figure 7.1 is the top view of the experimental set-up for decorrelation analysis. It is similar to the set-up used in the approach of rotating the receiving transducer. But the difference is that the angle range is restricted to be $-35^{o} \sim 35^{o}$ with an angle increment of 5^{o}. That is, when the receiving transducer is at position 1, the corresponding angle is -35^{o}. The angle then increases in steps of 5^{o} until the angle reaches 35^{o}, which is position 15. The reference signal is obtained when the receiving transducer is placed directly opposite to the transmitting transducer which is position 8.

The reason for choosing a relatively small angle variation range is that as the rotation angle of the receiving transducer becomes larger and larger, the received signal becomes more and more dominated by the scattering signal from the coral sample surface

and not too much information relating with the coral sample inner structure will be obtained. Since the angle range is small, a small angle increment is necessary.

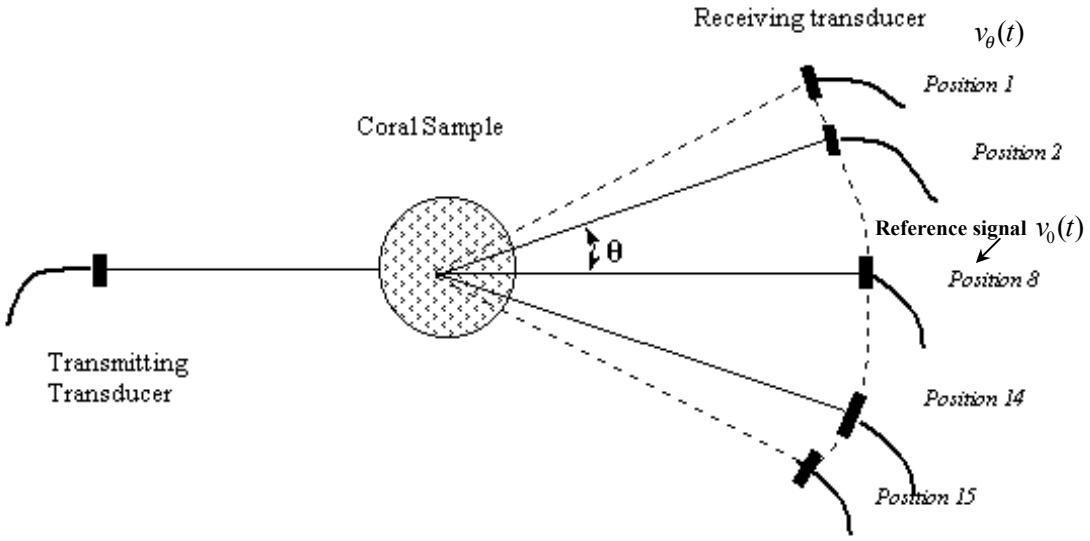

Figure 7.1 Top View of Decorrelation Analysis Experiment Set-up

As illustrated in Figure 7.1, if $v_0(t)$ represents the reference signal, $v_\theta(t)$ is the signal received when receiving transducer is placed at θ position, the correlation coefficient formula by applying Eq. 7.1 can be given as

$$r_\theta(t) = \frac{\int v_0(\tau) v_\theta(t+\tau) d\tau}{\left[\int v_0^2(\tau) d\tau \cdot \int v_\theta^2(\tau) d\tau\right]^{1/2}} \qquad (7.4)$$

where $-35^0 \le \theta \le 35^0$. The integration period is determined by the time length of the signal. If D is used to denote the denominator of Eq. 7.4, the Fourier transform of $r_\theta(t)$ will be

$$R_\theta(\omega) = \frac{V_0(\omega) \cdot V_\theta^*(\omega)}{D} \qquad (7.5)$$

As was stated in Chapter 6, the receiving transducer can only detect the pressure field, while analytic signal depicts the overall energy of the received signal. It is therefore of great interest to analyze the analytic signal corresponding to the $r_\theta(t)$ here as well.

To obtain the analytic signal of the correlation coefficients functions, the corresponding analytic signal of $v_0(t)$ and $v_\theta(t)$ should be first obtained, which are defined in frequency domain as (see Eq. 6.18)

$$\hat{V}_0(\omega) = \begin{cases} 2V_0(\omega), & \omega \geq 0 \\ 0, & \omega < 0 \end{cases} \tag{7.6}$$

$$\hat{V}_\theta(\omega) = \begin{cases} 2V_\theta(\omega), & \omega \geq 0 \\ 0, & \omega < 0 \end{cases} \tag{7.7}$$

That is, the analytic signal only contains the positive frequency component. When substituting Eq. 7.6 and Eq. 7.7 into Eq. 7.5, the analytic signal of the normalized correlation coefficients in frequency domain is then given as

$$\hat{R}_\theta(\omega) = \frac{\hat{V}_0(\omega) \cdot \hat{V}_\theta^*(\omega)}{D} \tag{7.8}$$

Using inverse Fourier transform, we can get $\hat{r}_\theta(t) = ifft(\hat{R}_\theta(\omega))$ in time domain. The decorrelation analysis will be implemented based on the magnitude of $\hat{r}_\theta(t)$.

7.2 Measurement Procedure

The decorrelation technique consists of the following steps:

- Calculate the decorrelation rate for given transducers with no sample present

The decorrelation properties of the received signals may vary with distance to the transducer, and may also be different for different types of transducers [35]. Thus, the correlation coefficients of the receiving transducer at each position needs to be calibrated for the transducer type that is used. For this calibration, there is no sample present, but only water between the transmitting transducer and the receiving transducer.

Figure 7.2 (a) and (b) show the received signals and the peak amplitude values of the corresponding normalized analytic correlation coefficients.

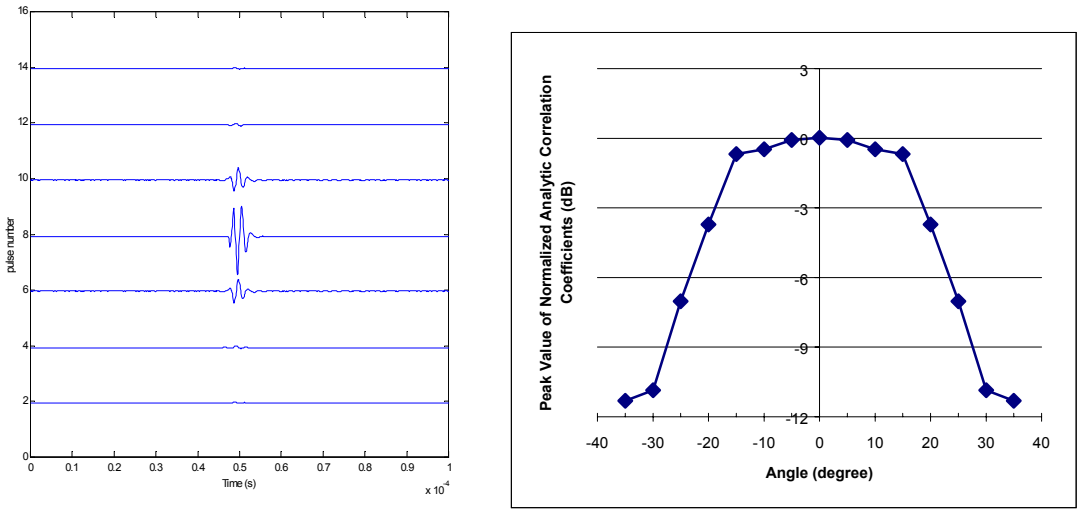

(a) **(b)**

Figure 7.2 (a) Received signal for the calibration of the transducer and (b) peak amplitude of the corresponding normalized analytic correlation coefficient

In Figure 7.2 (a), the signal received at different receiving transducer position is plotted from bottom to top along the "pulse number" axis (due to the space limitations of

the figure, only every other signals are displayed). Therefore, the pulse number indicates the position of the receiving transducer at which the pulse is received. Figure 7.2 (b) illustrates the analytic correlation coefficients between the received signals and the reference signal. It can be seen that both the received signals and the peak amplitude of the normalized correlation coefficients are symmetrical with respect to the reference angle and decrease sharply after the angle $|\theta|>15^{o}$. The peak amplitude of the normalized correlation coefficients when $|\theta| =35^{o}$ are near –12dB.

- Calculate the decorrelation rate for given transducers, using homogeneous sample

The homogenous sample made of plastics with the same dimension as the coral sample is used for additional calibration. The purpose is to use the results of the homogeneous sample as a reference for the results of the inhomogeneous coral sample. Due to the cylindrical shape of the samples that are used, the scattering signal from the sample surface will exist in the received signal when the receiving transducer rotated away from the straight ultrasound wave path. Furthermore, the refracted ultrasound signal will exist in the received signal as well after the ultrasound propagates through the homogeneous sample and then propagates into water again because the sound speed of plastics is different from that of the water. It will be helpful if the decorrelation slope for the effect of the scattering signal and the refraction signal could be observed before the coral samples are measured. The signals received are shown in Figure 7.3 (a) and the corresponding peak amplitudes of the normalized analytic correlation coefficients as a function of angles are shown in Figure 7.3 (b).

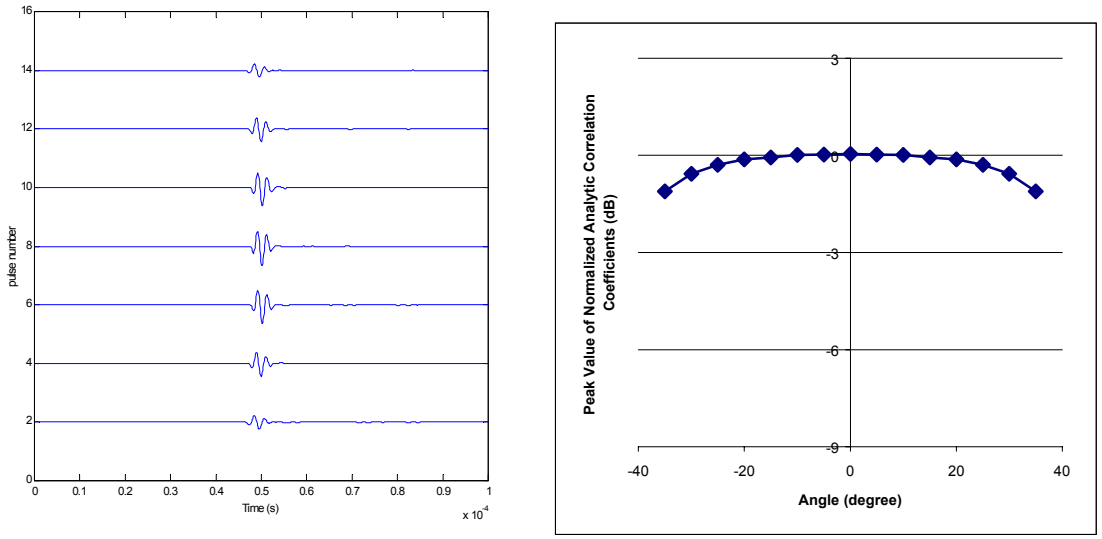

(a) (b)

Figure 7.3 (a) Received signal from homogeneous plastics sample and (b) the peak value of the corresponding normalized analytic correlation coefficient

From Figure 7.3 (a) and (b) above, it can be seen that the received signal amplitude also varies less when the receiving transducer is rotated further and further away from the straight insonifying signal path. However, the speed of the decorrelation is slow. The peak amplitude of the normalized correlation coefficients when $|\theta|$ =35^{o} are about –1.5dB.

- Decorrelation analysis for the coral samples

Angular decorrelation analysis, as discussed above, was carried out for all 9 coral samples at original density, and for 6 of them (sample 4 to sample 9) after light decalcification, and for 3 of them (sample 7 to sample 9) after heavy decalcification. The samples were placed at the 0^{o} with respect to the reference orientation. Results are shown in Figure 7.4 to Figure 7.5 below.

Figure 7.4 (a), (b) and (c) show the peak value of the normalized analytic correlation coefficients in dB for all the 9 coral samples when they are at original density.

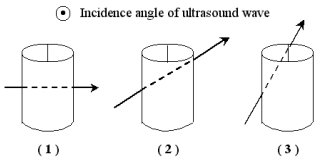

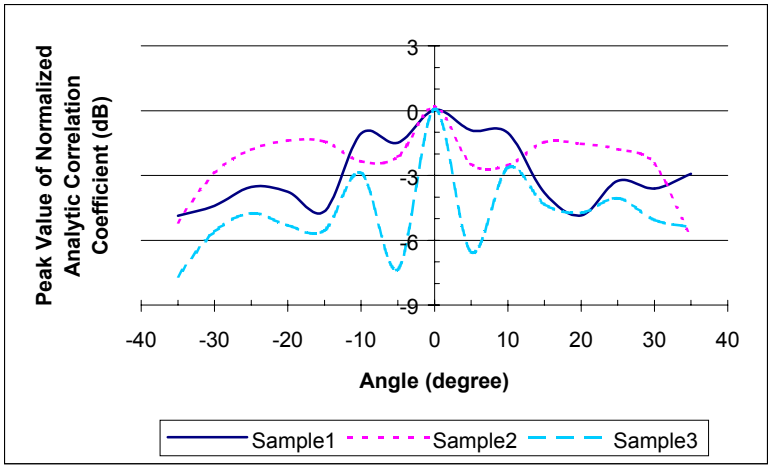

(a)

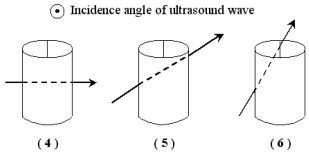

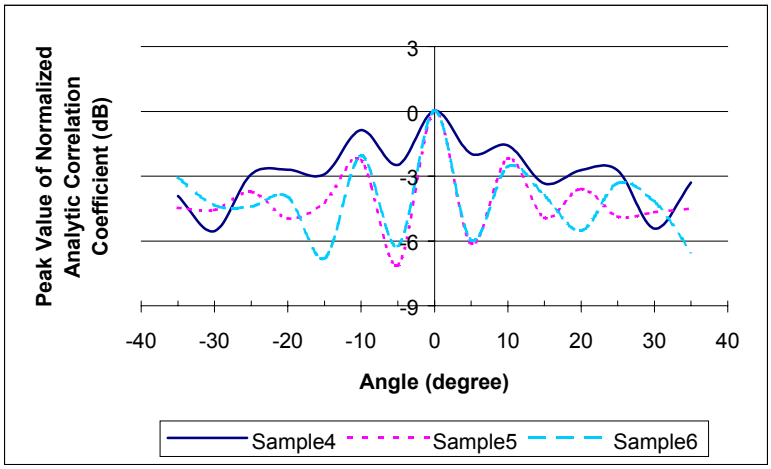

(b)

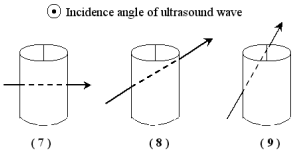

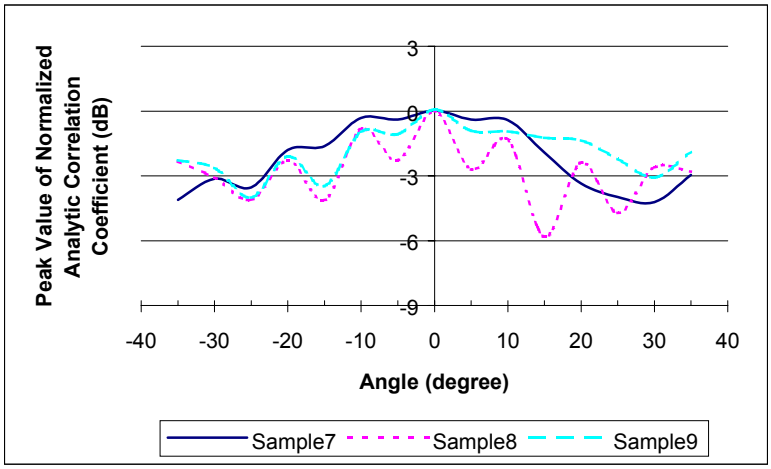

(c)

Figure 7.4 Peak amplitude of the normalized analytic correlation coefficient of 9 coral samples at original density and placed at 0^{o} with respect to the reference orientation

From Figure 7.4, it is observed that the peak amplitude versus angle of the analytic correlation coefficients for the coral samples exhibits a very different pattern from the calibration results obtained with the homogeneous sample. There are many ripples when the correlation coefficients value decrease. It indicates that the received signal varies in a complex way. However, in general, for sample 1, 4 and 7, which have the horizontal growth axes, or growth axis in the measurement plane, the peak amplitudes of the normalized analytic correlation coefficients decorrelate slower with angle than those of the other coral samples. That is, the width at –3dB of the decorrelation curves for sample 1, 4 and 7 are wider than the decorrelation curves for the other samples.

After the coral samples have been lightly decalcified, the peak amplitudes of the normalized analytic correlation coefficients for the coral samples with the 3 different growth axes are very similar and hard to distinguish, as shown in Figure 7.5 (a) and (b).

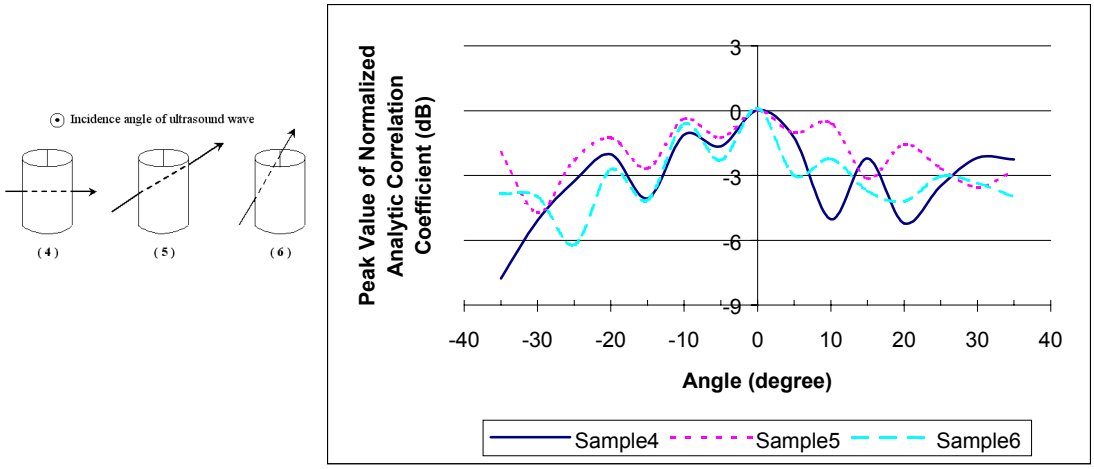

(a)

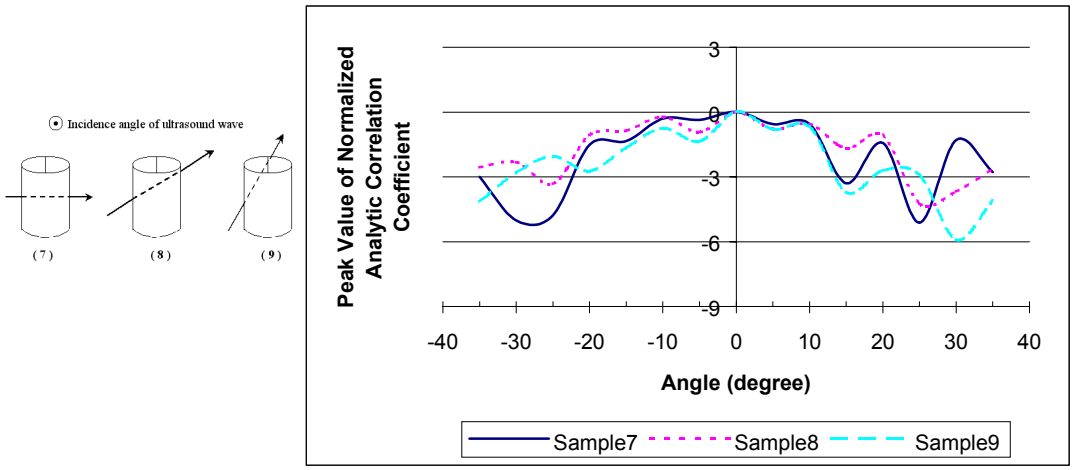

(b)

Figure 7.5 Peak amplitude of the normalized analytic correlation coefficient of 6 coral samples after light decalcification and placed at 0^{o} with respect to the reference orientation

When the coral samples are heavily decalcified, the peak amplitudes of the coral samples 7, 8 and 9 decrease fast again, as shown in Figure 7.6.

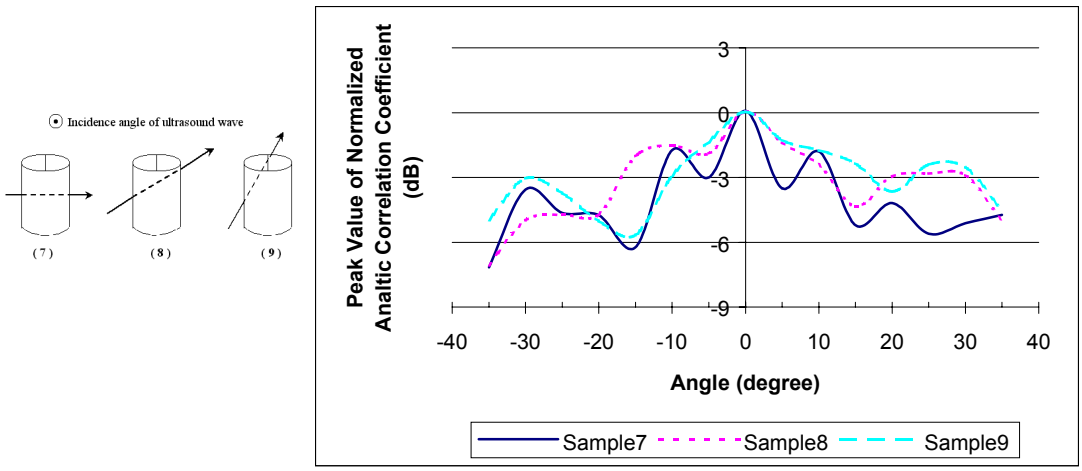

Figure 7.6 Peak amplitude of the normalized analytic correlation coefficient of 3 coral samples after heavy decalcification and placed at 0^o with respect to the reference orientation

To better track the variation of the peak amplitude of the normalized analytic correlation coefficients for the coral samples, Figure 7.7 to Figure 7.12 give a comparison of the decorrelation function with angle at different densities for the coral samples 4 to 9.

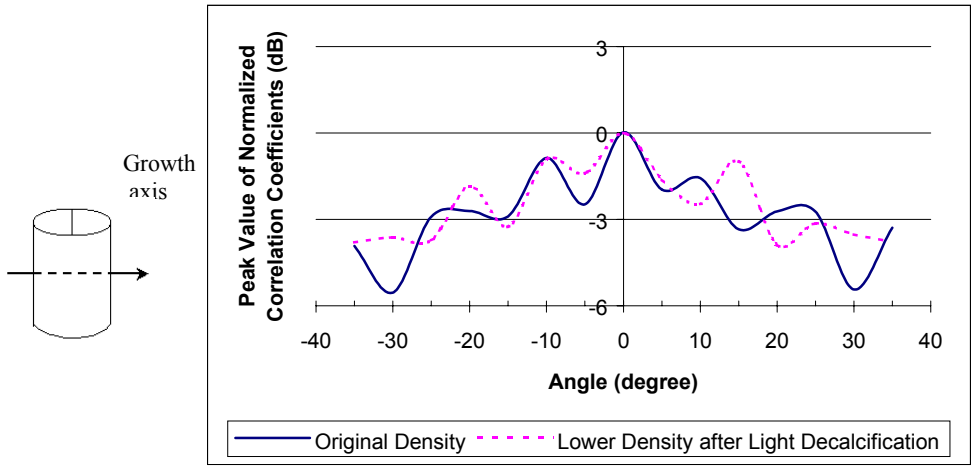

Figure 7.7 Comparison of normalized analytic correlation coefficient with different densities for Sample 4 placed at 0^o with respect to the reference orientation

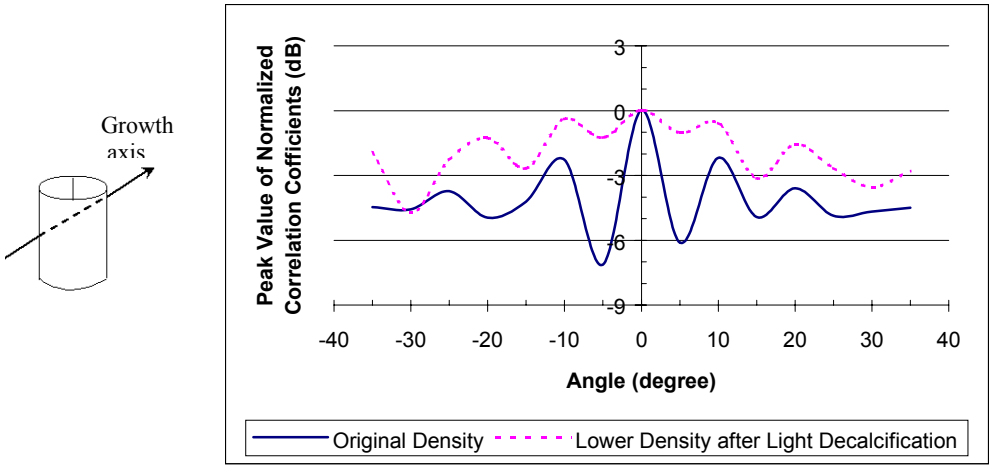

Figure 7.8 Comparison of normalized analytic correlation coefficient with different densities for Sample 5 placed at 0^o with respect to the reference orientation

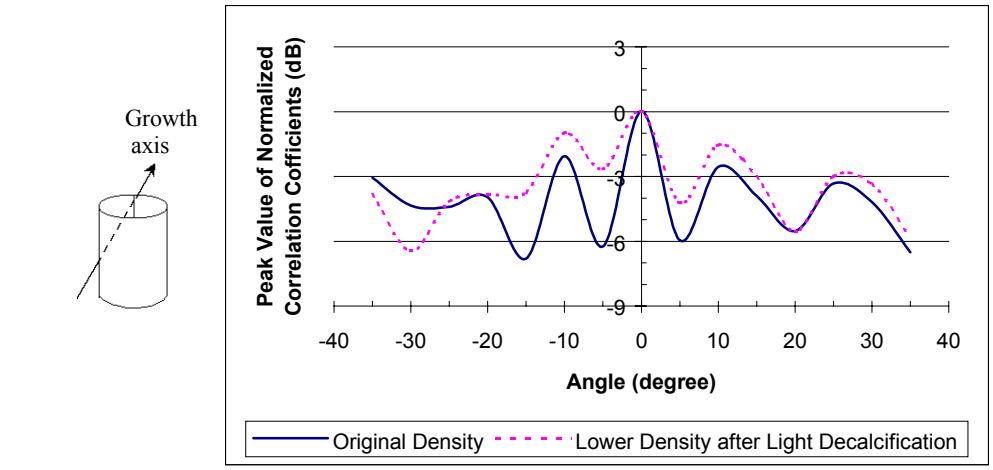

Figure 7.9 Comparison of normalized analytic correlation coefficient with different densities for Sample 6 placed at 0^o with respect to the reference orientation

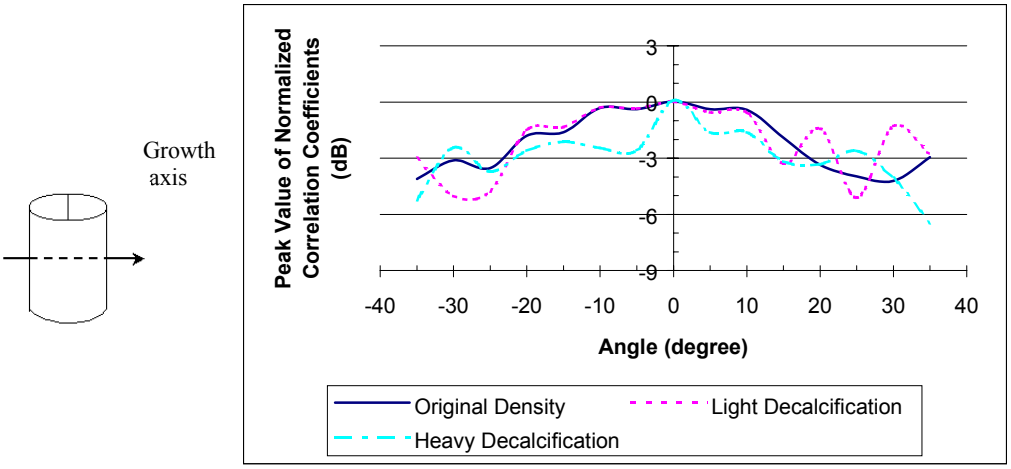

Figure 7.10 Comparison of normalized analytic correlation coefficient with different densities for Sample 7 placed at 0^o with respect to the reference orientation

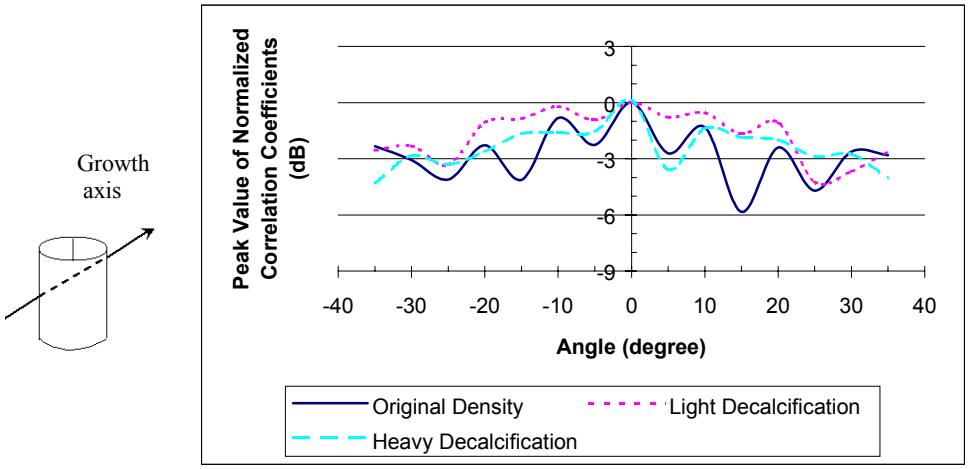

Figure 7.11 Comparison of normalized analytic correlation coefficient with different densities for Sample 8 placed at 0^o with respect to the reference orientation

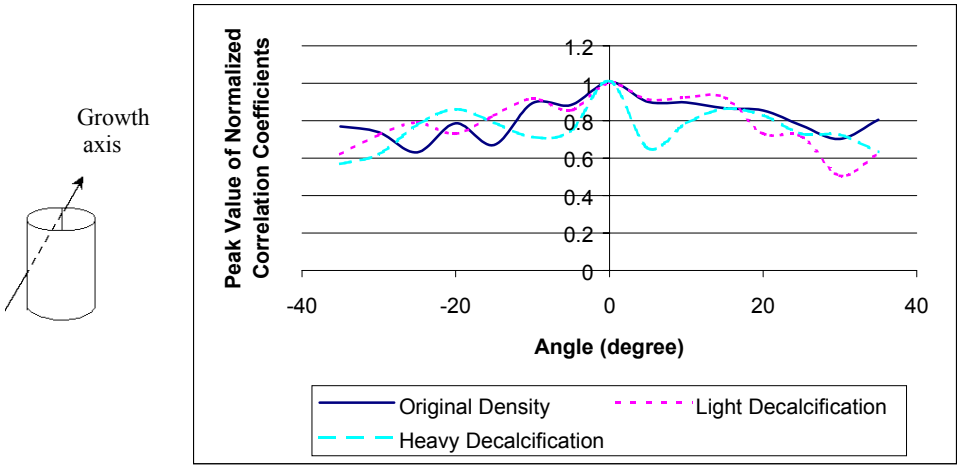

Figure 7.12 Comparison of normalized analytic correlation coefficient with different densities for Sample 9 placed at 0^o with respect to the reference orientation

It can be seen that for sample 4 and 7, there is no apparent changes between the peak values of the normalized correlation coefficients when they are at original density and after they are lightly decalcified. But for coral samples 5, 6, 8 and 9, the decorrelation curves become wider after the samples are lightly decalcified, which means that the signals decorrelate slower. After the coral samples 7, 8 and 9 have been heavily decalcified, however, the decalcification curves for all of them become narrower again.

To compare the effect of different coral sample microstructure orientation on ultrasound signals, we carried out measurements on the coral samples when their reference orientation is changed clockwise 20^o, counter clockwise 20^o, and then counter clockwise 90^o. Figure 7.13 to Figure 7.15 show the comparison of the results at different reference orientations for the coral sample 1 to 3 when they are at original density. In Figure 7.13 to Figure 7.15, "-20^o" represents the clockwise rotation of 20^o, "20^o" represents counter clockwise rotation of 20^o, "90^o" represents counter clockwise rotation of 90^o.

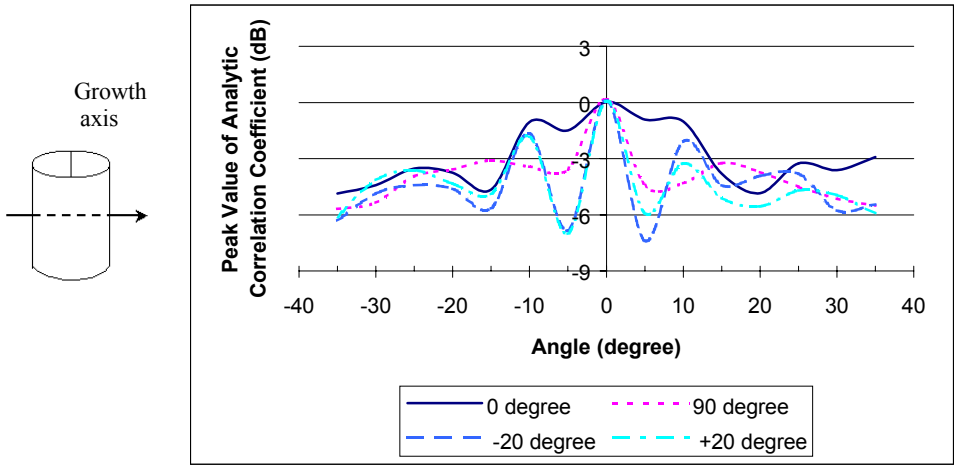

Figure 7.13 Comparison of normalized analytic correlation coefficient with different reference orientation for Sample 1 at original density

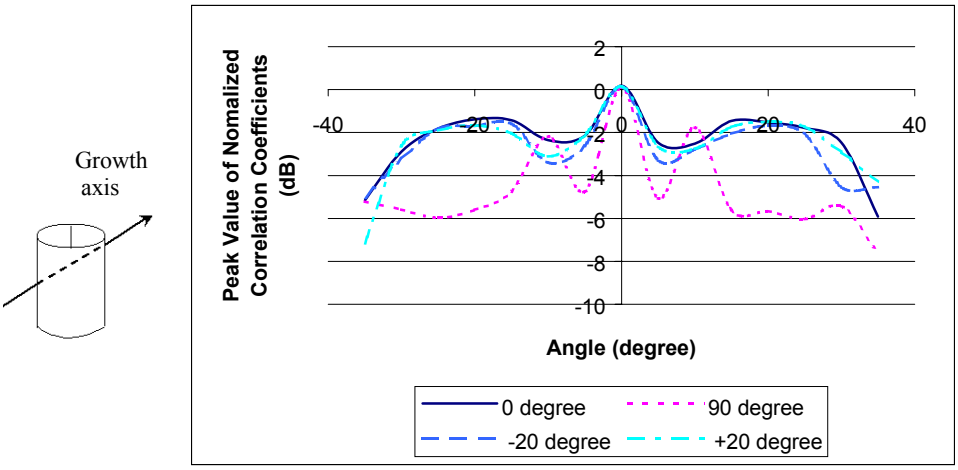

Figure 7.14 Comparison of normalized analytic correlation coefficient with different reference orientation for Sample 2 at original density

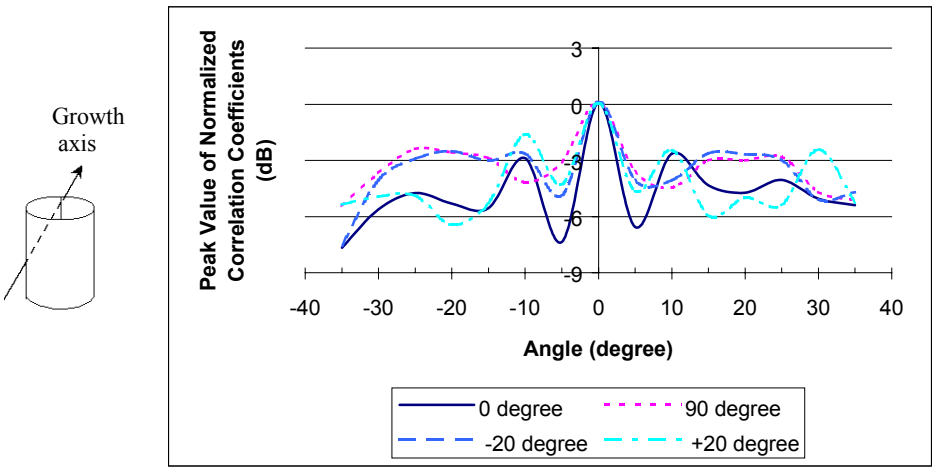

Figure 7.15 Comparison of normalized analytic correlation coefficient with different reference orientation for Sample 3 at original density

Figure 7.16 to Figure 7.18 below show the comparison of the results of different reference orientations for the coral samples 4 to 6 after they are lightly decalcified. Same as in Figure 7.13 to Figure 7.15, "-20^{o}" represents the clockwise 20^{o}, "20^{o}" represents counter clockwise 20^{o}, "90^{o}" represents counter clockwise 90^{o}.

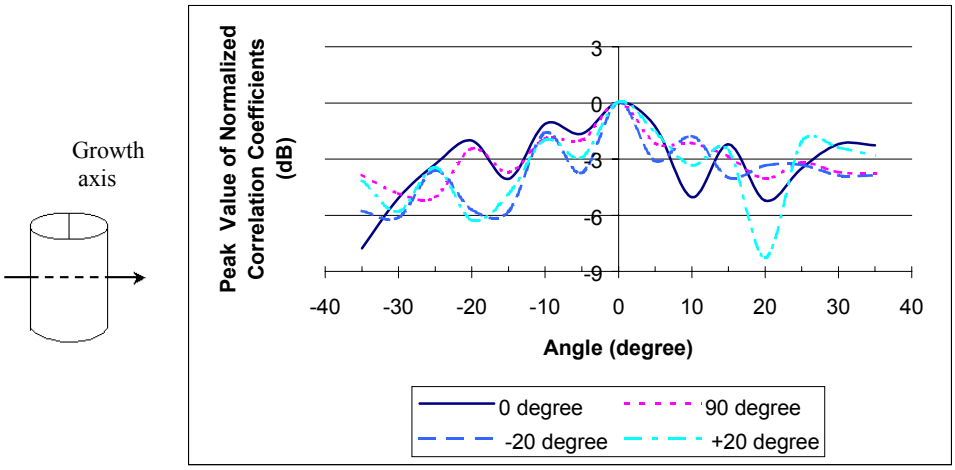

Figure 7.16 Comparison of normalized analytic correlation coefficient with different reference orientation for Sample 4 after lightly decalcification

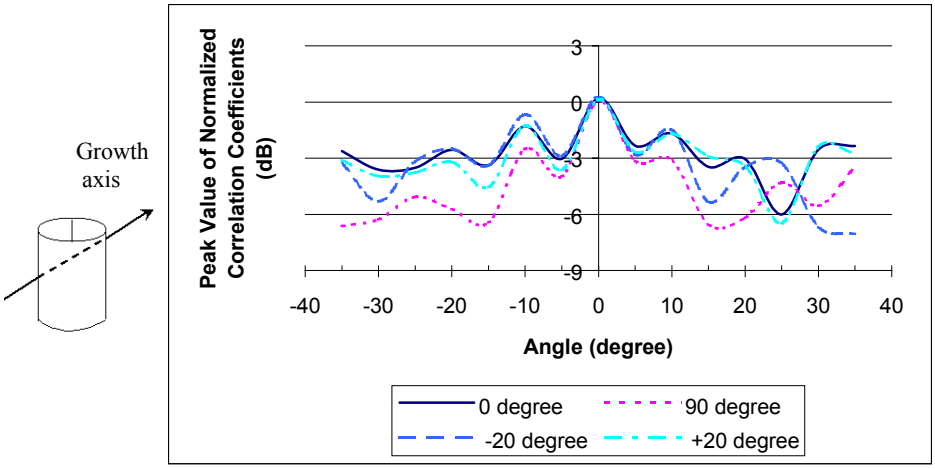

Figure 7.17 Comparison of normalized analytic correlation coefficient with different reference orientation for Sample 5 after light decalcification

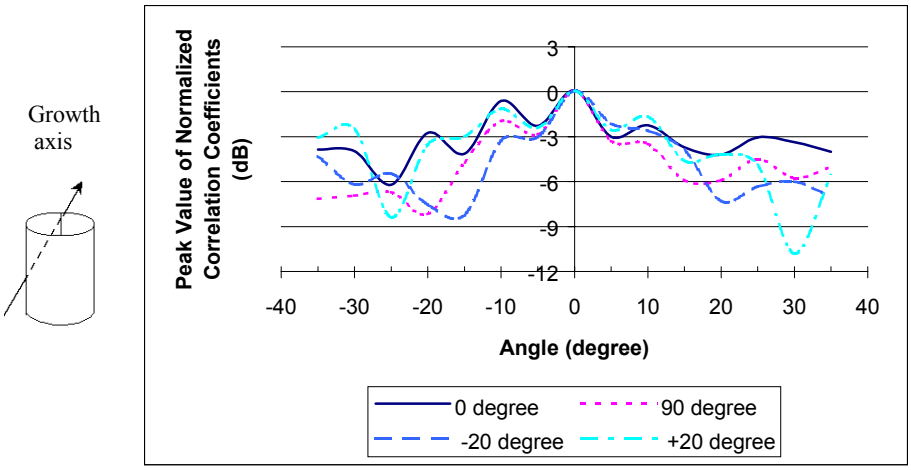

Figure 7.18 Comparison of normalized analytic correlation coefficient with different reference orientation for Sample 6 after light decalcification

Figure 7.19 to Figure 7.21 below show the comparison of the results of different reference orientations for the samples 7, 8 and 9 after they are heavily decalcified.

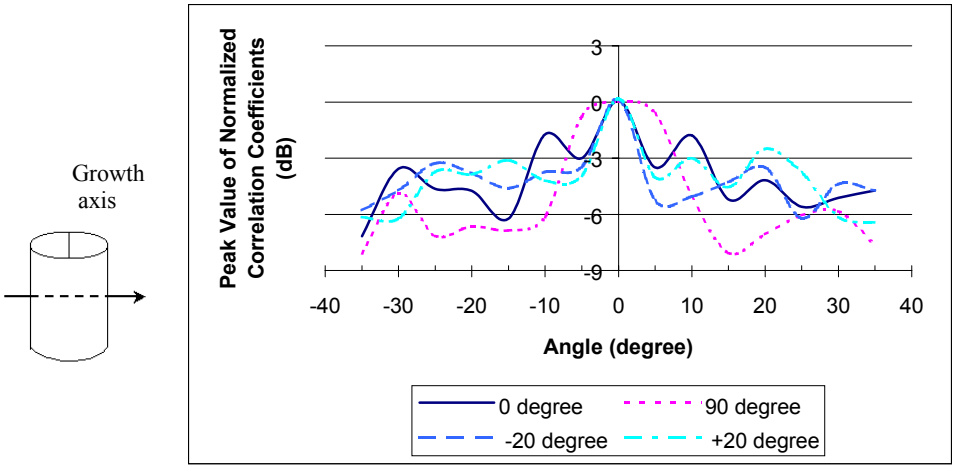

Figure 7.19 Comparison of normalized analytic correlation coefficient with different reference orientation for Sample 7 after heavy decalcification

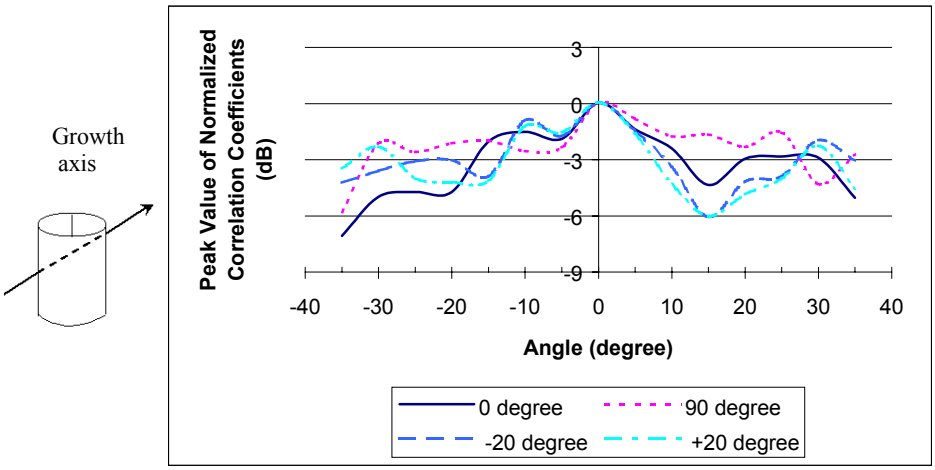

Figure 7.20 Comparison of normalized analytic correlation coefficient with different reference orientation for Sample 8 after heavy decalcification

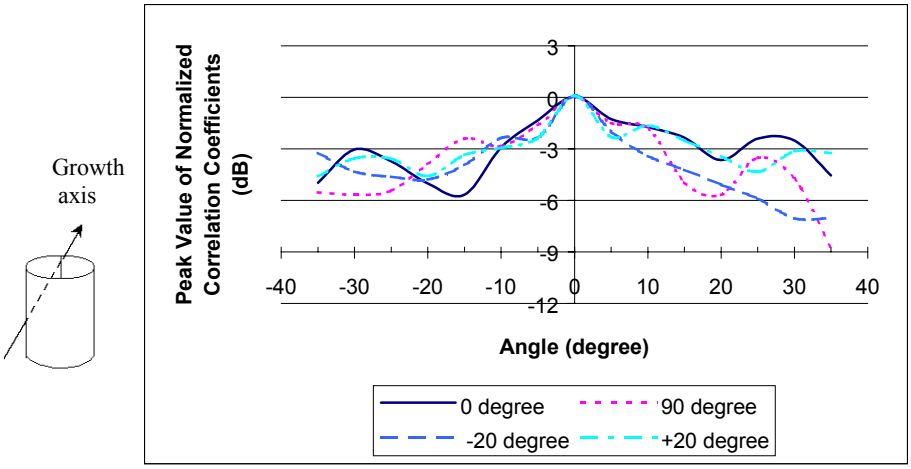

Figure 7.21Comparison of normalized analytic correlation coefficient with different reference orientation for Sample 9 after heavy decalcification

From Figure 7.15 to Figure 7.21, since the decorrelation curves of each sample for different angles are close or vary randomly, it is hard to draw any conclusion from the results.

7.3 Discussion

Based on simple visual inspection of the data, the results of angular decorrelation analysis indicate that there is no readily quantifiable association between the received signals in the coral sample measurements. That is, when the coral samples are oriented at a given reference orientation and then the receiving transducer is rotated, the values of the analytic correlation coefficients peak for the received signals decrease at first and then become independent of angle when the rotation angle of the receiving transducer $|\theta| > 20^{o}$. This depicts the complex variation of the received signal.

It is observed that there are no obvious differences among the curves of the analytic correlation coefficients peak values for each coral sample when the sample is

placed at several different angles (90^o, 20^o, -20^o). But we do find that there are differences among the decorrelation curves for coral samples with different growth axes. Specifically, when the coral samples are at their original density, the peak amplitudes of the normalized analytic correlation coefficients for sample 1, 4 and 7, which have their horizontal growth axes in measurement plane, decorrelate slower with angle than those of the other coral samples.

Furthermore, the decorrelation curves are also weakly related with densities of the coral samples, i.e., in general, the curves are wider when the coral samples are lightly decalcified than at original density, and then narrow again when the coral samples are heavily decalcified, which is similar as the BUA variation with the coral sample density.

The advantage of using angular decorrelation analysis is that it is applied to the entire signals to find the association between the received signals. For this research work, we feel that the results of the decorrelation might provide further information if the angle increment was set even smaller so that more fine detail of the signal change might be observed.

Chapter 8
Conclusion

In this thesis work, new approaches have been implemented for analyzing the received signals from a through-transmission ultrasound system, using coral samples as models for trabecular bones. The purpose is to evaluate new measurement approaches and new signal processing techniques so as to improve osteoporosis diagnosis methods. The effect of the growth axis direction of a given coral sample on the received signals was investigated by rotating the coral sample and by rotating the receiving transducer. The decalcification of the coral samples to different density levels was adopted to mimic the stages of osteoporosis.

Nine coral samples with the same dimensions were differentiated by their different growth axes and were categorized into three different sets, such that the distribution of growth axis directions was nearly the same in each set. Then three groups of coral samples were created by making each group contain three coral samples with different growth axis directions. The coral samples in the three different groups were then processed differently, such that one group would not be decalcified at all, one group would only be lightly decalcified and one group would first be lightly decalcified, and then later heavily decalcified. Three ultrasound parameters: BUA, analytic signal of the sample impulse response and the analytic signal of the cross-correlation coefficients, were extracted by the signal processing procedures applied to the received ultrasound signal. The parameters were calculated at different decalcification levels of the

corresponding coral samples. To find the correlation of the ultrasound parameters with the density and the microstructure of the coral sample, 3 non-ultrasonic parameters were used as the references for the physical characteristics of the coral sample. These are DEXA BMD value, dry weight of the coral sample and the physical observation of the coral sample growth axis. The results and the relationship between the ultrasound parameters and the non-ultrasound parameters have been discussed in the previous chapters.

Two signals components are observed in the received signal due to the ultrasound propagating through the coral sample. These components consist of a fast wave and a slow wave and are associated with the motions of the different components of the coral sample, as stated by Biot's theory. When rotating the coral sample, periodic variation of the fast wave amplitude, the fast wave velocity, the fast wave BUA, and the analytic signal of the fast wave impulse response function can be observed when the coral samples are at original density. This indicates that the fast wave signal may be an important signal which contains the information about the microstructure orientation for the coral sample. The fast wave may also provide information about the density variation of the coral sample, i.e., when the density of the coral sample decreases, the velocity of the fast wave at most rotation angles of the coral sample also decreases, but the velocity of the slow wave does not. This makes the two signals overlap when the coral sample density is below a certain level. In this case, there is no alternative but to process the entire signal instead of the fast wave and the slow wave separately.

A non-linear relationship is found between the BUA average value (fast wave and entire signal) and the BMD value, as well as between the average value of the peak

magnitude of the analytic signal of the impulse response and the BMD value, and between the decorrelation rate of the signal and the BMD value. That is, the average value of the BUA, the peak magnitude of the analytic signal of the impulse response and the width of the decorrelation curve actually increase as the density decreases to the intermediate density level, and then these values decrease as the density decreases further with heavy decalcification. This could possibly make the ultrasound prediction of osteoporosis harder if this also holds for the trabecular bone since it is difficult to distinguish the normal bone ultrasound parameter values from the osteoporotic ultrasound parameter values. Thus, further research is needed.

When the receiving transducer, rather than the coral sample, is rotated, the signals is much more complex to analyze although this approach has more practical usage. Improvements in measurement procedure and signal processing to obtain the ultrasound parameters may be needed to exclude the scattering and refraction signal effect from the inhomogeneous coral sample. For the three ultrasound parameters we have obtained, it is observed that the variations of coral sample BUA and the analytic signal of the coral sample impulse response are more sensitive to the growth axis variation and the density variation.

All in all, in this thesis work ultrasound has been shown to be a promising technique for osteoporosis prediction or fracture risk estimation since it is safe and contains the information not only related with the density but also the microstructure of the coral sample.

Bibliography

[1] T. Gillespie III and M.P. Gillespy. "Osteoporosis" , *Radiol. Clinics of N. Am*., Vol. 29, 1991, pp. 77-84

[2] E.A. Holland and L.F. Rogers, "Osteoporosis: Impact on the elderly, societal concerns, and the role of radiology," *Curr. Probl. Diagn. Radiol.*, Vol. 18, NO. 2., 1989, PP.41 -61

[3] S.A. Goldstein, "The mechanical properties of trabecular bone: Dependence on anatomic location and function", *J. Biomechanics*, Vol. 29, No. 12, 1987, pp. 1055 -1061

[4] G. Brandenburger et al, "In-vivo measurement of osteoporotic bone fragility with apparent velocity of ultrasound", *IEEE Ultrasonics Symp. Proc.*, Montreal, Canada, 1989, pp. 1023 – 1027.

[5] D.T. Baran et al, "Broadband ultrasound attenuation of the calcaneus predicts lumbar and femoral neck density in Caucasian women: A preliminary study", *Osteoporosis Int.*, Vol. 1, 1991, pp. 110 – 113.

[6] M.L. McKelvie et al, "In vitro comparison of Quantitative Computed Tomography and Broadband Ultrasonic Attenuation of Trabecular Bone", *Bone*, Vol. 10, 1989, pp. 101-104

[7] J. G. Berryman, "Confirmation of Biot's theory", *Appl. Phys. Lett*. Vol. 37, 1980, pp. 382-384

[8] E.Wakamatsu and H.A. Sissons, "The cancellous bone of the iliac crest", *Calcified Tissue Research*, Vol. 4, 1969, pp. 147 – 161

[9] A. Meunier et al. "Ultrasonic characterization of some pathological human femora", *1982 IEEE Ultrasonics Symposium Proceedings*, San Diego, CA, Oct. 1982, Ed. B.R. McAvoy, IEEE, New York 1982, pp. 713 – 717

[10] M. B. Tavakoli, "The effect of bone structure on ultrasonic attenuation and velocity". *Ultrasonics*, Vol. 30, No. 6, 1992, pp. 389 – 395

[11] M.L. McKelvie and S.B. Palmer. "The interaction of ultrasound with cancellous bone", *Phys. Med. Biol*., Vol. 36, No. 10. 1991, pp. 1331-1340

[12] Ralph Holmes, M.D., et al, "A Coralline Hydroxyapatite Bone Graft Substitute: Preliminary Report", *Clinical Orthopedics and Related Research*, pp. 252 – 262

[13] P. H. F. Nicholson, et al, "Do Quantitative Ultrasound Measurements Reflect Structure Independently of Density in Human Vertebral Cancellous Bone?", *Bone*, Vol. 23, No.5, November, 1998, pp. 425-431

[14] L.E. Kinsler, et al, "Fundamentals of Acoustics", 4th Edition, John Wiley & Sons, Inc. New York, 2000

[15] D.P. Orofino and P.C. Pedersen, "Efficient Angular Spectrum Decomposition for Acoustic Sources. Part I: Theory," *IEEE Transactions on Ultrasonics, Ferroelectrics, and Frequency Control*, May, 1993

[16] Frederick W. Kremkau, "Diagnostic Ultrasound", 5th Edition, W.B. Saunders Company. Philadelphia, 1998

[17] Elinor Ruth Hughes et al, "Ultrasonic Propagation in cancellous bone: A new stratified model", *Ultrasound in Med. & Biol*., Vol. 25, No.5, pp 811-821, 1999

[18] Abendschein W, Hyatt GW. "Ultrasonic and selected physical properties of bone", *Clin. Orthopedic Related Res* 1970, Vol. 69, pp. 294-301

[19] Carter DR, Hayes WC. "Compressive behavior of bone as a 2-phase porous structure". *J. Bone Joint Surg.* 1977, Vol. 59, pp.954-962

[20] Rho JY. "Ultrasonic characterization in determining elastic modulus of trabecular bone material", *Med. Biol. Eng. Computing* 1998; Vol. 36, pp.57 – 59

[21] Hosokawa A. Otani T. "Ultrasonic wave propagation in bovine cancellous bone", *J. Acoustic Soc Am.*, 1997, Vol. 101, pp. 558-562

[22] M.A Biot, "Theory of propagation of elastic waves in a fluid-saturated porous solid. I. Low-frequency range," *J. Acoust. Soc. Am.* 1958, Vol. 28, pp.168 – 178

[23] M.A Biot, "Theory of propagation of elastic waves in a fluid-saturated porous solid. II. Higher frequency range," *J. Acoust. Soc. Am.* 1958, Vol. 28, pp.179 – 191

[24] M.A. Biot, "Generalized theory of acoustic propagation in porous dissipative media," *J. Acoust. Soc. Am.* 1962, Vol. 34, pp.1254 – 1264

[25] McKelvie ML, Palmer SB. "The interactions of ultrasound with cancellous bone", *Phy. Med. Biol.* 1991, Vol. 36, pp. 1331-1340

[26] T. W. Geerits, O. Kelder. "Acoustic wave propagation through porous media: Theory and experiments", *J. Acoust. Soc. Am.*1997, Vol. 102(5), pp. 2495-2510

[27] D.L. Johnson, "Equivalence between fourth sound in liquid *He* II at low temperature and the Biot slow wave in consolidated porous media, ", *App. Phys. Lett*. 1980, Vol. 37, pp. 1065-1067

[28] D.L.Johnson and T.J.Plona, "Acoustic slow waves and the consolidation transition," *J. Accoust. Soc. Am.* 1982, Vol. 72, pp. 556 – 565

[29] Hubbuck ER, et al. "A theoretical study into factors affecting the Biot slow wave in cancellous bone" *ISVR Techn. Rep.* 271, 1998

[30] Robert C. Weast, et al. "CRC Handbook of Chemistry and Physics", *CRC Press,* 59th Edition, 1979.

[31] C.M.Langton, et al. "The measurement of broadband ultrasonic attenuation in cancellous bone", *Engineering in Medicine*, Vol. 13, No.2, 1984

[32] A. Hosokawa and T. Otani, "Acoustic anisotropy in bovine cancellous bone", *J. Accoust. Soc. Am.* Vol. 103(5), 1998, pp. 2718-2722

[33] A.J. Clarke, et al, "A Phantom for quantitative ultrasound of trabecular bone", *Phys. Med. Biol.* Vol. 39, 1994, pp1677-1687

[34] R. Hodgskinson, et al. "The non-linear relationship between BUA and porosity in cancellous bone", *Phys. Med. Biol.*. Vol. 41, 1996, pp. 2411-2420

[35] Louie J Serpe and Jae-Young Rho, "Broadband ultrasound attenuation value dependence on bone width *in vitro*", *Phys. Med. Biol.,* Vol. 41, 1996, pp.197-202

[36] C.M. Langton et al. "Prediction of Mechanical Properties of the Human Calcaneus by Broadband Ultrasonic Attenuation", *Bone,* Vol. 18, No. 6, 1996, pp.495-503

[37] Williams J L, et al. "Prediction of frequency and pore size dependent attenuation of ultrasound in trabecular bone using Biot's theory", *Mechanics of poroelasticity,* 1996, pp. 263-271

[38] Avinash C. Kak. "Digital Picture Processing", Version 1, *Academic Press*, 1976

[39] E. O. Brigham, et al. "An iterative technique for determining inverse filters", *IEEE Trans. Geosci. Electron. GE-6*, 1968, pp. 86-96

[40] P. M. Gammell. "Improved ultrasonic detection using the analytic signal magnitude", *Ultrasonics,* March, 1981, Vol. 19, pp. 41-44

[41] S. S. Kohles et al. "Ultrasound wave velocity measurement in small polymeric and cortical bone specimens", *Trans. ASME*, August, 1997, Vol. 119, pp. 232- 236